RICE UNIVERSITY

Inner Magnetospheric Modeling During Geomagnetic Active Times

by

Jian Yang

A THESIS SUBMITTED
IN PARTIAL FULFILLMENT OF THE
REQUIREMENTS FOR THE DEGREE

Doctor of Philosophy

APPROVED, THESIS COMMITTEE:

F To [signature]

Frank R. Toffoletto, Associate Professor
Physics and Astronomy Department
Chair of Thesis Committee

[signature]

Stanislav Sazykin, Senior Faculty Fellow
Physics and Astronomy Department

[signature]

Colin A. Zelt, Professor
Department of Earth Science

HOUSTON, TEXAS
OCTOBER, 2009

ABSTRACT

Inner Magnetospheric Modeling
During Geomagnetic Active Times

by
Jian Yang

In this thesis we show that the entropy parameter $PV^{5/3}$, where P is the pressure and V is the volume of a flux tube with unit magnetic flux, plays a central role in the earthward plasma convection from the near- and middle-Earth plasma sheet to the inner magnetosphere. This work presents a series of numerical simulations, investigating the relationship between the value of $PV^{5/3}$ and the different features of plasma earthward transport that occur during different types of events in geomagnetic active times. The simulations are conducted using the Rice-Convection-Model (RCM) and the Rice-Convection-Model-Equilibrium (RCM-E) that have carefully designed boundary conditions to simulate the effect of various values of $PV^{5/3}$. In Chapter 3 we present results of an RCM simulation of a sawtooth event where it is found that a dramatic reduction of $PV^{5/3}$ on the boundary along a wide range of local times produces interchange convection in the inner magnetosphere and drives spatially quasi-periodic Birkeland currents that suggest an explanation for the finger-like aurora usually observed during this type of event. In Chapter 4 we present results of an RCM-E simulation of an

isolated substorm, which is done by imposing depleted $PV^{5/3}$ (a bubble) in the expansion phase. The results of this simulation reproduce typical features of a substorm and agree fairly well with multipoint observations. Chapter 6 presents a detailed analysis of the RCM-E expansion phase simulation which indicates that the reconfigurations of $PV^{5/3}$, plasma pressure and magnetic field in an idealized bubble injection event can be quite complicated. Chapter 7 presents results of a superposed epoch study using Geotail data showing that the time variations of $PV^{5/3}$ are different in isolated substorms, pseudo-breakups and convection bay events, suggesting that bubbles have different characteristics in different modes of earthward transport. We follow this up with three corresponding RCM-E simulations by representing a sustained bubble, a transient bubble and sustained low $PV^{5/3}$ plasma along the boundary. The simulations are roughly consistent with theoretical suggestions, superposed epoch results and some other observations. These simulations provide a systematic description of inner magnetospheric configuration during various active events, suggesting the temporal and spatial characteristics of $PV^{5/3}$ in the plasma sheet as a key in the magnetospheric convection.

Acknowledgements

First of all, I would like to express my heartfelt gratitude to my advisor Dr. Frank Toffoletto for his invaluable advice and guidance. He shows unlimited patience in our discussions. He is not only tolerant to my unconstraint thoughts, but also expresses interests and encouragement, and unselfishly contributes his creative ideas, which always help me out of troubles and push me towards brighter directions in the research. I would like to thank Dr. Richard Wolf for many of his profound thoughts and warm encouragement during these years. I am very grateful to Dr. Stan Sazykin and Dr. Bob Spiro for their help and many useful discussions. I would like to thank Dr. Colin Zelt for serving as my committee member.

This work cannot be done without the great data provided by generous Pontus Brandt, Michael Henderson, Harald Frey and Michelle Thomsen. The sawtooth event simulation cannot be done without Nikolai Tsyganenko's substorm current wedge model source code. My work is also benefited by intuitive discussions with them, and Gary Erickson, Xiaoyan Xing, Xin Tao, Liang Wu, Colby Lemon, Chaosong Huang, Geoff Reeves, Mei-Ching Fok, Shin Ohtani, Larry Lyons, Mikhail Sitnov, Dae-Young Lee, Yukinaga Miyashita, Richard Kaufmann.

I am deepest grateful to my wife Huang, Hui and my mother Liu, Yuying, for their greatest support, encouragement and love.

To my father

Table of Contents

List of Figures

Chapter 1

Theory on Magnetospheric Convection

1.1 The Earth's Magnetosphere

The Earth internal magnetic field is compressed by and interacts with the solar wind plasma and interplanetary magnetic field. *Parker* [1958] theoretically predicted that the solar wind would be supersonic at Earth's orbit (1 AU). The following year the solar wind was first directly observed by the Soviet Luna 1 spacecraft, confirming Parker's predictions [*Ness*, 1968]. The solar wind mostly consists of protons and electrons, with typical values at 1 AU of 5cm^{-3} number density, velocity of 400km/s, proton temperature of 10^5K, and interplanetary magnetic field (IMF) [*Coleman et al.*, 1960] of 5nT in magnitude, but often with fairly large variations.

The interaction of the solar wind and the Earth's magnetosphere is of fundamental importance in the magnetic field configuration and plasma circulation in the whole magnetosphere as it is the major controller of energy input to the magnetosphere. In a simple picture, shown in Figure 1.1, merging of the IMF with the Earth's magnetic field at the magnetopause (MP) occurs when the IMF direction is pointed in a southward direction. When this occurs, the Earth's magnetic field reconfigures, leading to the connection of the internal magnetic field to the IMF, and the solar wind acts as a driver to add magnetic flux to the night side, which results in the storage of magnetic field energy in the magnetotail. When some internal instability threshold is reached, the magnetic field reconnects in the near magnetotail resulting in the removal of magnetic flux from the magnetotail. In ideal MHD, the electric field is always assumed perpendicular to the magnetic field, and the plasma particles are attached to specific magnetic field lines, until magnetic reconnection breaks this condition. In this ideal picture, the plasma is a perfect conductor and it is "frozen" to the magnetic field. Figure 1.1 provides an approximate picture of plasma circulation and energy transfer as a result of this frozen-in condition. This large scale plasma transport is called magnetospheric convection.

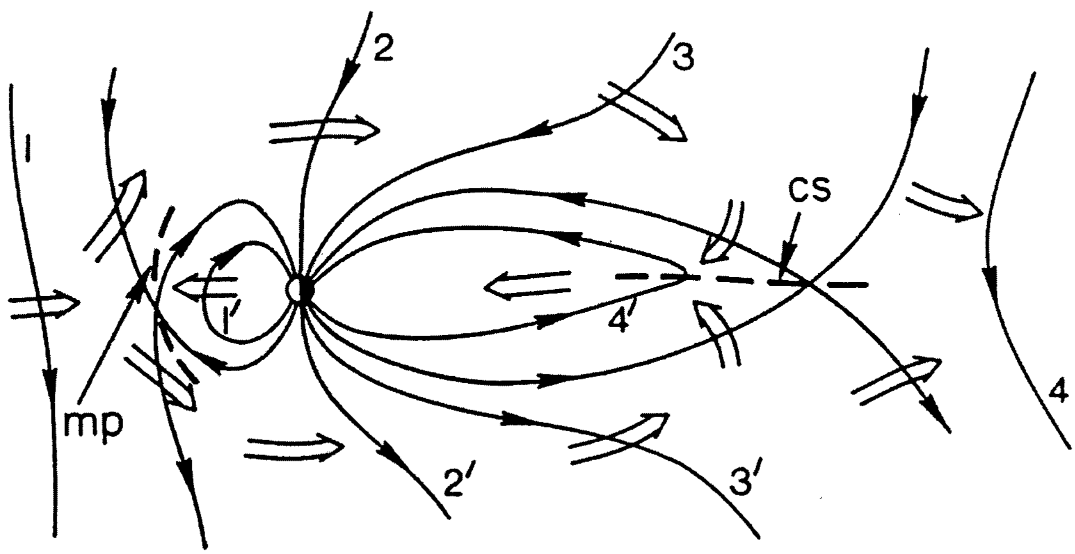

Figure 1.1. Sketch of the noon-midnight meridian plane view of the idealized large scale magnetospheric convection during southward IMF B_Z. Solid lines represent magnetic field lines with arrows representing directions. Large arrows represent plasma flow. The solar wind blows from left to right. In the closed field line region in the magnetosphere, the averaged plasma flow is sunward. Dashed lines are magnetopause (MP) and current sheet (CS) in the tail. Adapted from *Hill* [1983].

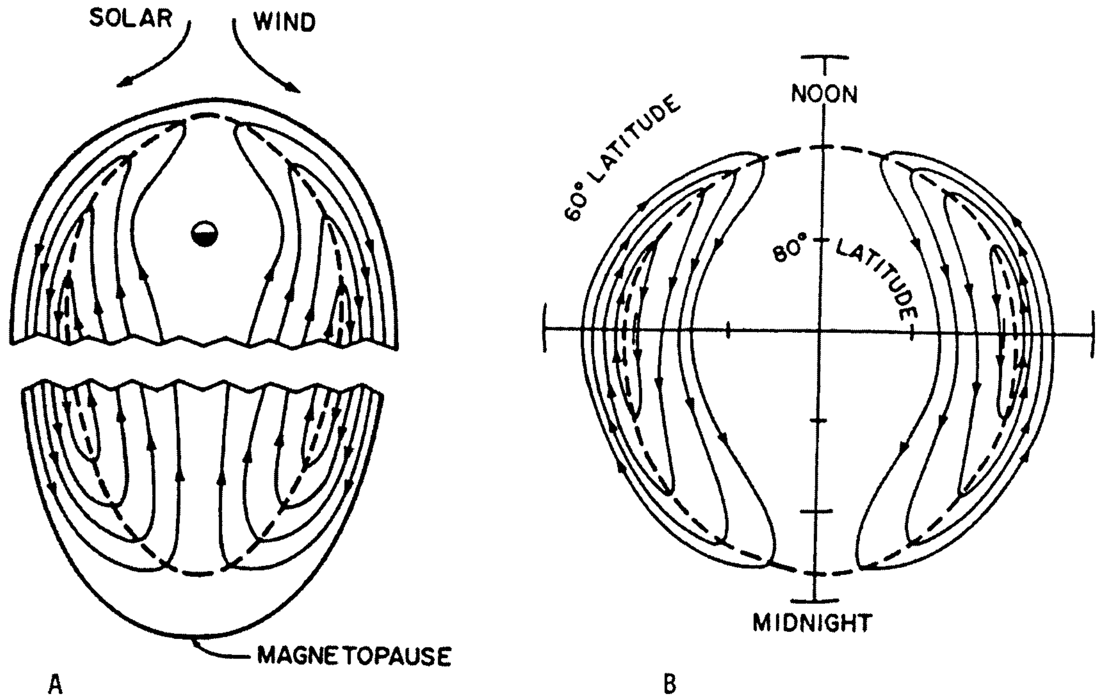

Figure 1.2. Sketch of equatorial view (A) and ionospheric view (B) of large scale magnetospheric convection. Solid lines with arrows represent plasma flow. The flow is generally sunward near midnight, but anti-sunward near flanks. The two plots are essentially equivalent due to the magnetic field mapping without parallel potential drops. The sun is to the top. Adapted from *Hill* [1983].

The Electromotive Force (EMF), defined as $\int \vec{E} \bullet dl = -\int \vec{v} \times \vec{B} \bullet dl$, is the difference of electric potential if the electric field is always perpendicular to the magnetic field. As shown in Figure 1.2A (equatorial view), anti-sunward flow is confined to the boundary layers of the magnetopause and the potential drop $\int \vec{E} \bullet dl$ is directly related to the strength of the flow. The integral $\int \vec{E} \bullet dl$ is measured by a spacecraft moving across the polar cap above the ionosphere and is called the polar cap potential (PCP) drop, it is the most common measure of the strength of global convection. On average, the PCP drop is about 40 kV during quiet times but can exceed 200kV during active times. The interpretation and parameterization of the PCP drop as a function of solar wind conditions have been studied extensively both theoretically and empirically [e.g., *Hill et al.*, 1976; *Reiff et al.*, 1981; *Siscoe et al.*, 2002]. For example, *Boyle et al.* [1997] developed a statistical relation, called Boyle index as shown in the following equation,

$$\mathrm{PCP} = 10^{-4}v^2 + 11.7B\sin^3(\theta/2)\ \mathrm{kV} \tag{1.1}$$

where v is the solar wind velocity in units of km/s, B is the magnitude of the interplanetary magnetic field in units of nano-Tesla, θ=arcos($B_Z/|B|$), B_Z is the IMF Z-component in GSM coordinate system. The GSM coordinate system is the geocentric solar magnetospheric system, which has its X-axis from the earth to the sun, its Y-axis as the cross product of the X-axis and the Earth's northern magnetic pole and its Z-axis that completes a right-handed orthogonal set [*Russell*, 1971].

If the IMF is southward and there are no parallel electric field (no electric potential drop along the magnetic field line), magnetospheric convection from an ionospheric view is a two-cell convection pattern (Figure 1.2B).

The Rice Convection Model (RCM) and its more advanced versions, e.g., the Rice Convection Model with an Equilibrium magnetic field, a.k.a., RCM-E (see Chapter 4 for details) are simulation models describing magnetospheric convection inside the closed magnetic field region. This region is inside the dashed line in Figure 1.2A, which is the inner magnetosphere with excluded magnetopause (outside dashed line), or the lower latitude region of the ionosphere outside the dashed line in Figure 1.2B.

The Earth's magnetosphere is far more complex than the sketches shown in Figures 1.1 and 1.2. Figure 1.3 shows a slightly more detailed picture. When the supersonic solar wind (from the left) comes across the Earth, a bow shock (white thick line) forms, decelerating the supersonic flow to sub-sonic. The Earth's magnetic field is compressed on the dayside and stretched to a tail-like configuration in the nightside. The yellow region centered near the equatorial plane on the nightside is the plasma sheet, which consists of closed magnetic field lines with magnitude of several to a couple of tens of nano-Tesla; these field lines have footprints in both the northern and southern ionospheres. The plasma sheet is usually several earth radii (R_E, $1R_E \approx 6400$km) thick, but can be compressed as thin as ~1000km during a substorm growth phase (see Chapter 4). Inside the central plasma sheet, the plasma particle pressure dominates over the magnetic field pressure ($B^2/2\mu_0$), and the plasma population can be represented as an isotropic distribution. Statistically, the flow in the plasma sheet is earthward (several to tens of km/s), but with large variations consisting of turbulent and sporadic fast earthward and tailward flows (up to 2000km/s) during geomagnetic active times. Since the magnetic field in the plasma sheet is tailward in the southern hemisphere and earthward in the northern hemisphere, a dawn-dusk current layer exists between them, which is known as the cross-tail current. In the higher latitude region, the lobes (light blue region) are in both northern and southern hemispheres with open field lines, in which the plasma pressure is generally negligible compared to the magnetic field pressure. The brown region earthward of the inner edge of the plasma sheet on the nightside and inside the magnetopause on the dayside is full of trapped particles, consisting of particles with energies of keV to hundreds of keV (the ring current) and the higher energy particles of the radiation belts. The plasma in the blue region inside the ring current is called plasmasphere, mainly consisting of dense ($\sim 10^3\,\mathrm{cm}^{-3}$) and cold ($\sim 1\mathrm{eV}$) plasma filled up to several earth radii in altitude around the earth.

It should be emphasized that, although the main aim of this thesis work is to describe the large scale convective processes in the inner magnetosphere, other processes in geospace are also important. As will be described later, microscopic wave-particle, chaotic motion are essential in making the plasma distribution isotropic; electron collisions with the upper atmosphere are essential for enhancing ionospheric conductance and the powering of the aurora; magnetic reconnection in the tail is directly related the substorms and storms, in which the convection in the magnetosphere is significantly changed. However, the physics of these processes are not explicitly included as a subject in this thesis, and their effects are included in very simple ways. For example, the elastic particle scattering is introduced as the an assumption to maintain an plasma isotropic distribution; electron precipitation [*Wolf et al.*, 1991] and ion charge exchange are highly parameterized using theoretical models (e.g., based on a model by *James Bishop*, private communication, 1988); magnetic reconnection in the near-Earth tail is considered for its role in reducing plasma content on the RCM tailward boundary (to be described in the following chapters).

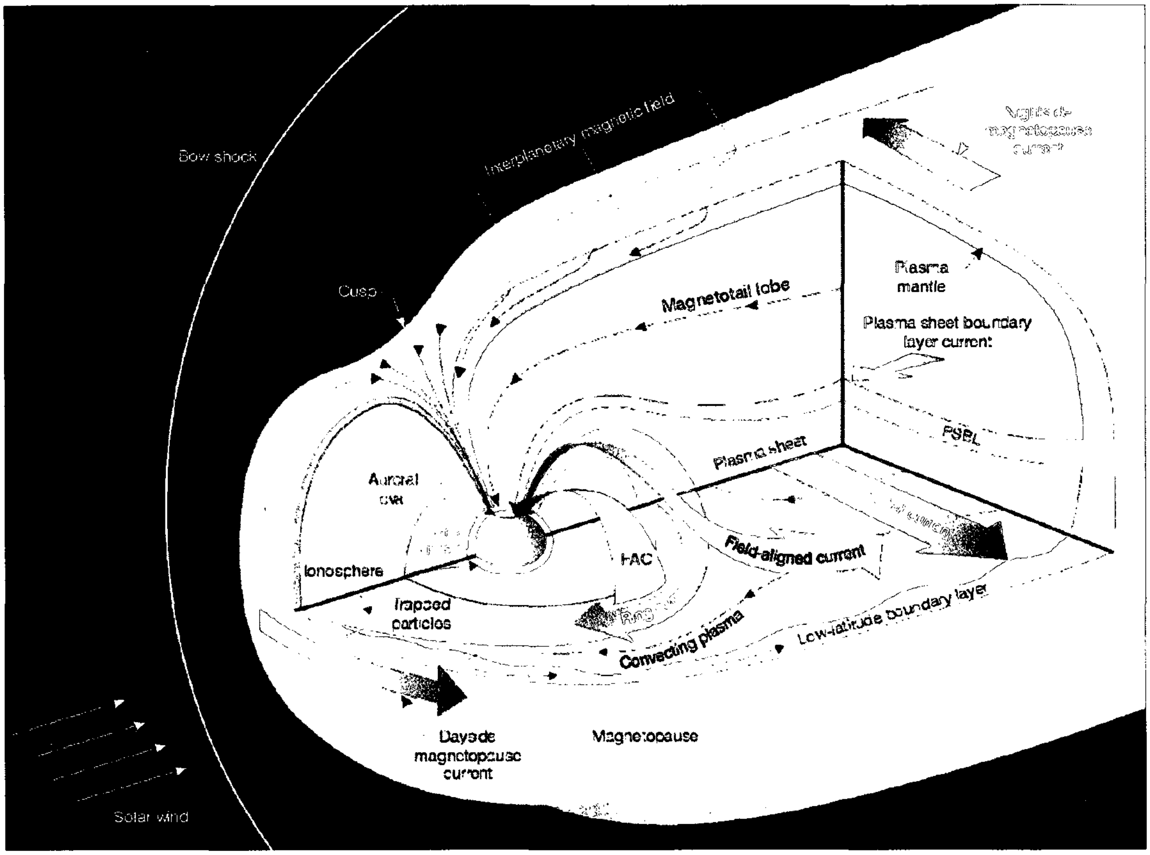

Figure 1.3. Cut-away drawing of the Earth's magnetosphere. The solid lines with arrows on the equatorial plane represent plasma flows. The solid lines linked to the high latitude region of the ionosphere represent the magnetic field. The sun is to the left. Figure Courtesy of *J. Burch*.

1.2 Geomagnetic storms and substorms

Over wide local times in the mid- and low-latitude region of the Earth's surface, the horizontal intensity of the magnetic field is observed to decrease and subsequently recover during geomagnetic storms [e.g., *Chapman and Bartels*, 1940]. The decrease is usually largely due to an enhancement of trapped particles carried by the symmetric and partial ring current (at nightside) at about 2~6 R_E altitude in which up to hundreds of keV energetic ions and electrons are drifting in westward and eastward directions, respectively. To monitor the intensity of storms, the Dst index was created. It is computed by averaging the horizontal component of magnetic field measured at four mid- and low-latitude ground stations, with an averaged quiet time baseline value subtracted off (http://swdcwww.kugi.kyoto-u.ac.jp/dstdir/dst2/onDstindex.html). In a storm main phase, the Dst index is increasingly negative; while during the recovery phase of the storm the Dst index increases from its minimum. On average, a geomagnetic storm main phase can last for several to up to twenty hours; while a geomagnetic storm recovery phase can last up to several days. For statistical studies, geomagnetic storms can be categorized as great or intense storms when their minima Dst<-100nT, as moderate from -100nT to -50nT, and as small or weak from -50nT to -30nT [*Sugiura and Chapman*, 1960]. Geomagnetic storms are primarily associated with large dawn-to-dusk electric field during the passage of southward IMF B_Z for sufficiently long periods [*Gonzalez et al.*, 1994]. *Gonzalez and Tsurutani* [1987] suggested that there is a threshold value of B_Z<-10nT for >3 hours for the presence of intense storms (minimum Dst<-100nT). Statistical studies showed that the overall geomagnetic activity is closely related to the phases of the solar cycle [e.g., *Sugiura*, 1980; *Gonzalez et al.*, 1990], which has 11-year periodicity characterized by the sunspot number. However, the intense storms tend to show dual peaks in one solar cycle, one near the solar maximum and the other 2-3 years after solar maximum, which is coincident with a prolonged intense negative IMF B_Z distribution [*Gonzalez et al.*, 1990]. On average, we expect about 5 intense storms per year in solar minimum years but about 20 per year when the sun is very active [*Gonzalez et al.*, 1990].

Substorms are less intense, shorter-lived and more frequent phenomena than storms. Substorms typically occur at a rate of four to five per day, and each can last up to several hours, including the growth phase, expansion phase and recovery phase. The substorm growth phase usually starts when IMF B_Z turns southward, which enhances the dayside reconnection so that it exceeds tail reconnection [e.g., *Hones*, 1977]. This unbalanced magnetic reconnection leads the storage of magnetic energy in the magnetotail. Typical features in the growth phase include the magnetic field stretching in the near-Earth plasma sheet, intensification of the cross-tail current, and equatorward motion of the poleward boundary of the aurora. The magnetic energy reservoir is tapped at substorm onset and transformed into particle kinetic and thermal energy in the substorm expansion phase. The most prominent phenomenon during substorm expansion phase is probably the brightening of the aurora, which is mainly attributed to the collision of atoms and particles in the ionosphere with energetic electrons that are precipitating from the magnetosphere onto the ionosphere along magnetic field lines. *Akasofu* [1964] invented the concept of the substorm when he studied the features of aurora. He summarized the auroral development from all-sky camera images, including the initial arc brightening and the following westward travelling surge in a complicated pattern in the post-midnight sector [*Akasofu*, 1968]. For many years there have been two popular scenarios concerning the cause of substorm onset. The Near-Earth-Neutral-Line model (NENL, or sometimes referred as the outside-in model) [e.g., *Baker et al.*, 1996] proposes that magnetic reconnection happens first in the magnetotail at X~-20R_E and that triggers subsequent processes in the plasma sheet, such as earthward flow inside 20 R_E and tailward flow flow outside 20 R_E, magnetic field dipolarization in the near-Earth plasma sheet, the formation of the substorm current wedge and associated ground magnetic field disturbances. In contrast, the current disruption model (CD, or sometimes simply referred as the inside-out model) proposes that current related instabilities occur first near the transition region, where the magnetic field configuration changes from dipole-like to tail-like, and that instability launches a rarefaction wave down to tail, which then can eventually trigger magnetic reconnection in the tail [*Lui*, 1996]. During the substorm expansion phase, the horizontal component of ground magnetic field shows substantial disturbance primarily due to the induction of the westward auroral electrojet in the ionosphere. The AU, AL and AE indices are created as a measure of the maximum strength of the eastward, westward and sum of auroral electrojets respectivtely and are based on measurements done at a number of auroral zone stations longitudinally around the world. Usually, the intensity of a substorm can be approximately gauged by the strength of AL or AE index, both of which increase sharply near the substorm onset and can remain as strong as about 1000nT in the substorm expansion phase; while the AU index has only slight change. An example of AE index is shown in Figure 4.1. The substorm recovery phase is a period when everything gradually returns to the pre-substorm condition.

The RCM or RCM-E based simulations described in this thesis do not directly model magnetic reconnection and instabilities thought associated with substorm onset, but only model the convective scale plasma transport, magnetic and electric field configurations that are the consequences of substorms. What the models can do is make specific predictions of the large scale consequences of various substorm scenarios that could be used to test the ideas related to substorm onset and expansion [e.g., *Toffoletto et al*, 1996].

The relationship of storms and substorms is still not very clear. An outstanding question is that whether storms develop as a result of frequently occurring substorms. Though intense substorms are usually observed during storm main phase, there are occasions where the aurora are quiet even during some storm main phase and substorms also happen during non-storm times [*Gonzalez et al.*, 1994].

There is an another widely used index in magnetospheric physics, called the Kp index, which is three-hour averaged and normalized between 0 and 9. The Kp index monitors the overall magnetic activities around the world and can be associated with both substorms and storms. In chapter 2, the Kp index is classified to represent geomagnetic quiet times (Kp=0 and 1), moderate times (Kp=2, 3 and 4) and active times (Kp≥5).

1.3 Motivation for this study

The geospace system can be viewed as a giant plasma physics laboratory that is rich in complex physical processes such as magnetic reconnection, plasma acceleration and deceleration, shock waves, wave-particle interactions and etc. The study presented in this thesis is to address some questions that occur during geomagnetic active times on the convective scale and to provide a powerful tool for the modeling plasma transport and the related electromagnetic dynamics. They are related to the following two questions:

(1) The role of the entropy parameter $PV^{5/3}$ (see section 2.1 for the definition) in the different modes of plasma earthward convection (substorm growth phase, isolated substorm expansion phase, sawtooth event, pseudo-breakups and convection bays);

(2) The injection of low $PV^{5/3}$ plasma from near-Earth plasma sheet and its effect on the inner magnetosphere (current system, magnetic field configuration, plasma pressure, aurora).

The application of the understanding of the geospace environment to society is commonly referred to as space weather. During geomagnetically active times, space weather effects can have severe impacts on human activities [e.g., *Moldwin*, 2008; *Bothmer and Daglis*, 2006]. For example, during large storms, the induced ground currents from magnetic field disturbances can damage electrical power grids in high and middle latitude countries, and can also damage the pipe lines by accelerating corrosion. The dynamic current systems in the ionosphere during active times are one of the major predictions in the RCM/RCM-E simulations since it calculate the currents generated in the magnetosphere-ionosphere coupling system. Satellite signals can also be disrupted by a disturbed ionosphere, during which communication to the ground can be lost. In the space environment, high energy particles can damage satellites during some major geomagnetic events. The energetic particle fluxes in the inner magnetosphere are also primary predictions in the RCM/RCM-E simulations.

In additional, aurora is of great interest to the general public. Typically the aurora can only be viewed in the high latitude regions, but in rare cases it can be seen in middle and even low latitude regions [e.g., *Rassoul et al.*, 1993; *Chung et al.*, 2007]. If accurate forecasts of the aurora were available, including the intensity, time, and location, that would attract a lot of attention by people who want to see aurora. The aurora, which is caused by the energetic particle precipitation to the ionosphere, is closely related to the magnetospheric phenomena such as substorms, storms and solar energetic particle events. The modeling presented in this thesis [*Yang et al.*, 2008; *Yang et al.*, 2009a, *Yang et al.*, 2009b] mainly focuses on the dynamics during substorms and storms, which can be further improved to a useful tool for forecasting the begotten aurora.

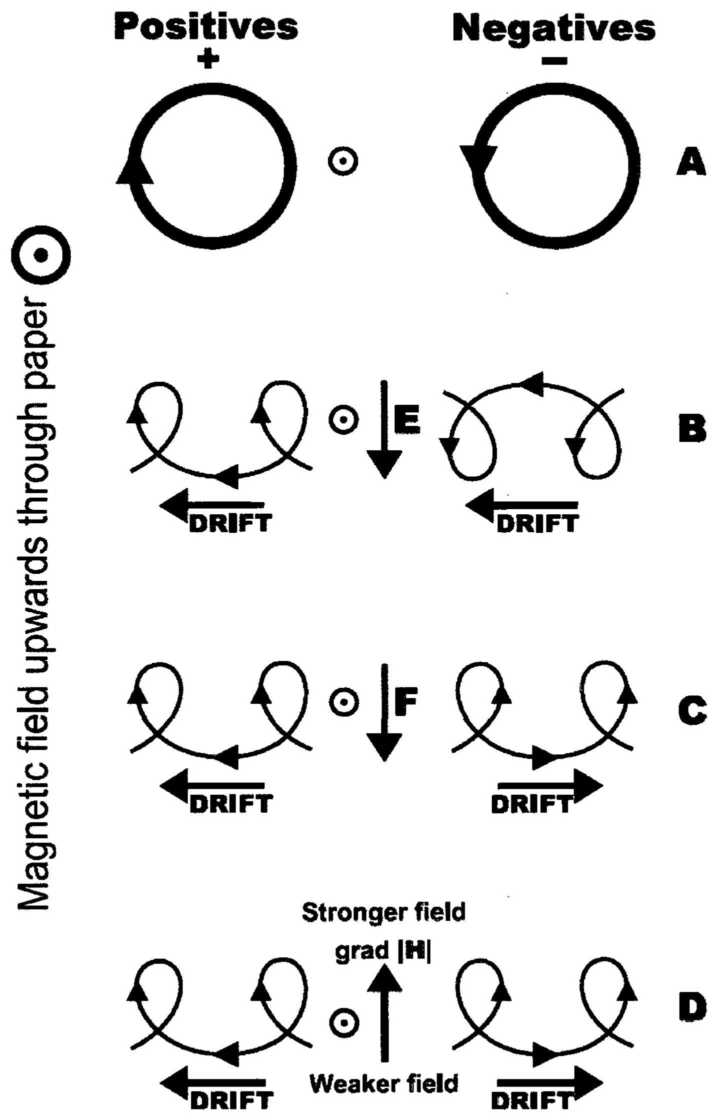

Figure 1.4. Single positive (left) and negative (right) particle trajectories in uniform magnetic field (A), in uniform magnetic field and perpendicular electric field (B), in uniform magnetic field and perpendicular external force (C) and non-uniform magnetic field (D). Figure from http://en.wikipedia.org/wiki/File:Charged-particle-drifts.svg

1.4 Particle motion in the inner and middle magnetosphere

1.4.1 Gyro motion, bounce motion and drift motion

The force on a single non-relativistic charged particle motion in an electric and magnetic field is described by the Lorentz force as

$$\vec{F} = q(\vec{E} + \vec{v} \times \vec{B}) \tag{1.2}$$

where $\vec{E}$ is the electric field, $\vec{B}$ is the magnetic field, $\vec{v}$ is the velocity of the particle, q is the particle charge.

In a simple case of uniform magnetic field and no electric field (Figure 1.4A), the particle gyrates in a circular motion in the plane perpendicular to the magnetic field. The radius from the guiding center to the particle is given as

$$r = \left| \frac{mV_{\perp}}{qB} \right| \tag{1.3}$$

where $V_{\perp}$ is the velocity perpendicular to the magnetic field. This is particle gyro motion.

If the parallel velocity of the particle is not zero, the particle will move freely along direction of the uniform magnetic field (left plot of Figure 1.5). If the magnetic field is convergent in the parallel direction, a particle moving towards the region of stronger magnetic field will increase its perpendicular energy at expense of its parallel energy, until the particle reaches a point where the parallel velocity reverses (middle plot of Figure 1.5). The particle bouncing back and forth inside this kind of convergent magnetic field is called bounce motion.

If an electric field is imposed perpendicular to the magnetic field, the particle will drift in the direction perpendicular to both electric field and magnetic field with the velocity of $\vec{v}_{EB} = \frac{\vec{E}\times\vec{B}}{B^2}$ regardless the charge of the particle (Figure 1.4B). It has been shown [e.g., *Northrop*, 1963] that if the magnetic field is inhomogeneous, a particle will experience gradient (Figure 1.4D) and curvature drift in the form of

$$\vec{v} = \frac{W_\perp \vec{B}\times\nabla B}{qB^3} + \frac{2W_\parallel \vec{B}\times\vec{\kappa}}{qB^2} \tag{1.4}$$

where the first term is the gradient drift and the second term is the curvature drift, $W_\perp = \frac{mv_\perp^2}{2}$ and $W_\parallel = \frac{mv_\parallel^2}{2}$ are kinetic energy perpendicular and parallel to the magnetic field, $\vec{\kappa} = (\hat{b}\bullet\nabla)\hat{b} = -\frac{\hat{R}_c}{R_c}$ is the curvature vector, R_c is the radius of curvature of the magnetic field line and $\hat{R}_c$ is a unit vector outward from the center of curvature.

Although the trajectory of a particle motion in an electromagnetic field can be extremely complicated, it is convenient to separate a particle motion into three components: (1) gyro motion about the magnetic field; (2) bounce motion along the magnetic field; (3) drift motion perpendicular to magnetic field. For a typical particle (approximately several eV to up to hundreds of keV electron, proton and oxygen inside 10 R_E) in the inner magnetosphere, the characteristic time scale for gyro motion is orders of magnitude shorter than the bounce motion; and the time scale of bounce motion is orders of magnitude shorter than the drift motion [*Schulz and Lanzerotti*, 1974]. With this ordering of timescales, three adiabatic invariants can be introduced associated with these three motions. The first adiabatic invariant is the magnetic moment of the particle gyro motion, $\mu = \frac{mv_\perp^2}{2B}$. The second adiabatic invariant is the longitudinal invariant associated with particle bounce motion, $J = \oint mv_{\parallel} ds$. The third adiabatic invariant, is associated with drift motion, and has been shown to be equivalent to the conserved magnetic flux encircled by the closed drift shell [*Northrop,* 1961]. Theoretical descriptions on the theory of adiabatic particle motion can be found in *Northrop* [1963] and *Roederer* [1970].

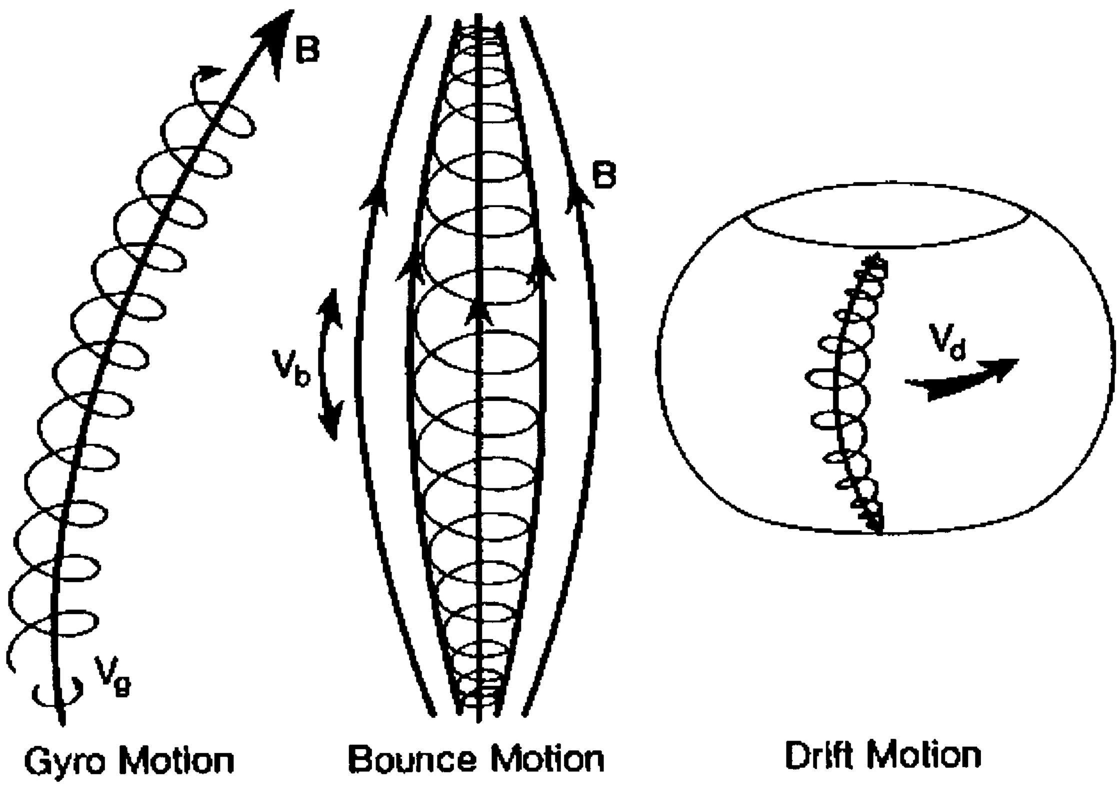

Figure 1.5. (left) Particle gyro motion perpendicular to the magnetic field and free motion along the magnetic field line direction. (middle) Bounce motion in the non-uniform magnetic tube. (right) Drift motion around the magnetic shells.

1.4.2 Bounce-averaged gradient/curvature drift of an isotropic plasma

Plasma in the plasma sheet undergoes strong elastic pitch angle scattering, and is observed to have an isotropic distribution [*Stiles et al.*, 1978]; this allows a very convenient simplification for the drift equations. With the isotropic distribution assumption, the gradient/curvature drift can be written as

$$\vec{V}_{GC} = \frac{\vec{B} \times \nabla W_K(\lambda_s)}{qB^2} \tag{1.5}$$

where W_K is the kinetic energy of the particle, $\lambda_s = W_K V^{2/3}$ is the energy invariant, $V = \int ds / B$ is the flux tube volume per unit magnetic flux. Therefore, the average bounce-averaged drift for a flux tube filled with isotropic plasma can be written as

$$\vec{V}_D = \vec{V}_{EB} + \vec{V}_{GC} = \frac{\vec{E} \times \vec{B}}{B^2} + \frac{\vec{B} \times \nabla W_K(\lambda_s)}{qB^2} \tag{1.6}$$

If the electric field is purely the potential electric field, the drift velocity can be written as

$$\vec{V}_D = \frac{\vec{B} \times \nabla (q\Phi + \lambda_s V^{-2/3})}{qB^2} \tag{1.7}$$

where Φ is electric potential. In the case of anisotropic distribution, the particle drift equation 1.6 remains the same form, but the particle kinetic energy W_K is not characterized by the energy invariant λ_s, but by the first and second adiabatic invariants [*Fok et al.*, 2001].

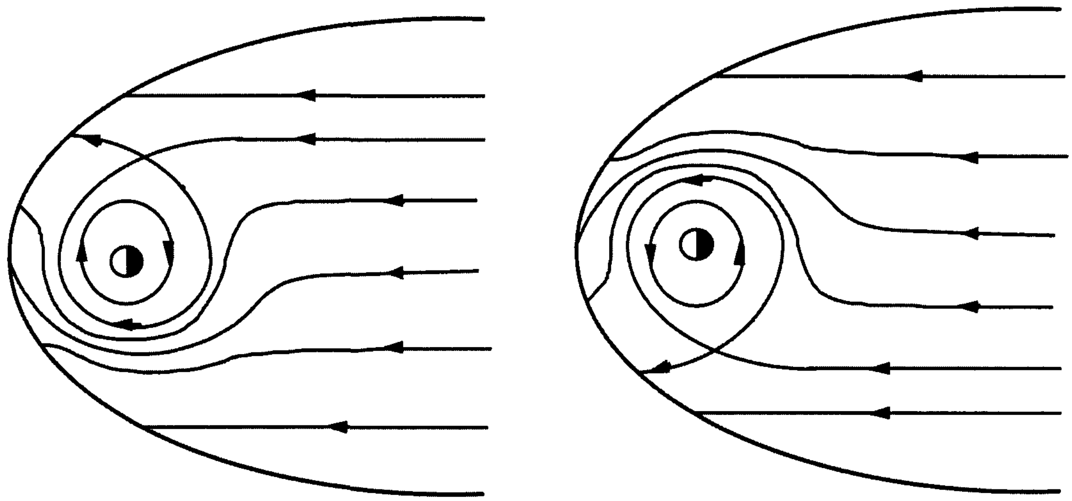

Figure 1.6. Theoretical sketch of equatorial view of the bounce-averaged particle drift paths for hot positive (left) and negative (right) particles. $E \times B$ and gradient/curvature drifts are included. The sun is to the left. Figure Courtesy of *R. A. Wolf.*

Generally, for hot plasma-sheet particles, the $E \times B$ drift is predominant in the magnetotail. Both ions and electrons convect in the sunward direction. The gradient/curvature drift is comparable to or exceeds the $E \times B$ drift in the near-Earth region, for example inside ~10R_E, where ions drift in the westward direction while electrons drift in the eastward direction (Figure 1.6).

1.4.3 Conservation laws

If we define the density invariant η_s (flux tube content) to be the number of particles per unit magnetic flux for a specific energy invariant λ_s and a specific chemical species, the particle conservation law can be written as

$$\frac{\partial \eta_s}{\partial t} + \vec{V}_D \bullet \nabla \eta_s = -\frac{\eta_s}{\tau_s} \tag{1.8}$$

where $\vec{V}_D$ is the bounce-averaged drift velocity described in equation 1.7, τ_s is the particle loss time, due to, for example, ion charge exchange with geo-corona neutral atoms and electron precipitation. This form of particle conservation is an expression equivalent to conservation of the density invariant η_s along a specific particle drift path if losses and sources are negligible. It has also been shown that the energy invariant λ_s and specific entropy parameter $P_s V^{5/3}$ are conserved along drift path if neither losses nor sources is included and there is no non-adiabatic heating,

$$\frac{\partial \lambda_s}{\partial t} + \vec{V}_D \bullet \nabla \lambda_s = 0 \tag{1.9}$$

$$\frac{\partial P_s V^{5/3}}{\partial t} + \vec{V}_D \bullet \nabla P_s V^{5/3} = 0 \tag{1.10}$$

where P_s is partial particle pressure due to specific chemical species for a given energy invariant λ_s.

The plasma moments can be calculated from energy and density invariants and flux tube volume as follows,

$$N = \frac{\sum_s \eta_s}{V} \tag{1.11}$$

$$T = \frac{\frac{2}{3} V^{-\frac{2}{3}} \sum_s \lambda_s \eta_s}{\sum_s \eta_s} \tag{1.12}$$

$$P V^{\frac{5}{3}} = \frac{2}{3} \sum_s \lambda_s \eta_s \tag{1.13}$$

The description of the bounce-averaged particle drift in equation 1.7 is very convenient. In principle, the specification of η_s for all invariant energy levels is equivalent to specifying the plasma distribution function (see equation 4.11 as an example). Then if we know the electric and magnetic field configuration in a specified closed field line region, we can compute the particle drift velocity as well as the conservation of η_s along each drift path according to equations 1.8. Then the plasma distribution and moments can be obtained everywhere inside the modeling region in equations 1.11, 1.12 and 1.13. This is one of cornerstones of the Rice Convection Model.

1.5 Magnetosphere-Ionosphere Coupling

1.5.1 Introduction to the ionosphere

In contrast to the magnetosphere with almost fully ionized collisionless plasma, the ionosphere is partially ionized caused by solar radiation and strong collisions. Therefore, the currents in the ionosphere are largely driven by the electric field rather than the magnetic and electric drift. The ionosphere is no longer treated as a perfect conductor as is the magnetosphere. The conductivity of the ionospheric plasma is essentially due to the collisions of electrons and ions with neutral molecules. The electric current in the rest frame of the Earth can be summarized in the following equation as

$$\vec{J} = \sigma_0(\vec{E}+\vec{v}_n\times\vec{B})_{\|}\widehat{e_B} + \sigma_1(\vec{E}+\vec{v}_n\times\vec{B})_{\perp} + \sigma_2\widehat{e_B}\times(\vec{E}+\vec{v}_n\times\vec{B}) \tag{1.14}$$

The first term is the current directly due to the electric field applied to the plasma and σ_0

is the "direct conductivity". $\vec{v}_n$ is the neutral particle velocity and $\widehat{e_B}$ is the unit vector along magnetic field direction. The second term is the Pedersen current perpendicular to the electric field and σ_1 is the Pedersen conductivity. The third term is the Hall current in the $-E \times B$ direction and σ_2 is the Hall conductivity.

The ionosphere, at an altitude of 100 to several hundred of kilometers above the Earth's surface, is usually modeled as a thin conducting shell. The "conductance" is considered a characteristic property of the shell, relating the surface current density and the electric field. The Pedersen and Hall conductance can be obtained by integrating the conductivity along altitude as

$$\Sigma_P = \int \sigma_1 dh \tag{1.15}$$

$$\Sigma_H = \int \sigma_2 dh \tag{1.16}$$

The current flowing across the field lines driven by the electrostatic potential Φ can be written as

$$\vec{J} = -\ddot{\Sigma} \bullet \nabla \Phi \tag{1.17}$$

The conductance tensor is defined as

$$\ddot{\Sigma} = \begin{pmatrix} \Sigma_{\theta\theta} & \Sigma_{\theta\phi} \\ \Sigma_{\phi\theta} & \Sigma_{\phi\phi} \end{pmatrix} \tag{1.18}$$

where

$$\Sigma_{\phi\phi} = \Sigma_{\theta\theta} \sin^2(I) \approx 2\Sigma_P \tag{1.19}$$

$$\Sigma_{\theta\phi} = -\Sigma_{\phi\theta} \approx \frac{2\Sigma_H}{\sin(I)} \tag{1.20}$$

where I is the dip angle of the magnetic field in the ionosphere.

1.5.2 Fundamental equation of magnetosphere-ionosphere coupling

In 1970, Vasyliunas proposed a mathematical description of the coupling of magnetospheric convection to the ionosphere, which is called the Vasyliunas equation [*Vasyliunas*, 1970] as

$$\frac{J_{\parallel in}}{B_{in}} - \frac{J_{\parallel is}}{B_{is}} = \frac{\hat{b}}{B} \bullet \nabla V \times \nabla P \tag{1.21}$$

where $J_{\parallel in}$ and $J_{\parallel is}$ are current densities down into the northern and southern ionosphere, B_{in} and B_{is} are magnitude of magnetic field at the point where field line intersects the ionospheric shell, V, P, B and $\hat{b}$ are flux tube volume, plasma pressure, magnetic field strength and unit vector along the magnetic field. Equation 1.21 can be derived from the adiabatic drift theory by applying the particle conservation law in the magnetosphere [*Wolf*, 1995] or from MHD theory [*Heinemann and Pontius*, 1990] or from the Vlasov equation [*Birmingham*, 1992].

The conservation of current $\nabla \bullet \vec{J} = 0$ on a conducting ionospheric shell can be expressed as

$$\nabla_h \bullet (-\vec{\Sigma} \bullet \nabla_h \Phi) = (J_{\parallel in} - J_{\parallel is}) \sin(I) \tag{1.22}$$

where the subscript "h" represents a 2D vector operator on the ionospheric shell surface, Φ is the electrostatic potential, and $\vec{\Sigma}$ is the field-line integrated conductivity tensor due to both hemispheres [*Fejer*, 1953].

Combining the Vasyliunas equation and the current conservation law, we get the Fundamental Equation of Magnetosphere-Ionosphere Coupling,

$$\nabla_h \cdot (-\Sigma \cdot \nabla_h \Phi) = \sin(I) B_i (\frac{\hat{b}}{B} \cdot \nabla V \times \nabla P) \tag{1.23}$$

where $B_i = B_{in} = B_{is}$ with north-south symmetry assumption. The M-I coupling equation enables us to calculate the electrostatic potential self-consistently, which is another cornerstone of the Rice Convection Model.

1.6 The Rice Convection Model

The Rice Convection Model (RCM) was developed to compute adiabatic drift of plasma in the inner and middle magnetosphere using equation (1.7), treating the plasma as many fluids with assumptions of slow-flow and isotropic pressure distribution along the magnetic field line. The electric field is calculated by solving the Vasyliunas equation [*Vasyliunas*, 1970] (equation 1.21) in the coupling of the magnetosphere and ionosphere (equation 1.23). Figure 1.76 shows a flowchart outlining the logical loop of the calculations is adapted from *Sazykin* [2000] (a modified version of the one originally developed by *Vasyliunas* [1970]). The current version of the RCM assumes that (1) the region is within the "slow-flow" region in the magnetosphere; and (2) the plasma distribution is isotropic. However a comprehensive ring current model (CRCM) which coupled the RCM to the Fok kinetic model is able to trace the plasma pitch angle distribution [*Fok et al.*, 2001]; (3) the field-aligned potential drop along each magnetic field line is assumed to be zero; however a version of the RCM is currently being developed and tested by *Yang Song*, *Stanislav Sazykin* and co-workers that uses a procedure similar to that of *Knight* [1973] to calculate field-aligned potential drops; (4) the Earth's dipole moment is aligned with the Earth's spin axis, but a version with non-zero dipolar tile angle is under development by *Bob Spiro* and co-workers; (5) the magnetic field is prescribed, but it is not necessarily force-balanced. The RCM is now coupled with the Magneto-Friction code (see section 4.3 for details), which calculates a self-consistent magnetic field in force equilibrium. The coupled code, which is called RCM-E (for equilibrium) was developed by *Frank Toffoletto*, *Colby Lemon, Stanislav Sazykin* and co-workers.

Essentially, the RCM inputs include the flux tube volume (computed from the magnetic field model), the plasma distribution and electric potential at the high latitude boundary, and the magnetic-field-integrated conductance due to solar radiation. The outputs include the flux tube content for each energy channel, the electric potential and the ionospheric conductance (including auroral enhancement). These parameters are calculated throughout the simulation region. The time cadence is about 1~2 seconds typically with ionospheric spatial grid resolution of 1~2 degrees in longitude and as fine as ~0.1 degrees in latitude near the aurora zone.

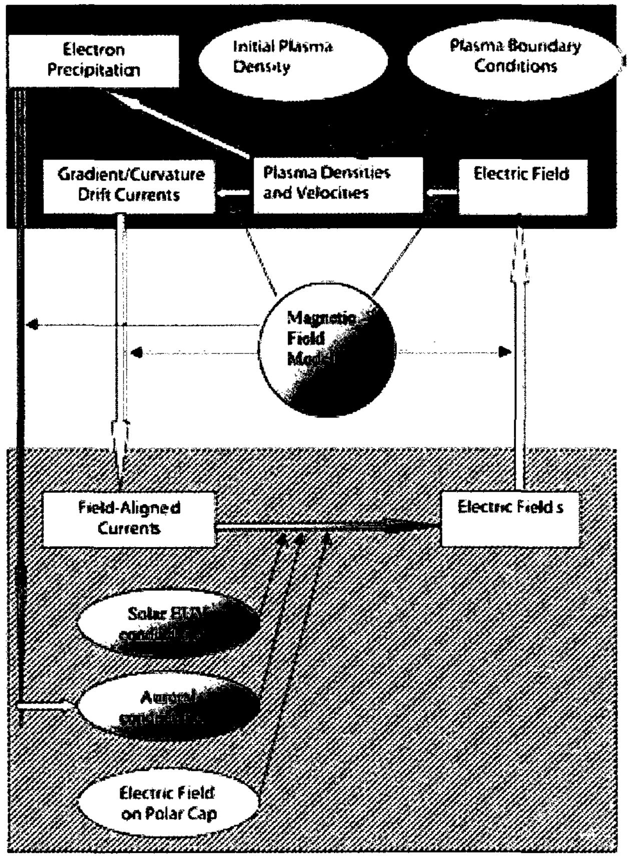

Figure 1.7. Flowchart that represents the logic structure of the Rice Convection Model. The upper and lower parts of the figure represent magnetospheric and ionospheric quantities, respectively. Rectangles are computed quantities, and the gray circle and ovals are model inputs. Thick white lines represent computations while black thin lines are for model inputs. Adapted from *Sazykin* [2000].

In Chapter 2, we review the important role of the entropy parameter $PV^{5/3}$ in the plasma transport from the plasma sheet to the inner magnetosphere and find that the values of $PV^{5/3}$ are statistically small in geomagnetic active times. In Chapter 3, An RCM simulation of a sawtooth event is presented to show the evidence of interchange instability in the inner magnetosphere. To theoretically calculate the magnetic field self-consistently, we introduce the RCM-E in Chapter 4 and present an isolated substorm event simulation using RCM-E, reproducing a number of typical features of the substorm. Chapter 5 presents results of how longitudinal grid-size dependence affects RCM and RCM-E simulations of low $PV^{5/3}$ injections. In Chapter 6, we show the reconfigurations of several key parameters in the course of an idealized isolated bubble injection by using RCM-E. A superposed epoch study of $PV^{5/3}$ during isolated substorms, pseudo-breakups and convection bays in Chapter 7 indicates that the time variations of $PV^{5/3}$ are distinct in the near-Earth plasma sheet, and preliminary RCM-E simulations by imposing different boundary conditions reproduces basic features of these three kinds of events.

Chapter 2

The role of $PV^{5/3}$ in plasma-sheet plasma transport

In this Chapter, we will review the role of $PV^{5/3}$ in the convection of plasmas in the near-Earth plasma sheet and the inner magnetosphere. We will discuss possible mechanisms for the formation of bubbles and will show results from RCM-based simulations of bubble injections. By applying the method developed by *Wolf et al.* [2006a], we will show results of the estimated $PV^{5/3}$ and V in the plasma sheet from a large number of Geotail data, binned by geomagnetic activities. What we found is that during geomagnetic active times, when the Kp index is higher, power law fits of $PV^{5/3}$ with radial distance suggests a higher probability of observing lower $PV^{5/3}$ bubbles in the near-Earth plasma sheet than during quiet times. We find that higher earthward velocities are correlated with slightly smaller $PV^{5/3}$ in the plasma sheet beyond 15 R_E. These results suggest that we may expect more earthward flowing bubbles during geomagnetic active times and that bubbles with lower $PV^{5/3}$ plasma convect significantly faster than the background plasma.

2.1 Pressure crisis

It can be shown that in slow flow ideal MHD, the entropy parameter $PV^{5/3}$ is conserved along a flow streamline. This quantity is associated with the entropy per particle s as

$$PV^{5/3} = K\exp(\frac{2s}{3}) \tag{2.1}$$

where K is a constant related to the number of particles in the flux tube, the shape of the plasma distribution function and the particle mass, but not to the temperature or density [*Wolf et al.*, 2009].

Erickson and Wolf [1980] found that if $PV^{5/3}$ is conserved during magnetospheric convection from distant and middle magnetotail to the inner magnetosphere, as suggested by ideal MHD theory, the inferred plasma pressure calculated from empirical magnetic field models is too high compared to observations in the inner magnetosphere. This has been called the "pressure crisis" or "pressure catastrophe", although it was pointed out by *Wolf et al.* [2009] that the phrase "entropy inconsistency" is a more accurate description. *Erickson and Wolf* [1980] further pointed out that the "pressure crisis" was not a result of an inaccuracy in the magnetic field model, since theoretical models that are in force balance can find configurations that are consistent with adiabatic convection but with a magnetic field that is much more stretched than statistical models [*Hau*, 1991; *Erickson*, 1992; *Wolf et al.*, 2009 and references therein], but can be resolved by a time-dependent process, such as substorms, which can non-adiabatically reduce $PV^{5/3}$. This insight was significant as it suggests that the substorms could be an inherent process which helps ease the "pressure crisis" even during stable solar wind conditions.

Recently, *Xing and Wolf* [2007] calculated the flux tube volume using an empirical magnetic field model combined with an empirical plasma pressure model, and showed that $PV^{5/3}$ in the plasma sheet decreases significantly from magnetotail to the inner magnetosphere (Figure 2.1). It has been shown that, for isotropic plasma which undergoes strong pitch angle scattering, pure ionospheric losses are insufficient to account for this reduction, because the precipitation loss for plasma sheet ions is on a time scale of many hours [*Kennel*, 1969] and the ion charge exchange time-scale with neutrals is slow outside geosynchronous orbit [*Fok et al.*, 1991]. *Borovsky et al.* [1998] estimated the ionospheric dissipation due to the auroral processes, concluding that the overall auroral loss can account for the observed entropy decrease. In the following two sections, two other mechanisms, gradient/curvature drifts and bubble injections, which are closely associated with plasma earthward steady convection and dynamic flows, will be reviewed briefly as the roles in reducing $PV^{5/3}$ in the inner magnetosphere.

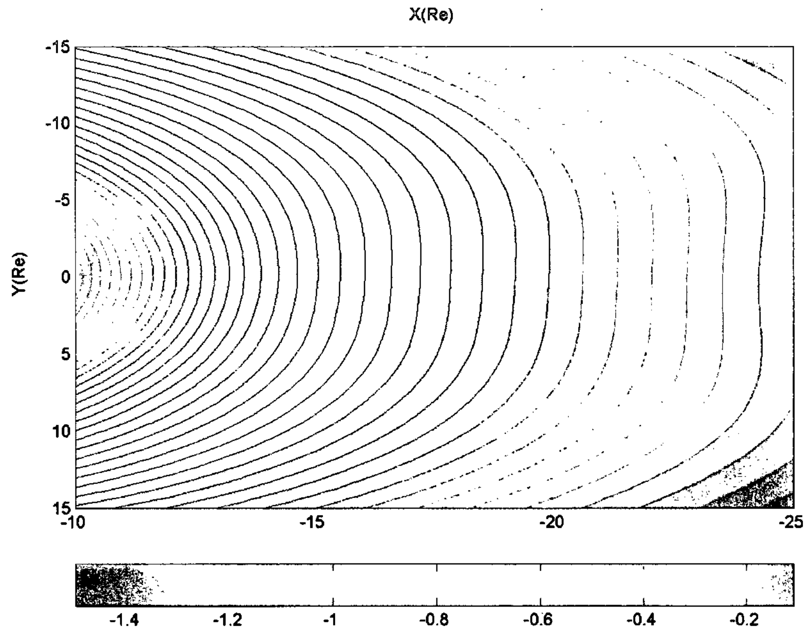

Figure 2.1. $PV^{5/3}$ (in $\log_{10}$(nPa(R_E/nT)$^{5/3}$)) on the equatorial plane. The plasma pressure is from empirical plasma-sheet plasma model [*Tsyganenko and Mukai*, 2003]; the flux tube volume is calculated based on statistical magnetic field model T96 [*Tsyganenko and Stern*, 1996]. The solar wind conditions are V_{sw}=400km/s, n_{sw}=5cm^{-3}, IMF B_X=5nT, B_Y=5nT and B_Z=5nT. Adapted from *Xing and Wolf* [2007].

2.2 The role of gradient/curvature drifts

As discussed in Chapter 1, including the bounce-averaged gradient/curvature drifts with the slow flow and isotropic assumption, one can show that specific entropy parameter $P_sV^{5/3}$ for each species s and associated energy invariant λ_s, is conserved along each drift trajectory. Gradient/curvature drifts, in contrast to $E \times B$ drifts, are energy-dependent, and energetic electrons and ions (greater than ~keV) drift eastward and westward as they approach the inner magnetosphere. Since these energetic particles (mainly ions) contribute substantially to the total plasma pressure, gradient/curvature drifts of hot plasma can alleviate the pressure crisis sufficiently especially during times of weak convection [e.g., *Kivelson and Spence* 1988; *Spence and Kivelson* 1990; 1993 and *Wang et al.* 2001].

During times of strong convection, it is still unclear whether gradient/curvature drifts are sufficiently strong to resolve the pressure crisis [*Wang et al.*, 2004; *Wang et al.*, 2009; *Wolf et al.*, 2009]. If the answer is affirmative, then the suggestion by *Erickson and Wolf* [1980] on the role of substorms in resolving the pressure crisis requires a major revision. However it has been shown that quasi-periodic substorms, known as sawtooth events [*Borovsky et al.*, 1993; *Belian et al.*, 1995], occur during fairly stable solar wind conditions that have prolonged periods of southward IMF B_Z. For example, the sawtooth event on 18 April 2002 [*Huang et al.*, 2003b; *Henderson et al.*, 2006a; *Clauer et al.*, 2006; *Ohtani et al.*, 2007; *Reeves et al.*, 2004; *Yang et al.*, 2008], may be an example of substorms that occurred as an internally-triggered process during strong convection and stable solar wind conditions. However, the physics behind triggering mechanisms are still controversial [e.g., *Lee et al.*, 2004; *Henderson et al.*, 2006a].

2.3 Plasma sheet bubble injection

2.3.1 Plasma sheet bubbles

Pontius and Wolf [1990] pointed out that flux tubes with depleted entropy parameter $PV^{5/3}$, as compared to their background, move earthward due to the interchange instability. Figure 2.2 illustrates a simple explanation of the interchange instability in the magnetic equatorial plane. Suppose a disturbance of plasma distribution occurred in the midnight region, represented by the earthward bulge of higher flux tube content η (left plot), gradient/curvature drifts move plasma westward, resulting in the buildup of positive particles at the westward edge of the bulge. In the coupled magnetosphere-ionosphere system, the Pedersen currents with closure via the FACs tend to flow eastward across the bulge, corresponding to an eastward electric field. The consequent E×B drift pushes the bulge tailward, stabilizing the system. Therefore, the plasma distribution shown in the left of Figure 2.2, with higher plasma content (equivalent to the $P_sV^{5/3}$) far away from the Earth, is interchange stable. In contrast, the configuration shown in the right, with higher plasma content nearer the Earth, is interchange unstable, because the resulting E×B drift tends to push the bulge more tailward.

Theoretically, *Xing and Wolf* [2007] showed that the plasma sheet is interchange stable, if

$$\nabla PV^{5/3} \bullet \nabla V > 0 \tag{2.2}$$

which is statistically satisfied since both $PV^{5/3}$ and V are roughly increasing in the radial direction (see Figure 2.1). However, this condition is violated if a bubble is embedded in the plasma sheet. A significant depletion of $PV^{5/3}$ would also result in a bubble that is moving earthward much faster than the average convection and/or gradient/curvature drift speeds. Since the bubble contains lower entropy plasma, which is non-adiabatically reduced locally in the magnetotail, the earthward motion of the bubble reduces the pressure crisis significantly.

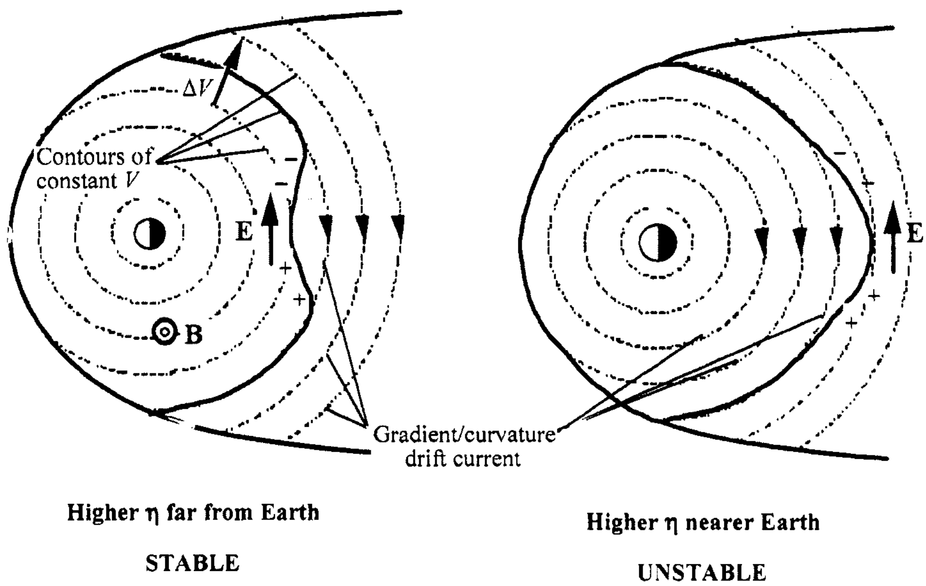

Figure 2.2. Equatorial view of flux tube content η distribution. (left) With higher η tailward of the solid thick line, the system is interchange stable; (right) with higher η earthward of the solid thick line, the system is interchange unstable. The dotted thin lines are contours of constant V, with arrows representing the gradient/curvature drift directions. Adapted from *Wolf* [1995].

A possible mechanism for the formation of such plasma bubbles in the plasma sheet is magnetic reconnection in the magnetotail [e.g., *Kan et al.* 2007]. Magnetic reconnection changes the topology of a magnetic field tube, cutting a long flux tube into a shorter closed flux tube and a plasmoid or flux rope that moves tailward (Figure 2.3). From the plasma physics point of view, the particles that are attached to the plasmoid or the flux rope are ejected into distant tail, which results in a reduction of $PV^{5/3}$ (equation 2.1). From a magnetic field point of view, the short closed flux tube has a (much) smaller flux tube volume, which also significantly reduces the entropy. *Sitnov et al.* [2005] estimated the change of the flux tube volume as

$$\delta V \sim \int_{plasmoid} \frac{ds}{B} \approx 4 \int_0^{h/2} \frac{dz}{B_z} \sim \frac{2h}{B_n} \tag{2.3}$$

where h is the thickness of the plasmoid in Z-direction, and B_n is the equatorial magnetic field strength before the formation of the plasmoid.

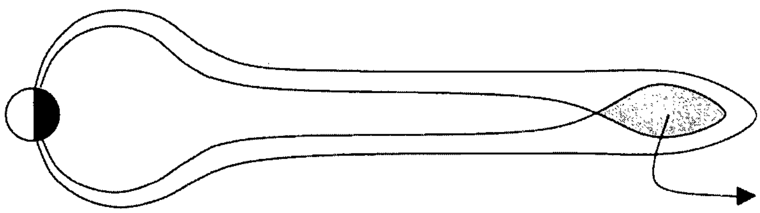

Figure 2.3. A cartoon of tailward escaping of a plasmoid. Adapted from *Sitnov et al.* [2005].

An alternative mechanism for bubble formation is the current disruption scenario [e.g., *Lui*, 1996], as sketched in Figure 2.4 (adapted from *Wolf et al.* [2009]). The top cartoon shows the magnetic field topology near the end of substorm growth phase, where the shaded area near the transition region usually has a large cross-tail current density and the magnetic field-line 2 is highly stretched. The bottom cartoon shows the topology after the magnetic field-line 2 slips earthward related to the plasma due to a current disruption instability. Consequently, the flux tube volume and the resulting $PV^{5/3}$ decrease between field lines 2 and 3, which form a bubble that moves earthward; while the flux tube volume and the resulting $PV^{5/3}$ increase between field lines 1 and 2, which form a blob that moves tailward.

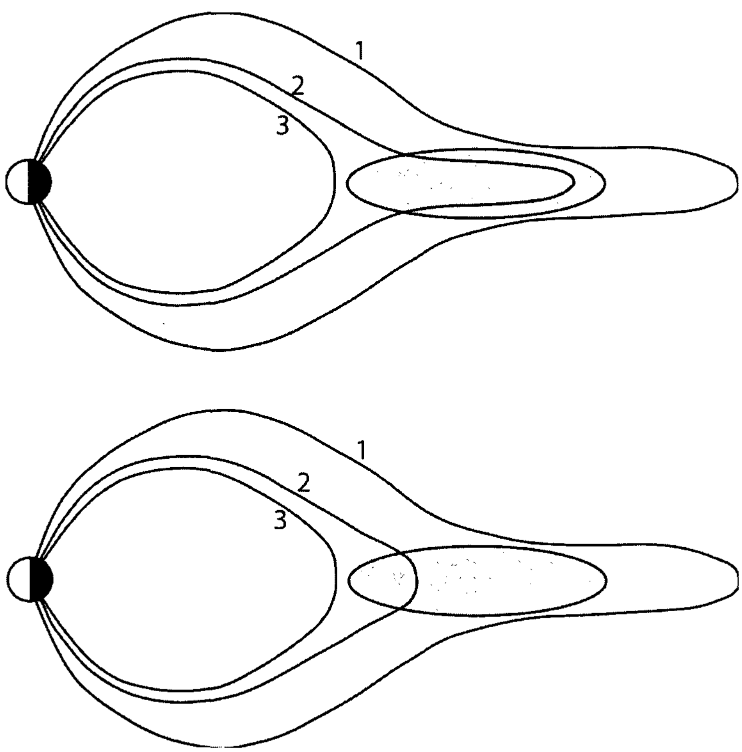

Figure 2.4. Cartoon of the formation of a bubble (and a blob) due to the current disruption [e.g., *Lui*, 1996]. The top shows the magnetic field configuration in the midnight meridian plane near the end of a growth phase. Magnetic field line 2 is highly stretched. After the current disruption, the magnetic field line 2 slips earthward with respect to the plasma, making the flux tube volume and $PV^{5/3}$ between field lines 2 and 3 decrease (a bubble) and making flux tube volume and $PV^{5/3}$ between 1 and 2 increase (a blob). Adapted from *Wolf et al.* [2009].

The Magnetosphere-Ionosphere (M-I) coupling model [e.g., *Lyons et al.*, 1996, *Lyons et al.*, 2003] also implies the depletion of $PV^{5/3}$ during early substorm expansion in the midnight sector. Figure 2.5 shows an equatorial view of gradient drift distribution in the near-Earth region. The model suggests that the increased gradient of plasma pressure near the end of growth phase results in the slower and faster gradient drift in the post- and pre-midnight sector. This particle drift divergence leads the reduction of plasma content in the flux tubes at midnight, which further leads to the formation of the current wedge and the initiation of substorm expansion phase.

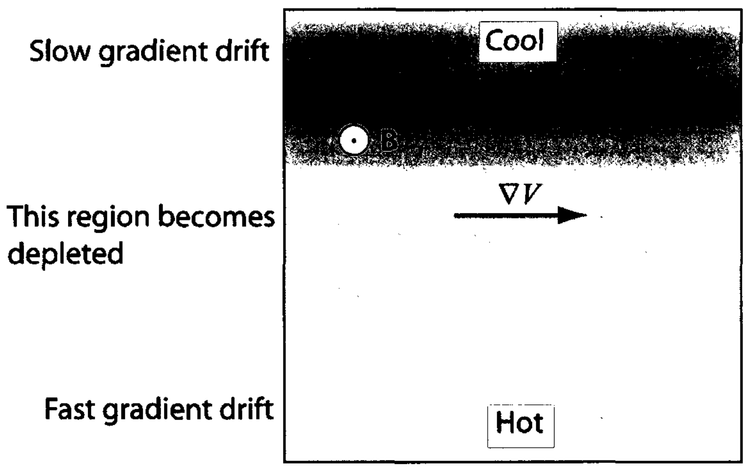

Figure 2.5. The cartoon of plasma depletion in the M-I coupling substorm model. The purple-blue and yellow-red regions represent slow and fast gradient drift regions in the post- and pre-midnight. The horizontal and vertical directions should be thought of as radial and azimuthal directions. The sun is to the left. The gradient of flux tube volume is tailward. Adapted from *Wolf* [2009 GEM Summer Workshop tutorial].

2.3.2 Previous observations and simulations of bubbles

A number of single spacecraft and multipoint observations have been related to plasma bubbles in the plasma sheet. At about the same time that the proposed picture of plasma bubbles by *Pontius and Wolf* [1990] was published, *Baumjohann et al.* [1990] and *Angelopoulos et al.* [1992] identified the bursty bulk flows (BBFs) in the plasma sheet; BBFs are viewed as an important component in the magnetotail dynamics affecting the nightside plasma circulation. Many observations of BBFs have been interpreted as plasma bubbles [e.g., *Sergeev et al.*, 1996b; *Kauristie et al.*, 2000; *Nakamura et al.*, 2001; *Walsh et al.*, 2009]. Using Geotail observations, *Lyons et al.* [2003] found that there was a reduction of the number of particles for all energy invariants inside bubbles during substorm injection events. *Walsh et al.* [2009] presented results from direct multipoint observations of a plasma bubble in the near-Earth plasma sheet, whose size was estimated to be less than $3R_E$ in cross-tail extent and about $4R_E$ along its direction of motion.

There are at least two approaches to the simulation of bubble injections/motions: one is MHD simulations and the other is based on RCM simulations. Following the theoretical idea of a "bubble" by *Pontius and Wolf* [1990], *Chen and Wolf* [1993, 1999] conducted 2D MHD simulations by launching thin filaments with depleted $PV^{5/3}$, and modeled the earthward flow of the filament and a subsequent reflection of the motion when the filament reached "terminal velocity" near Earth. An example of the time evolution of a filament, as calculated by *Chen and Wolf* [1999], is shown in Figure 2.6.

Full 3D MHD simulations have been done by *Birn et al.* [2004] who basically found results to be consistent with *Chen and Wolf* [1999].

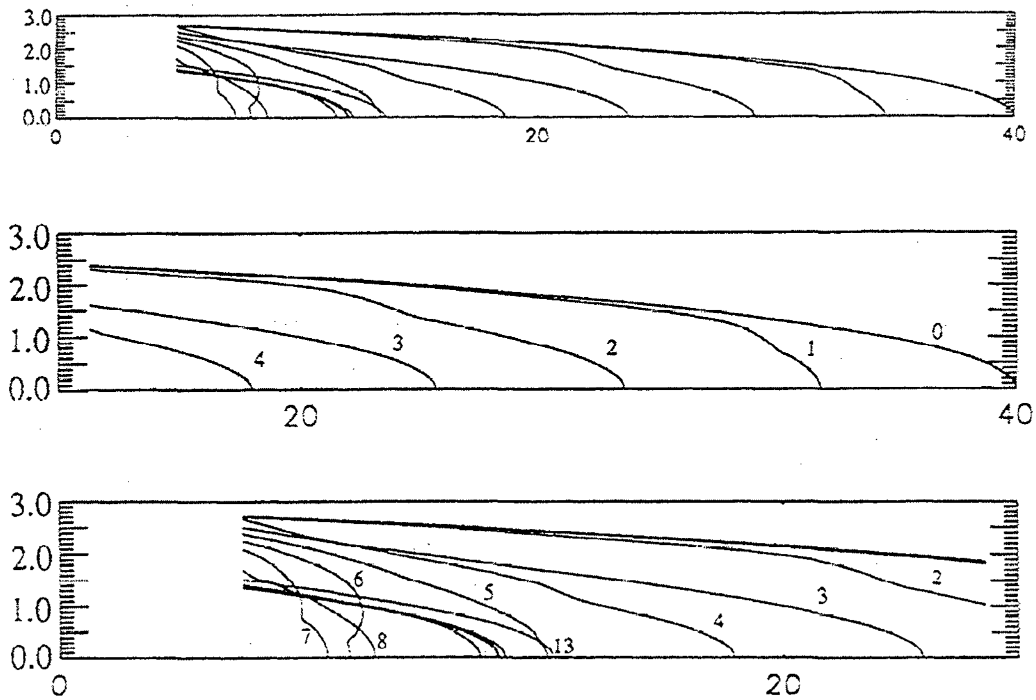

Figure 2.6. The top panel shows the shapes and positions of the filament at different times in XZ plane. The motion is earthward. The bottom two panels show the enlarged views of tailward and earthward portion of the top panel. The numbers near each field line represent time in units of minutes. Adapted from *Chen and Wolf* [1999].

The RCM-based simulations have been performed by *Zhang et al.* [2008] for an idealized bubble injection and *Zhang et al.* [2009a, 2009b] for a real bubble injection during an isolated substorm event. The bubble injection from the tail to the inner magnetosphere (its equivalent picture from high latitude region to low latitude region on the ionosphere is illustrated in Figure 2.7), was initiated by placing a region of depleted

$PV^{5/3}$ along a midnight-centered section of the RCM high latitude boundary. The RCM simulation of an ideal bubble injection event [*Zhang et al.*, 2008], showed an enhanced partial ring current after the plasma was depleted at the high latitude region. *Zhang et al.* [2009a, 2009b] presented a more sophisticated RCM simulation for a real substorm event, where the magnetic field was carefully adjusted to match the Geotail observations at around -9R_E near the midnight sector. Figure 2.8 shows the overview results. The magnetic field model used T89 model adjusted to agree with Geotail measured plasma pressure and magnetic field using solutions of Grad-Shafranov equation to represent the magnetic field stretching during substorm growth phase and the Tsyganenko substorm current wedge model [*Tsyganenko*, 1997] to represent the field dipolarization during substorm expansion phase. Their results well presented (1) the region-1 sense FACs along the SCW; (2) the resemblance of a dent-like plasma injection boundary [*McIlwain*, 1974]; (3) the prompt penetration of electric field [*Fejer et al.*, 1990] at subauroral latitudes. However, their modeling can be improved by adding the following features in the RCM [*Zhang et al.*, 2009b]: (1) a more sophisticated SCW model for greater consistency with plasma pressure; (2) a model of field-aligned potential drops; (3) the azimuthal expansion of the injection bubble; (4) a non-zero-tilted RCM.

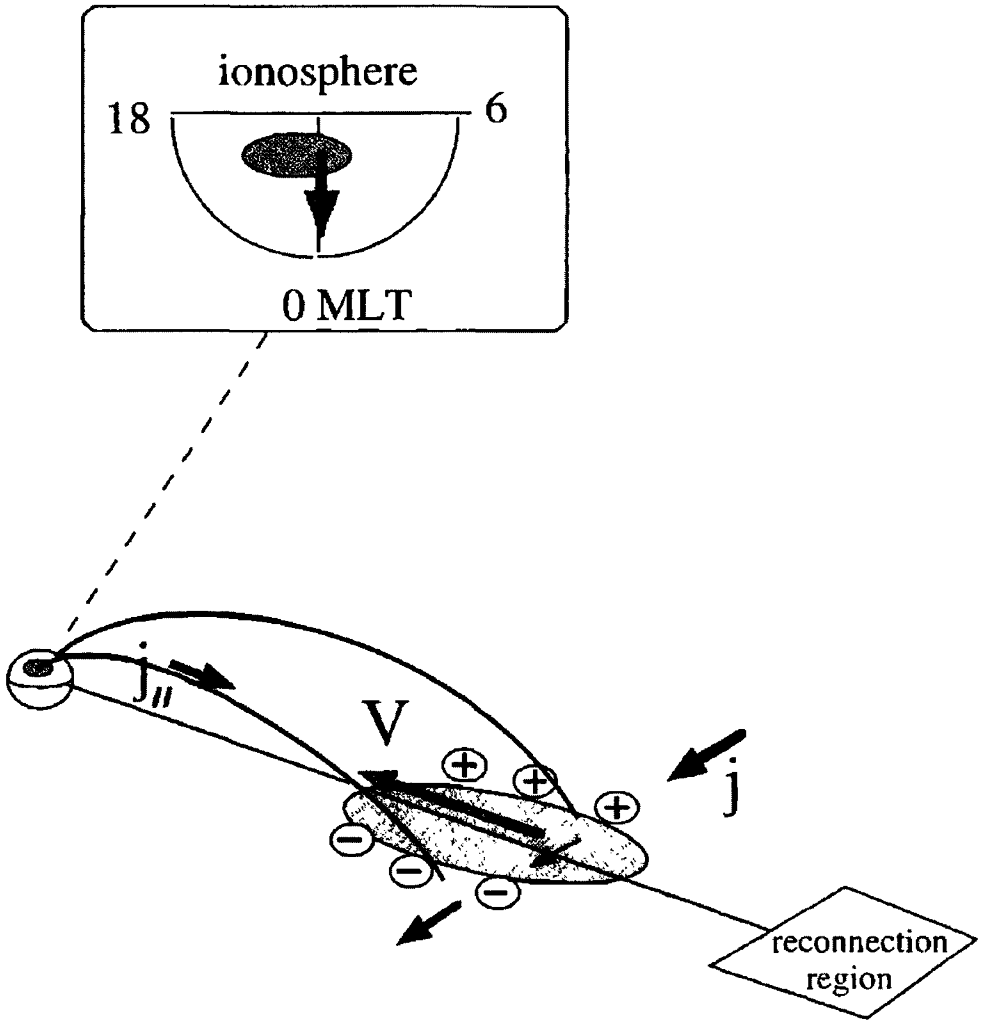

Figure 2.7. Conceptual sketch of the plasma bubble and its relation to the ionospheric plasma transport. Adapted from *Nakamura et al.* [2001].

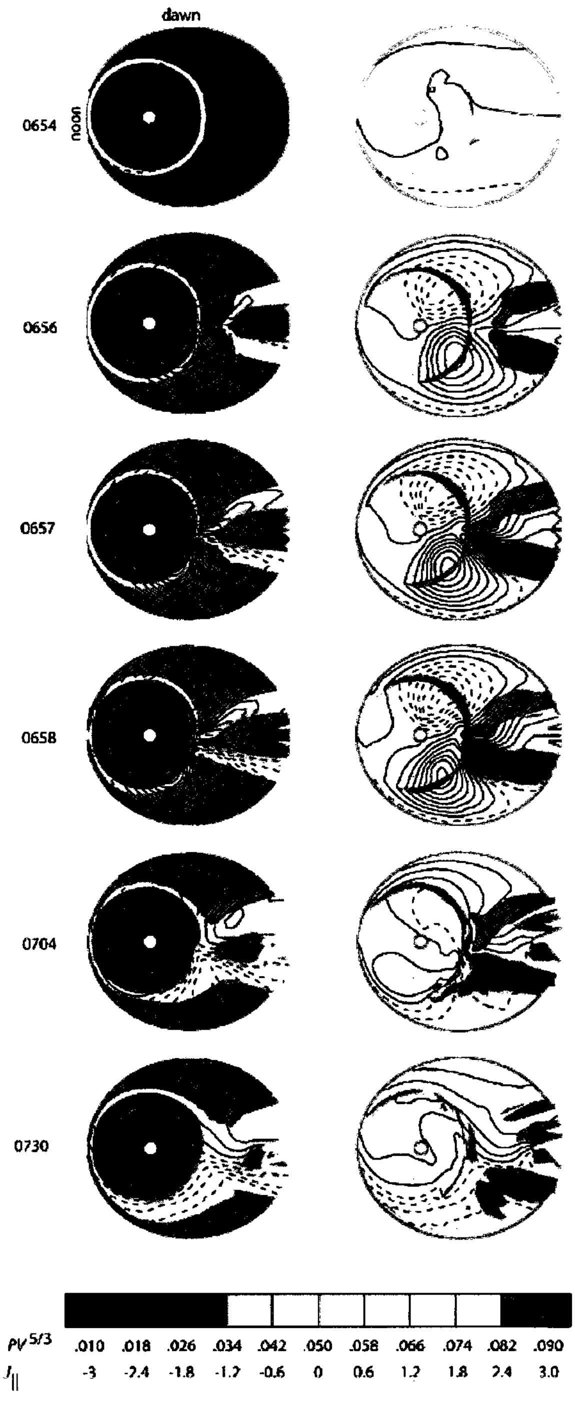

Figure 2.8. The equatorial view of $PV^{5/3}$ (left, in units of nPa(R_E/nT)$^{5/3}$) and FACs (right, in units of μA/m^2). The line contours are effective equipotentials every 5kV, with (left) and without (right) corotation potentials. The substorm onset is at 0655UT. The sun is to the left. The purple circles represent geosynchronous orbit. Adapted from *Zhang et al.* [2009b].

2.4 Estimation of $PV^{5/3}$ in the plasma sheet

The precise calculation of $PV^{5/3}$ at any point in the magnetosphere is a challenge. This requires an evaluation of the flux tube volume V which is defined as an integral quantity, where only single point measurements are available. However, statistical values of the $PV^{5/3}$ can be estimated by combining empirical magnetic field models with empirical models of the plasma sheet plasma. *Xing and Wolf* [2007] calculated $PV^{5/3}$, using T96 [*Tsyganenko*, 1995; *Tsyganenko and Stern*, 1996] magnetic field models and the Tsyganenko-Mukai (TM2003) plasma-sheet plasma pressure model [*Tsyganenko and Mukai*, 2003] for the nominal solar wind conditions V_{sw}=400km/s, n_{sw}=5cm^{-3}, IMF B_X=5nT, IMF B_Y=5nT, IMF B_Z=5nT, to produce Figure 2.1.

It is of interest to evaluate the $PV^{5/3}$ for a specific event rather than statistically. To this end, *Wolf et al.* [2006a] developed a model, based on a simplified equilibrated current sheet model derived from Magneto-Friction equilibrium code [*Lemon et al.*, 2003], to estimate the magnetic equatorial $PV^{5/3}$ from a single spacecraft measurement. Figure 2.9 illustrates the basic idea. The model starts from a force-balanced 2D Grad-Shafranov equation [*Voigt and Wolf*, 1988], but extrapolates the solution to a more realistic current sheet model parameterized with several coefficients. These coefficients are determined by fitting to various relaxed Tsyganenko models. Two examples of bubble injection events during substorms observed by Geotail spacecraft near the midnight at the near-Earth plasma sheet show a clear reduction of $PV^{5/3}$ after substorm onsets [*Wolf et al.*, 2006a]. For a reliably accurate estimation, this method should be used only when the spacecraft is close to the neutral sheet, i.e. when,

$$0 < \sqrt{B_x^2 + B_y^2} / B_z < 4 \tag{2.4}$$

where B_X, B_Y and B_Z are three components of the locally observed magnetic field. They found that the extrapolation error of the estimation of equatorial V using the magnetic configuration off the equatorial plane increases systematically with increasing ratio of $\sqrt{B_x^2 + B_y^2} / B_z$. The overall error of the method for the observation satisfying equation 2.4 is ~15% for V and ~20%-30% for $PV^{5/3}$. They also found that their method can overestimate the $PV^{5/3}$ by a factor of 2~3 when applied to a fast moving flux tube, because the bubble has not relaxed to equilibrium with the background plasmas.

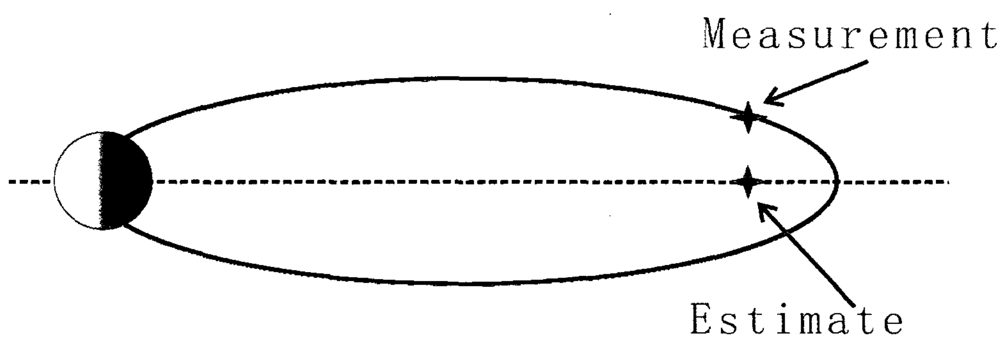

Figure 2.9. Conceptual sketch of the idea for estimating the equatorial $PV^{5/3}$ and V (at red star) from single spacecraft measurements (at blue star) near the center of the current sheet. The dotted line denotes the current sheet and the solid curve denotes the magnetic field line threading the spacecraft. The sun is to the left.

2.5 Statistical results of $PV^{5/3}$ and V in the plasma sheet derived from Geotail data

In this section we show results of applying the method developed by *Wolf et al.* [2006a], to estimate $PV^{5/3}$ and V in the plasma sheet from Geotail data.

2.5.1 Data selection criteria

The data set we use here is the Geotail plasma and magnetic field data from year 1993-2005. The plasma moments (pressure, number density and temperature) are from the Geotail Low Energy Particle (LEP) instrument, which measures the <40keV ion moments averaged every 12 seconds [*Mukai et al.*, 1994]. We assume a constant ratio of the ion and electron temperatures as 7.2 [*Baumjohann et al.*, 1989]. The magnetic field data is 3 seconds averaged from magnetic field instrument (MGF) [*Kokubun et al.*, 1994].

We selected Geotail data points measured in the central plasma sheet with the following criteria

(1) plasma flow velocity was less than 400km/s and earthward;

(2) $0 < \sqrt{B_x^2 + B_y^2} / B_z < 1.5$;

(3) proton temperature and number density ratio T_p/N_p>5.0 keV/cm^{-3};

(4) plasma beta value β was larger than 0.5.

The data points were averaged over 1 minute. Criterion (1) selects earthward flows in this study that are not bursty bulk flows (BBFs) according to generally accepted criteria [e.g., *Baumjohann et al.*, 1990; *Angelopoulos et al.*, 1992]. Criterion (2) requires a more restrictive limitation on the spacecraft location with respect to the neutral sheet, which is aimed at reducing the extrapolation error introduced by the method itself. Criterion (3) eliminates magnetosheath and low latitude boundary layer (LLBL) data points [*Tsyganenko and Mukai,* 2003]. Criterion (4) limits the data points to the central plasma sheet. A total of 78893 data points are used in this study.

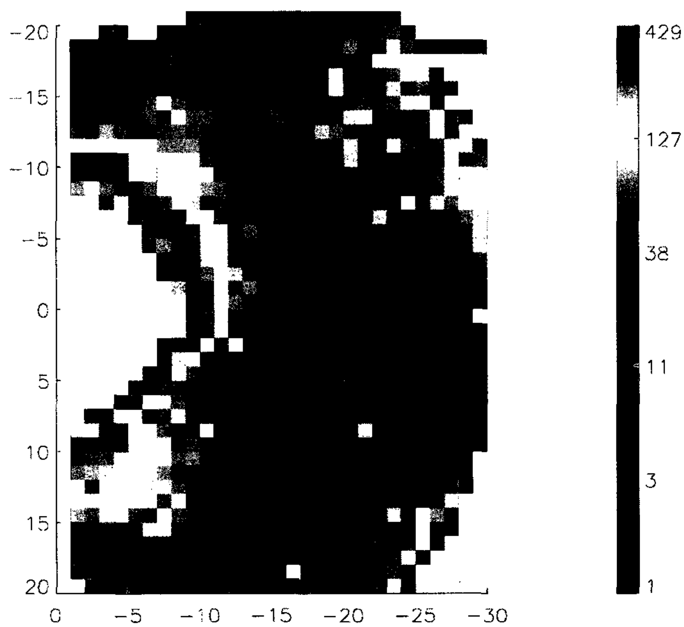

Figure 2.10. Numbers of the selected Geotail data points on the GSM X-Y plane, binned in $1R_E \times 1R_E$ box. The sun is to the left.

2.5.2 Results

Figure 2.10 shows the data point distribution on the X-Y plane in GSM coordinate system, binned over $1R_E \times 1R_E$. Due to the characteristics of the Geotail trajectory, we have more observations near the inner edge of the plasma sheet at ~10 R_E and near apogee, fewer data points in the middle regions from -15 to -25 R_E. On average, for most of the regions except for the very flanks, more than 20~30 data points fall in each cell.

Figure 2.11 shows the averaged flux tube volume V (left) and specific entropy $PV^{5/3}$ (right) in each cell. Approximately, both V and $PV^{5/3}$ are increasing tailward and with increasing radial distance. The results obtained by *Xing and Wolf* [2007], based on T96 magnetic field model [*Tsyganenko*, 1995; *Tsyganenko and Stern*, 1996] and the empirical plasma-sheet plasma pressure model TM2003 [*Tsyganenko and Mukai*, 2003], are roughly consistent with this study.

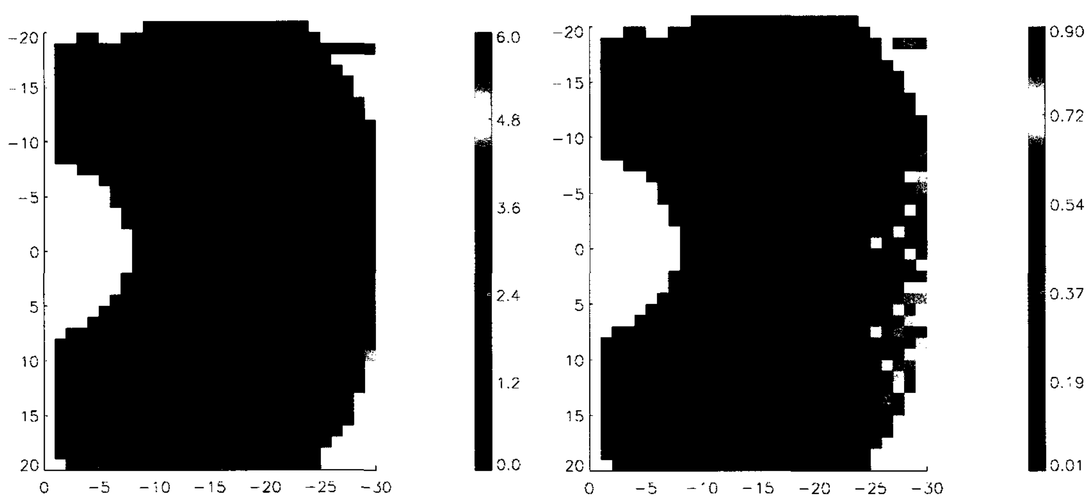

Figure 2.11. The averaged flux tube volume V in units of R_E/nT (left) and specific entropy $PV^{5/3}$ in units of nPa$(R_E/nT)^{5/3}$ (right) in each cell.

2.5.3 V and $PV^{5/3}$ in quiet, moderate and active geomagnetic times

We classify geomagnetic activities into three classes based on the 3-hour Kp index, quiet for Kp=0 and 1, moderate for Kp=2, 3 and 4, active for Kp$\geq$5. Table 2.1 shows the numbers of data points associated with different Kp indices.

Table 2.1. Numbers of data points binned into different Kp indices.

Kp	0	1	2	3	4	5	6	7	8	9
Numbers of data points	8631	24576	22719	14080	6233	2034	415	198	7	0

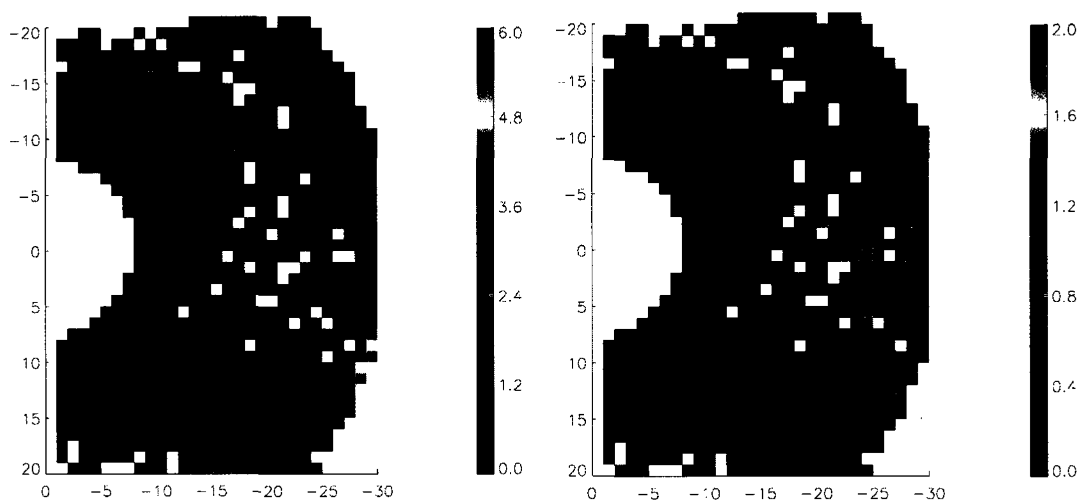

Figure 2.12. The averaged flux tube volume V in units of R_E/nT (left) and specific entropy $PV^{5/3}$ in units of nPa$(R_E/nT)^{5/3}$ (right) in each cell, for Kp=0 and 1 conditions.

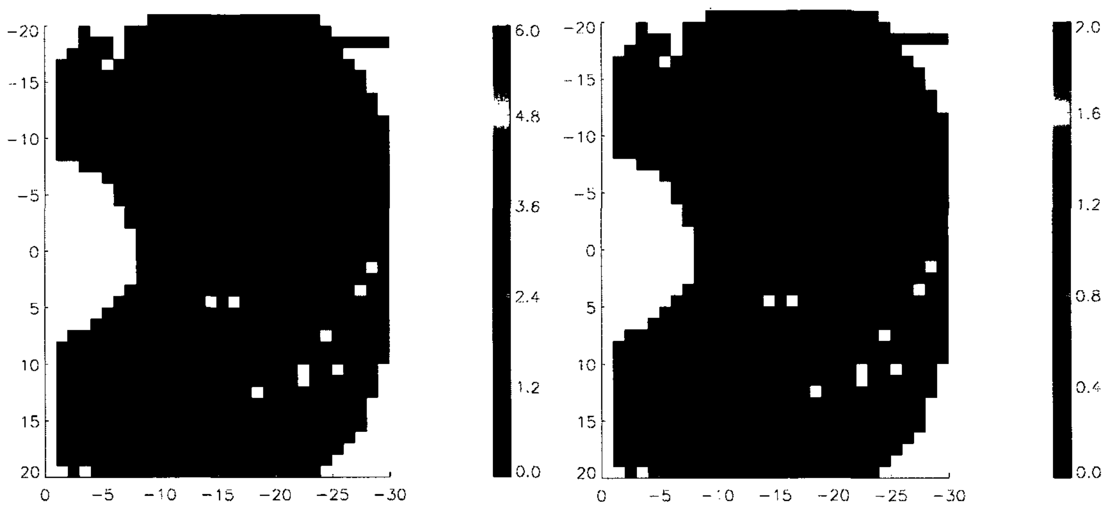

Figure 2.13. The averaged flux tube volume V in units of R_E/nT (left) and specific entropy $PV^{5/3}$ in units of nPa(R_E/nT)$^{5/3}$ (right) in each cell, for Kp=2, 3 and 4 conditions.

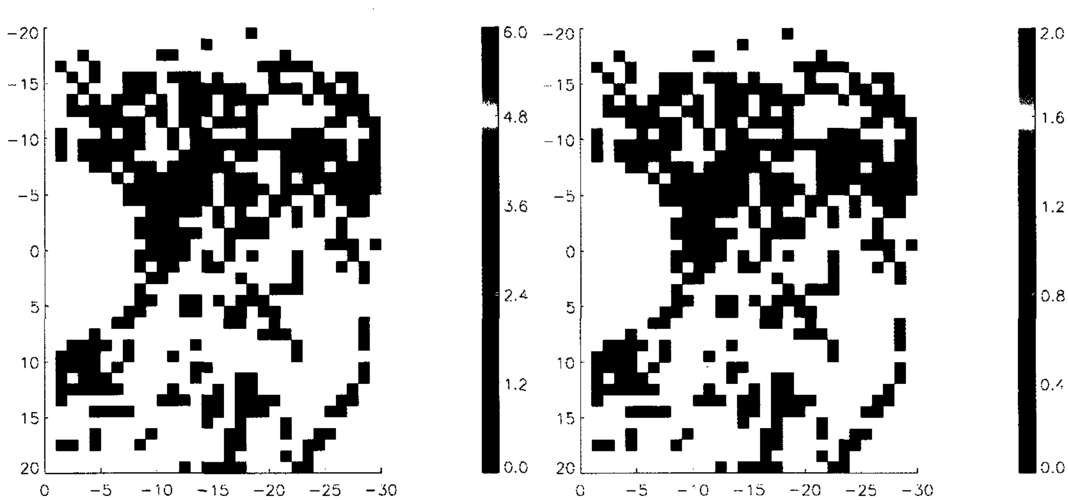

Figure 2.14. The averaged flux tube volume V in units of R_E/nT (left) and specific entropy $PV^{5/3}$ in units of nPa(R_E/nT)$^{5/3}$ (right) in each cell, for Kp$\geq$5 conditions.

Comparing Figure 2.12, 2.13 and 2.14, it is hard to infer distinguishing features of $PV^{5/3}$. However, the flux tube volume V during moderate conditions is smaller than that in quiet conditions beyond $20R_E$, and V in active times, despite a large portion of null data points in some regions, is smaller than that in the moderate conditions near apogee.

Plots of V and $PV^{5/3}$ as a function of radial distance R (R_E) are shown in Figure 2.15. Here we fit the data points to a power law (red lines), and the fitting results and correlation coefficients are listed in the upper left corner of each plot. Two notable features are (1) scatter increases with radial distance, especially beyond $20R_E$ for both V and $PV^{5/3}$; (2) the power law fitting results of both V and $PV^{5/3}$ give smallest and largest values in the middle magnetotail beyond 20 R_E for active times and for quiet times. This is consistent with the basic picture of the dynamics in plasma sheet during different geomagnetic times. Generally speaking, during geomagnetic active times, when Kp index is relatively high, there is more opportunity to observe more earthward flows due to magnetotail reconnection or other internal instabilities. Therefore, we expect to encounter more low $PV^{5/3}$ bubbles during active times in the middle plasma sheet, which can attribute to the lower fitting values in both V and $PV^{5/3}$.

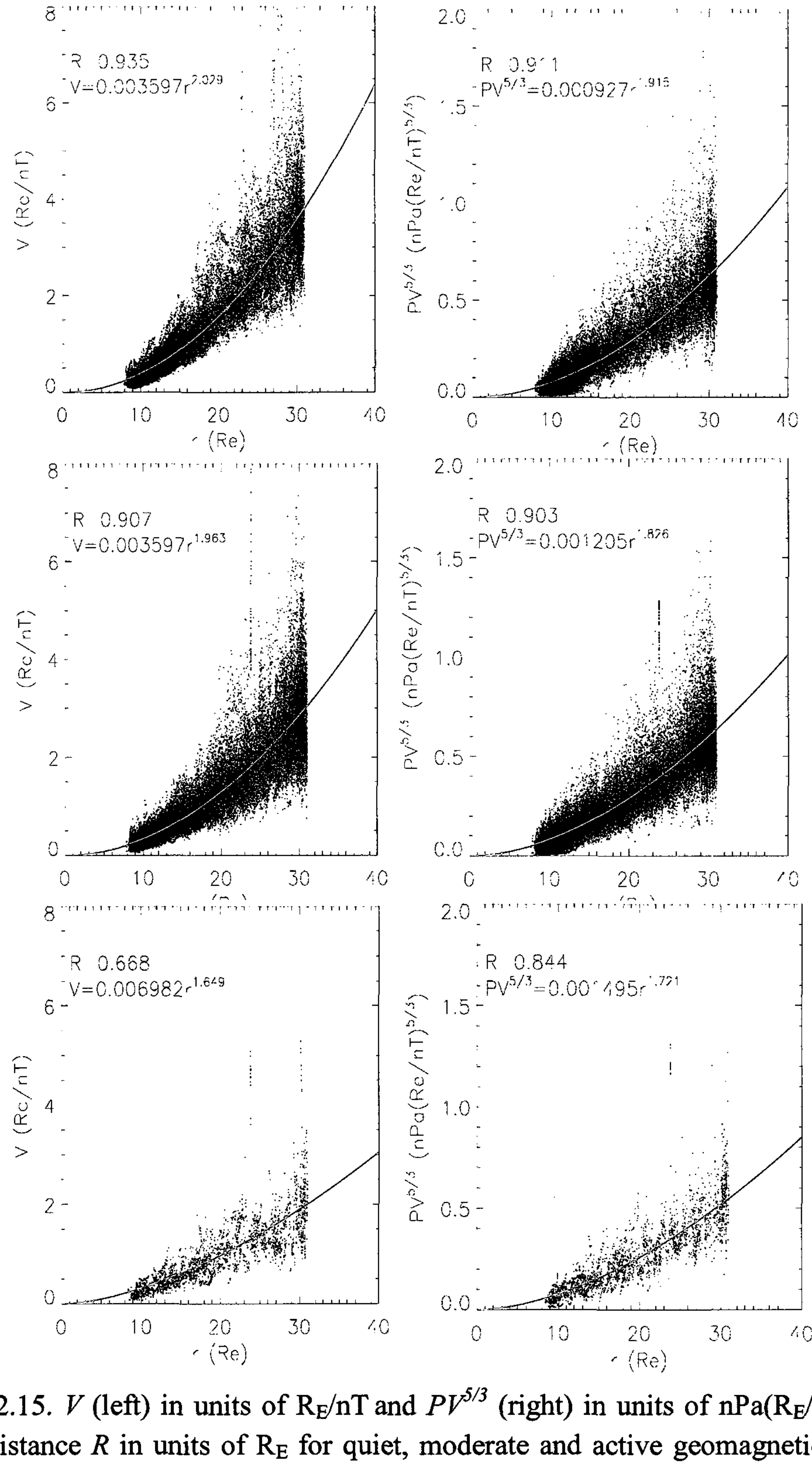

Figure 2.15. V (left) in units of R_E/nT and $PV^{5/3}$ (right) in units of nPa$(R_E/nT)^{5/3}$ versus radial distance R in units of R_E for quiet, moderate and active geomagnetic times from top to bottom. The red line represents power law fitting with correlation coefficient and fitting result shown on the upper left corner of each plot.

2.5.4 V and $PV^{5/3}$ for different velocities.

Figures 2.16 to 2.18 show V and $PV^{5/3}$ as functions of radial distance R in units of R_E, for velocities 0-20, 20-50, 50-100, 100-150, 150-200, 200-250, 250-300, 300-350, 350-400 km/s respectively. As before, we have fit the data points to a power law (red lines), and the fitting result and correlation coefficient are listed in the upper left corner of each plot. It is not surprising that similar features emerge as the results for different Kp indices in Figures 2.15: scatter increases with radial distance, especially beyond $20R_E$ for both V and $PV^{5/3}$. The fitting results do not show distinct differences for various velocity categorizations except for those with higher than 350km/s velocity, which has only very few data points in the plots.

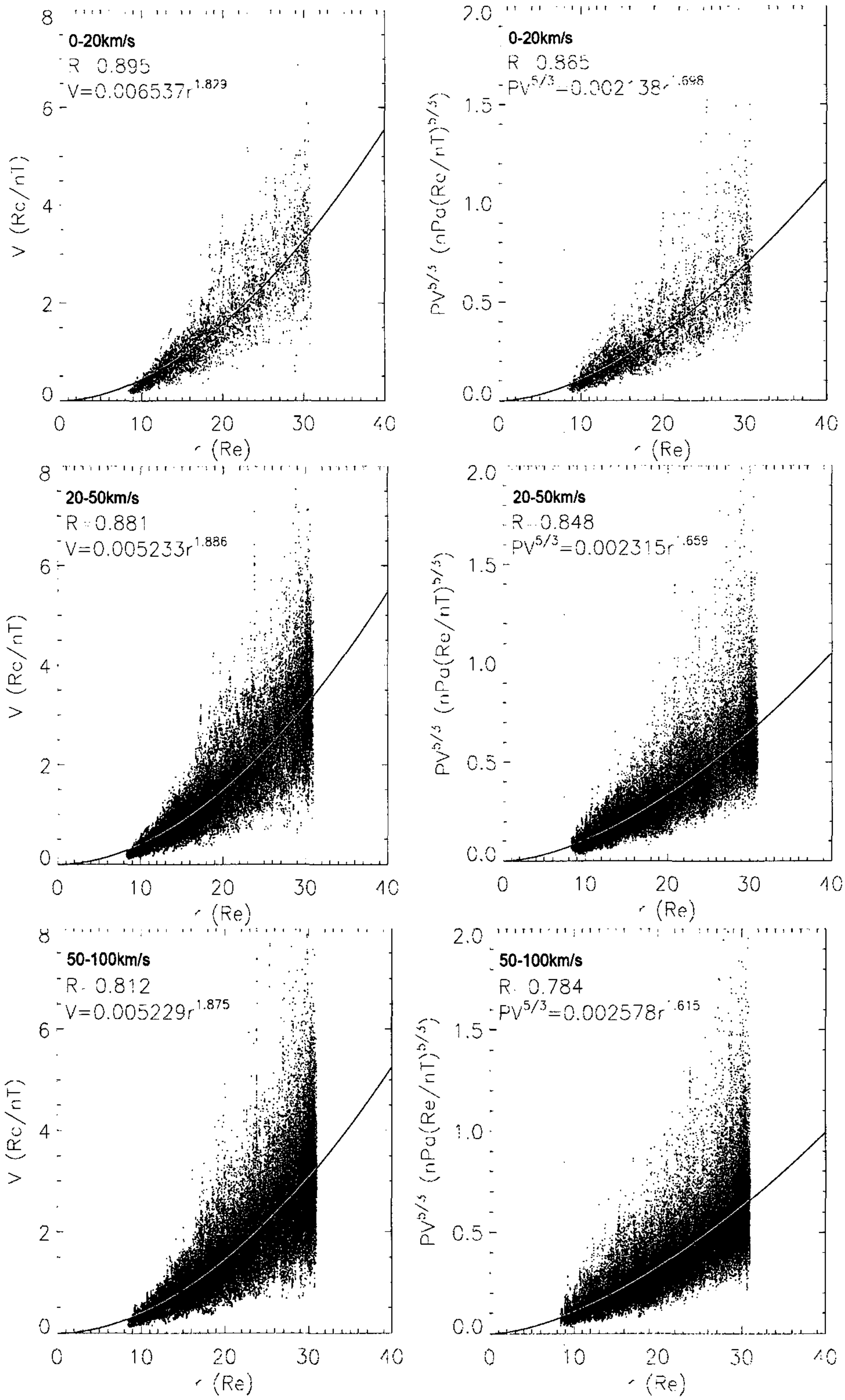

Figure 2.16. V (left) and $PV^{5/3}$ (right) versus radial distance R for velocities 0-20, 20-50 and 50-100 km/s respectively. The red line represents power law fitting with correlation coefficient and fitting result on the upper left corner of each plot.

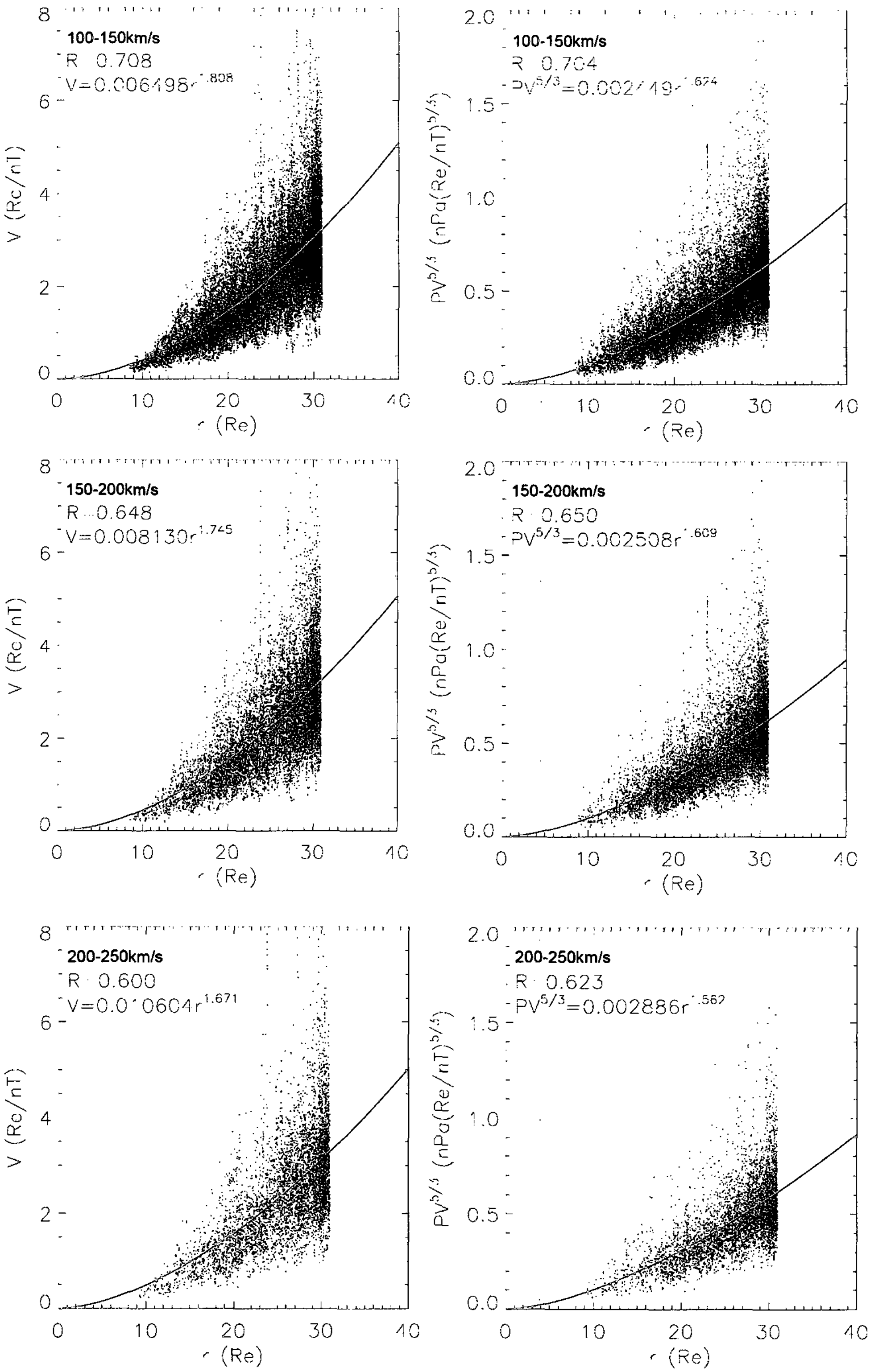

Figure 2.17. Similar to Figure 2.16, but for velocities 100-150, 150-200 and 200-250 km/s respectively.

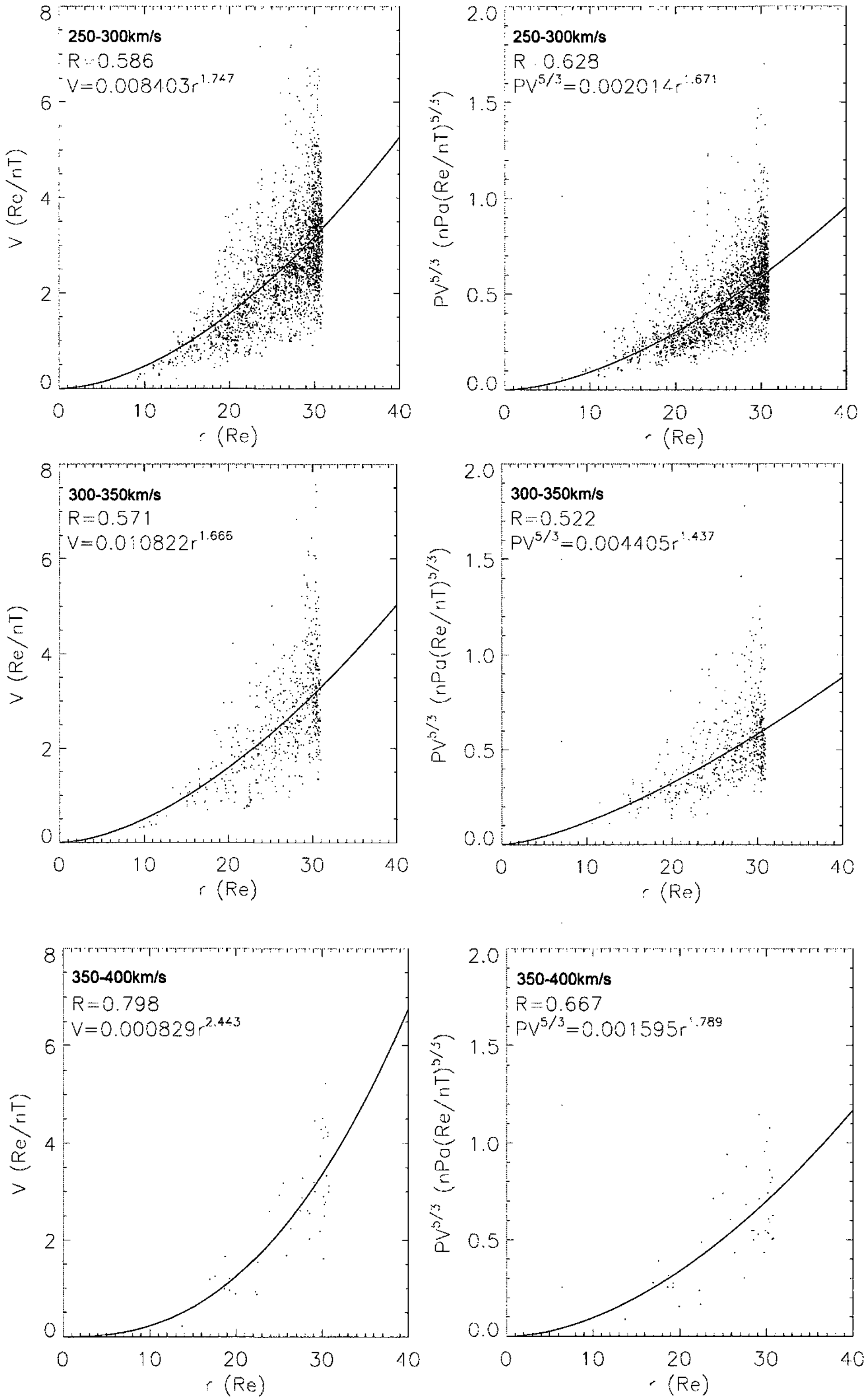

Figure 2.18. Similar to Figure 2.16, but for velocities 250-300, 300-350 and 350-400 km/s respectively.

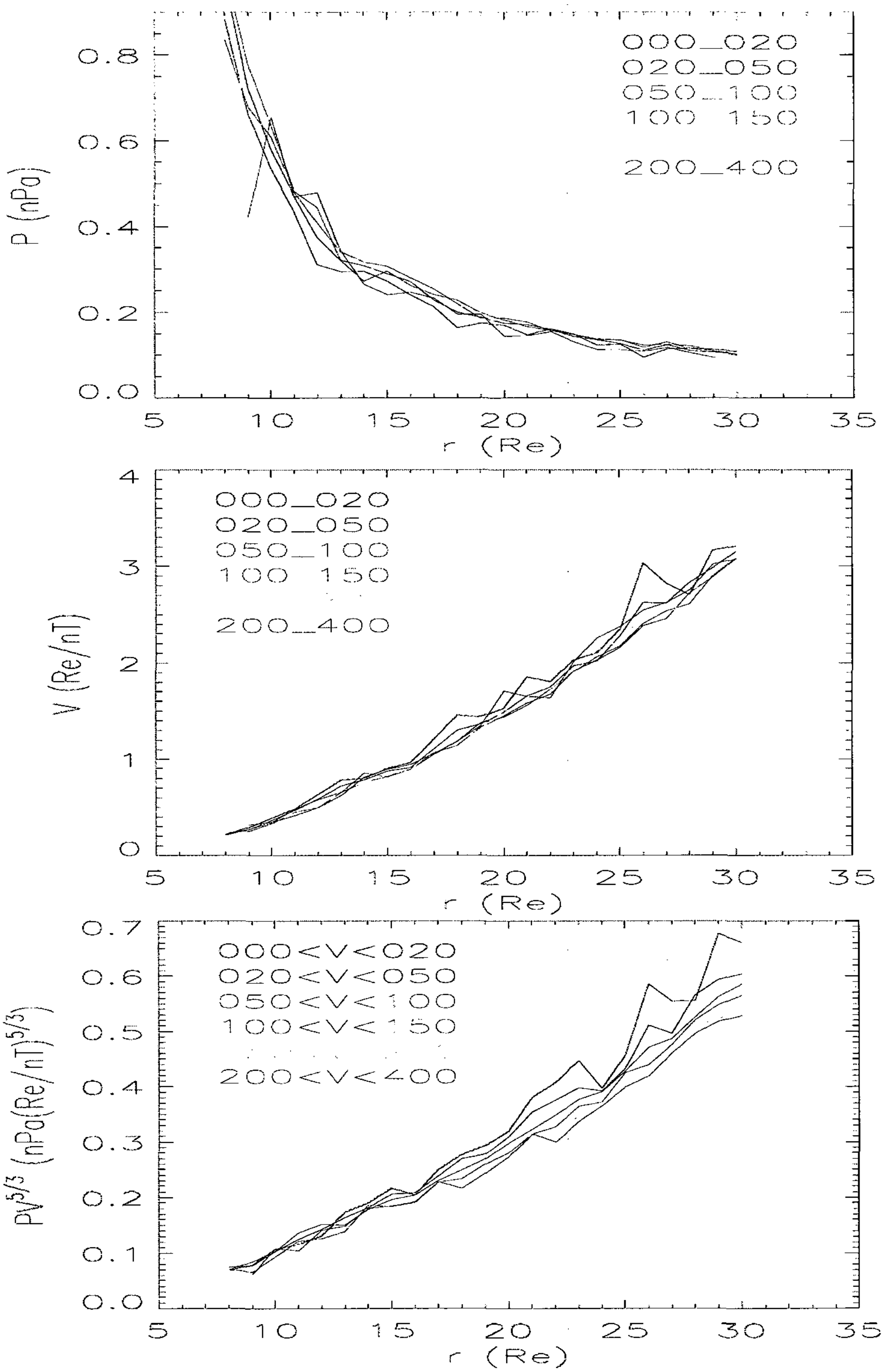

Figure 2.19. Mean values of equatorial plasma pressure (top), flux tube volume (middle) and specific entropy $PV^{5/3}$ (bottom), as a function radial distance (R_E) binned every 1 R_E for different velocities (km/s).

However, the mean values of the $PV^{5/3}$ (bottom plot of Figure 2.19) show a tendency that with higher earthward velocity, $PV^{5/3}$ is slightly smaller in the middle plasma sheet beyond 15 R_E. *Kaufmann and Paterson* [2006] showed that both V and $PV^{5/3}$ depend only weakly on the transport rate. This implies that statistically the flux tubes with higher earthward flowing velocities tend to have larger probability of carrying lower $PV^{5/3}$ plasmas, however this doesn't suggest that higher-velocity flux tubes necessarily contain lower $PV^{5/3}$ than lower-velocity flux tubes. In the bubble picture, it is usually true that a bundle of flux tubes with lower $PV^{5/3}$ than its neighbors tends to move faster. Those bubbles have a profound effect on the plasma circulation from middle and tail plasma sheet to the inner magnetosphere [e.g., *Wolf et al.*, 2009; *Erickson and Wolf* 1980, *Pontius and Wolf*, 1990; *Lemon et al.*, 2004; *Angelopoulos et al.*, 1994; *Sergeev et al.*, 1996b; *Nakamura et al.*, 2001], although the data selected here don't meet the conventional criteria for BBFs.

The reader may note that the estimation of both V and $PV^{5/3}$ have large scatter for either quiet times or active times, and for either low velocities or high velocities. There are four points to be made about this. (1) The nature of the flow pattern and its associated plasma moments and other parameters (e.g., $PV^{5/3}$) are highly variable in the plasma sheet. (2) We don't have sufficient knowledge about how the earthward flow forms with the dependence on the lower $PV^{5/3}$, although some theoretical work has made progress [e.g., *Sitnov et al.*, 2005; *Birn et al.*, 2004]. (3) The estimation method [*Wolf et al.*, 2006a] used here is only an approximate approach based on equilibrium assumption, which can introduce a factor of 2~3 error when applied to fast moving bubbles. (4) Based on the discussion above, it is hard to evaluate whether the large scatter is real or artificial.

As discussed by *Wolf et al.* [2006a], an improvement of this method or an alternative method on accurate estimation flux tube volume is vitally important in studying and understanding the dynamics in the plasma sheet.

In Chapter 7, I will present result from a superposed epoch study of $PV^{5/3}$ during substorms, pseudo-breakups and convection bays, also using this approach to estimate $PV^{5/3}$.

Chapter 3

An RCM simulation of the 18 April 2002 sawtooth event and evidence for interchange instability

We present results of a Rice-Convection-Model (RCM) simulation of the 18 April 2002 sawtooth event, which has been published in 2008 [*Yang et al.*, 2008]. This event occurred as a series of quasi-periodic substorms during fairly-stable solar wind conditions. It is modeled by: (1) prescribing a solar-wind-driven magnetic field model (T01_s) augmented by additional current loops representing the magnetic effects of the substorm current wedge and, (2) by carefully specifying a substorm-phase dependent plasma distribution at the RCM outer boundary at $8R_E$ where a plasma distribution with higher temperature and lower number density is used after every substorm onset. Input parameters were adjusted to make the simulation results agree with the primary signatures of the sawtooth event, specifically the sequence of magnetic-field stretching and dipolarization observed by the GOES spacecraft and the associated sharp increases and gradual decreases in the flux of energetic protons measured by the LANL SOPA (Synchronous Orbit Plasma Analyzer) instruments on other geosynchronous spacecraft. The results suggest the important role that higher temperature and lower density plasma-sheet plasma plays in producing flux enhancements at geosynchronous orbit. The results also confirm that induction electric fields associated with magnetic field collapse after substorm onsets can serve as a likely mechanism for the energization of particles up to 25 keV. Synthetic high-energy neutral atom images are compared with IMAGE/HENA measurements for 10-60keV hydrogen atoms. Magnetic field dipolarization over a large range of local time was associated with a dramatic reduction in the plasma entropy parameter $PV^{5/3}$ on the boundary. The simulation indicates that the ring current intensified 10-20 min after every onset, associated with the injection of low $PV^{5/3}$ flux tubes through the boundary. The low $PV^{5/3}$ plasma also produced interchange instability in the inner magnetosphere, which drives Birkeland currents in a spatially quasi-periodic upward-downward pattern with a lifetime of 40-60 minutes and spatial extent of 1.5-2.0 hours. The results suggest that the spatial quasi-periodic and nearly north-south aligned auroral arcs observed by the IMAGE/FUV WIC detector might be caused by interchange instability.

3.1 Introduction to sawtooth events

Sawtooth events are generally identified as quasi-periodic oscillations of energetic particle fluxes at geosynchronous orbit [*Borovsky et al.*, 1993; *Belian et al.*, 1995]. They usually occur during storm times, with a periodicity of approximately 2-4 hours and can last for up to 5-8 cycles [*Huang et al.*, 2003a; *Henderson et al.*, 2006a]. By analyzing solar wind conditions, *Huang et al.* [2003b] and *Henderson et al.* [2006a] found that sawtooth events can occur under fairly stable solar wind conditions characterized by a continuous southward IMF B_Z. However, *Lee et al.* [2004] interpreted every sawtooth onset as the result of a solar wind pressure enhancement. While their triggering mechanisms are still the subject of some debate, sawtooth events are generally viewed as a series of quasi-periodic substorms. *Huang et al.* [2003b] analyzed Geotail data during two sawtooth events, concluding that there were near-tail reconnections and plasmoid formations with a mean period of ~2.7 hours. *Henderson* [2004] re-examined the CDAW-9C interval and analyzed it as a sawtooth event, which placed tail reconnection inside -11 R_E. During sawtooth events magnetic field stretching and dipolarization can be very strong in both the nightside and dusk sectors [*Pulkkinen et al.*, 2006].

During a substorm, the magnetospheric magnetic field can be very dynamic and plasma quantities are highly variable. During the growth phase, the field in the magnetotail stretches and the plasma sheet thins. In the subsequent expansion phase, the field collapses to a more dipole-like configuration, which may be associated with the development of a substorm current wedge as suggested by *McPherron et al.* [1973]. *Tsyganenko* [1997] developed an empirical model to describe the magnetic field produced by the current wedge.

In the convection picture of magnetospheric substorm dynamics, after substorm onset, conservation of the specific entropy parameter $PV^{5/3}$ is violated, where P is plasma pressure and V is the flux tube volume per unit magnetic flux. Both the near Earth X-line model of a substorm [*Hones*, 1977] (Figure 2.2) and the cross-tail current disruption model [*Lui et al.*, 1992] (Figure 2.3) suggest the creation of a dipolarized bubble, which reduces the flux tube volume dramatically. *Wolf et al.* [2006a] estimated the specific entropy of flux tubes at around -10 R_E during two substorms, finding that $PV^{5/3}$ was reduced by a factor of 2-3 after onset. *Lemon et al.* [2004] simulated an idealized storm with a depletion channel of low $PV^{5/3}$, leading to an injection of plasma sheet plasma into the ring current. Since sawtooth event plasma injections are typically very wide in local time and occur almost simultaneously all around geosynchronous orbit [*Huang et al.*, 2003b; *Reeves et al.*, 2004], and since each injection is associated with the escape of a plasmoid [*Huang et al.*, 2003b], it is plausible to assume that $PV^{5/3}$ is reduced in the plasma sheet over a wide range of local times. *Kaufmann and Paterson* [2006] found that magnetic field stretching and dipolarization change during substorm phases are associated with changes of the plasma temperature, density and pressure on a flux tube, even when $PV^{5/3}$ is conserved. Yet another important substorm-associated process that could influence plasma sheet plasma parameters is ionospheric outflow. The ion outflow rate can be as large as 10^{25} ions s^{-1} [*Yau et al.*, 1985] in total; for up to 90 minutes after substorm onset, ion conic events near the auroral/polar cap boundary can produce 10^{22} to 10^{24} ions s^{-1} [*Tung et al.,* 2001]. Ion outflow would tend to make the plasma sheet population colder and denser in the substorm recovery phase [*Wing et al.*, 2007]. Cold plasma can also enter the plasma sheet via the low latitude boundary layer [*Fujimoto et al.*, 1998].

Simulations of the 18 April 2002 event have been carried out using different techniques. *Goodrich et al.* [2007] investigated the magnetospheric responses to steady solar wind conditions using global MHD simulations (LFM), finding that the reconnection in the mid-tail is intermittent and patchy in a sawtooth event, while the reconnection during steady magnetospheric convection (SMC) is quasi steady. *Kuznetsova et al.* [2007] modified the MHD Ohm's law in the regions of likely reconnection to include non-gyrotropic pressures, which could reproduce quasi-periodic reconnections when driven by a steady southward IMF. With this modification, *Taktakishvili et al.* [2007] modeled the ring current buildup and the oscillation of energetic flux at geosynchronous orbit by coupling the BATS-R-US code and the Fok Ring Current Model, providing a detailed picture of inner-magnetospheric particles, based on MHD-computed electric and magnetic fields.

In this chapter, we present results from a Rice Convection Model (RCM) simulation of the 18 April 2002 sawtooth event. Our approach is to impose quasi-periodic boundary conditions on the plasma number density, temperature, and entropy parameter at the RCM outer boundary to reflect what is known about the substorm-phase-dependent phenomenology of the plasma sheet plasma distribution as described above. Since there are no measurements available along the modeling boundary to directly constrain the RCM's plasma boundary condition, we adjust solar wind driven empirical plasma parameters in a reasonable range, comparing the results with multipoint observations until reasonable agreement is achieved between model results and the classic sawtooth behavior exhibited by the LANL/SOPA data. Inputs to the magnetic field model are also adjusted for reasonable agreement with measurements by GOES magnetometers.

Using prescribed magnetic field configurations, the RCM computes energy-dependent, bounce-averaged particle distribution functions as well as currents and electric fields in the closed field line region of the inner and middle magnetosphere. The RCM calculation is self-consistent, in that the effect of the particle distribution is considered in the calculation of the Birkeland current and electric potential distribution. Assuming strong-elastic-pitch-angle scattering and neglecting sources and losses, the specific entropy parameter $P_sV^{5/3}$ and the energy invariant $\lambda_s=E_sV^{2/3}$, are conserved along the drift path, where P_s is the partial pressure for a given value of λ_s and E_s is particle kinetic energy. By defining the number of particles per unit magnetic flux η_s with invariant λ_s, the plasma number density N, temperature T, and entropy parameter $PV^{5/3}$ can be calculated as equations 1.11 to 1.13. Detailed descriptions and applications of the RCM have been given by *Wolf* [1983] and *Toffoletto et al.* [2003].

Section 3.2 reviews observations of the 18 April 2002 sawtooth event. Since the magnetic field configuration and plasma distribution are important inputs to the RCM, Section 3.3 focuses on how we specify both the magnetic field within the simulation region and plasma boundary conditions at the RCM outer boundary. Section 3.4 demonstrates the degree to which we were able to adjust boundary conditions to fit

GOES and LANL/SOPA data; model predictions are then compared with other data sets, namely, lower-energy particle fluxes measured by LANL/MPA, 10-60 keV fluxes from IMAGE/HENA, and auroral patterns from IMAGE/FUV.

3.2 Observational overview

The 18 April 2002 sawtooth event occurred during a two-day long magnetic storm, which began early on 17 April (top plot of Figure 3.1). This event was well covered by multiple satellite observations and has been studied extensively [e.g., *Huang et al.,* 2003b, *Henderson et al.,* 2006a, *Clauer et al.,* 2006, *Ohtani et al.,* 2007, *Reeves et al.,* 2004]. During this event, the solar wind velocity had a sudden change at around 0010UT on 18 April, followed by a number density peak at about 0100UT. Thereafter, the solar wind velocity gradually decreased from 530 km/s to 450 km/s; the solar wind density remained fairly stable as low as 2 cm^{-3}; the IMF B_Z was continuously southward with variations from -6 to -12 nT (bottom plot of Figure 3.1). *Huang et al.* [2003b] identified seven teeth in the sawtooth event, beginning at around 0036, 0241, 0530, 0812, 1142, 1413 and 1634 UT respectively. The onset times were determined by analyzing the peaks of the magnetic field and the southward turnings of B_Z in the magnetotail at Xgsm=-22~-29 R_e, Ygsm=-7~-14 R_e, Zgsm=7~12 R_e observed by Geotail (Figure 3.2). In contrast, *Henderson et al.* [2006a] extracted seven teeth from 0239 UT to 2104UT, determined by the combination of electron and proton flux enhancements from LANL/SOPA detectors.

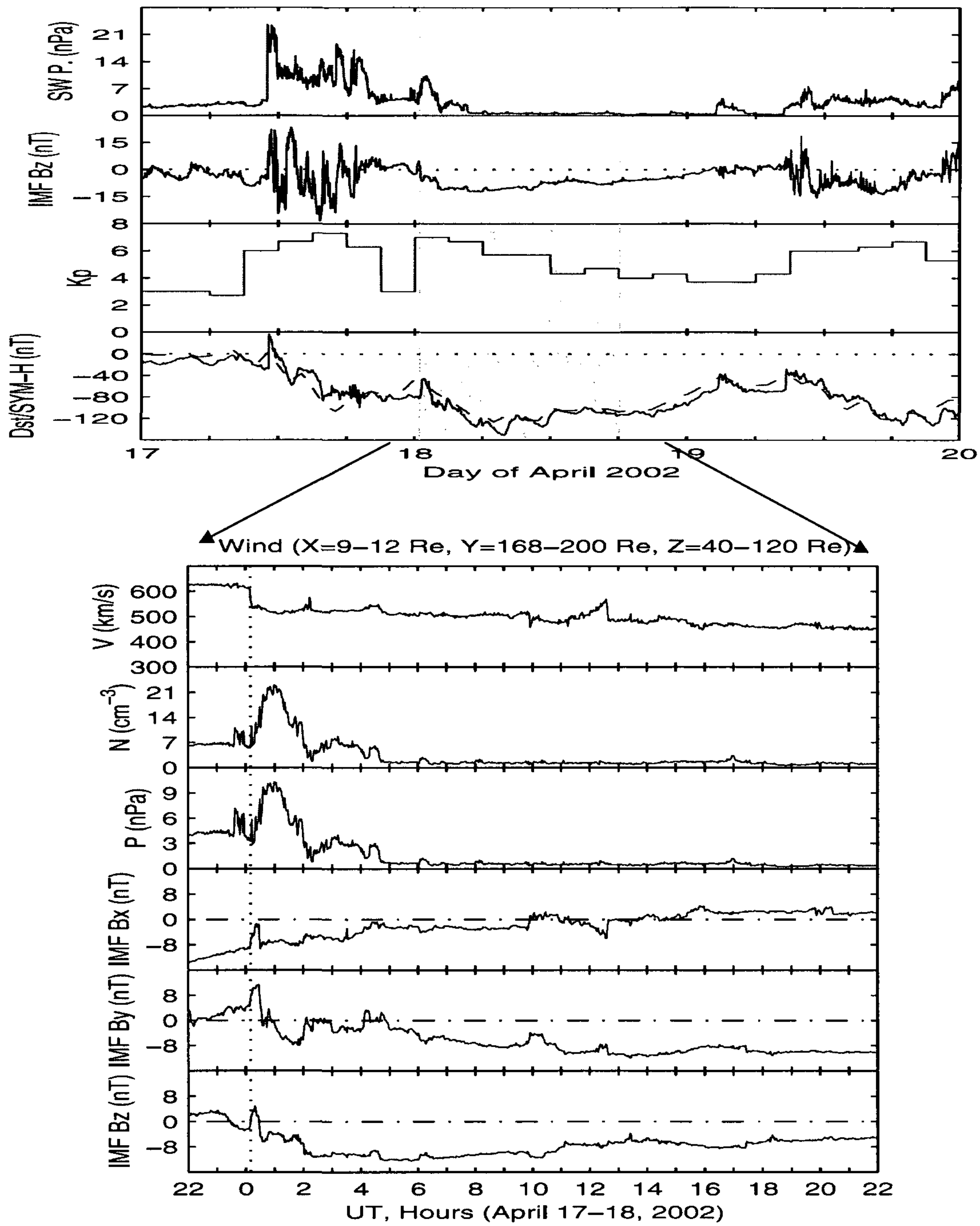

Figure 3.1. (top) The solar wind dynamic pressure, IMF BZ component, Kp index, Dst index (dashed line) and SYM-H index (dotted line) for day 17-19 April, 2002. The shaded region indicates the sawtooth event interval. (bottom) Details of solar wind conditions and IMF during the day 17-18 April, 2002, observed by WIND. Adapted from *Huang et al.* [2003b].

High resolution SOPA measurements, consisting of electrons in the range 50-500 keV and protons in the range 50-400 keV, show dispersionless particle flux enhancements after every onset in the dusk and midnight sector, but dispersive in the post dawn sector [*Henderson et al.*, 2006a; *Reeves et al.*, 2004]. Relating the drift times of particles of different energies with the dispersive increase on the dayside, *Reeves et al.* [2004] estimated the injection boundary to extend across the nightside from the pre-dusk sector to the post-dawn sector (17-7 hours LT). *Clauer et al.* [2006] examined ground magnetograms during this event, and found the disturbance for each tooth to be similar to the disturbance associated with a typical substorm except that the sawtooth oscillations affect a wider range of local times.

Ohtani et al. [2007] analyzed Cluster observations from 0700 to 1030UT. At the 0812 UT onset, when Cluster located at about 4.6 R_E radial distance was deep in the inner magnetosphere near 2100MLT, the particle fluxes recorded by RAPID instrument increased without obvious dispersion, and the *in situ* plasma movement was dominated by radial motion, due to an azimuthal induction electric field.

Results of remote sensing of the inner magnetosphere and the north polar region have also been presented [e.g., *Henderson et al.,* 2006a, *Huang et al.,* 2003b, *Clauer et al.,* 2006, *Ohtani et al.,* 2007]. IMAGE/HENA observations around the 1142UT onset show westward drift and little hydrogen intensity enhancement [*Henderson et al.*, 2006a]. The auroras during this event were very active and long-lasting during each tooth cycle

[*Huang et al.*, 2003b]. A double oval configuration and eastward propagation of omega-band forms were also observed during this event [*Henderson et al.*, 2006b]. *Ohtani et al.* [2007] characterized the auroral structure as quasi-periodic in space, after the onset at around 0812UT.

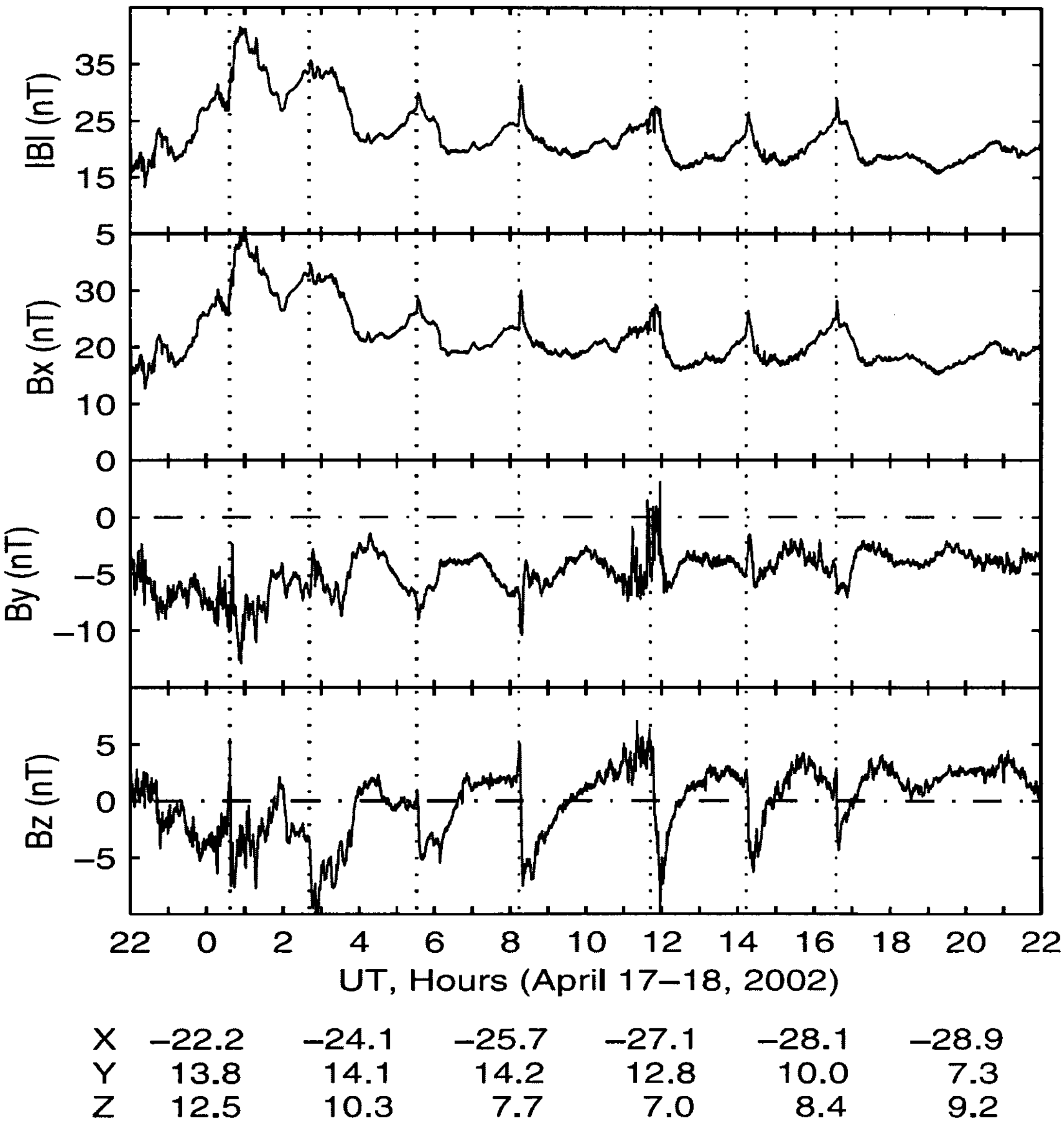

Figure 3.2. Magnetic field strength and components (in GSM) observed by Geotail. The vertical dotted lines indicate the substorm onsets. Adapted from *Huang et al.* [2003b]

3.3 Simulation setup

In an effort to match simulation results with observations, we have carefully adjusted the various RCM model inputs to best reflect conditions during the sawtooth event of 18 April 2002, as described below.

3.3.1 Magnetic field inputs

The blue, black and red dashed lines in Figure 3.3 show the total magnetic field, the B_Z component and the inclination angle in GSM coordinates observed by GOES 8 and GOES 10 in the top and bottom panels, respectively. The six vertical dotted lines, at 0241, 0530, 0812, 1142, 1413, and 1634 UT, represent times of southward B_Z turnings and total field strength peaks as identified by *Huang et al.* [2003b] from Geotail observations. As shown in Figure 3.3, these times correlate well with indicators of magnetic field dipolarization at geosynchronous orbit, namely, increases in total field strength, B_Z, and inclination angle. Located at different magnetic local times, GOES 8 and GOES 10 detected 3 and 4 dipolarizations in the dusk and midnight sector, respectively, and no dipolarizations on the dayside. Before the sudden dipolarization, the B_Z component and the inclination angle decreased gradually, representing field stretching in the growth phase of substorms.

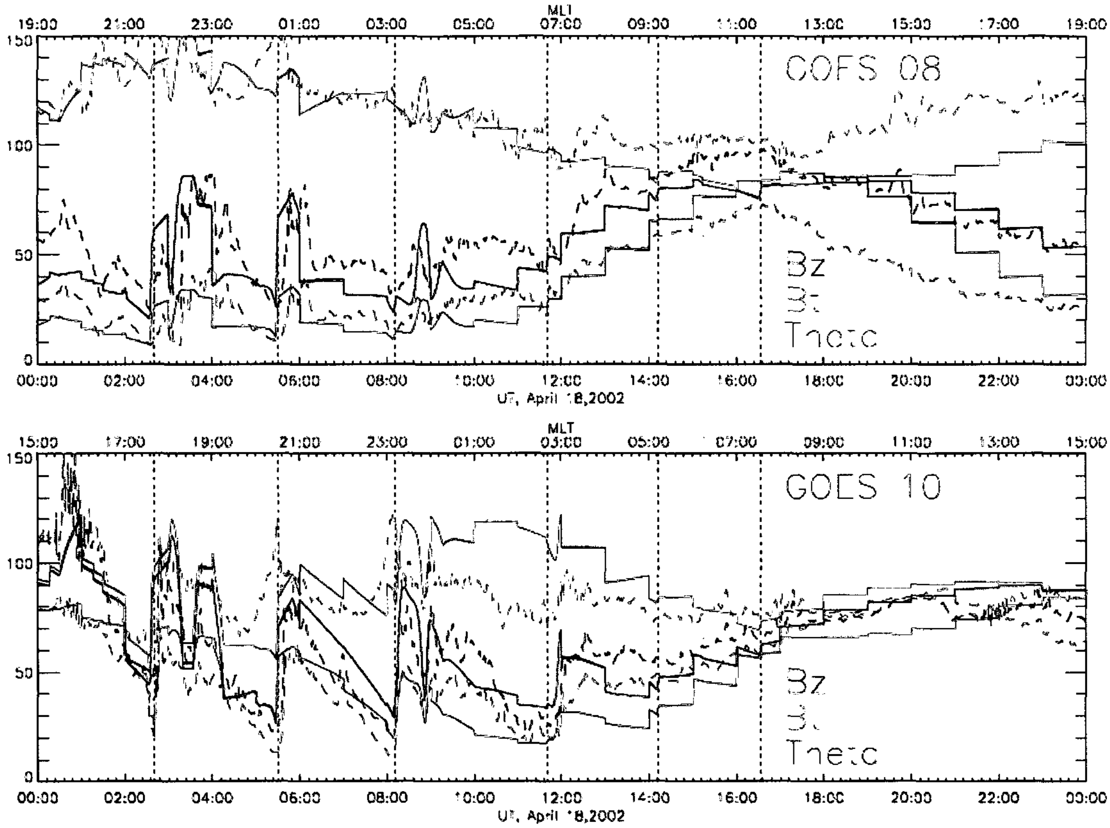

Figure 3.3. Comparison of the magnetic field observed by GOES 8 and GOES 10 at geosynchronous orbit (dashed lines) and the field given by T01_s model, augmented by a Tsyganenko-based substorm current wedge model (solid lines). The blue, black and red dashed lines represent the total magnetic field, the B_Z component and the inclination angle in GSM coordinate. The top and bottom panels are for GOES 8 and GOES 10 respectively. The vertical dotted lines at 0241, 0530, 0812, 1142, 1413, and 1634 UT indicate the southward turnings of B_Z and peaks of the field strength at Geotail, taken from *Huang et al.* [2003b].

In order to reproduce the storm time magnetic field and dipolarization associated with the substorm expansion phase, we combine the T01_s magnetic field model [*Tsyganenko*, 2002a, 2002b] with a substorm current wedge model based on *Tsyganenko* [1997]. The solar wind driven T01_s magnetic field alone does not reproduce the strong growth-phase magnetic field stretching and subsequent dipolarization, since the solar wind parameters were fairly stable and the magnetic indices Dst and Kp did not show sawtooth-like oscillations. *Tsyganenko* [1997] proposed an empirical substorm current wedge to model the dipolarized field in the substorm expansion phase. It is a simple analytic magnetic field model describing the current distribution and the corresponding magnetic field disturbance after substorm onset. The model applies a pair of current loops with a spread-out volume current density to represent the geometry and magnitude to the substorm current wedge [*McPherron et al.*, 1973]. The original code provided by Tsyganenko consists of five adjustable parameters, i.e., "AMPL", wedge amplitude coefficient, to specify the magnitude of the current; "R0", loop initial radius; "AL", loop stretch amplitude; "BETA", loop extension amplitude; "GAMMA", loop inclination angle with respect to equatorial plane in radians. The definition of these parameters can be found in equations (1), (2) and (3) of *Tsyganenko* [1997]. The last five panels in Figure 3.4 show the five parameters used in our simulation versus time. Basically, AMPL=100 yields about +10 to +20 nT disturbance inside the wedge; R0, AL and BETA describe the geometry of the pair of current loops, which remain unchanged throughout the run; the inclination angle of the loop with respect to the equatorial plane, i.e., GAMMA, is changing. The original substorm current wedge model assumes that the wedge is always centered at midnight, which is not the case in this event. Both the magnetic field disturbances recorded by ground magnetometers [*Clauer et al.*, 2006] and SOPA energetic particle flux analysis [*Reeves et al.,* 2004] suggest that the substorm current wedge and the associated plasma injection boundary are unusually wide and centered at local times varying from close to the dusk terminator to near midnight. Therefore, we introduce a new parameter "Rotation Degree" to be able to rotate the whole structure of the Tsyganenko substorm current wedge about the dipolar axis. The top panel of Figure 3.4 shows this parameter versus time where a positive angle represents a westward rotation. It is clear that for most of the time, the current wedge is centered in the dusk-midnight sector. To best match the dipolarizations observed by GOES 8 and GOES 10 during this event and for technical simplicity, we tune only three parameters of the current wedge model, "AMPL", "GAMMA" and "Rotation Degree", keeping the other three parameters unchanged. Obviously, "AMPL" also shows sawtooth-like oscillations, because the current magnitude is strong after every onset and then gradually decreases to zero in the late recovery phase and the next growth phase.

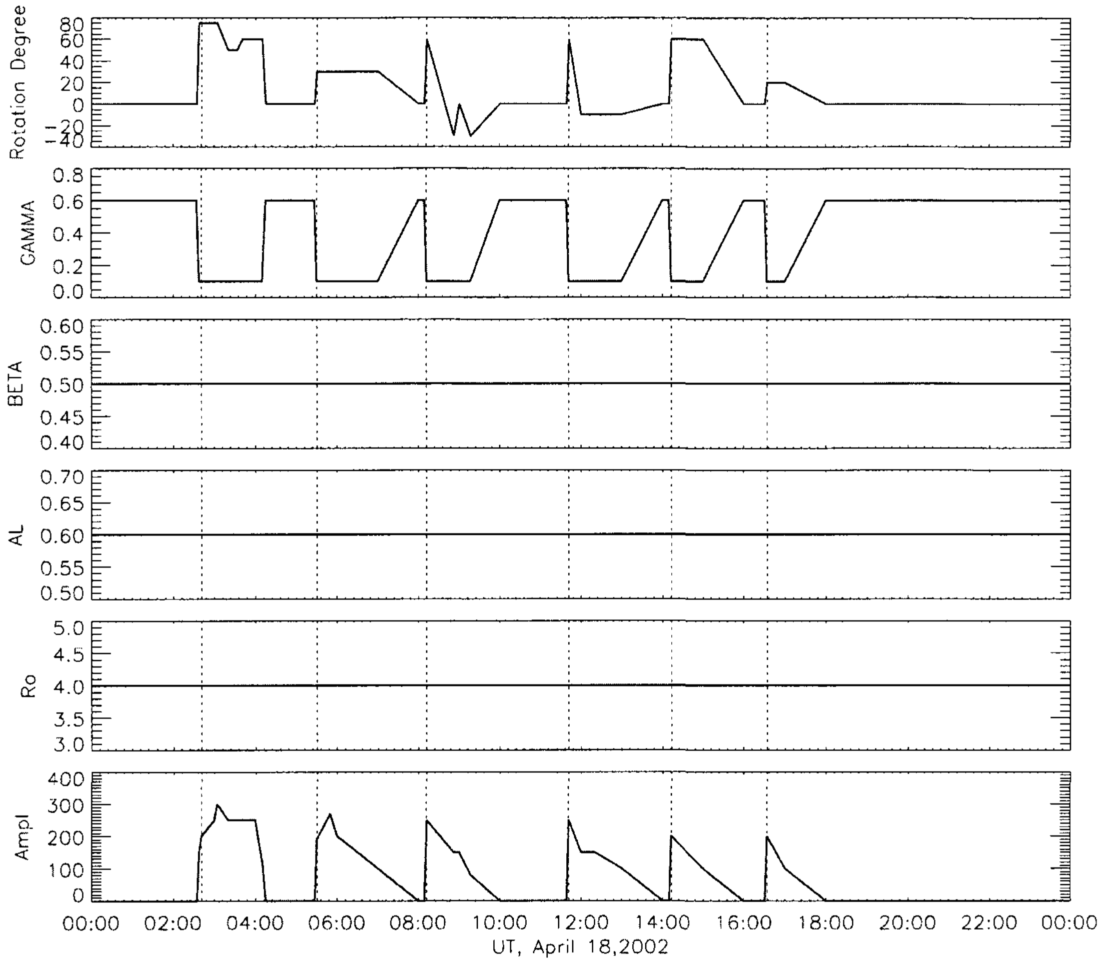

Figure 3.4. Six parameters of the substorm current wedge model in this run versus time. The vertical dotted lines are at the same times as in Figure 3.3.

We carefully adjusted input parameters for the substorm current wedge to best fit the dipolarizations observed by GOES 8 and GOES 10. Since these two satellites did not observe dipolarizations at around 1413, and 1634 UT, when they were on the dayside, we used the 1142UT set of substorm current wedge parameters as input for the last two dipolarizations. Comparing observation and model magnetic field results (Figure 3.3), we attribute discrepancies to two main causes. First, we did not take tilt into account in our implementation of the T01_s model, since the present version of RCM assumes zero tilt angle of Earth's internal field, but the GOES satellites are assumed to be on the equatorial plane at a distance of 6.6 R_E in GEO coordinate system. This discrepancy is apparent by comparing GOES 8 observations and model results from 1700 to 2400 UT. The second discrepancy is apparent from 0200 to 0800UT when GOES 10 was in the dusk sector, where the observation shows stronger stretching prior to every onset than that given by the T01_s model. *Pulkkinen et al.* [2006] has suggested that the field stretching in the dusk sector could be as strong as on the nightside prior to sawtooth event onsets.

3.3.2 Electric potential distribution on the simulation boundary

During active times, it is reasonable to assume that the plasma sheet and the injection boundary move closer to the Earth [*Mauk and Meng*, 1983]. Throughout our modeled sawtooth event interval, the Kp index remained above 6. We set the outer boundary of the RCM to be a circle of radius 8 R_E, which is well inside the magnetopause standoff distance which ranged from 8.5 to 11.7 R_e as calculated using observed solar wind parameters, following *Shue et al.* [1998]. We suspect that a more distant boundary would require a more sophisticated treatment of the electric potential distribution at the boundary in combination with the substorm current wedge magnetic field model to insure the characteristic dispersionless sawtooth pattern observed; this will be left for further study.

The total polar cap potential (PCP) drop calculated using the Boyle formula [*Boyle et al.* 1997] varies in the range from 100 to 144 kV. In the period when the magnetic field is stretching, we scale the total PCP by the ratio 8.0/magnetopause-standoff-distance to estimate the potential drop across the 8 R_E region. When the field dipolarizes, we apply the total PCP across the 8 R_e region. The plasma inflow region corresponds to the region of westward electric field on the RCM boundary, adjusted to match the dusk and dawn bounds for the first four injections as given by *Reeves et al.* [2004], i.e., the inflow regions were from 1500 to 0100 MLT for the 0241 UT injection, from 1400 to 0700 MLT for the 0530 UT injection, from 1400 to 0100 MLT for the 0812 UT injection, and from 1800 to 0100 MLT for the 1142 UT injection, respectively. The last two plasma inflow boundaries are assumed to be the same as that at 1142 UT.

3.3.3 Plasma distribution on the boundary

Using the *Tsyganenko and Mukai* [2003] empirical model, which relates solar wind and IMF parameters to the temperature and number density of the central plasma sheet from -10 to -50 R_E, we calculate the plasma sheet temperature (*Tps*) to range from 8 to 10 keV and number density (*Nps*) to range from 0.19 to 0.53 cm^{-3}, at -10 R_E during the period of relatively stable solar wind conditions after 0200UT. *Borovsky et al.* [1998] fitted plasma sheet parameters with data at geosynchronous orbit and 11.5-22.5 R_E in the neutral sheet to power law functions of radius *r*. Using the power law dependence given by *Borovsky et al.* [1998], $N\sim (r/R_E)^{-1.38}$, $T\sim(r/R_E)^{-0.56}$, we determine the plasma sheet $T=(0.8)^{-0.56}*Tps\sim8.5\text{-}11.5$ keV and $N=(0.8)^{-1.38}*Nps\sim0.24\text{-}0.70$ cm^{-3} at the -8 R_E RCM simulation boundary. However, these statistical models alone cannot be expected to fully reflect plasma sheet parameter variations during a sawtooth event. Therefore during one tooth cycle, from the beginning of the field dipolarization to the end of the field stretching, we take substorm-related processes into account by substantially modifying the above statistical plasma sheet temperature and number density estimations.

Wing et al. [2007] showed that, during both the substorm growth phase and recovery phase, the plasma sheet number density near -8 to -10 R_E could be 2~3 times larger than that during the expansion phase. The denser plasma sheet is associated with ion outflow from the auroral zone [*Yau et al.,* 1985; *Tung et al.*, 2001]. Normally the ion outflow peaks 20~30 minutes after substorm onset, and lasts as long as 90 minutes [*Wilson et al.* 2004]. The auroral activity associated with each tooth cycle during this event was extremely intense and long [*Huang et al.* 2003b; *Henderson et al.* 2006a], resulting in a substantially denser plasma sheet during the recovery and growth phase than that during expansion phase. Therefore we set the plasma number density at the boundary just before the substorm onset as $N=2.73*(0.8)^{-1.38}*Nps$. After the substorm onset, the plasma density within the current wedge is significantly decreased [*Lyons et al.*, 2003]. Therefore we set the plasma number density on the boundary just after the substorm onset as

N=1.33*(0.8)$^{-1.38}$*Nps, which is a reduction by a factor of 2 compared with the pre-onset condition.

Plasma temperature enhancements after substorm onset have been attributed to reconnection and induction electric field acceleration. *Lyons et al.* [2003] associated the temperature increase and flux enhancement after substorm onset with compression of the magnetic field within the dipolarization current wedge. The induction electric field due to the magnetic field collapse tends to accelerate particles, which is actually equivalent to adiabatic compression if the energy invariant is conserved during the field collapse [*Wolf et al.* 2006b]. Therefore the plasma temperature on the boundary just before every onset is set as T=(0.8)$^{-0.56}$*Tps; while the plasma temperature on the boundary just after substorm onset is 2 times higher than that, i.e., T=2.0*(0.8)$^{-0.56}$*Tps.

The conservation of $PV^{5/3}$ is violated by reconnection in the plasma sheet. The stretched closed flux tube collapses into a dipole-like closed field line with smaller flux tube volume, plus an escaping plasmoid. *Wolf et al* [2006a] estimated that the flux tube volume could decrease by a factor of 2~3 during substorm expansion phase. The RCM cannot self-consistently represent the effects of reconnection and/or other processes that violate the adiabatic drift laws, processes that apparently play a vital role in substorm and sawtooth events. Thus, we place the outer boundary of our calculation earthward of those processes and represent their influence on the inner magnetosphere in terms of boundary conditions. We use the RCM to model the inner magnetospheric effects of the sawtooth event, not the sawtooth event *per se*. During this sawtooth event Geotail detected quasi-periodic strengthening of magnetic field and southward turning of B_Z component in the magnetotail (Xgsm=-22~-29R_E, Ygsm=-7~-14R_E, Zgsm=7~12R_E), which implies that there were quasi-periodic reconnections and plasmoid escapes in the plasma sheet [*Huang et al.*, 2003b]. However, the amount of flux tube volume reduction in every expansion phase is uncertain and impossible to directly measure by one spacecraft. For the results presented here, the flux tube volume reduction factor on the boundary is taken to be 2.0, which was determined by trial and error.

Taking these processes into account, two sets of plasma distributions on the model boundary are used for every tooth cycle. At the end of the substorm growth phase, we set the distribution function to be a double Maxwellian function [*Borovsky et al.*, 1998]: a cooler Maxwellian with $T=(0.8)^{-0.56}*Tps$ and $N=2.73*(0.8)^{-1.38}*Nps$, and a hotter Maxwellian with $5T$ and $0.0003N$, which contributes less than 0.5% to the total plasma pressure. With the T01_s model, we compute the flux tube volume V at -10 R_E at midnight, to complete the setup of the distribution function of $\eta_s(\lambda_s)$. We set the distribution function as a κ=2 distribution just after the substorm onset, with $T=2.0*(0.8)^{-0.56}*Tps$ and $N=1.33*(0.8)^{-1.38}*Nps$, but with the non-adiabatically reduced flux tube volume $0.5V$. We set the plasma boundary at -8 R_E, and the plasma distribution on the boundary during the whole cycle of one tooth is found by interpolation between these two distributions. For this simulation, since there were no plasma parameter measurements at ~8 R_E on the night side, those factors were mainly determined by making a number of runs and comparing RCM-calculated geosynchronous fluxes with LANL/SOPA observations. Reasonable changes were made in this set of parameters until the results were qualitatively consistent with the observations. The plasma parameters at the center of the inflow boundary are plotted as a function of time in Figure 3.5. The number density of electrons on the boundary is set equal to the number density of protons, and the electron temperature is a factor of 7.8 lower than the proton temperature, following *Baumjohann et al.* [1989]. The ratio of the number density of oxygen ions to protons is based on the AE index, following *Daglis et al.* [1994], assuming the two ion species have the same temperature.

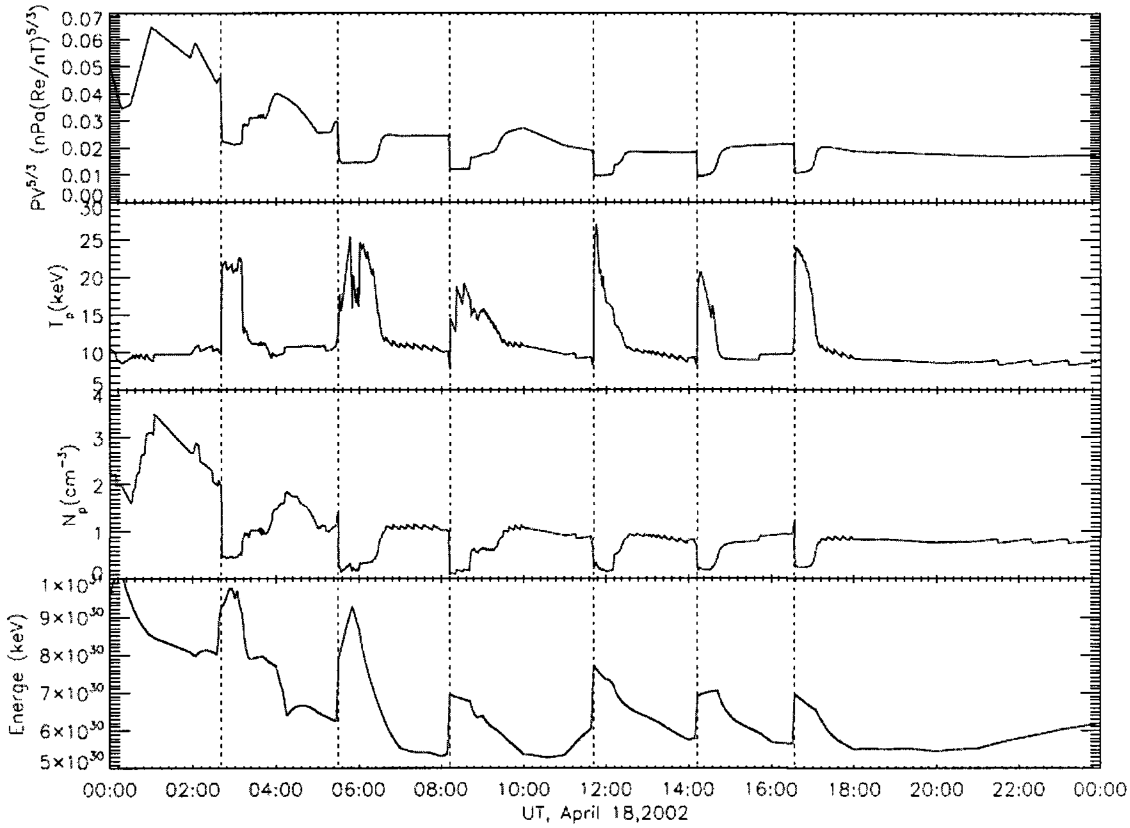

Figure 3.5. The time-dependent proton number density N_p, proton temperature T_p and the total entropy parameter $PV^{5/3}$ at the center of the inflow boundary. The bottom panel shows the total energy of particles within the simulation region. The vertical dotted lines are at the same times as in Figure 3.3.

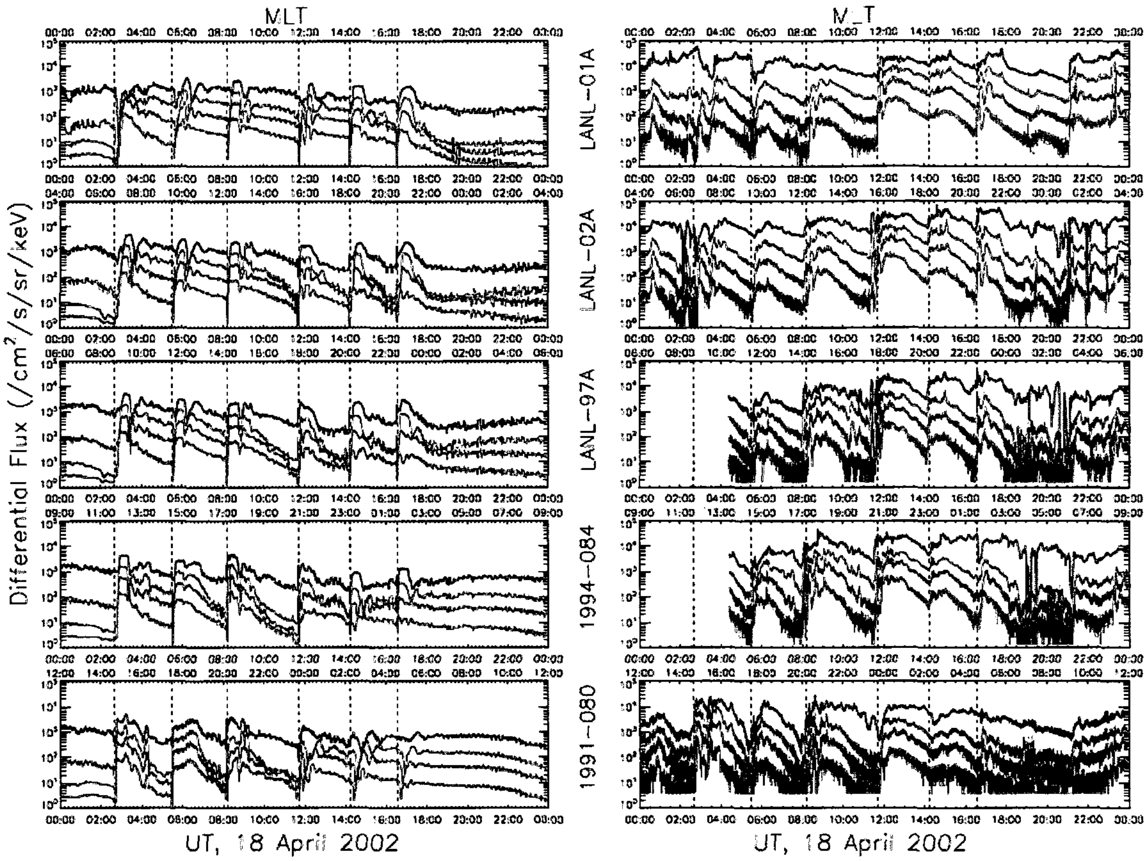

Figure 3.6. The observed energetic proton flux data (on the right) and the corresponding simulation results (on the left) for five geosynchronous satellites. The energies are 75-113, 113-170, 170-250, 250-400 keV from blue to green. The vertical dotted lines are at the same times as in Figure 3.3.

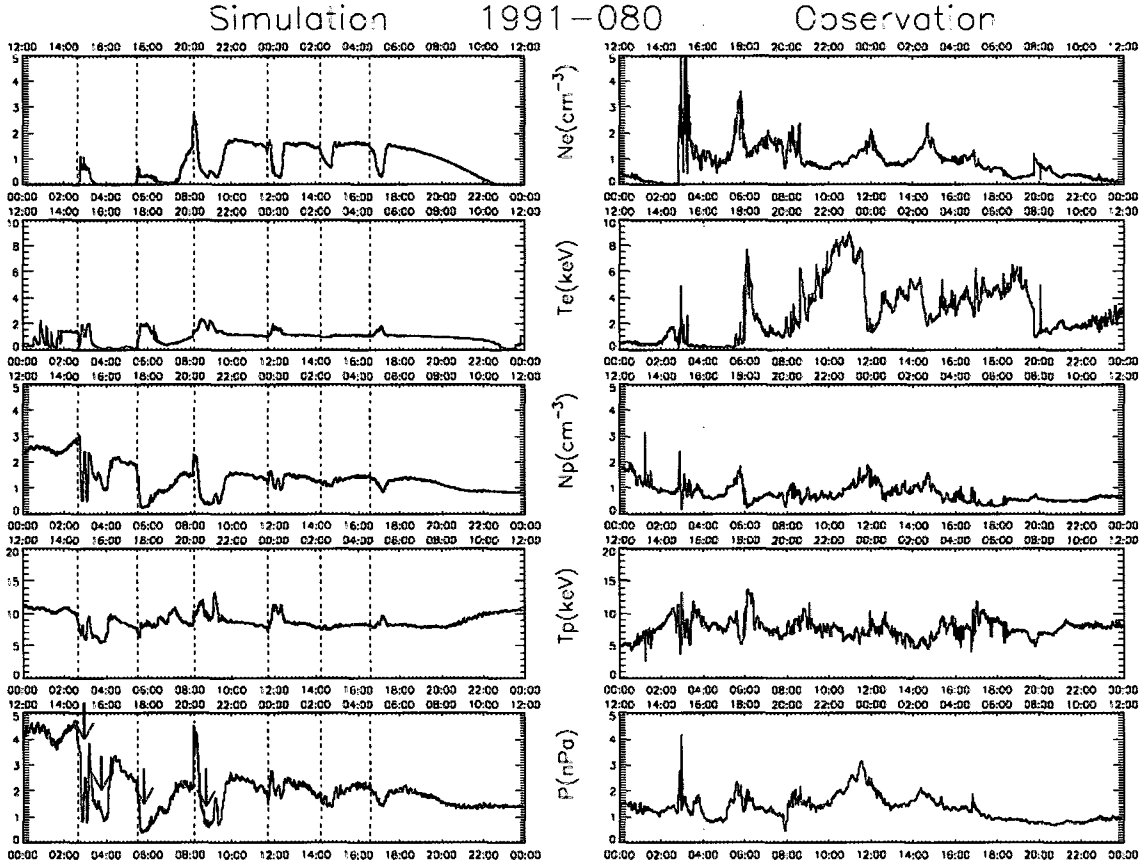

Figure 3.7. The observed 1991-080 MPA data (right) and the corresponding simulated values (left). The electron number density N_e, electron temperature T_e, proton number density N_p, proton temperature T_p and the particle pressure P (assuming $P=k_B(T_eN_e+N_pT_p)$) are plotted from top to bottom. The red arrows indicate the times when the 1991-080 was inside the ingoing low $PV^{5/3}$ undulations.

3.4 Simulation results and discussions

3.4.1 Energetic proton fluxes at geosynchronous orbit

Figure 3.6 compares model results (left panel) with observed geocentric proton fluxes in four different energy bands from five different satellites. Since the RCM assumes the dipole axis to be untilted, the five geosynchronous satellites in the model are confined on the equatorial plane at a distance of 6.6 R_E from the Earth. The simulation results (left) are consistent with the observations (right) both in shape and magnitude, indicating sudden enhancement in flux after every onset and subsequent gradual decline. We also computed the partial pressure for particles having energies less than 45 keV at the geosynchronous orbit, which is varying in the range of 0.3~5 nPa, consistent with the 0.3~4 nPa variations observed by the MPA detector. Figure 3.7 shows the particle moments observed by 1991-080 MPA instrument for the whole day and the corresponding simulated results, which indicates rough qualitative agreement especially for electron number density, proton number density, proton temperature and particle pressure. Since we set the electron temperature/proton temperature ratio to be fixed at 1/7.8 on the simulation boundary, the modeled electron temperature may be dramatically lower than observation for some periods of time. From the viewpoint of the simulation, the rapid increase in flux is mainly contributed by the injection from the boundary of κ=2 and T~25keV plasma, which has a high energy tail. To best match the SOPA observation, we find that a high temperature plasma distribution is needed and the 25 keV temperature of plasma in the near-Earth plasma sheet at 8 R_e is much higher than the usual 5~15 keV during quiet and some active times. One interesting and controversial question from this simulation is: Could the ion temperature at -8 R_E just after substorm onset be as high as 25 keV? If so, what mechanism could energize the particles to that high temperature? One possibility is that the electric field induced by the magnetic field collapse accelerates the particles outside the simulation boundary. The self-consistent simulations using the RCM-E in Chapter 6 indicate that the ion temperature near the geosynchronous orbit can be doubled to 20~30keV during the substorm expansion phase associated with electric field induced by magnetic field dipolarization. Considering strong stretching and dipolarization in both the dusk and midnight sectors during sawtooth injections [*Pulkkinen et al.*, 2006], particles at -8R_E are possibly accelerated to ~25keV during the magnetic field collapse intervals.

3.4.2 IMAGE/HENA fluxes and the ring current

Figure 3.8 shows energetic neutral atom fluxes observed by IMAGE/HENA and the corresponding synthetic flux calculated from the simulation for the third tooth cycle, beginning with the jump of B_Z in the tail that was detected by Geotail at 0812 UT. To synthesize the flux from the RCM simulation, we assume a virtual detector at the same location as the IMAGE satellite with the same spin axis direction. We integrate the calculated line-of-sight atom flux produced by charge exchange, with the assumption of isotropic particle pressure along field lines prescribed by the T01_s plus substorm-current-wedge magnetic field model used in the simulation. Observations and simulation results for 10-60 keV hydrogen atoms agree very well, indicating the intensification and westward expansion of flux after the onsets. Although the flux intensification is partially attributed to the gradual approach of the satellite to the Earth, the intensification of hydrogen flux is not very pronounced. Since we assume an isotropic pitch angle distribution in our integration algorithm, the synthetic images always overestimate the flux compared to observations, especially for those lines-of-sight near the Earth. For 10-60 keV hydrogen fluxes, the observed images show the peak flux around midnight, while the simulation images indicate more duskward peaks, which implies that our simulated partial ring current shown in Figure 3.8 was more duskward than the real partial ring current.

Figure 3.9 shows the computed total particle pressure of the RCM simulation for one tooth cycle. The six plots from (a) to (f) are snapshots at 0800, 0810, 0820, 0830, 0850 and 0920 UT, which approximately span the substorm growth, expansion, and recovery phases of the substorm with onset at around 0812UT. The pressure in the growth phase is mainly attributed to the partial ring current centered in the dusk-midnight sector with peak value of 100 nPa. The pressure increases after onset and peaks at ~117 nPa 10 minutes later, after the field dipolarization and the plasma injection at local time from 1400 to 0100 MLT with low $PV^{5/3}$ [*Lemon et al.*, 2004, *Lyons et al.*, 2003]. Since the plasma pressure and flux tube volume increase tailward during steady convection, the pressure balance inconsistency [*Erickson and Wolf*, 1980] suggests that the fresh plasma cannot be injected from the magnetotail until the plasma entropy $PV^{5/3}$ is reduced by some mechanism. Reconnection could non-adiabatically cut the long flux tube into a shorter closed flux tube and a plasmoid and also generate fast earthward flows, upsetting the well established shielding of the inner and middle magnetosphere. Concomitant with interchange convection, the plasmas containing $PV^{5/3}$ as low as about 0.02 nPa$(R_E/nT)^{5/3}$ tend to inject deep to L~3.5 region where the $PV^{5/3}$ is about the same as the injected plasma. The bottom panel of Figure 3.5 shows the total particle energy within the simulation region, which clearly indicates that the particle injection occurred almost immediately after every onset. The sudden energy increase at each field collapse is mainly due to: (1) many plasma-populated flux tubes are suddenly transported from outside the RCM boundary to inside after each substorm onset; (2) many nightside and duskside flux tubes that were in the RCM region before the field collapse get compressed inside the substorm current wedge, raising the average energy of the particles on those tubes. The reverse process occurs between the collapses, i.e., as the field re-stretches, the amount of magnetic flux in the RCM region decreases and other tubes experience an increase in volume, which de-energizes the particles on them.

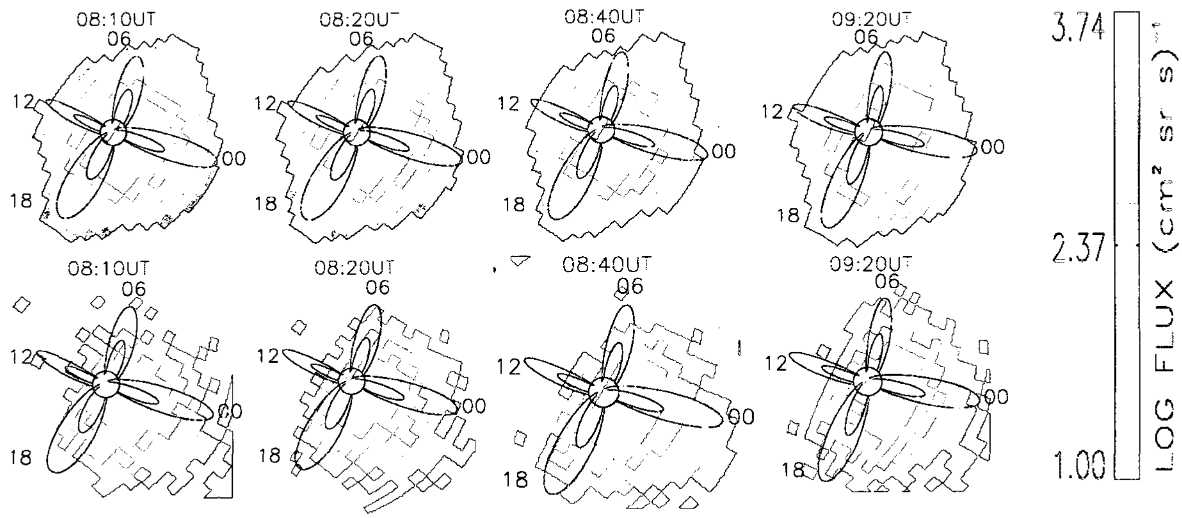

Figure 3.8. Energetic neutral atom flux of 10-60 keV hydrogen, as measured by IMAGE/HENA (second row), compared with the corresponding synthetic flux from RCM simulation results (first row). The images for four times 0810, 0820, 0840 and 0920UT are shown, from left to right. The circle at the center of each image represents the Earth, and the curves are L=4 and 8 dipole field lines at four local times.

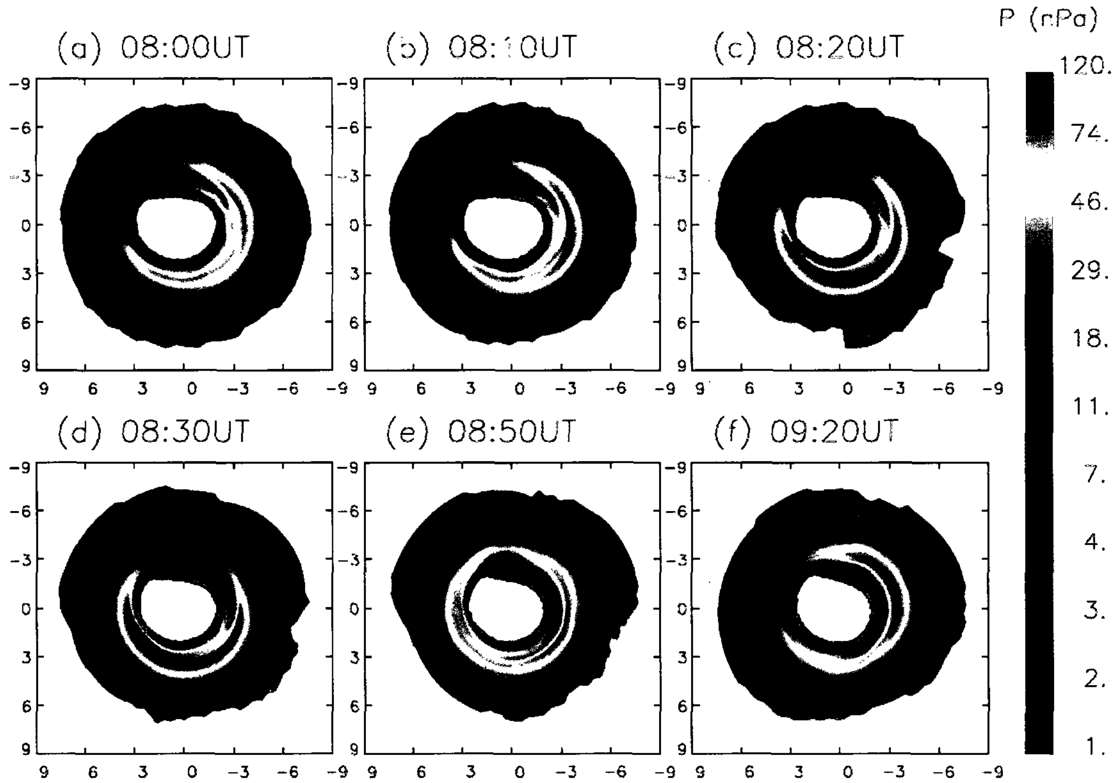

Figure 3.9. Total equatorial particle pressure for 0800, 0810, 0820, 0830, 0850 and 0920 UT. The Sun is to the left.

3.4.3 Interchange and IMAGE/FUV observations

Schmidt [1979] showed the interchange criterion for two adjacent flux tubes (one with volume V and pressure P and the other with $V+dV$ and $P+dP$) as $dV*d(PV^{5/3})<0$, within the assumption of ideal MHD. *Xing and Wolf* [2007] and *Erickson and Wolf* [1980] estimated $PV^{5/3}$ using empirical models and found that the inner and middle plasma sheet is generally interchange stable. However, reduction of $PV^{5/3}$ on flux tubes coming from the tail occurs during substorms [*Lyons et al.*, 2003; *Wolf et al.*, 2006a] or storms [*Sazykin et al.*, 2002], which can result in a situation where $PV^{5/3}$ decreases tailward, which would meet the criterion for interchange instability. An RCM simulation of interchange convection that was carried out for an observed storm event by *Sazykin et al.* [2002] showed that flux tubes with high $PV^{5/3}$ in the inner magnetosphere were replaced by low $PV^{5/3}$ flux tubes injected from geosynchronous orbit.

The left column of Figure 3.10 shows the RCM simulation of the $PV^{5/3}$ distribution in the equatorial plane at times 0537, 0543, 0549, 0559 and 0617 UT on 18 April 2002. It is clear that low-$PV^{5/3}$ plasma near the boundary gets injected deep into the near-earth region at around L=3~4, while plasma of high $PV^{5/3}$ that was originally closer to Earth moves outward, producing quasi-periodic swirl patterns in electric potential and ripple-like convection cells. The interchange structure began near 0537UT, about 7 min after the 0530UT onset. The injection boundary of this tooth cycle was extremely wide, from 1400 to 0700 MLT [*Reeves et al.*, 2004], and $PV^{5/3}$ dropped from 0.030 to 0.016 nPa (Re/nT)$^{5/3}$ in that sector. Up to 8 interchange convection cells are visible at 0559UT, with azimuthal width of ~25 degrees. The Vasyliunas equation

$$J_{\parallel} = \frac{\hat{b} \cdot \nabla V \times \nabla P V^{5/3}}{V^{5/3}} \tag{3.1}$$

implies that the interlacing of low and high $PV^{5/3}$ would produce quasi-periodic upward and downward field-aligned currents above the ionosphere. The middle column plots of Figure 3.10 show the modeled field-aligned currents mapped onto the ionosphere, with the red color representing upward currents. A close view of a specific current footprint indicates that regions of both upward and downward current grow and move equatorward and westward. The IMAGE/FUV WIC observed quasi-periodic and westward drifting auroral structures during this event [*Ohtani et al.*, 2007]. The plots on the right column of Figure 3.10 show the WIC snapshots closest to the times at 0537, 0543, 0549, 0559 and 0617 UT, but only nightside images are shown to avoid air glow contamination on the dayside. The auroral arcs brighten first in the midnight sector, and then grow to a spatial periodic structure covering the whole nightside. At about 0559 UT, they stretch out to an almost north-south-aligned finger-like structure, very similar to the simulation results. We suggest that this auroral pattern is associated with the strong periodic field-aligned current caused by interchange, because strong electron auroras tend to occur in regions of strong upward field-aligned current. Figure 3.11 clearly shows how plasma moments of protons change for this period. Low-number-density, high-temperature plasma is injected along a wide section of the RCM boundary and drifts into the inner magnetosphere, producing quasi-periodic spatial distributions there. Flux tubes carrying relatively low thermal pressure and $PV^{5/3}$ from the boundary could penetrate inside geosynchronous orbit. According to the model, the virtual 1991-080 satellite was just inside the inflowing $PV^{5/3}$ plasma in the dusk to pre-midnight sector for four periods at around 03:00, 03:50, 05:50 and 0830UT as indicated by the red arrows in the simulated MPA proton pressure in Figure 3.7.

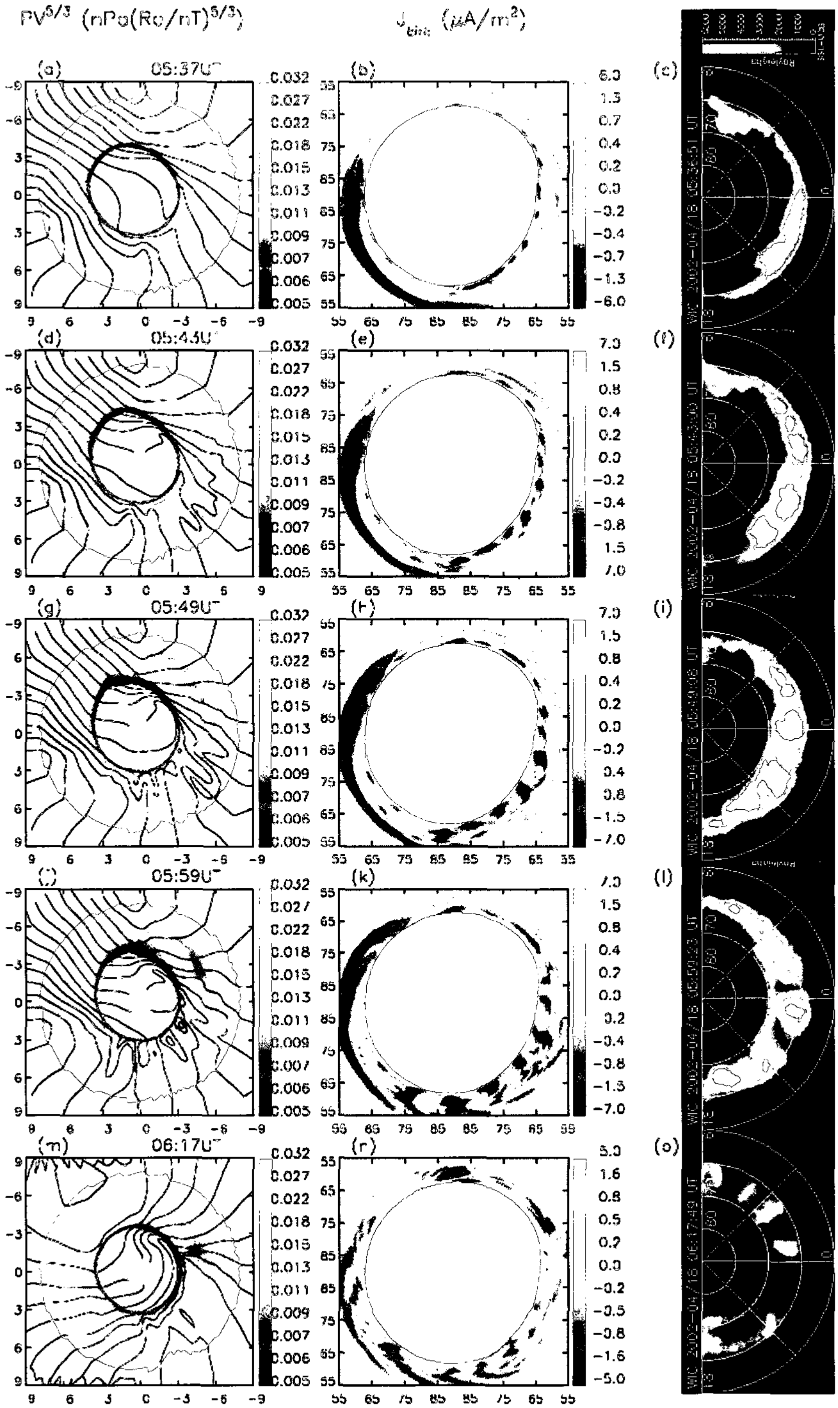

Figure 3.10. The equatorial values of $PV^{5/3}$(left column), the Birkeland current in the ionosphere (middle column), and the IMAGE/FUV WIC images (right column) at times 0537, 0543, 0549, 0559 and 0617 UT from top to bottom. The sun is to the left. The solid lines (left column) are the electric potential lines every 8 kV. Red and yellow colors in the middle column represent upward Birkeland current.

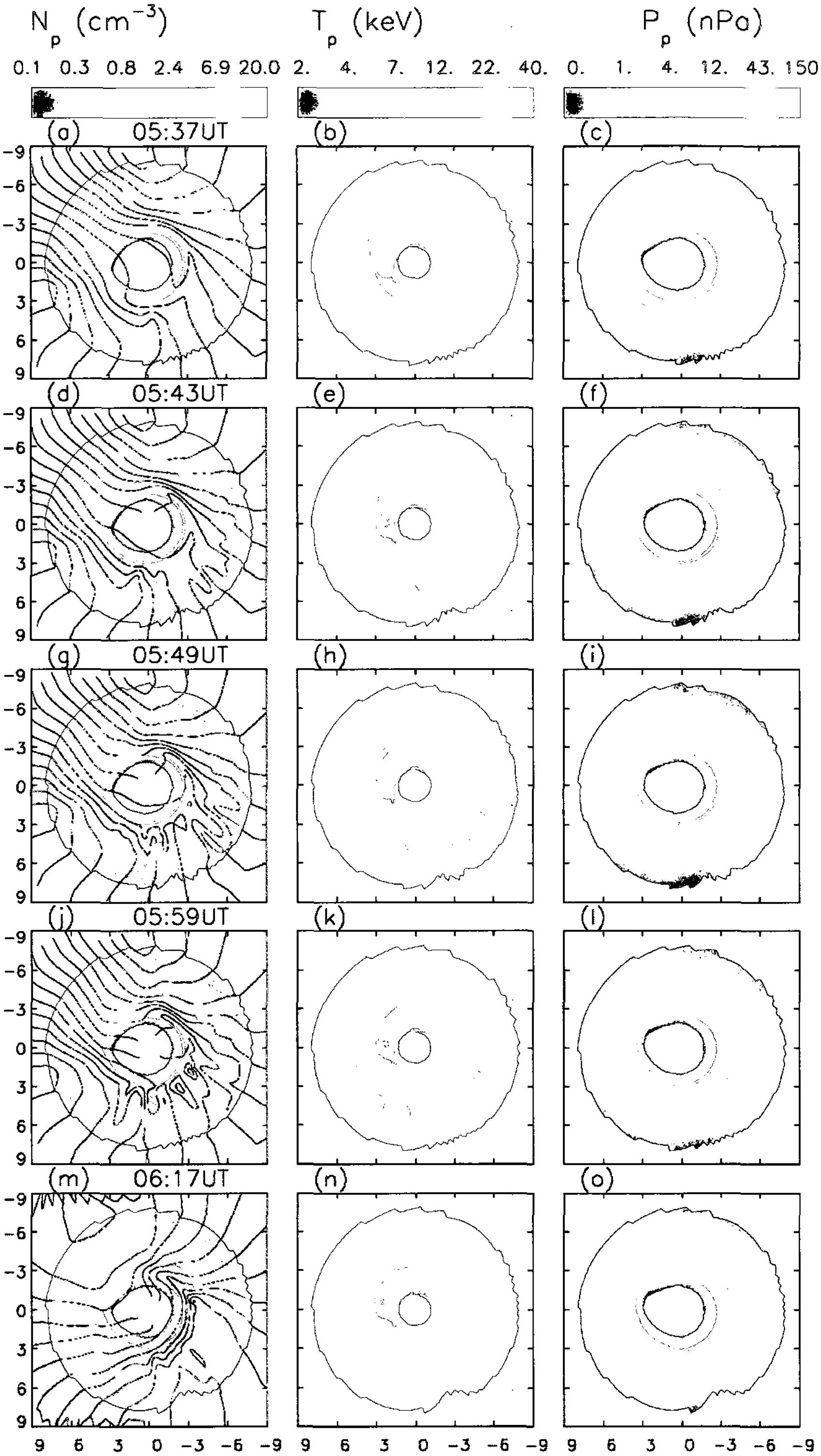

Figure 3.11. The proton number density (N_p) on the left, the proton temperature (T_p) in the middle and the proton pressure (P_p) on the right, at times 0537, 0543, 0549, 0559 and 0617 UT from top to bottom. The sun is to the left. The solid lines (left column) are the electric potential lines every 8 kV.

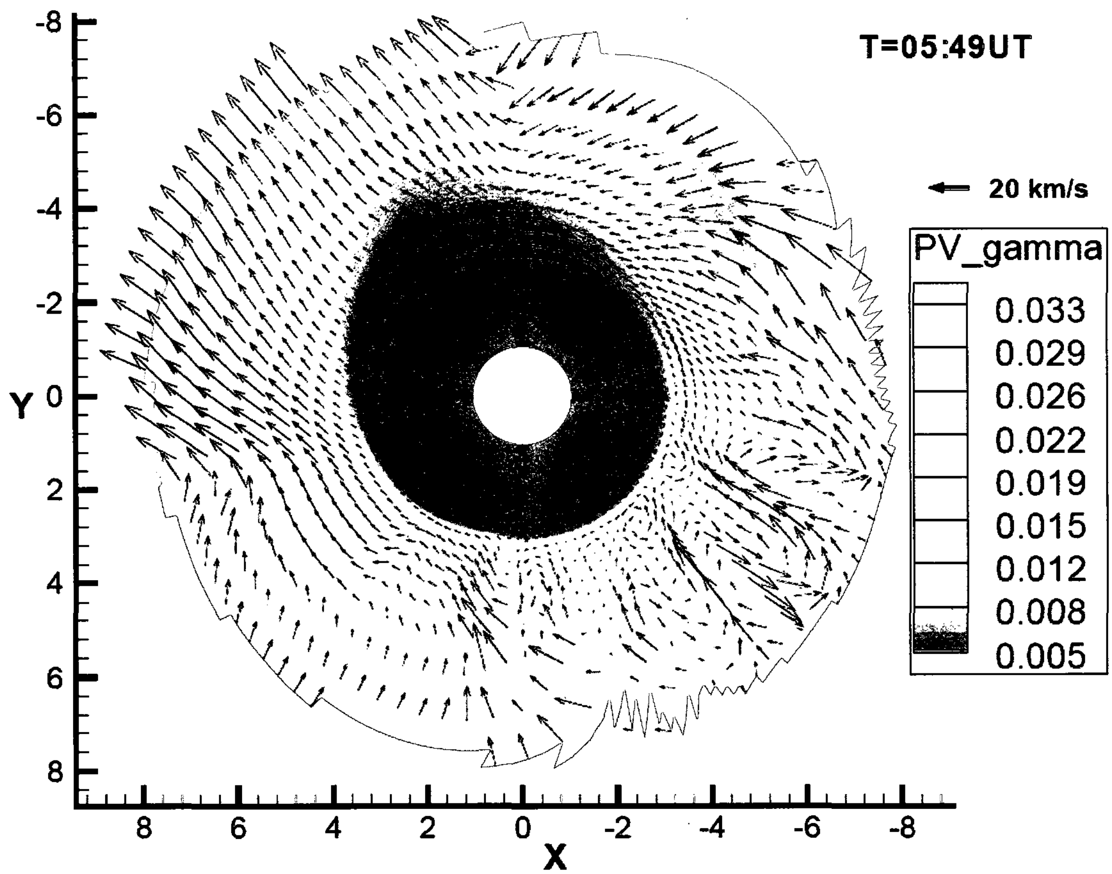

Figure 3.12. Equatorial $E \times B$ drift velocities in the potential electric field in corotating frame at time 05:49UT. Colors represent the $PV^{5/3}$ on the equatorial plane.

The electric field plays an important role in the plasma injection. As indicated in Figure 3.12, the self-consistently computed potential electric field swirls tend to produce almost azimuthal electric field, which drives $E \times B$ drift mainly in the radial direction, with low $PV^{5/3}$ plasma moving inward and high $PV^{5/3}$ plasma moving outward. This pattern helps the interchange-unstable system to reconfigure itself to a stable state.

Actually, the simulation indicates that the interchange instability and the concurrent periodic upward-downward Birkeland currents occur in every tooth cycle. These auroral structures have been identified by eye, with no rigorous morphological criterion applied. In general, the RCM results produce 4~8 coupled pairs of downward-upward Birkeland currents with averaged spatial periodicity of 1.5 hours to 2.0 hours local time and lifetime of 40~60 minutes, while the IMAGE observation shows 3~7 auroral fingers with average spatial periodicity of 1.5 to 1.8 hours in local time and lifetime 20~75 minutes. Note that the first tooth cycle was actually observed to be more complicated, because it was a double-onset event [*Clauer et al.*, 2006], but our simulation set up only one injection for that period. The average spatial periodicity of 1.5~2.0 hours of these finger-like auroral structures implies that the reduction of $PV^{5/3}$ on an unusual wide local time is important in the formation of several concurrent interchange convection cells in the sawtooth event. This suggests that the dynamic reconfiguration of magnetic field and plasma during sawtooth events may provide optimal conditions for interchange instability. *Sazykin et al.* [2002] used plasma data at geosynchronous orbit to set up boundary conditions during the sawtooth-event storm that occurred September 25, 1998, producing interchange convection in the inner magnetosphere. As far as we know, there are no direct *in situ* observations reported regarding interchange convection in the magnetosphere. Coordinated satellite observations might be used to investigate one or several of the following features associated with interchange convection: swirl-like electric potential, radially moving plasma, interlacing high- and low- plasma entropy parameter $PV^{5/3}$ [*Wolf et al.*, 2006]. It is also important to note that the choice of RCM grid spacing influences the computed number and scale size of fingers; for example an RCM run with a finer longitudinal grid increases the number of fingers, so a one-to-one comparison between RCM results and observations should be interpreted with some degree of skepticism. A preliminary study of the dependence of the properties of the interchange fingers on numerical resolution will be represented in Chapter 5.

The reader may note that the observed quasi-periodic auroral structures appear to extend to nearly 70° magnetic latitude, while the corresponding RCM structures are confined to the region equatorward of the model boundary, which is at about 65°. If we had placed the boundary further out in the tail, the modeled interchange fingers would have extended further poleward. However, since the fingers arise in periods when the magnetic field is significantly dipolarized, the 70° magnetic latitude may not map too far out in the tail. Mapping along our event-specific magnetic field model, the equatorial crossings of the 70° magnetic latitude points are approximately 11.9, 11.8, and 10.3 R_E in the pre-midnight sector after the first three substorm onsets, respectively.

It should also be noted that none of the previous modeling papers on this event, mentioned in Section 1, show clear evidence of interchange instability in the inner magnetosphere. The pure-MHD paper of *Goodrich et al.* [2007] and the modified-MHD paper of *Kuznetsova et al.* [2007] do not present any detail about the inner magnetosphere. *Taktakishvili et al.* [2007] does emphasize the inner magnetosphere, and the results do not seem to show any evidence of interchange instability there. It is not clear why there is such a difference between the predictions of the models. Of course, one way in which the RCM differs from the others is that its plasma boundary condition is set from observations rather than pure theory. The reason for the discrepancy also may lie in numerical diffusion in the MHD code. The Fok code resolves the inner magnetosphere well but is limited by its use of MHD-computed electric fields. Our approach is to use the RCM to provide a detailed picture of the ring current, but using a Tsyganenko magnetic field model tuned for the event and potential electric fields that are computed self-consistently with the inner-magnetosphere particles. This active particle-field coupling in the RCM produces electric fields and Birkeland currents that are quite different from the results of the BATS-R-US/Fok simulation. RCM grid spacing and numerical method are, of course, specifically designed for resolving inner-magnetospheric processes, and it computes its potential electric field self-consistently.

3.5 Conclusions

We have simulated the 18 April 2002 sawtooth event using the Rice Convection Model with inputs carefully adjusted to give optimum agreement with observed LANL-SOPA data and magnetic field data at geosynchronous. The six tooth oscillations were treated as six substorms with broad injection fronts and unusually wide substorm current wedge during the expansion phase. Therefore, substorm-related processes, i.e., strong stretching and dipolarization of the magnetic field, intense ionosphere outflows and reconnection and plasmoid formation in the magnetotail, were taken into consideration by adjusting the T01_s magnetic field model augmented by a modified Tsyganenko substorm current wedge model for approximate consistency with the magnetic field measured at geosynchronous orbit and by imposing different plasma distributions on the simulation boundary at $-8R_E$ during different substorm phases.

1. Our model results imply that highly elevated SOPA fluxes require up to ~25 keV temperature plasma boundary conditions in the near-Earth region after every onset. We suggest that the temperature enhancement would be attributed to the acceleration due to the induction electric field when the magnetic field collapses strongly in an unusually wide local time range during the sawtooth event.
2. The simulated energetic neutral atom fluxes are consistent with the IMAGE/HENA fluxes for 10-60 keV hydrogen. The ring current pressure peaks around 10~20 minutes after every onset. We believe that the intensification of ring current is associated with strong dipolarization process, which energizes particles and also brings flux tubes into the inner magnetosphere.
3. Our simulation produced interchange convection cells with lifetimes of 40~60 minutes and average spatial periodicity of 1.5~2.0 hours in local time and corresponding 4~8 pairs of downward-upward field-aligned currents, although the exact details of the interchange pairs appears to be dependent on numerical

resolution and will be discussed in Chapter 5. However, this interchange pattern is consistent with quasi-periodic finger-like north-south aligned auroral structures observed in IMAGE/FUV WIC images in both spatial and temporal scales. We suggest that this spatially periodic interchange pattern naturally occurs when the large $PV^{5/3}$ reduction happens over a wide range of local time.

Chapter 4

An RCM-E simulation of an isolated substorm event

In this chapter, we present initial results from a simulation of an isolated substorm that occurred on 29 Oct., 2004, using the Rice Convection Model coupled with a magneto-friction equilibrium solver (RCM-E). This model includes the self-consistent feedback of both the ionospheric electric potential coupled with magnetospheric convection and the magnetic field equilibrated with the particle pressures. The expansion phase is modeled by imposing low values of $PV^{5/3}$ at the RCM's high latitude boundary. The plasma distribution on the tail boundary for the expansion phase is carefully tuned to match Geotail (~-9R_E) observed plasma moments. The model results are in fairly good agreement with Geotail observed magnetic field, estimated local flux tube volume V and the entropy parameter $PV^{5/3}$, number density, temperature and pressure for <45keV particles as well as differential fluxes for >50 keV particles from multipoint observations at geosynchronous orbit and magnetic field at GOES satellite.

The model results support the global view of a typical substorm growth phase, including stretching of the magnetic field, enhancement of the cross tail current density, earthward motion of the plasma sheet, sharpening of the transition region and dropouts of the energetic particle flux at geosynchronous orbit. The induction electric field in the growth phase calculated from the model is of comparable magnitude to the convective electric field, and thus has a significant effect on the plasma drifts. At the end of the growth phase, the model produces a very stretched magnetic field and B_Z minimum at ~-13 R_E.

A global view of several typical features of the expansion phase associated with strong plasma injection is also provided, including significant enhancement of the partial ring current, short-lived large dawn-to-dusk electric field, prompt over-shielding patterns of electric potentials, dramatic magnetic field dipolarization outside partial ring current region. It is found that the strong plasma injection is associated with the reduction of $PV^{5/3}$ below a certain value between 0.04 to 0.1 nPa$(R_E/nT)^{5/3}$ after several minutes of onset, which is possibly a result of lobe tail magnetic reconnection. It confirms the central role of $PV^{5/3}$ in the plasma transport from magnetotail to near-Earth magnetosphere. Time-dependent region-1 and region-2 field-aligned currents (FACs) are calculated based on the equilibrium magnetic field, where the region-1 FACs are associated with the substorm current wedge (SCW). The simulation shows that the region-2 FACs, with closure to enhanced partial ring current, decrease quickly following plasma injection; however the total current carried by SCW with magnitude of 10^6A remains roughly constant for at least ten minutes.

4.1 Introduction

Unlike the controversial mechanisms related to substorm onset, the physical picture of substorm growth phase is generally well-accepted, i.e., unbalanced dayside reconnection and tail reconnection leading to an increase of magnetic flux in the lobe and the storage of magnetic energy in the tail, which also forces the plasma sheet to thin to equilibrate the increasing lobe field pressure. One of the significant uncertainties in substorm physics is the configuration at near- the middle-Earth tail near the end of the growth phase, which may be critical in determining the feasibility of some instabilities that may be closely related to the trigger mechanisms of substorm onset, e.g., the current disruption [e.g., *Lui*, 1996] or the near-Earth-neutral-line [e.g., *Baker et al.*, 1996]. It was suggested by *Lui et al.* [1992] that a current density of 27~80 nA/m^2 prior to the onset in the dipole-tail transition region may induce the cross-field current disruption. It is still uncertain in what exact conditions the growth phase transforms into the expansion phase, although there is speculation that some threshold conditions should be met just prior to the fully developed unloading process [e.g., *Koskinen et al.*, 1993; *Henderson et al.*, 2006a]. Accurate modeling of an individual substorm may provide a global view of the change of plasma sheet and magnetic field configuration.

In global magnetospheric-ionosphere coupling, the magnetic field line mapping is an important link in the one-to-one correspondence of activities between the magnetotail and the ionosphere. However, since there are large variations between substorms, statistical models often smooth out the highly stretched feature of the magnetic field prior to substorm onset. One approach is the event-oriented magnetic field modeling [e.g., *Pulkkinen et al.*, 1991b, 1991c], which basically modifies the free parameters and/or mathematical representations of module(s) in Tsyganenko models. Rather than choosing solar wind and geomagnetic indices driven parameters, module parameters are set to best match multipoint magnetic field observations. *Kubyshkina et al.* [1999, 2002] included particle pressure information to further constrain the choice of free parameters. Since these event-oriented models apply almost all available observations to fit their model and the number of parameters in the model is of the same order of the number of simultaneous observations, it is difficult to independently evaluate model accuracy. Furthermore, the model results are critically dependent on the choice of mathematical representations. For example, in the same substorm growth phase event modeled by *Pulkkinen et al.* [1994] with symmetric ring current module, *Kubyshkina et al.* [1999] found that using an asymmetric ring current module gave quite different cross tail current densities. We present here an alternative approach that uses self-consistently computed magnetic field balanced with plasma pressure using the RCM-E.

Various models have been developed to represent substorm growth phases, including models that require force equilibrium [e.g., *Lemon et al.*, 2003; *Zaharia and Cheng*, 2003]. *Zaharia and Cheng* [2003] compared the equilibrium states by solving 3D force-balance in an Euler potential coordinates, to demonstrate the field and current distribution for two different (quiet and active) initial conditions. *Zaharia et al.* [2006] also coupled this equilibrium code with RAM model (ring current-atmosphere coupling model, see *Jordanova et al.* [1997] for reference) inside geosynchronous orbit to test the feedback of magnetic field in a geomagnetic storm. *Lemon et al.* [2003] calculated the force balance state of the magnetotail, as well as inner magnetosphere, by modifying the ideal MHD equation with an additional frictional dissipation term. The magneto-friction equilibrium code has been coupled to the RCM, by assuming adiabatic convection inside the RCM modeling region (see section 4.3 for details). The initial attempt to model a substorm using the RCM-E was done by *Toffoletto et al.* [2001] who found that the assumption of the near-Earth neutral line resulted in a specific ionospheric signature related to the interchange instability. The RCM-E has also been used to simulate an idealized storm, using a sophisticated depleted boundary condition [*Lemon et al.*, 2004].

The substorm expansion phase is an explosive unloading process following the growth phase. It is believed to be powered by magnetic reconnection in the magnetotail, transforming stored magnetic field energy to plasma thermal and kinetic energy [e.g., *Hones*, 1977; *Baker et al.*, 1996] or triggered by internal instabilities such as the ballooning instability [e.g., *Roux et al.*, 1991] or the current disruption instability [e.g., *Lui*, 1996]. The currents in the inner and middle magnetosphere are diverted onto the ionosphere via field aligned currents (FACs) [*Vasyliunas*, 1970], completing the magnetospheric-ionosphere system with quite dynamic and nonlinear interactions. The complete simulation of this complicated system, especially during the substorm expansion phase, remains a challenge.

Based on the theory of plasma convection through the magnetotail to the inner magnetosphere and the proposed bubble injection picture [e.g., *Pontius and Wolf*, 1990; see section 2.3 for details], the basic idea of substorm expansion phase simulation using the RCM-E is to investigate the injection of low $PV^{5/3}$ plasma by specifying plasma boundary conditions. Theoretically, the modeling using convection models is able to depict the macroscopic configuration of electromagnetic dynamics of plasma in convective spatial and temporal scale, rather than the microscopic physics, such as substorm triggering, reconnection, and various plasma instabilities such as ballooning. As discussed earlier in section 2.3.2, an initial test using the RCM for the simulation of an idealized bubble injection was completed by *Zhang et al.* [2008] by specifying a depleted plasma boundary condition in the tail around midnight and an enhanced *Y*-direction electric field. This resulted in an increased partial ring current, which is often observed during substorm expansion phase. Using similar techniques and along with an empirical model of the substorm current wedge [*Tsyganenko*, 1997], *Zhang et al.* [2009a, 2009b] were able to model a real substorm event by reproducing a more realistic the magnetic dipolarization inside the wedge. However, it was found that empirical magnetic field models may not fully represent the feedback of plasma distribution to the magnetic field, especially in specific substorm expansion phase modeling when the magnetic field is extremely dynamic. In this chapter, we present results of the first modeling of a real substorm (an event that occurred on Oct. 29, 2004) using the RCM-E, which imposes the requirement of force balance between the RCM-computed plasma pressure and the magnetic field.

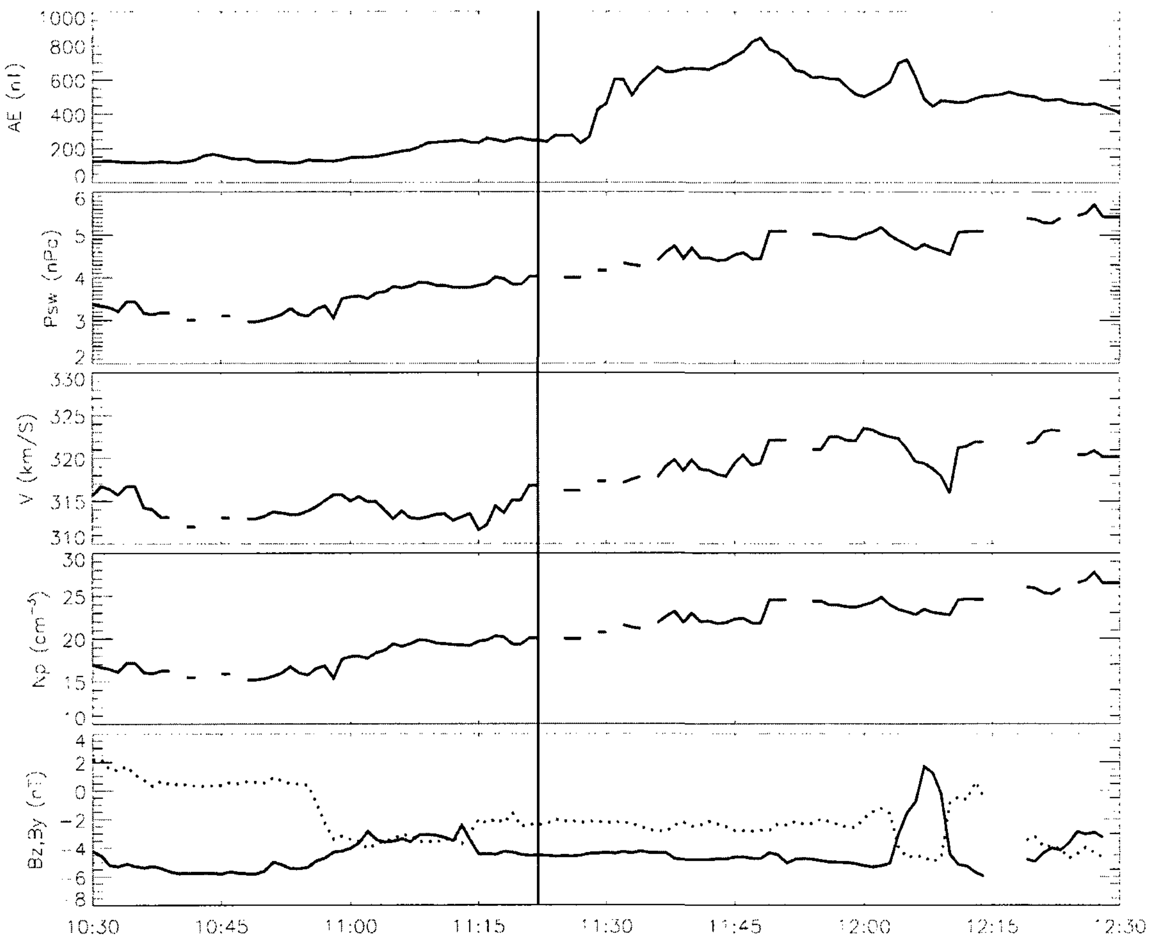

Figure 4.1. Overview of solar wind parameters shifted to the Earth magnetopause and AE index. From top to bottom are AE index, solar wind raw pressure P_{SW}, flow velocity V, proton number density N_P, magnetic field in GSM B_Z (solid line) and B_Y (dotted line). The vertical solid line indicates the substorm onset time 11:22UT determined by ground magnetometers.

4.2 Event Overview

Figure 4.1 shows the AE index and some solar wind parameters for the modeled substorm event on Oct. 29, 2004 from 10:30UT to 12:30UT. The IMF B_Z (in GSM coordinates) turned south at around 03:45UT and remained southward with variations from -6nT to -1nT until around 12:00UT. The solar wind proton number density increased from around 10 cm^{-3} at 03:45UT to around 25 cm^{-3} at 12:00UT, and the flow velocity was relatively low at about 300 to 320 km/s. The AE index increased from 0nT to about 100nT at 06:20 UT, which suggests that convection was enhanced after that. The ground station at Dawson, CGM Latitude=65.76 and CGM longitude=273.66, recorded Pi2 pulsations beginning at 11:22UT, so we set 11:22UT as the substorm onset time. During this event, the Kp index varied between 2 and 3, and the absolute value of Dst index was less than 10nT, suggesting that this was a non-storm substorm. The AE index increased sharply at 11:28UT, 6 minutes after the Pi2 pulsation at Dawson.

During the southward IMF B_Z interval, the earthward plasma convection was enhanced, indicated by the negative bay in the AL index, which suggested that the period before substorm onset was possibly an convection bay or SMC (Steady Magnetospheric Convection) event [e.g., *Pytte et al.*, 1978; *Sergeev et al.*, 1996a; *Sergeev et al.*, 2001], although the AE index did not exceed the statistical threshold 200nT [e.g., *Sergeev et al.*, 1996a; *O'brien et al.*, 2002]. Since we used Geotail observations as a guide to set the inputs for the simulation, the results presented in this chapter started at 10:47UT rather than 03:45UT, when Geotail data is available. During this time, Geotail was moving to cross the plasma sheet from the southern hemisphere to the northern hemisphere; it entered the central plasma sheet at time 10:46UT when the ion beta value exceeded 1.0 which is usually used as a criterion for central plasma sheet [e.g., *Tsyganenko and Mukai*, 2003]. We set out to model the substorm growth phase at 10:47UT with relaxed magnetic field (the detailed initial condition and boundary condition setup is described in Section 4.4).

4.3 Introduction to the RCM-E

The RCM is an adiabatic drift code that treats the plasma in the inner and middle magnetosphere as many fluids with assumptions of slow-flow and isotropic pressure distribution along the magnetic field line (see section 1.4 to 1.6 for details, or refer to *Toffoletto et al.*, 2003). In the traditional RCM, the magnetic field is prescribed by using a sophisticated empirical model, such as the Tsyganenko models [*Toffoletto et al.*, 2003 and references therein].

To self-consistently calculate the magnetic field configuration, we use the magneto-friction equilibrium code which evolves the system toward static force equilibrium when $\vec{J}\times\vec{B}$ equals the gradient of plasma pressure as

$$\vec{J}\times\vec{B}=\frac{1}{\mu_0}(\nabla\times\vec{B})\times\vec{B}=\nabla P \qquad (4.1)$$

The code solves the modified ideal MHD equations 4.2 to 4.7 that include a frictional dissipation term in the momentum equation (equation 4.6)

$$\frac{\partial \rho}{\partial t} = -\nabla \bullet (\rho \vec{v}) \tag{4.2}$$

$$\frac{\partial \vec{B}}{\partial t} = -\nabla \times \vec{E} \tag{4.3}$$

$$\vec{E} = -\vec{v} \times \vec{B} \tag{4.4}$$

$$\vec{J} = \frac{1}{\mu_0}(\nabla \times \vec{B}) \tag{4.5}$$

$$\rho \frac{d\vec{v}}{dt} = \vec{J} \times \vec{B} - \nabla P - \alpha \rho \vec{v} \tag{4.6}$$

$$\frac{\partial P}{\partial t} = -\nabla \bullet (P\vec{v}) - (\gamma - 1)(\nabla \bullet \vec{v})P \tag{4.7}$$

where ρ is plasma density, $\alpha \rho \vec{v}$ is friction term and α is friction parameter. α is adjusted to optimize convergence towards equilibrium:

$$\vec{F} = \vec{J} \times \vec{B} - \nabla P = 0 \tag{4.8}$$

During an RCM run, the magnetic field is held fixed, after it has run for a designated exchange time. For the growth phase the exchange time between the RCM and the equilibrium code was several minutes (see sections 4.4.1, 5.2, 6.2 and 7.3), while for the expansion phase it was one minute (see section 4.4.5, 5.2, 6.2 and 7.3). After the RCM has run, it provides the plasma pressure to the equilibrium code, which in turn returns the equilibrated magnetic field to the RCM. Further details of the equilibrium code are described by *Lemon et al.* [2003].

The current version of the RCM-E assumes a zero-tilted Earth dipole field, so that the center of the neutral sheet always lies on the Earth's magnetic equatorial plane. This would introduce a systematic error in data-model comparison when the measurement is off the neutral sheet. To circumvent this, we utilize an empirical current sheet model [*Tsyganenko and Fairfield*, 2004; hereinafter referred to as TF2004] to estimate the distance from the center of the neutral sheet to the Earth's magnetic equatorial plane. We transform the satellite's location in GSM coordinate system (x,y,z) to GSW system (X,Y,Z), using the solar wind direction and the dipole field tilt angle. We then estimate Z_n, the Z-coordinate of the center of the local neutral sheet in the GSW system, as a function of solar wind parameters and (X, Y). Then we treat the satellite as located $(X,Y,Z\text{-}Z_n)$ in the RCM-E and also treat the normal direction of the current sheet in GSW as the normal direction of equatorial plane in RCM-E model. Therefore, A physical parameter S at $(X,Y,Z\text{-}Z_n)$ in our model should be compared with the *in-situ* physical parameter S' at (x,y,z) in GSM measured by the satellite. A similar procedure has been used in an RCM simulation of a substorm event [*Zhang et al.*, 2009a]. Since the solar wind conditions during this event were fairly steady, we applied the averaged solar wind parameters from 10:47UT to 11:22UT to determine the coefficients G_0, G_1, S and R_H in equations (1) and (2) in TF2004, i.e., V_x=-313 km/s, V_y=25.0 km/s, B_y=-2.07 nT, B_z=-4.28 nT, P_{sw}=3.59 nPa. We set α=2.4 in order to best fit our initial magnetic field and plasma moments to Geotail observations.

4.4 Model setup

4.4.1 The initial and boundary conditions for the growth phase

During the growth phase simulation, the RCM and the equilibrium code exchange the plasma pressure and magnetic field every 5 minutes, from 10:47 to just before onset at 11:22. For simplicity, the ionospheric Hall and Pederson conductances were assumed to be uniform and set to 5 S for each hemisphere. To initiate the growth phase simulation, we started with the magnetic field model T89 [*Tsyganenko*, 1989] parameterized with the instant value of Kp=3 and plasma pressure [*Tsyganenko and Mukai*, 2003; hereinafter referred to as TM2003], which have been relaxed using equilibrium code [*Lemon et al.*, 2003]. The solar wind parameters used to set up coefficients to drive the TM2003 model are the same as those used in TF2004 model. For the region outside $10R_E$, the plasma moments are set according to TM2003 empirical model. (The TM2003 empirical model is only valid in the plasma sheet outside $10R_E$.) For the region inside $10R_E$, the plasma moments are tuned more arbitrarily to match the Geotail observed plasma moments but are required to be within a reasonable range relative to statistical models. Specifically, the plasma pressure within 10 R_E is set to the power law $P=A*R^B$, where R is the distance to the center of the Earth in units of R_E. The power law form of the plasma pressure distribution as a function of radial distance was adapted by *Borovsky et al.* [1998], partially adapted by *Spence and Kivelson* [1993] in the statistical study and by *Zaharia and Cheng* [2003] in initial condition setup in a growth phase simulation. The coefficients A and B are set to fit the pressure at Geotail orbit and the pressure at $10R_E$ as specified by TM2003 model at midnight. The ion temperature outside $10R_E$ is given by TM2003 model, while the ion temperature inside $10R_E$ is set as

$$T_i = C^*\cos(\pi R/20.0) + T_{i}\_10 \quad (4.9)$$

where, T_i_10 is the ion temperature at 10 R_E at midnight given by TM2003, and C is the coefficient so that T_i=9.0 keV at geosynchronous orbit. This gives a decreasing ion temperature as increasing radial distance, consistent with statistical models, but a different form from the power law suggested by *Borovsky et al.* [1998]. The ratio of ion temperature and electron temperature is given as

$$T_i/T_e = 4.0 + 2.0^*\tan^{-1}(R-7.0) \quad (4.10)$$

which gives the ratio of 3.23 at geosynchronous orbit and larger than 6.50 outside of 10 R_E. This is set to reproduce the observations that the ion-electron temperature ratio falls between 5.5 and 11 for most conditions in the plasma sheet [*Baumjohann et al.*, 1989] and that the ratio near geosynchronous orbit is usually smaller. The initial ion number density and electron number density are calculated everywhere as $N_e = N_i = P/k_B(T_i + T_e)$, where k_B is the Boltzmann constant. The numbers for the plasma pressure (1.8nPa), number density (1.2cm^{-3}) and ion temperature (9.0keV) at geosynchronous orbit are roughly consistent with the statistical results of *Borovsky et al.* [1998], which are 1.6nPa, 1.0cm^{-3} and 10.0keV respectively. Statistically, the plasma sheet particle distribution is a kappa distribution during geomagnetic quiet times (AE<100nT) [*Christon et al.*, 1989], in terms of energy invariant and density invariant it is written as,

$$\eta(\lambda)=\frac{2}{\sqrt{\pi}}((\kappa-1.5)k_B T)^{-\frac{3}{2}}\frac{\Gamma(\kappa+1)}{\Gamma(\kappa-0.5)}\frac{N\sqrt{\lambda}\Delta\lambda}{(1+\frac{V^{-2/3}\lambda}{(\kappa-1.5)k_B T})^{\kappa+1}} \tag{4.11}$$

We set $\kappa=6$ initially outside 8 R_E as well as on the tailward boundary in the nightside, as suggested by *Christon et al.* [1989]. Arbitrarily, the plasma distribution elsewhere is set as a $\kappa=4$ distribution. The plasma moments on the boundary are provided by the TM2003 model.

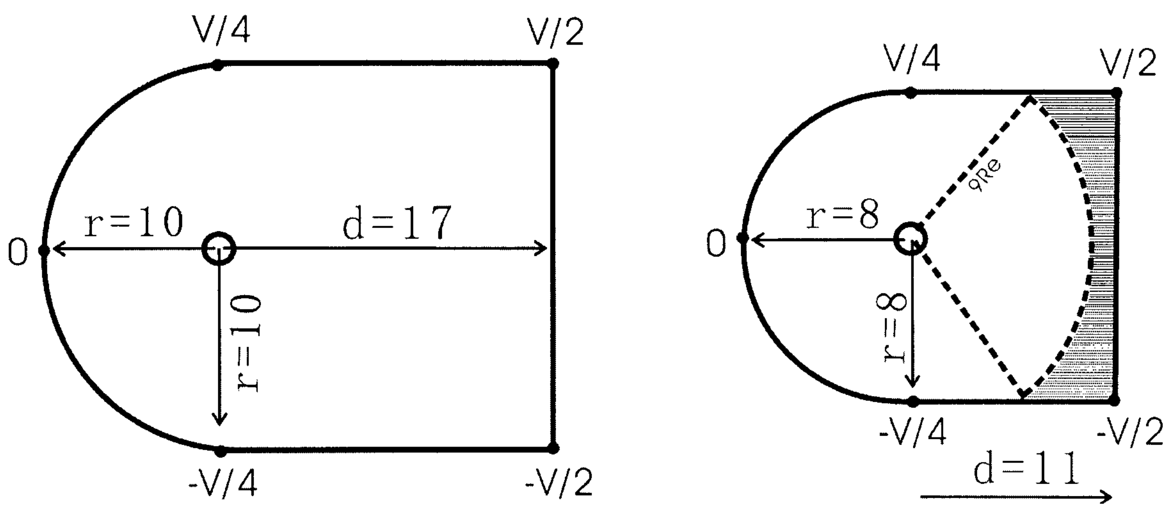

Figure 4.2. The equatorial view of D-shape RCM simulation region for growth phase (left) and expansion phase (right). The sun is to the left. The values near black spots on the boundary indicate the polar cap potentials, where V=57kV.

4.4.2 The RCM simulation region

The modeling region is a D-shape region as shown in Figure 4.2, but the region in the expansion phase simulation is smaller than that for the growth phase, because

1. The RCM modeling region is the closed-field line region in the inner and middle magnetosphere. Although the statistical results based on Geotail observations showed that the magnetic reconnection probably occurs in the pre-midnight sector between X_{GSM}=-30R_E and X_{GSM}=-20R_E prior to substorm onset [*Nagai et al.*, 1998], it has also been reported that the reconnection site may be as close as -11R_E near midnight [*Henderson*, 2004]. During this event, there is no direct observation on the location of the reconnection site during the expansion phase, therefore, to try to avoid open magnetic field lines, we arbitrarily confine our RCM modeling region within 11R_E in the magnetotail.
2. The slow-flow assumption in the RCM may be violated in the near-Earth magnetotail region due to the fast convective velocity when the magnetic field rapidly collapses to a dipole-like field during early expansion phase. *Zhang et al.* [2009b] estimated that the convective flow velocity in the induction electric field could be comparable or greater than the local sound speed for most of the region beyond X=-15 R_E in the tail in an RCM simulation.

Therefore we carefully designed the simulation region as an equatorial D-shape, limited to X>-11 R_E in the tail and X<8 R_E in the dayside magnetosphere.

4.4.3 Electric potentials on the boundary

The D-shape region on the equatorial plane, as shown in Figure 4.2, is convenient for setting up electric potential distribution on the boundary during the growth phase. For simplicity, the electric potential drop is made to vary linearly along the boundary, i.e., from *V*/2 at (*X*, *Y*)=(-17,-10) to *V*/4 at (0,-10) along the dawn side, from –*V*/2 at (-17, 10) to –*V*/4 at (0, 10) along the dusk side, from *V*/2 to –*V*/2 on the tail boundary, and from *V*/4 to 0 to –*V*/4 along the dayside boundary, respectively. Since the solar wind condition was fairly stable, we take the averaged polar cap potential drop *V*=57kV through the entire substorm event, estimated using the *Boyle et al.* [1997] formula.

Although the simulation region shrinks during the expansion phase, we assume the total potential drop remains unchanged at 57kV over the tail boundary. However, the distribution along tailward boundary is modified to a more sophisticated form, following *Lemon et al.* [2004], who applied an enhanced electric field inside the depleted channel [e.g., *Nakamura et al.*, 2001]. The potential on the night side boundary is given as,

$$V_b(\phi) = V\frac{F_V(\phi)}{F_{V,MAX} - F_{V,MIN}} \tag{4.12}$$

Where

$$F_V(\phi) = -\frac{\sin(\phi)}{2} + \left\{\frac{1}{4(\phi_e - \phi_w)}\ln[\frac{\cosh(2(\phi-\phi_w))}{\cosh(2(\phi-\phi_e))}] - \frac{\phi}{2\pi} + \frac{1}{2}\right\} \tag{4.13}$$

$F_{V,MAX}$ and $F_{V,MIN}$ are the maximum and minimum values of $F_V(\phi)$; ϕ is the azimuthal angle with respect to the dayside meridian plane; $\phi_e = \pi + \tan^{-1}(8.0/11.0) \approx 1.2\pi$ and

$\phi_w = \pi - \tan^{-1}(8.0/11.0) \approx 0.8\pi$. The solid line in Figure 4.3 shows the potential distribution in the tailward boundary at -11R$_E$ as a function of Y during the early expansion phase from 11:22 to 11:35UT. Compared to the corresponding curve for the growth phase (dashed line), the expansion-phase potential electric field is indeed enhanced throughout the boundary. During the late expansion phase and recovery phase, the potential drop is kept at 57kV, but the potential distribution on the tailward boundary is changed to the first term in equation (4.13). Comparing with the late expansion and recovery phase (dotted line), the specified electric field near midnight during the early expansion phase (solid) is stronger and the electric field in growth phase (dashed) is weaker.

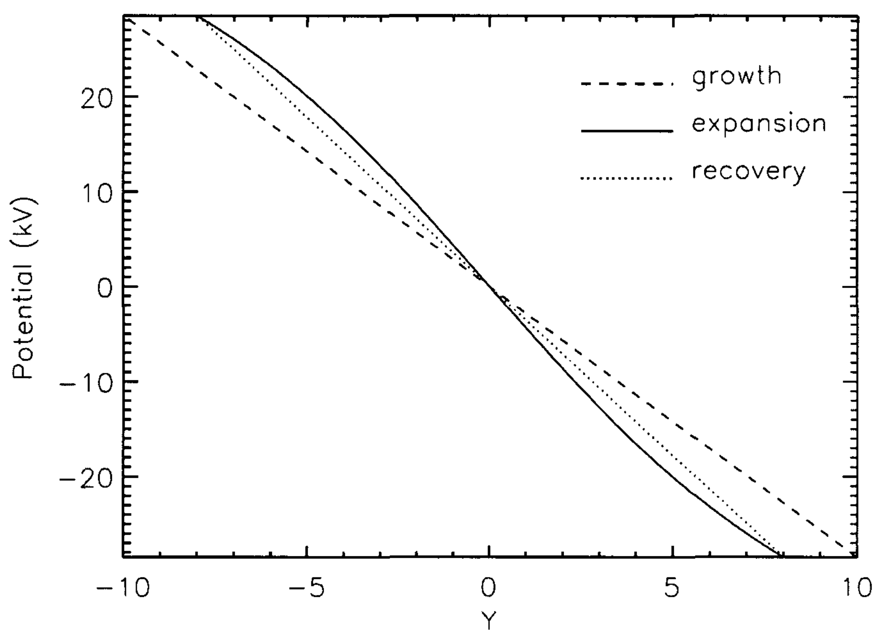

Figure 4.3. Electric potentials along the tail boundary for growth phase (dashed line), early expansion phase (solid line) and late expansion phase and recovery phase (dotted line). The potential drop is 57kV.

4.4.4 Reduction of $PV^{5/3}$ at onset

Although either magnetic reconnection in the tail [e.g., *Hones*, 1977] or other mechanisms related to current disruption [e.g., *Lui*, 1996] may non-adiabatically reduce the entropy parameter $PV^{5/3}$ during the early expansion phase, it is still unclear what the spatial extent of the non-adiabatic reduction of $PV^{5/3}$ is. In the event modeled by *Zhang et al.* [2009a, 2009b] using the RCM with reduced $PV^{5/3}$ near midnight at onset, the plasma pressure showed considerable increase in both simulation and observation in the first 3 minutes after substorm onset, which was interpreted as the rush of plasma with high $PV^{5/3}$ ahead of the depleted low $PV^{5/3}$ plasma. In the event presented in this Chapter, the plasma pressure observed by Geotail at -9R_E, was roughly constant in the first 5 minutes, followed by a sharp decrease at 11:27 to 11:28UT (Figure 4.5), implying distinct feature of the plasma earthward transport from *Zhang et al.* [2009a], i.e., there was possibly very weak earthward moving plasma with high $PV^{5/3}$ or the earthward moving plasma during the first 5 minutes contained low $PV^{5/3}$ which was already reduced at onset. Therefore, the spatial extent of non-adiabatic depletion of plasma in this simulation is quite different from that presented by *Zhang et al.* [2009a], who reduced $PV^{5/3}$ along the boundary along a more limited region at onset.

Using the solar wind parameters at substorm onset 11:22 UT, the *Tsyganenko and Mukai* [2003] empirical plasma sheet model (TM2003) provides the ion number density and temperature in the central plasma sheet at location (X, Y, Z)=(-11, 0, 0), as T_{TM}, N_{TM}.

At the end of the growth phase 11:22-ε UT, the plasma pressure and the flux tube volume at the same location are P_g in units of nPa and V_g in units of R_E/nT. In this run, at the substorm onset 11:22, we force the $PV^{5/3}$ to decrease to value 0.14 nPa(R_E/nT)$^{5/3}$ from the region of outside of 9 R_E in the nightside to the tail boundary at -11 R_E (the shaded region in Figure 4.2). To impose the reduction of $PV^{5/3}$, we set up the plasma moments, particle pressure P, ion and electron number density N_i and N_e, ion and electron temperature T_i and T_e, as

$$P = P_g \frac{0.14}{P_g V_g^{5/3}} = 0.43 P_g \tag{4.14}$$

$$N_i = N_e = aN_{TM} = 0.65 N_{TM} \tag{4.15}$$

$$T_i = \frac{1}{a}\left(\frac{P}{P_g} T_{TM}\right) = \frac{1}{a}\frac{0.14}{P_g V_g^{5/3}} T_{TM} = \frac{1}{0.65}\frac{0.14}{P_g V_g^{5/3}} T_{TM} = 0.66 T_{TM} \tag{4.16}$$

$$T_i / T_e = 4.0 + 2.0 * \tan^{-1}(11.0 - 7.0) = 6.65 \tag{4.17}$$

The factor a=0.65 is included in equations (4.15) and (4.16), because the plasma sheet tends to be hot and tenuous after substorm onset. Therefore, in the shaded region of Figure 4.2, the density invariant $\eta(\lambda)$ is uniform at 11:22UT.

4.4.5 Plasma boundary condition during the expansion phase

The basic goal in the setup of the boundary condition in the expansion phase modeling is to match the proton moments (<40keV) observed at Geotail (~ -9R_E). Since there is no *in situ* measurement at -11R$_E$, we specify our boundary condition by modifying the TM2003 empirical model as follows,

$$P = \frac{PV^{5/3}}{V_f^{5/3}} \tag{4.18}$$

$$T_i = \frac{1}{b} T_{TM} \tag{4.19}$$

$$T_i / T_e = 4.0 + 2.0 * \tan^{-1}(11.0 - 7.0) = 6.65 \tag{4.20}$$

$$N_i = N_e = \frac{P}{k_B(T_i + T_e)} \tag{4.21}$$

The entropy parameter $PV^{5/3}$ is specified as a function of time as shown in Figure 4.4b and independent in *Y*-direction. V_f is the flux tube volume given by the magneto-friction equilibrium code at the tail boundary. Equation (4.18) provides the plasma pressure on the tail boundary. T_{TM} is the instantaneous ion temperature in the central plasma sheet given by TM2003 model. The ratio of ion temperature and electron temperature (equation 4.20) is fixed at 6.65 on the boundary in expansion phase formula similar to equation 4.10. The scale factor "*b*" in equation 4.19 is a reflection of the changing of plasma moments during the various phases of the substorm; *b*-values are shown in Figure 4.4a. During the growth phase, *b*=1; while during the early expansion phase b<1 when plasma sheet is hot and *b*>1 during late expansion phase and recovery phase when plasma sheet is cold, so as to be consistent with statistical models [*Wing et al.*, 2007]. The actual values of *b* were determined by trial and error. We use a $\kappa = 6$ distribution on the boundary [*Christon et al.*, 1989].

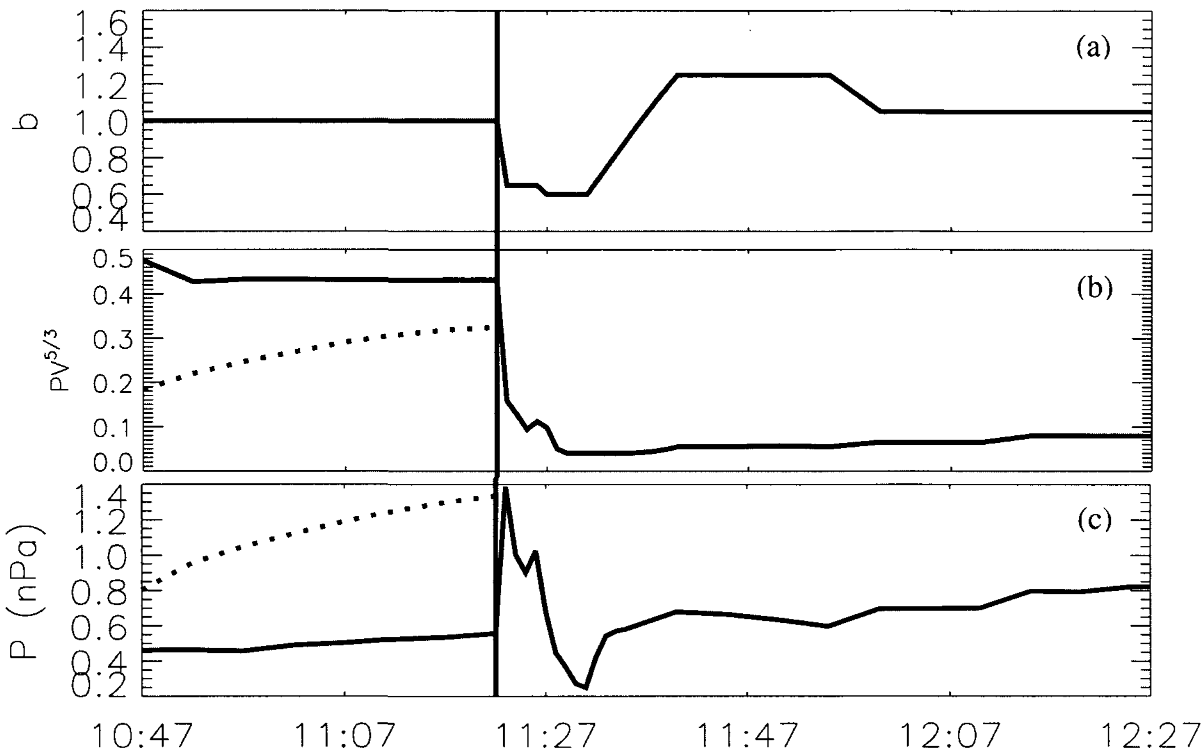

Figure 4.4. Scale factor b in equation 4.19 (top panel) and, $PV^{5/3}$ (middle) and P (bottom) in the grid closest the boundary inside simulation region at midnight (solid line) and plasma parameter at (-11, 0) R_E in the equatorial plane during growth phase (dotted line). The vertical solid line shows the substorm onset time 11:22UT.

Solid lines in Figure 4.4 show the plasma moments on the closest grid point to the boundary inside simulation region at midnight, i.e., X=-17R_E in the growth phase and X=-11R_E after onset; dotted lines show the plasma parameters at (X, Y)=(-11 ,0) R_E in the equatorial plane during growth phase. Several features are evident in the plasma boundary condition. (1) Both $PV^{5/3}$ (Figure 4.4b) and P (Figure 4.4c) at -11R_E decreased dramatically after onset. (2) The $PV^{5/3}$ remains less than 0.08 nPa/(R_E/nT)$^{5/3}$ after 11:27UT, with only slightly increasing in the late expansion and recovery phase. Calculated from equation 4.18, the plasma pressure P approximately follows the same trend as $PV^{5/3}$. (3) As discussed above, the scale factor b (Figure 4.4a) is unity during growth phase, ~0.6 during early expansion giving a hot plasma sheet, and ~1.2 to 1.05 in the late expansion and recovery phase representing a relatively cold plasma sheet.

4.5 Data-model comparison

In this section, we compare the simulation results with multipoint observations. Overall, the simulation results are in fairly good agreement with the observed magnetic field, electric field and plasma moments at Geotail (X=-9R_E) and with the magnetic field, energetic particle flux and plasma moments at geosynchronous orbit.

4.5.1 Comparisons with Geotail observations (~-9R_E)

The bottom three panels in Figure 4.5 compare the ion moments (<40keV) in the observations (dotted lines) and the simulation (solid lines). Dotted lines in the first and fourth panels show the equatorial entropy parameter $PV^{5/3}$ and flux tube volume V estimated from local Geotail observations [*Wolf et al.*, 2006a].

Due to careful adjustments of the boundary conditions, ion pressure P_i, number density N_i and temperature T_i agree well with Geotail observations during the growth phase. The gradual buildup of particle pressure indicates earthward transport of plasma. In the first five minutes from 11:22 to 11:27, P_i and N_i remained almost constant with small variations, while T_i decreased from ~7.5keV to 6keV. During this time, the entropy parameter $PV^{5/3}$ decreased from the peak value of 0.15 to nearly 0.08 nPa/(R_E/nT)$^{5/3}$. At 11:28, there are peaks in P_i, T_i and N_i, indicating a sharp change of local plasma distribution along with particle energization and density depletion, while $PV^{5/3}$ shows a simultaneous decrease to less than 0.08 nPa/(R_E/nT)$^{5/3}$. Meanwhile, the magnetic field dipolarized strongly (Figure 4.6), resulting an enhanced induction electric field in Y direction (Figure 4.7). Associated with the local decrease in $PV^{5/3}$ to less than a critical value of 0.08, the magnetic field dipolarized and the dawn-dusk electric field increased. *Lemon et al.* [2004] found that, with a self-consistent simulation of an idealized storm main phase using the RCM-E, that the ring current injection was greatly enhanced when the $PV^{5/3}$ depleted to a critical low value. From the inner magnetospheric point of view, the simulation of substorm expansion in this chapter and the storm main phase in *Lemon et al.* [2004] are similar in that both imposed a reduced $PV^{5/3}$ on the boundary. It is clear that the plasma injection in this event involves two steps, one before $PV^{5/3}$ decreased to ~0.08 nPa/(R_E/nT)$^{5/3}$, and one after that. After 11:30UT, the local $PV^{5/3}$ remained at a low value of 0.05~0.08 nPa/(R_E/nT)$^{5/3}$ until the end of the simulation, while the plasma moments, electric field and magnetic field dipolarization exhibited with relatively small variations. Further discussion concerning about the role of $PV^{5/3}$ in the dynamics of plasma and electromagnetic field in the inner magnetosphere will be given in section 4.6.4.

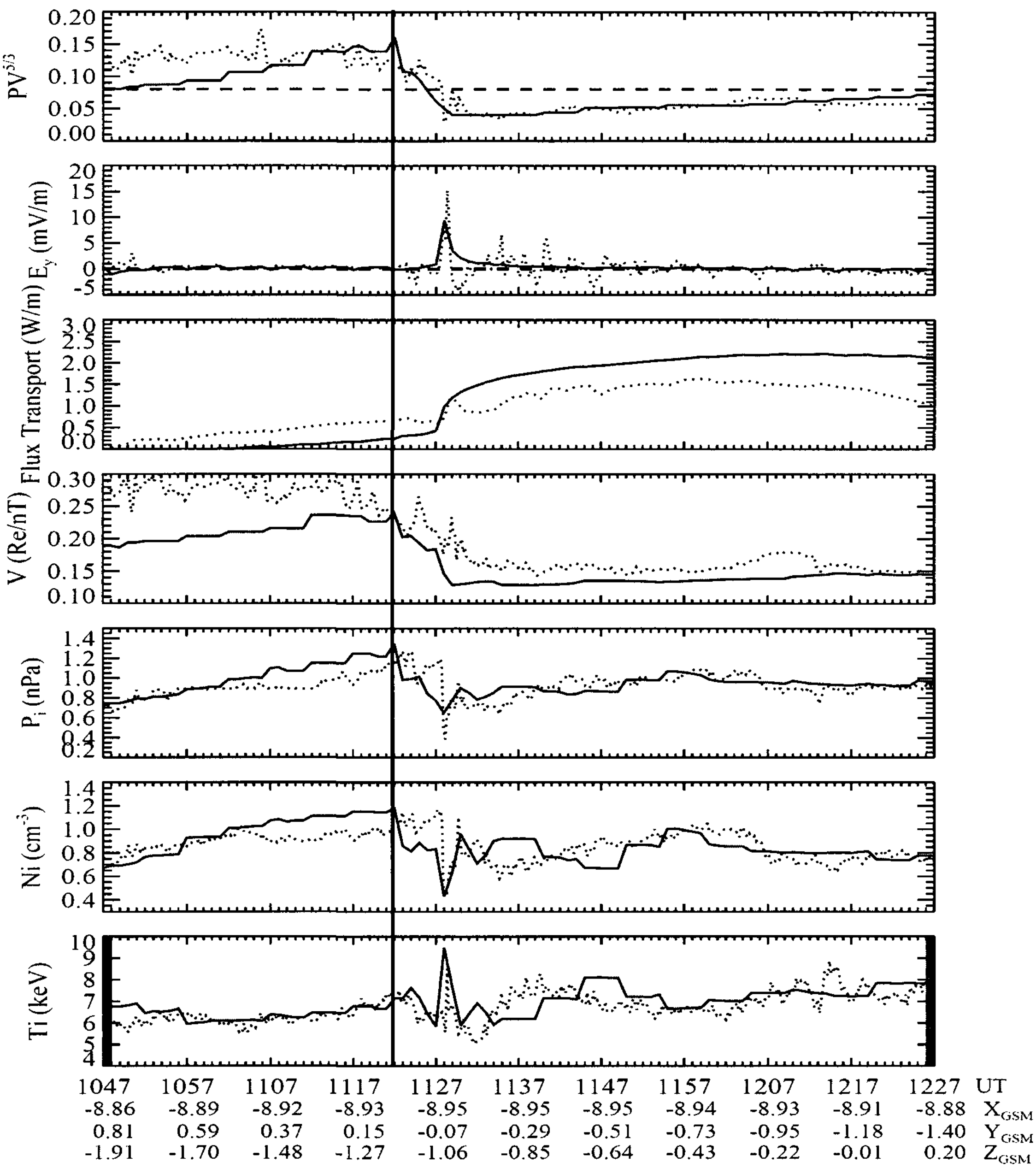

Figure 4.5. The Geotail observations (dotted line) and the modeling results (solid line). From top to bottom are plasma entropy parameter $PV^{5/3}$ (in units of nPa$(R_E/nT)^{5/3}$), Y component of electric field E_y, Flux Transport, flux tube volume V, proton thermal pressure P_i, number density N_i and temperature T_i. The P_i, N_i and T_i shown here are for energy less than 40keV protons as the same as Geotail LEP instrument. All data are in the GSM coordinate system. The vertical solid line shows the substorm onset time at 11:22UT.

Figure 4.6 shows the magnetic field observed by Geotail (dashed lines) and modeled by the RCM-E (solid lines). The discrepancy in B_y is because the current version of RCM-E is a simplified zero-tilted model with initial configuration adapted from T89 model with no tilt and assumes north-south symmetry in the magnetic field. It is clear that both the magnitude of B_Z and $|B|$ are decreasing throughout the growth phase, which is attributed to two effects, the spacecraft was approaching the center of neutral sheet from southern hemisphere to northern hemisphere and the magnetic field was stretching. Observationally, the plasma ion beta value reached a peak value of 10.5 at around 11:23UT and B_X changed its sign several times between 11:24 and 11:30UT, indicating that the spacecraft crossed the current sheet; while the model shows that the crossing happened once at 11:22 when Geotail was at the center of the estimated neutral sheet. This discrepancy is obvious in the bottom plot of Figure 4.6 that the magnetic field inclination angle, defined at $\tan^{-1}(B_Z/B_X)$, is greater than 90 degrees around ~11:25UT when Geotail was still below the current sheet; while the simulated results indicated that Geotail was above the current sheet. It should be noted that this discrepancy is largely due to the current sheet flapping at ~11:25UT, which cannot be captured in the RCM simulations. The left plot in Figure 4.16 shows that the magnetic field was stretching during this time, when B_z was decreasing from 10.0 to 2.8 nT at X=-9 R_E. It should be noted that results are an initial attempt to use the RCM-E for a real even although the modeled magnetic field B_Z in the simulation is smaller than the observed magnetic field by a factor of ~2, the basic feature of magnetic field stretching is consistent with observations. The modeling can be improved by specifying a more reasonable plasma boundary condition, especially the values of $PV^{5/3}$, which is an unknown parameter. The mismatch of the B_Z component can also attributed to the crude estimate of the current sheet location using an empirical model, whose parameters are set to best fit the magnetic field and plasma moments in the beginning of the run, while the gradient of B_Z component in *Z*-direction near the center of the current sheet in the growth phase is significant. Other reasons, such as the field-aligned potential drop and non-uniform conductances, are not excluded at this time as a possible explanation of this discrepancy.

The |B| is near minimum at onset, followed by a modest increase in the first five minutes in expansion phase. At about 11:28, a strong dipolarization occurs, shown by the sharp increase in B_z. The magnetic field collapse inside the RCM modeling region plays a role in particle acceleration, if slow flow and isotropic assumptions still hold [*Wolf et al.*, 2006b]. The increased B_z results in decreased flux tube volume, which then energizes plasma if the energy invariant is conserved, i.e., $\lambda_s = W_s V^{2/3}$. B_Z peaks at around 11:37UT, followed by gradual decrease in magnitude. It will be argued in section 4.6.5 that Geotail was inside the substorm current wedge, and observed the dipolarization.

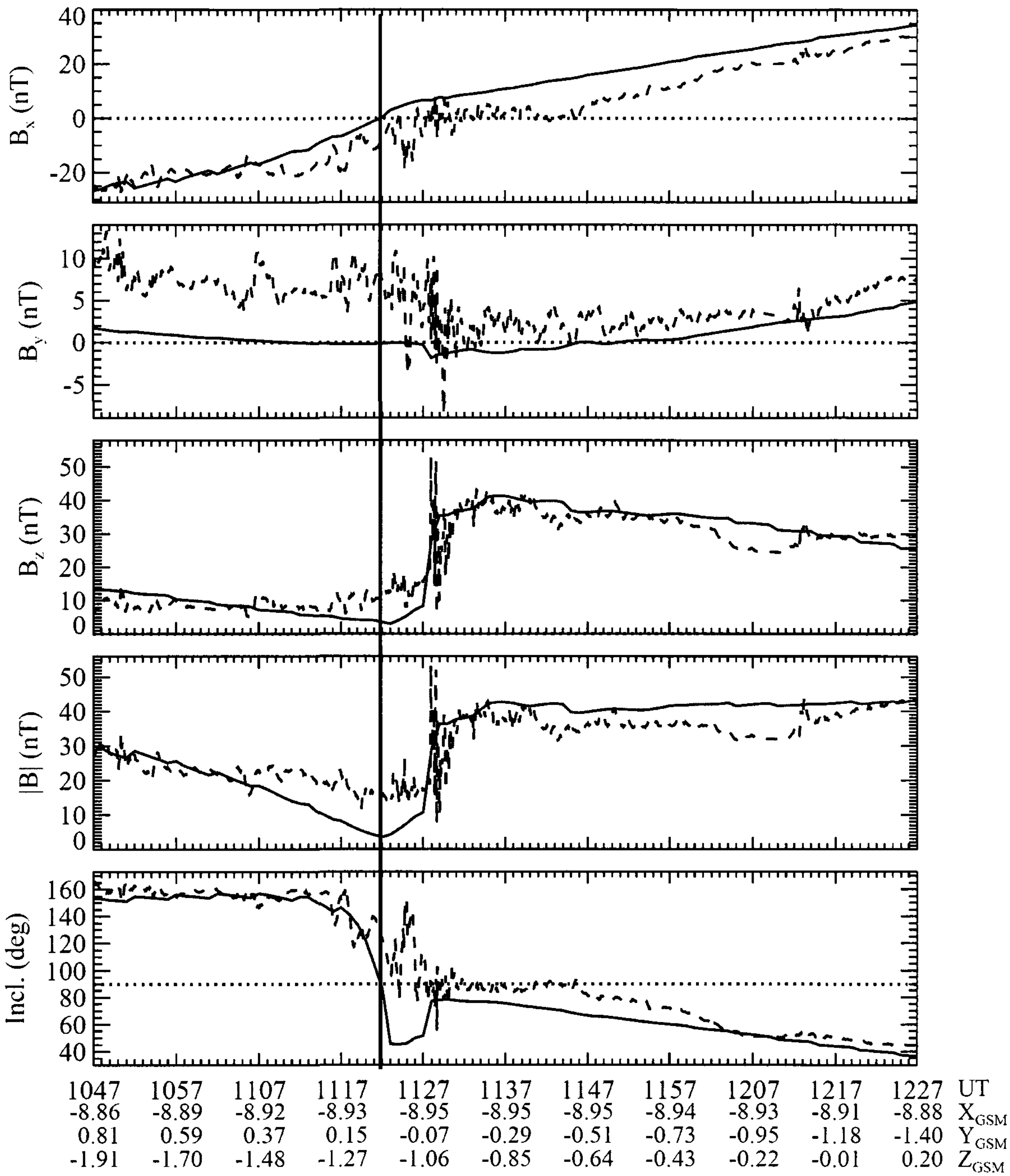

Figure 4.6. The Geotail observations (dashed line) and the modeling results (solid line). From top to bottom are X-, Y-, Z-component of magnetic field, the magnitude of magnetic field and inclination angle ($\tan(\theta)=B_z/B_x$), respectively. The three horizontal dotted lines indicate B_x=0, B_y=0 and θ=90. All data are in GSM coordinate system. The vertical solid line shows the substorm onset time 11:22UT.

Figure 4.7 shows the modeled *Y*-component of convection, induction and total electric field in green, red and blue lines respectively, as compared with observations at Geotail (black lines) through the simulation. The modeled E_y is roughly positive with the magnitude of 0.2mV/m during the growth phase, indicating that the net flux transport is earthward. The observed E_y shows short time scale wave-like oscillations, which cannot be captured using RCM-E; however, on average, the modeled E_y is consistent with the observed values. The induction electric field, calculated from the expression

$$\vec{E}_{induction} = -(\frac{\partial \vec{X}}{\partial t}) \times \vec{B} \tag{4.22}$$

where $\frac{\partial \vec{X}}{\partial t}$ is the local velocity of the mapped equatorial footprint of an ionospheric gridpoint [*Zhang et al.*, 2009a], is dawnward with the magnitude of about -0.3mV/m, which is an evident effect of magnetic field stretching. While the ~0.5mV/m convection electric field is always positive in the *Y* direction, which is a direct result of the imposed 57 kV potential drop over the 20R_E wide in dawn-to-dusk direction. The simulation results indicate that, at least in this case, the magnitudes of the induction and convection electric field were comparable. During adiabatic convection in the growth phase, the convection electric field transport plasma earthward mainly by E×B drift; while the induction electric prevents plasma injection from tail by stretching magnetic field. More detailed discussion of this will be given in section 4.6.1.

The fast magnetic field collapse induces an electric field mainly in the *Y* direction during early stage of substorm expansion phase. The middle panel of Figure 4.7 shows the early expansion phase results and the top panel shows the time from 11:34 to 12:27UT. Note that the scales of E_y and time are different in three panels. Although substorm expansion phase begins at 11:22UT, the induction electric field only increases slightly in the first five minutes from -0.5 to 0.5 mV/m, indicating transition from stretching to weak dipolarization. From 11:27 to 11:29, a spiky positive E_y is observed by Geotail, and simulation similarly shows up to 10 mV/m induction electric field, with negligible convection electric field. A negative E_y of -4 mV/m is observed later from 11:29 to 11:31, when earthward flow is diverted to tailward near the transition region [*Lui et al.*, 1999]. It is known that the flow bouncing is associated with field dipolarization and the electric current diversion from the cross tail current to field-aligned current when forming the substorm current wedge. MHD simulations have showed that both pressure gradient and inertial effects contribute to the braking, and the gradient of pressure is dominant and persistent in the expansion phase [*Birn et al.* 1999]. In this sense, since the RCM only calculates the bounce-averaged $E \times B$ and gradient/curvature drift rather than the inertial drift, it is fair to judge that our modeling cannot fully reproduce the effects of braking, but the predominant factors are included. Meanwhile, the plasma would bounce back and forth after injection, as indicated by the oscillations of E_y after 11:31. Our model cannot capture these wave-like variations. Therefore, as an integrated quantity, the flux transport (Figure 4.5), defined as $\int E_y dt$, does have a jump during the instant collapse around 11:28, but is followed by a stronger increase in simulation compared with observation.

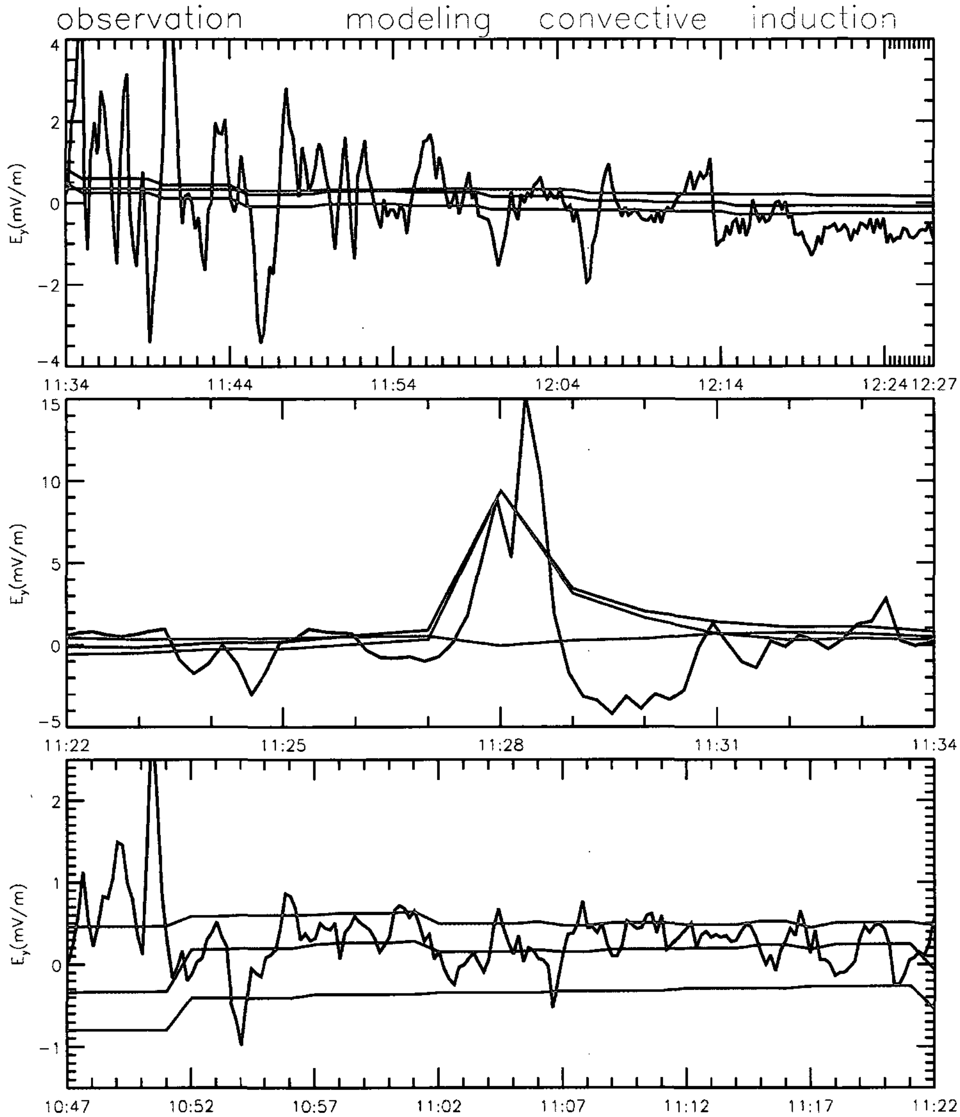

Figure 4.7. The Y-component of electric field E_y observed by Geotail (black lines), the modeled Y component of electric field (induction electric field in red, potential electric field in green and total electric field in blue). The three panels from bottom to top are for times 10:47 to 11:22UT, 11:22 to 11:34UT and 11:34 to 12:27UT, respectively.

4.5.2 Comparisons at geosynchronous orbit

Figure 4.8 shows the 3 components of magnetic field and tilt angle, defined as $\psi = \tan^{-1}(B_z / \sqrt{B_x^2 + B_y^2})$, observed by GOES-10 (dashed lines) and the corresponding simulation results (solid lines). During the growth phase, GOES-10 (MLT≈UT-9) is at the post-midnight sector. The magnetic inclination angle is decreasing from 80 to 75 degrees, indicating a moderate stretching at geosynchronous orbit. The modeled magnitude of magnetic field at GOES-12 on the dawnside shows qualitative agreement with *in-situ* observations (not shown), however we are unable to adjust the simulated magnetic field in this un-tilted model to the realistic GSM coordinate system because the mentioned neutral sheet warping estimation technique described in Section 3 cannot be applied in this sector far from midnight.

Following the field stretching in the growth phase, the dipolarization occurred during the expansion phase inside the substorm current wedge. It is obvious that the increase in B_z began within 2 minutes after onset (vertical line), which is consistent with the time when a weak plasma injection is observed at Geotail. A large change in B_x and B_y occurs after 11:27, associated with strong field collapse. From the force-balance point of view, the magnetic field changes are in response to changes in plasma pressure, which indicates that in this event, the particle pressure changes slightly in the inner magnetosphere right after onset, but the major dipolarization occurs around 5 minutes later. The GOES-10 spacecraft was inside the substorm current wedge (SCW)

[*McPherron et al.*, 1973], as indicated by the magnetic field change. In turn, the relative spatial configuration of GOES-10 at MLT=2.5 and the SCW illustrate that the wedge is at least 5 hours wide at 11:27 in longitude (assuming that it is dusk-dawn symmetric), and slightly wider than the azimuthal width of the tail boundary (4.8 hours). The previous RCM simulations of a substorm expansion phase were conducted by depleting $PV^{5/3}$ in a narrow channel [*Zhang et al.*, 2009a] or wide boundary [*Yang et al.*, 2008]. The width of the depletion channel or boundary requires multiple spacecraft observations. An alternative choice to help to determine the azimuthal extension of depletion would be to use magnetic field observations at geosynchronous orbit [*Yang et al.*, 2008] or with ground magnetometers [*Clauer et al.*, 2006; *Sergeev et al.*, 1996c]. In this simulation, the depletion was imposed all along the tail region.

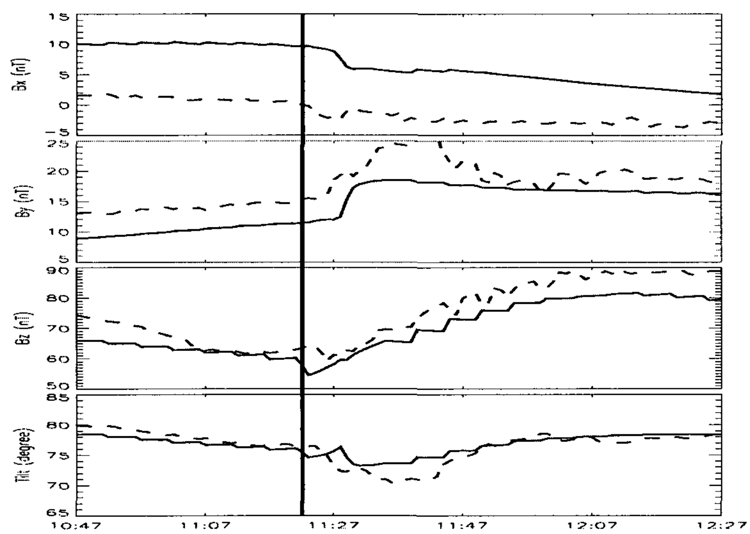

Figure 4.8. The comparison of GOES-10 observed magnetic field (dashed line) and the modeled magnetic field (solid line) in GSM coordinate system. The four plots from top to bottom indicate the X-, Y-, Z-components of magnetic field and the tile angle ψ ($\tan(\psi)=B_z/\sqrt{B_x^2+B_y^2}$).The vertical solid line shows the substorm onset time 11:22UT.

Figures 4.9 and 4.10 show the observed energetic particle fluxes from LANL-SOPA instruments (right panels) and simulation results (left panels) for electrons and protons, respectively. The energy ranges are from 50keV to 315keV for electrons and 50keV to 400keV for protons from black lines to green lines. Five spacecraft, LANL-01A, LANL-02A, LANL-97A, 1990-095 and 1991-080 are presented from top to bottom. Both the observations and simulation indicate the fluxes at LANL-97A, which show a typical energetic particle flux dropouts as a classical feature during growth phase, are distinctly different from other four spacecraft [e.g., *Baker and McPherron*, 1990; *Lopez et al.*, 1989]. The mechanism concerning this dropout was discussed by *Sauvaud et al.* [1996] as betatron deceleration by calculating particle trajectories in time-dependent, stretching magnetic fields near geosynchronous orbit. *Baker and McPherron* [1990] also suggested the importance of magnetic field stretching or current sheet thinning on energetic particle flux dropouts. While the two above mentioned results invoke the conservation of classic first and second invariants to accelerate particles, *Wolf et al.* [2006b] and *Zhang et al.* [2009a] demonstrated that the electric field induced by magnetic field changes can also accelerate and decelerate particles during adiabatic convection. Figure 4.11 shows the magnetic field configuration threading the three spacecraft, LANL-97A, 1991-080 and Geotail in the beginning (top plot) and the end (bottom plot) of the growth phase. During the growth phase, the equatorial footprint of the magnetic field threading Geotail changed little because Geotail was close to the equatorial plane; 1991-080, about 0.6~0.7 R_E off the magnetic equator, and was moving from pre-midnight to post-midnight; however, LANL-97A at about 21MLT, 1.6 R_E from the equator, was moving outward from dipole-like to tail-like near the transition region. The effect of field stretching dramatically changed the field configuration threading LANL-97A, the equatorial footprint moved from (*X*, *Y*)=(-5.4, 5.1) to (*X*, *Y*)=(-9.7, 7.1). Using the isotropic pressure assumption in the model, the increase of the flux tube volume tends to de-energize particles. A similar idea was shown in Figure 1 in *Lopez et al.* [1989].

The energetic particle flux enhancement after substorm onset is a typical characteristic of substorm expansion phase [e.g., *Reeves and Henderson*, 2001]. The energization is attributed to acceleration by an induction electric field [e.g., *Delcourt*, 2002; *Wolf et al.*, 2006b]. For example, the non-adiabatic acceleration during the magnetic field collapse in substorm expansion phase was investigated by *Delcourt* [2002], in which a number of single particle trajectories were calculated, showing that the first adiabatic invariant were violated. *Wolf et al.* [2006b] pointed out that the magnetic field collapse dramatically reduced the flux tube volume V threading the satellite, so that the particle kinetic energy W_s increased significantly to preserve the energy invariant $\lambda_s = W_s V^{2/3}$. Of the five available geosynchronous orbit satellites, LANL-97A (MLT≈20~21) in the pre-midnight sector and 1991-080 (MLT≈0~1) in the midnight is of particular interest since it recorded dispersionless enhancement of both electron and proton flux after onset. In contrast, 1991-080 showed only a very modest increase. As mentioned above, because the LANL-97A is 1.6 R_E was off the magnetic equatorial plane and in the vicinity of the transition region and 1991-080 was very close to the magnetic equator during growth phase, the magnetic field stretching effect was more clearly seen by LANL-97A; therefore, the adiabatic de-energization at LANL-97A is dramatic when the magnetic flux tube volume threading it increases significantly. In the expansion phase, this mechanism acts in opposite direction: when magnetic field dipolarizes, the kinetic energy of the particles on the field lines traversing LANL-97A increases associated with the decrease of flux tube volume . The other three satellites, LANL-02A, LANL-01A and 1990-095 on the dayside, observed a dispersive flux increase, indicated by the clear drift echoes in Figure 4.9 and Figure 4.10.

The <45keV plasma moments are compared in Figure 4.12 and Figure 4.13 for 1991-080 and LANL-97A, and show reasonably good qualitative agreement between the observation and simulation in the growth phase. However, in the expansion phase, only qualitative agreement was obtained, and the simulated plasma pressure at geosynchronous is about twice that of the observed value. The pressure contribution of the electron is about 40% and 20% of proton at 1991-080 (Figure 4.12) and LANL-97A (Figure 4.13). The modeled number density at both LANL-97A and 1991-080 is about double that of the observation. It is not surprising that the agreement in plasma moments at geosynchronous orbit is not as good as at Geotail, since both the initial and boundary plasma condition are tuned to match plasma moment only at Geotail, which was located only $2R_E$ earthward of Geotail in the expansion phase. The results may be improved by including the non-uniform conductance and field-aligned potential drops, which would change the plasma convection pattern to some extent.

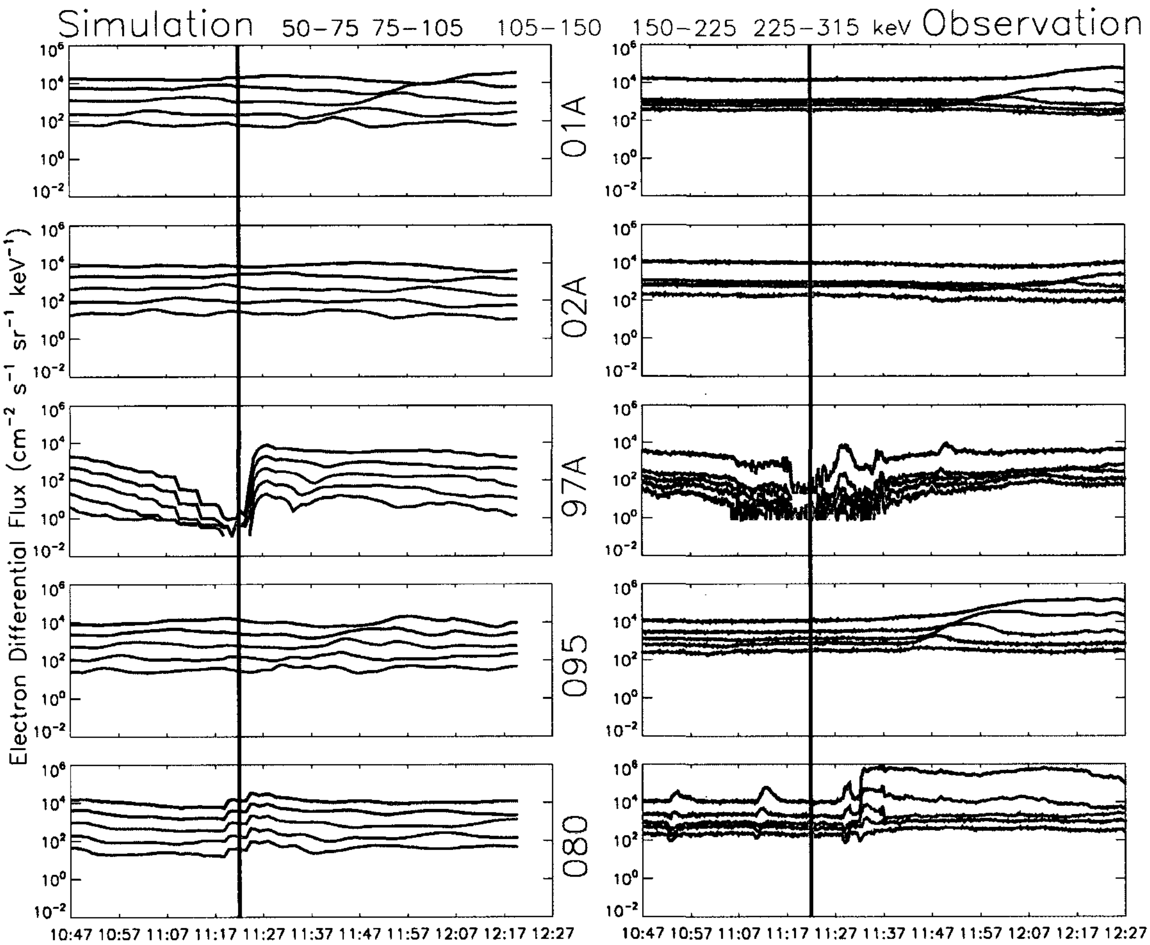

Figure 4.9. The observed energetic electron differential fluxes (right) at geosynchronous orbit and the simulated results (left). The black, dark blue, light blue, red and green lines indicate the 50-75, 75-115, 105-150, 150-225 and 225-315 keV energy range. The vertical solid line shows the substorm onset time 11:22UT. The local midnight for LANL-01A, LANL-02A, LANL-97A, 1990-095 and 1991-080 is at 23:20UT, 19:10UT, 13:55UT, 10:3 0UT, and 02:25UT respectively.

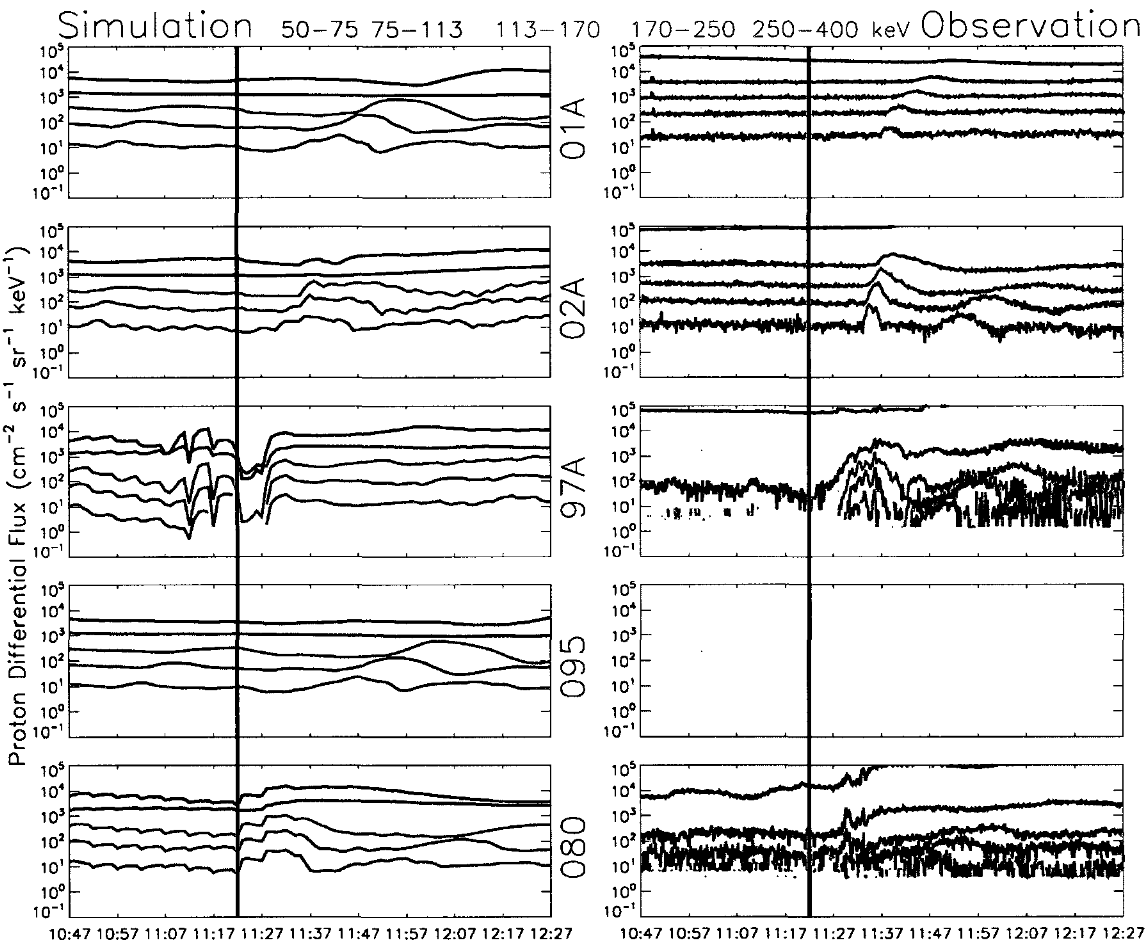

Figure 4.10. The observed energetic proton differential fluxes (right) at geosynchronous orbit and the simulated results (left). The black, dark blue, light blue, red and green lines indicate the 50-75, 75-113, 113-170, 170-250 and 250-400 keV energy range. Five panels from top to bottom are for LANL-01A, LANL-02A, LANL-97A, 1990-095 and 1991-080, respectively. The vertical solid line shows the substorm onset time 11:22UT.

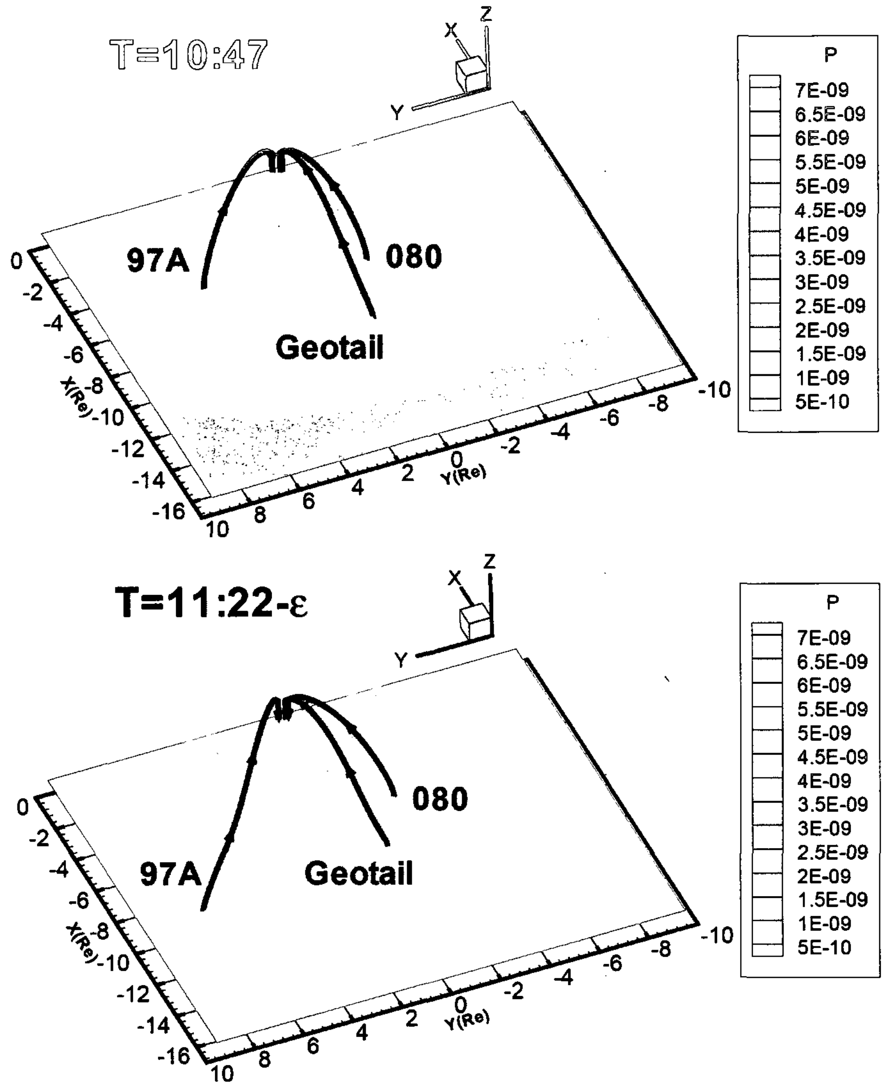

Figure 4.11. The magnetic field line mappings threading 1991-080, LANL-97A and Geotail, labeled as "080", "97A" and "Geotail" respectively. The colors show the plasma pressure on the equatorial plane. Top and bottom plots are for T=10:47UT and T=11:22-ε UT.

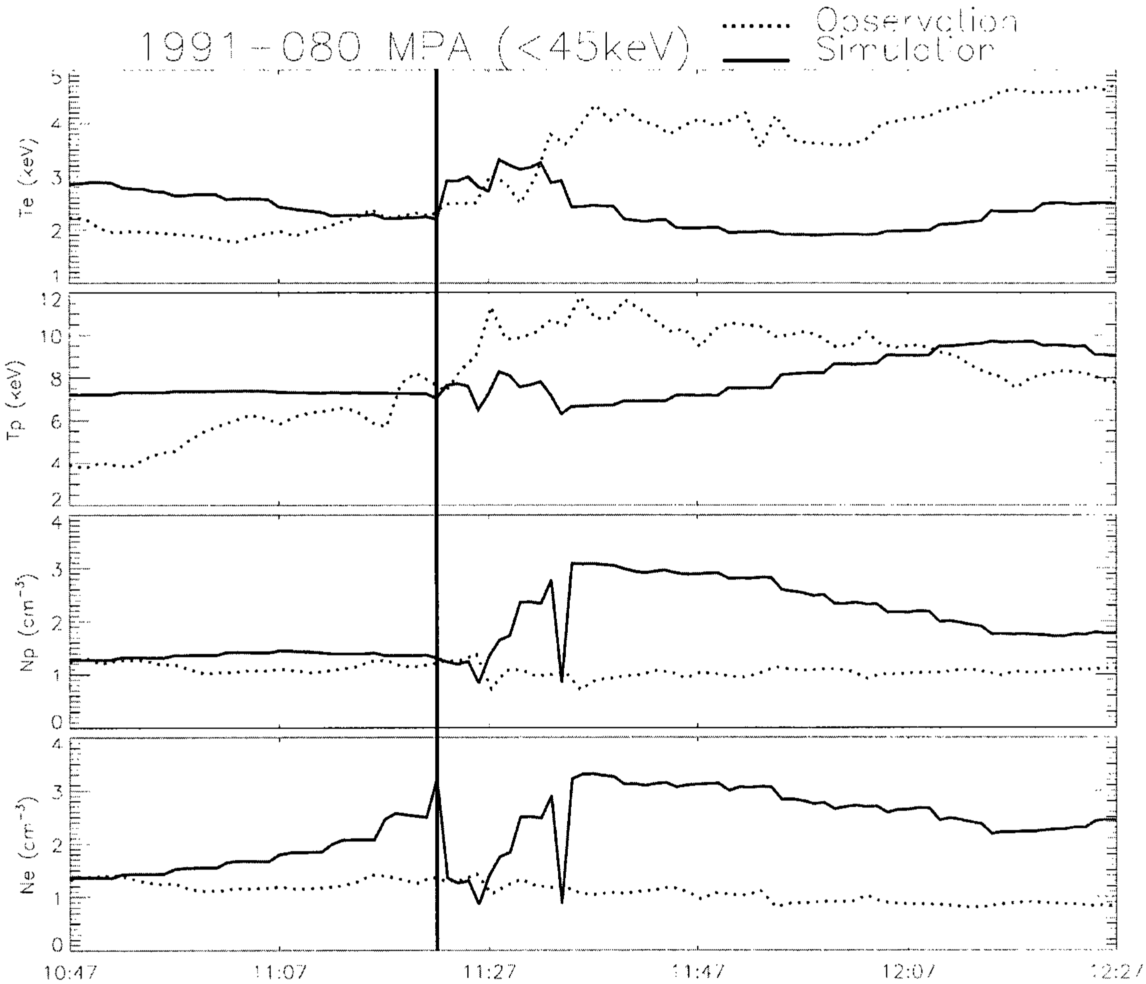

Figure 4.12. The 1991-080 MPA data (dotted line) compared with the simulated results (solid line). The electron temperature, proton temperature, proton number density and electron number density are shown from top to bottom. The vertical solid line shows the substorm onset time 11:22UT.

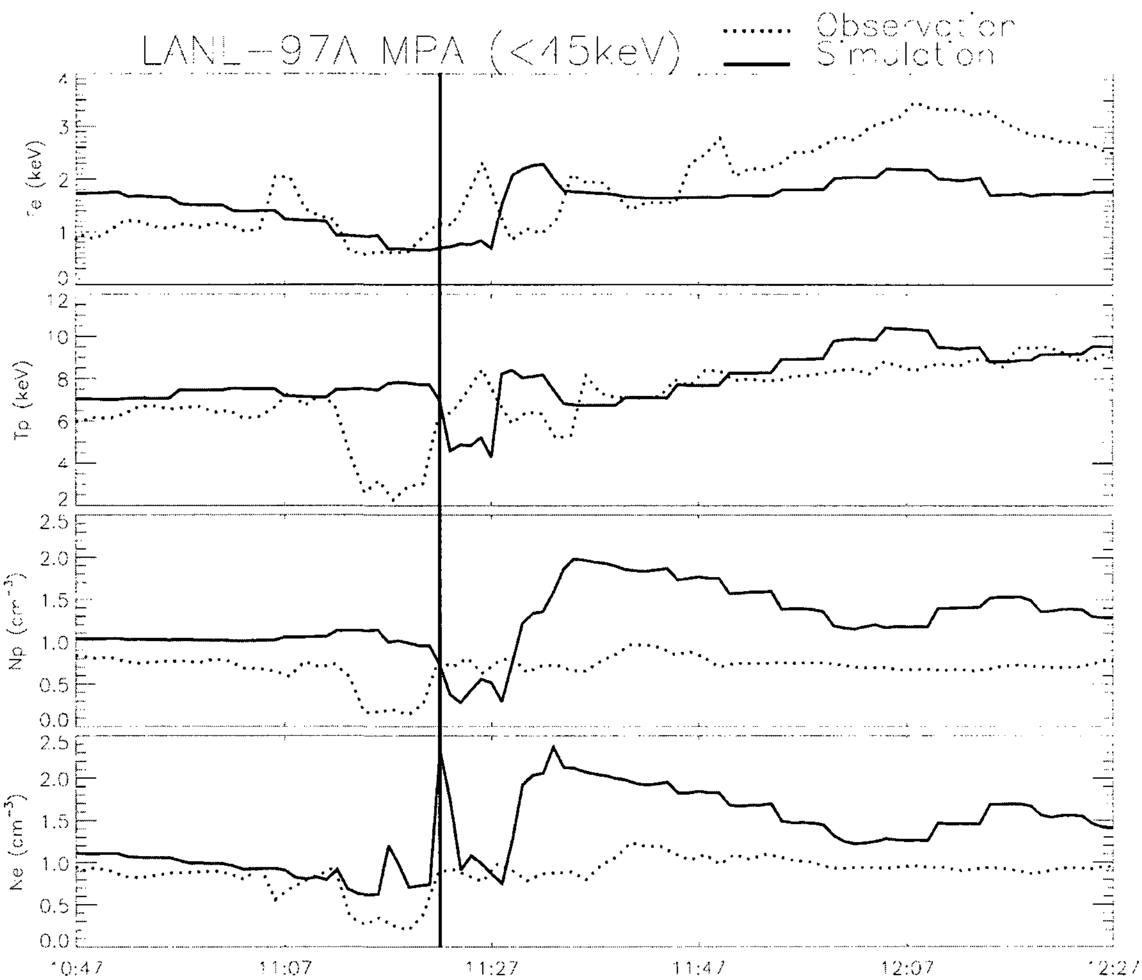

Figure 4.13. The LANL-97A MPA data (dotted line) compared with the simulated results (solid line). The electron temperature, proton temperature, proton number density and electron number density are shown from top to bottom. The vertical solid line shows the substorm onset time 11:22UT.

4.6 Discussion

4.6.1 Adiabatic convection in the growth phase

Several models have been developed that compute equilibrium solutions of the inner and middle magnetosphere [*Lemon et al.*, 2003; *Zaharia and Cheng*, 2003] and for the magnetotail [*Hesse and Birn*, 1993]. These simulations did not attempt to reproduce the time-dependent evolution of magnetic field and plasma pressure as a result of adiabatic convection during the growth phase, but provided a snapshot of force-balanced configuration based on empirical models. Earthward convecting plasma interacts with the magnetic field in such a way that the magnetic field will stretch to a tail-like configuration in response to increases in pressure. This magnetic field stretching will also result in an inductive dusk-to-dawn electric field, inhibiting plasma injection from the tail into the inner magnetosphere [*Toffoletto et al*, 2001]. The results of the RCM-E simulation of the growth phase provide us with a semi-global view of this field-plasma interaction during a growth phase.

Figure 4.14 shows (a) the entropy parameter $PV^{5/3}$, (b) plasma pressure P, (c) ion temperature T_i and (d) ion number density N_i along the X-axis at different times during the growth phase. The initial condition at 1047UT indicates, in solid lines, the specified symmetric ring current with the peak pressure at $3.8R_E$ and the ion temperature as monotonically decreasing with radial distance. Comparing the plasma pressure and ion number density at 1107UT and at the end of the growth phase 1122-εUT with the initial condition, both of these two parameters show a considerable increase, which is a sign of earthward moving plasma as a result of a net 0.2mV/m dawn-to-dusk electric field. In contrast, the ion temperature shows a 20% decrease just before 1122 UT compared with the initial condition at around X=-8 R_E. This is believed to be due to hot ions, which were initialized in the open drift paths and moved westward to the dusk side and away from the midnight sector. Near this transition region, where the gradient/curvature drift is significant, the ion temperature decrease is attributed to hot ions loss. It is noted that the $PV^{5/3}$ increases substantially outside 8R_E, and displays a knee-like profile, which is a result of the local B_Z minimum (left plot of Figure 4.16).

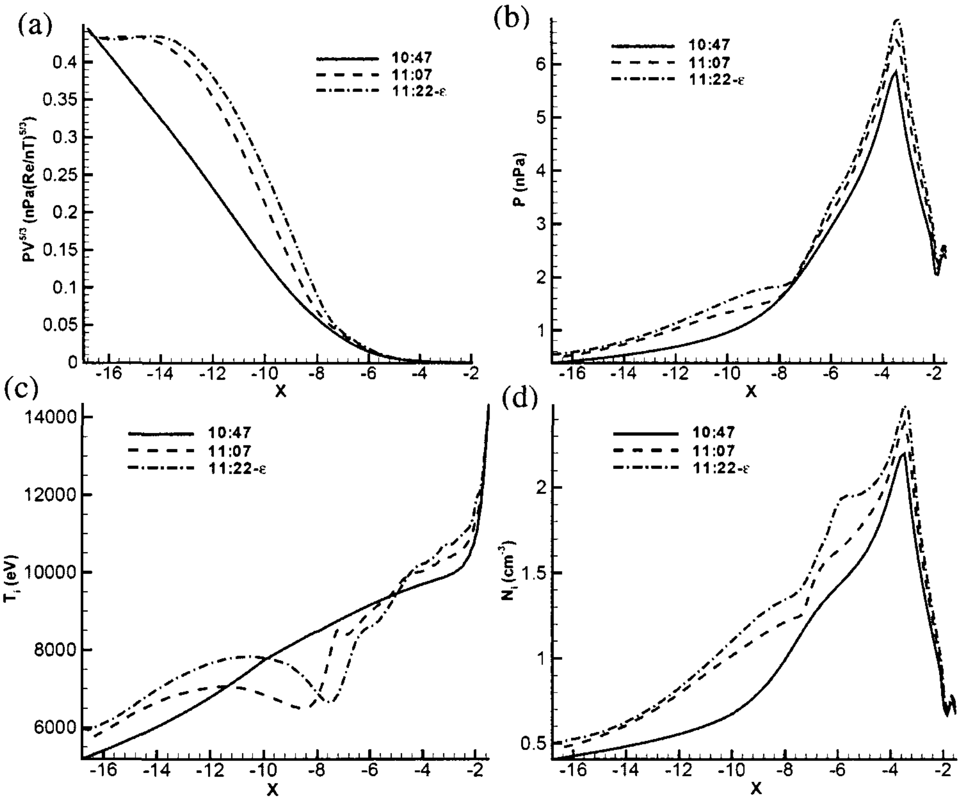

Figure 4.14. The entropy parameter $PV^{5/3}$, plasma pressure P, ion temperature T_i and ion number density N_i along the X-axis for three different times.

We also did an RCM-E run with a fixed magnetic field, i.e., all parameters were kept the same as in the previous RCM-E simulation, but the magnetic field was held in the initial configuration and was not allowed to vary in time. In this case, the code was run without the self-consistent magnetic field. The left plot of Figure 4.15 shows RCM-E result of the equatorial pressure distribution as well as equipotential lines (every 5kV) at 11:22-ε UT. Two prominent differences stand out in the constant magnetic field run shown in the right plot of Figure 4.15. First, a clearly asymmetric ring current has built up near X=-7 R_E with a peak value of about 7 nPa. The physical explanation of this difference is that the convection electric field ~0.5mV/m (green line in bottom panel of Figure 4.7) is strong enough to be able to transport plasma into the near-Earth region; while the induction electric field acts in an opposite direction to prevent the plasma from moving earthward. The total electric field is about 0.2mV/m (blue line in Figure 4.7) in the self-consistent RCM-E run, which is rather weak so that the particle ring current buildup is substantially suppressed. Second, there is a predominant shielding effect associated with the partial ring current in the RCM-E without the self-consistent magnetic field; while in the self-consistent RCM-E run, region-2 currents are too weak to generate shielding in the convective potential distribution. However, it should be mentioned that the weakness of the pressure peak in the RCM-E run may be exaggerated by the over-stretching in our simulation comparing the observed B_Z (~10nT) component at

Geotail at ~-9R$_E$ to the simulated result (~4nT), since the modeled dusk-to-dawn induced electric field could be substantially higher.

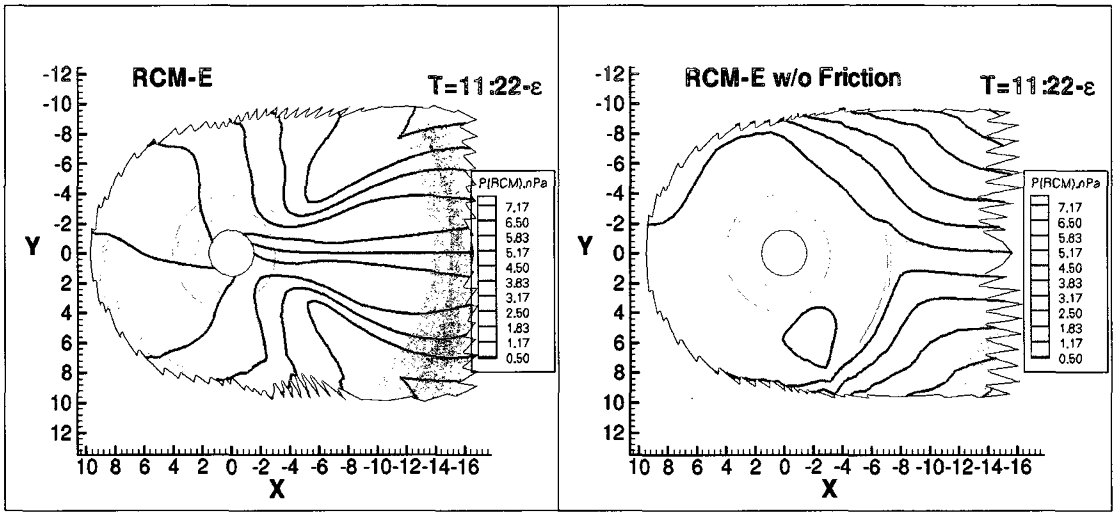

Figure 4.15. The equatorial plasma pressure and the equipotential lines (every 5kV) for RCM-E (left) and RCM-E without the equilibrium code (right) at the end of growth phase.

4.6.2 Local B_Z minimum in the growth phase

The B_Z component on the equatorial plane as a function of X-axis is shown in Figure 4.16. During adiabatic convection, the convective dawn-to-dusk electric field transports plasma earthward and the resulting force-balance magnetic field stretches to balance the RCM-computed pressure distribution. As a result, the magnetic field at the end of growth phase has a more stretched configuration inside 12 R$_E$ (dotted line) than the beginning of the simulation (solid line). A distinct B_Z minimum forms with a value of about 1.3nT at -13 R$_E$, which is consistent with earlier growth phase modeling [*Erickson and Wolf*, 1980, *Hau and Wolf*, 1987] and earlier RCM-E simulations [e.g., *Toffoletto et al.*, 2001]. Other equilibrium models [e.g., *Lemon et al.* 2003; *Zaharia and Cheng*, 2003] have also produced this kind of B_Z minimum. *Kubyshkina et al.* [1999] and *Kubyshkina et al.* [2002] reconstructed mathematical representations of the currents in modified the Tsyganenko model by fitting multipoint observations and including the plasma pressure information, and obtained B_Z minimum with roughly the same magnitude and location as our result. We compare our theoretically modeled highly stretched magnetic field against the Tsyganenko T89 model [*Tsyganenko*, 1989] in the left plot of Figure 4.16. The preliminary results show that the simulated B_Z is ~20nT smaller than the T89 model with Kp=3 from -6 to -8 R_E, and several nT smaller in the region outside -8R_E; while the magnetic field is actually about 60% smaller than the observed one at Geotail (Figure 4.6).

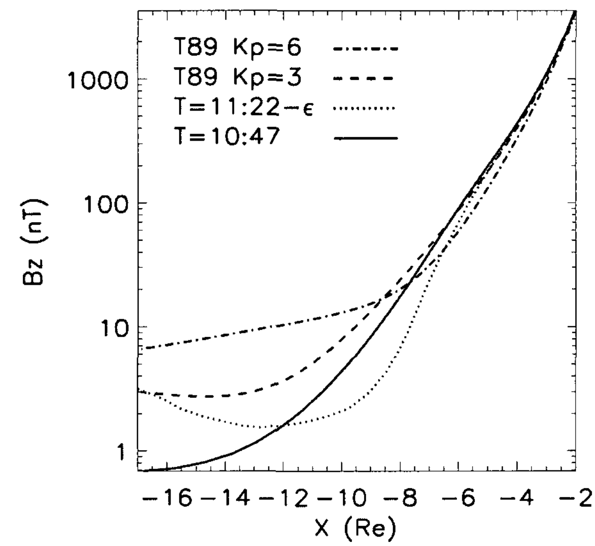

Figure 4.16. The magnetic field B_Z along the X-axis. Solid, dotted, dashed, dotted-dashed lines represent the modeled field in the beginning of the modeling (T=10:47), the modeled field in the end of the growth phase (T=11:22-ε), the T89 Kp=3 model, and the T89 Kp=6 model, respectively.

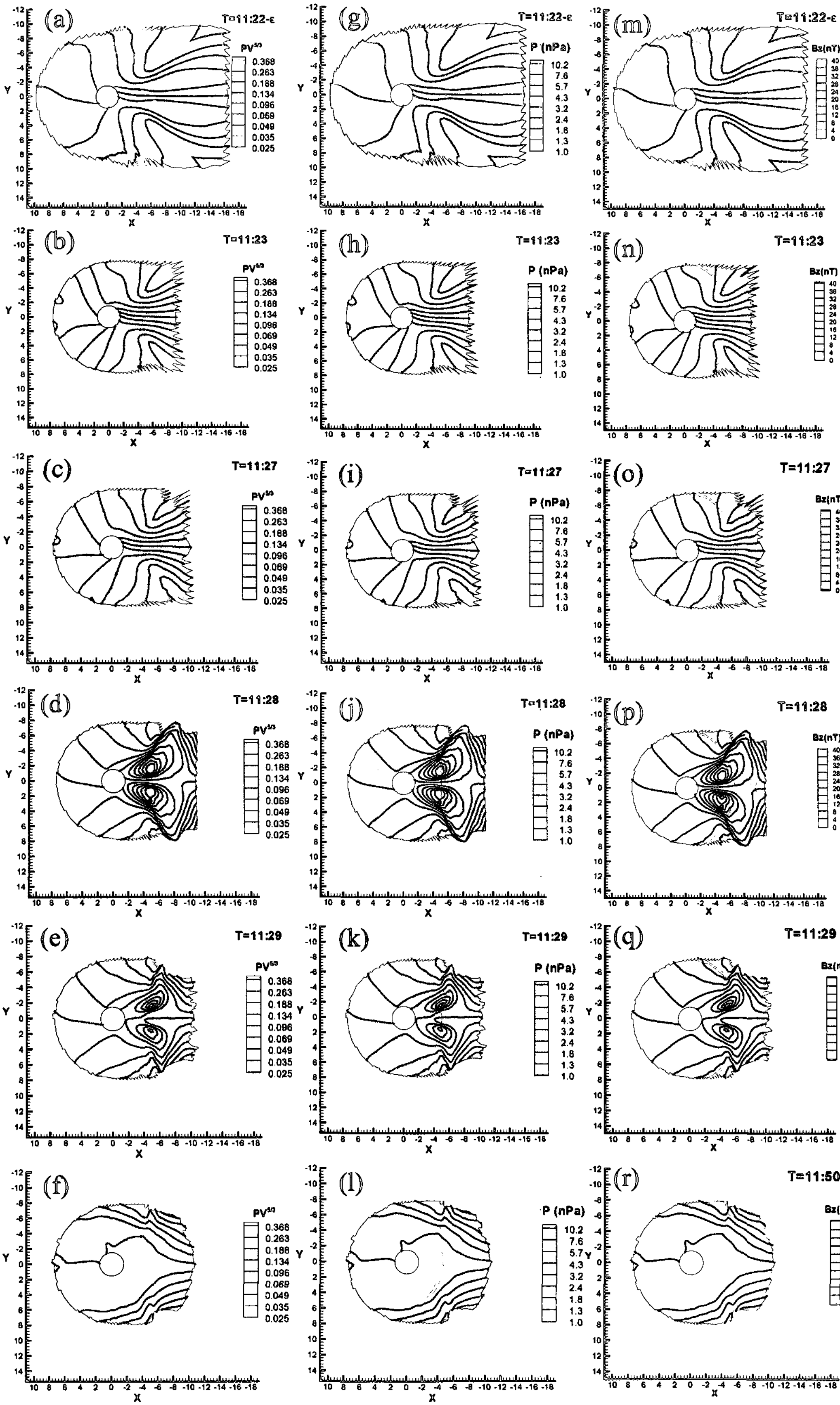

(a)
T=11:22-ε
(b)
T=11:23
(c)
T=11:27
(d)
T=11:28
(e)
T=11:29
(f)
PV^5/3
0.368
0.263
0.188
0.134
0.096
0.069
0.049
0.035
0.025
(g)
(h)
(i)
(j)
(k)
(l)
P (nPa)
10.2
7.6
5.7
4.3
3.2
2.4
1.8
1.3
1.0
(m)
(n)
(o)
(p)
(q)
(r)
T=11:50
Bz(nT)
40
36
32
28
24
20
16
12
8
4
0
X
Y

Figure 4.17. The equatorial view of $PV^{5/3}$ in units of $nPa(R_E/nT)^{5/3}$ (left column), plasma pressure (middle column) and B_Z for end of growth phase (11:22-εUT) and expansion phase (11:23, 11:27, 11:28, 11:29 and 11:55UT). Solid lines are equipotentials every 5kV.

4.6.3 Equatorial view of plasma injection

Using multipoint data-model comparisons gives us more confidence that the model is providing a global view of the plasma transport, electric field and magnetic field configuration during substorm expansion phase as outputs of the simulation. In this model, the plasma transport is described as bounce-average $E \times B$ and gradient/curvature drift in the closed field line region with an isotropic pitch-angle distribution; the magnetic field is force-balanced with plasma pressure; the electric field is calculated by solving the Vasyliunas equation in the coupled magnetosphere-ionosphere. Therefore, this global view of electromagnetic dynamics in the inner magnetosphere is physically self-consistent in the modeling region but not complete as some processes (e.g., electron precipitation, ion losses due to charge exchange, parallel potential drop and solar-radiation induced non-uniform conductance) are not included. As discussed by *Zhang et al.* [2009b], the validity of RCM modeling is limited to time scales longer than ~ 2 minutes and to flow speeds much less than the Alfven speed and sounds speed.

Figure 4.17 shows the equatorial view of $PV^{5/3}$ (left), plasma pressure (middle) and B_z (right) along with equipotentials (solid lines) from the end of the growth phase

(T=11:22-ε UT) to expansion phase at 11:50UT. The configuration at end of growth phase has been presented in the first row, followed by a smaller simulation region shown in the second row (T=11:23). Clearly, the $PV^{5/3}$ is dramatically reduced at X=-11 R_E, from 0.3 to 0.14 nPa(R_E/nT)$^{5/3}$ (Figure 4.5). The electric potential distribution along X=-11 R_E is also changed to accompany with an enhanced electric field on the boundary. Except these, there was no dramatic change in plasma pressure (Figure 4.17h) and magnetic field (Figure 4.17n) compared with end of growth phase. As the $PV^{5/3}$ on the boundary keeps decreasing to 0.1 nPa(R_E/nT)$^{5/3}$ at 11:27UT (Figure 4.17c), a noticeable buildup is seen in the plasma pressure (Figure 4.17i) and magnetic field dipolarization (Figure 4.17o) is evident near midnight. At 11:28UT, the $PV^{5/3}$ is continuously reduced to 0.04 nPa(R_E/nT)$^{5/3}$ (Figure 4.17d), and dramatic changes occur simultaneously in the plasma distribution, and in the magnetic and electric fields. Firstly, the ring current pressure increases outside the pre-existing symmetric ring current between about 21.7MLT and 2.3MLT, from ~3nPa to ~25nPa of peak value at about -5R_E near the midnight (Figure 4.17j). Secondly, the magnetic field dipolarizes significantly in two regions, one near the tail boundary due to the adjustment of reduced plasma pressure and one just tailward of the partial ring current due to the westward current (Figure 4.17p). Thirdly, an over-shielding type electric potential emerges with two large-scale swirls near flanks of the enhanced partial ring current. This prompt-penetration electric field in the middle and low latitude was also presented in a recent plasma bubble injection simulation using RCM [*Zhang et al.*, 2009b]. These changes can be explained in a self-consistent way. The plasma $PV^{5/3}$ decreases in the tail, leading the plasma injection into the inner magnetosphere, and then resulting in an enhanced partial ring current. The plasma sheet re-configures itself by adjusting the magnetic pressure to compensate for the reduced plasma pressure in the tail; the cross tail current decreases in association with a diversion of current into and from the ionosphere forming the substorm current wedge (Figure 4.18b). The enhanced partial ring current stretches the magnetic field earthward of it and dipolarizes the magnetic field tailward of it due to the westward current mostly carried by ions. The partial ring current is closed by strong region-2 current, producing the eastward prompt-penetration electric field. One minute later at 11:29UT, the plasma injection eases, associated with the weaker over-shielding electric field (Figure 4.17e) and the spreading partial ring current (Figure 4.17k). The magnetic field keeps adjusting itself by increasing its magnitude in the tail (Figure 4.17q). In the late expansion phase 11:55UT, the $PV^{5/3}$ recovers to 0.07 $nPa(R_E/nT)^{5/3}$ (Figure 4.17f), with dipole-like magnetic field configuration (Figure 4.17r). Meanwhile, the partial ring current continuously spreads azimuthally in both eastward and westward direction and becomes more symmetric. The electrostatic potential gradually emerges with under-shielding pattern.

4.6.4 The role of $PV^{5/3}$ reduction

As discussed in the RCM-E modeling of this event, the critical parameter on the boundary plasma distribution is $PV^{5/3}$. Therefore, it would be instructive to investigate how the reduction of $PV^{5/3}$ influences the injection of plasma and other dynamics on the convective scale. From onset 11:22 to 11:27UT, although the $PV^{5/3}$ reduces by a factor of 3, from 0.3 to 0.1 $nPa(R_E/nT)^{5/3}$ (Figure 4.4b), the plasma injection is still modest. The ring current is enhanced gradually and slightly until 11:27UT (Figure 4.17i). The dipolarization of magnetic field is very localized (Figure 4.17o). At 11:28UT when the $PV^{5/3}$ decreases to 0.04 $nPa(R_E/nT)^{5/3}$, a dramatic change occurs in the increased ring current, dipolarized magnetic field both tailward of the ring current and near the tail boundary and over-shielding electric potential (Figure 4.17 fourth row). Geotail observations also show a sharp dipolarization and an induced dawn-to-dusk electric field associated with hot plasma (Figure 4.5 and 4.6). The model demonstrates that strong plasma injection occur when $PV^{5/3}$ reduces below a critical value between 0.1 and 0.04 $nPa(R_E/nT)^{5/3}$. This agrees with the value of 0.08 $nPa(R_E/nT)^{5/3}$ proposed by *Lemon et al.* [2004] in which the a strong partial ring current buildup was reproduced by a sustained injection of depleted flux tubes in a idealized storm. After 11:28UT, the $PV^{5/3}$ remains very low with only a slight increase to 0.08, associated with continuous injection of plasma and dipolarization of magnetic field. Superposed epoch study by *Yang et al.*

[2009c] also suggests that the sustained (~0.08) low $PV^{5/3}$ necessary for the development of substorm expansion phase on a large scale.

One important question regarding the time dependent change of $PV^{5/3}$ is why it decreases below 0.08 nPa(R_E/nT)$^{5/3}$ not immediately after onset but about 5 minutes later. If one assumes that reconnection is the primary cause of the reduction of $PV^{5/}$ then one possibility is that the reduction is closely related to the nature of reconnection in the magnetotail, as inferred in a simple self-consistent modeling by *Sitnov et al.* [2005]. As shown in *Yang et al.* [2009c], $PV^{5/3}$ remains as low as 0.08 nPa(R_E/nT)$^{5/3}$ throughout the expansion phase, which implies persistent reconnection involving the open flux in the magnetotail; while if the reconnection is just taking place in the plasma sheet and is transient, it is more likely that the low $PV^{5/3}$ value will recover quickly and the disturbance will not expand. Regardless the mechanisms of the trigger of substorm onset, both near-Earth neutral line (NENL) model [*Baker et al.*, 1996] and current disruption (CD) model [*Lui*, 1996] have suggested that the magnetic reconnection can trigger the release the energy stored in the lobes and therefore tap the energy reservoir catastrophically ~ 5 to 15 minutes after onset. After the initiation of the disturbance in the neutral sheet followed by the reconnection in the lobes, the plasmoid is ejected to the tail with simultaneous field collapses in the near-Earth region [*Hones*, 1977]. Observationally, *Sergeev and Kubyshkina* [1996d] showed that the strong particle energization was found 3-4 min after substorm onset. In short, although no direct *in situ* observation was available further down the tail in the plasma sheet in this event, the results may provide some hints about what is happening tailward of the RCM modeling region. The near-Earth data and modeling results suggest that, in the first 4-5 minutes after onset in this event, reconnection occurred in the plasma sheet, substantially reducing $PV^{5/3}$ but with modest plasma injection; when reconnection in the lobes is dominant, $PV^{5/3}$ decreases below a critical value (<0.08 nPa(R_E/nT)$^{5/3}$), associated with the tapping of the large amount of stored energy and consequent strong plasma injection and field reconfiguration.

4.6.5 Region-1 and Region-2 currents in the early expansion phase

Two predominant current systems emerge during a substorm expansion phase, i.e., the region-2 (R2) current with closure to the enhanced partial ring current and region-1 (R1) sense substorm current wedge, which involves currents diverted from the disrupted cross tail current. The current density in the RCM-E modeling region is calculated in a force-balanced equilibrium state, $\vec{J} = \frac{1}{\mu_0}(\nabla \times \vec{B})$. Figure 4.18 shows the dynamics of plasma pressure (color contours), magnetic field mapping (solid lines) and R1/R2 field-aligned current (FAC) density (blue and red iso-surfaces). Since the low $PV^{5/3}$ plasma injection plays a central role of the reconfiguration in the inner magnetosphere, no major enhancement is seen in R1 and R2 FACs at 11:27UT (Figure 4.18a). There is a pair of weak R1 sense FACs, with its magnitude rarely larger than 2nA/m^2, linked to the magnetic equator and most of them are diverted to the magnetopause (top red and blue iso-surfaces in Figure 4.18a). Apparently, R2 FACs (lower red and blue iso-surfaces in Figure 4.18a) which link to a slightly enhanced partial ring current are stronger than R1 FACs. At 11:28UT when the strong plasma injection happens, the R1 FACs are increased dramatically (Figure 4.18b), forming a clear substorm current wedge (SCW) [*McPherron et al.*, 1973] with parallel current (top red) flowing along magnetic field line in the post-midnight and anti-parallel current in the pre-midnight sector (top blue). The morphology of the SCW is interesting in this case that the iso-surfaces (+2nA/m^2 and -2nA/m^2) are extended not radially but mostly azimuthally. The equatorial magnetic field mapping footprints (60 to 64 degree in latitude) move earthward inside the SCW. At 11:29UT, the strength of SCW and R2 FACs increases, associated with strong partial ring current (Figure 4.18c). Later the configuration during expansion phase (Figure 4.18d to Figure 4.18f) shows: (1) the cross section of iso-surfaces of R1 and R2 FACs shrink, indicating the spreading of FACs; (2) the width of the pair of both R1 and R2 FACs expands azimuthally; (3) the magnetic field mapping does not change much, which is consistent with the stable B_z component observed by Geotail (Figure 4.6).

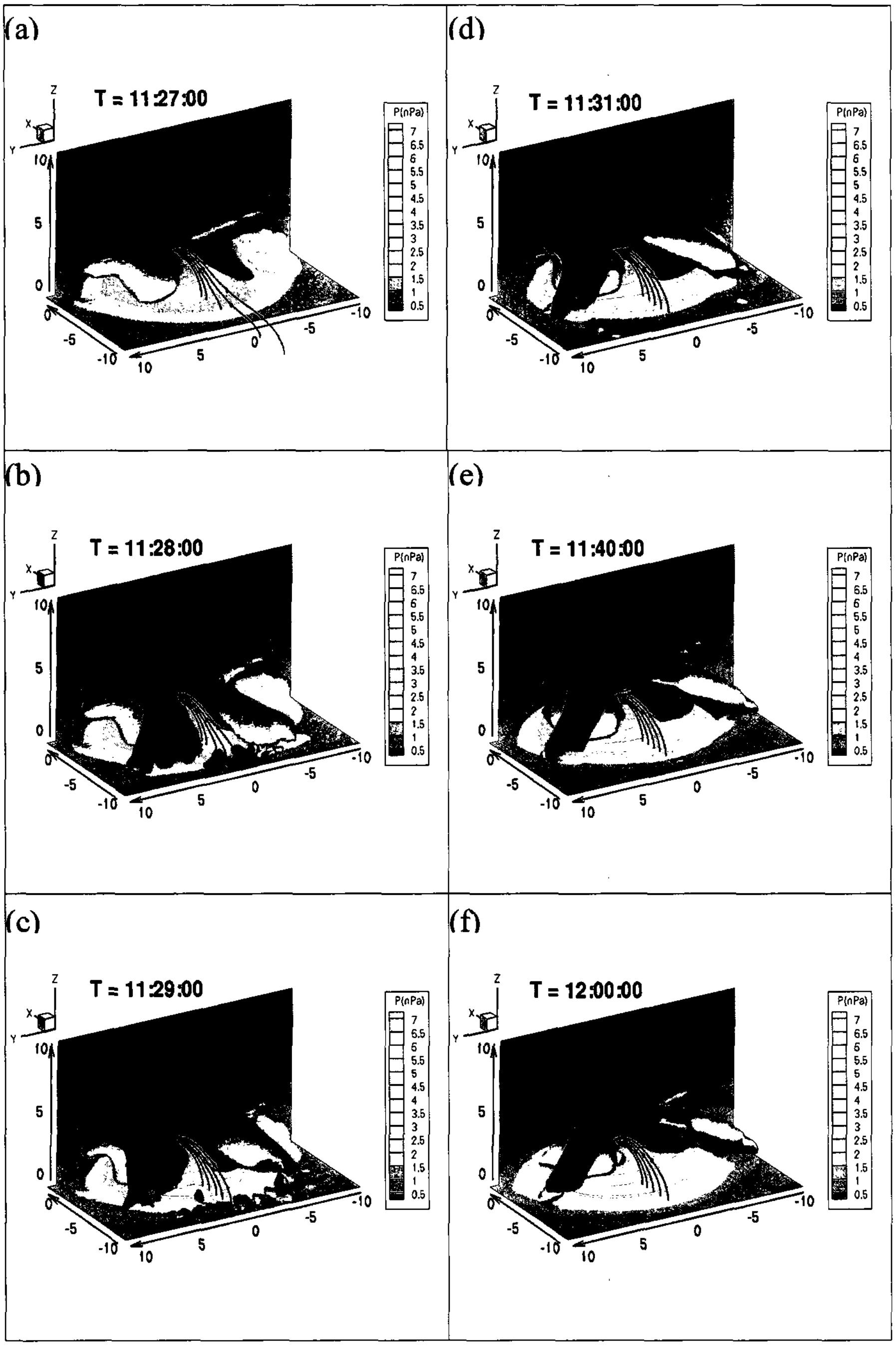

Figure 4.18. Side view from magnetotail above equatorial plane of plasma pressure in color contour on the X-Y plane (Z=0) and Y-Z plane (X=0), five magnetic field lines (black solid lines) with ionospheric footprints at 60, 61, 62, 63, 64 latitude and iso-surfaces of field-aligned current density (blue: -2nA/m^2; red: +2nA/m^2) for 6 times in expansion phase.

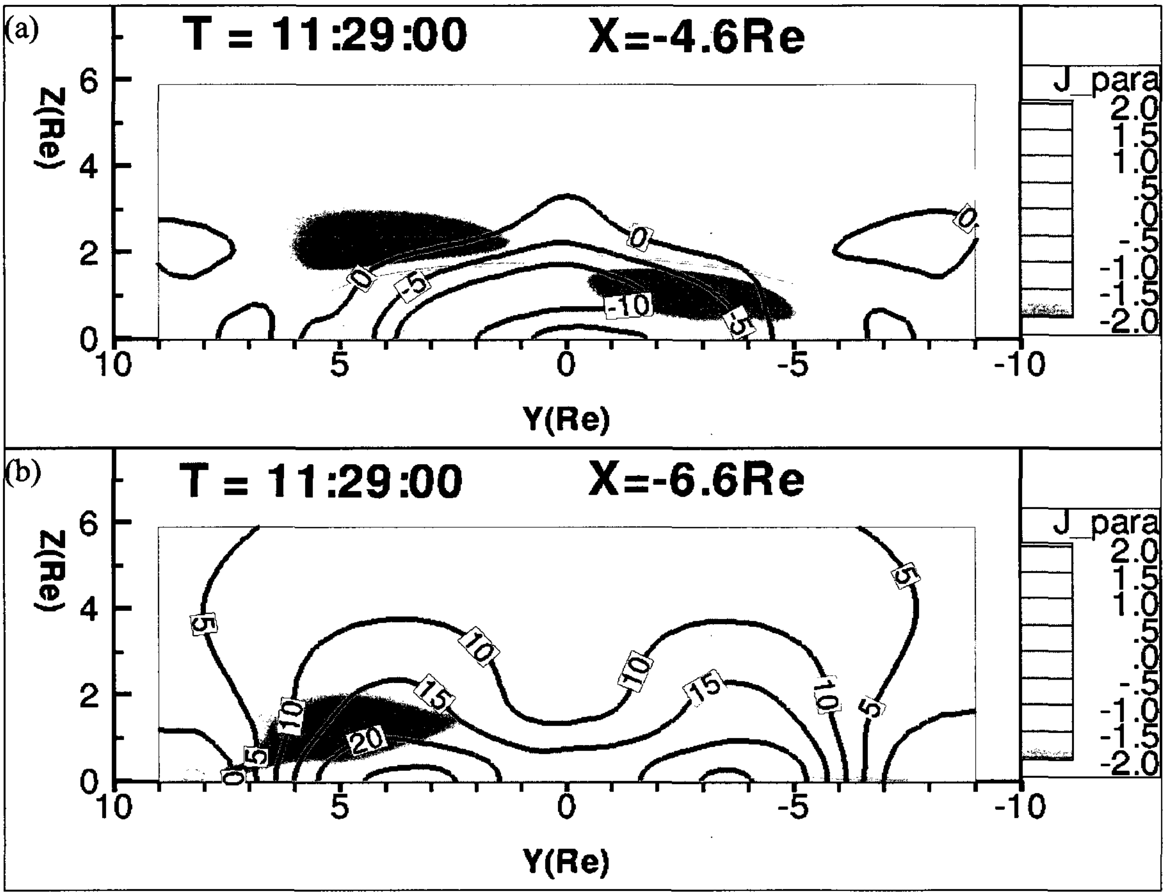

Figure 4.19. Field-aligned current density in color contours and the change of B_Z relative to the end of growth phase in black line contour on the Y-Z plane for X=-4.6 R_E (top) and X=-6.6 R_E (bottom) at T=11:29UT

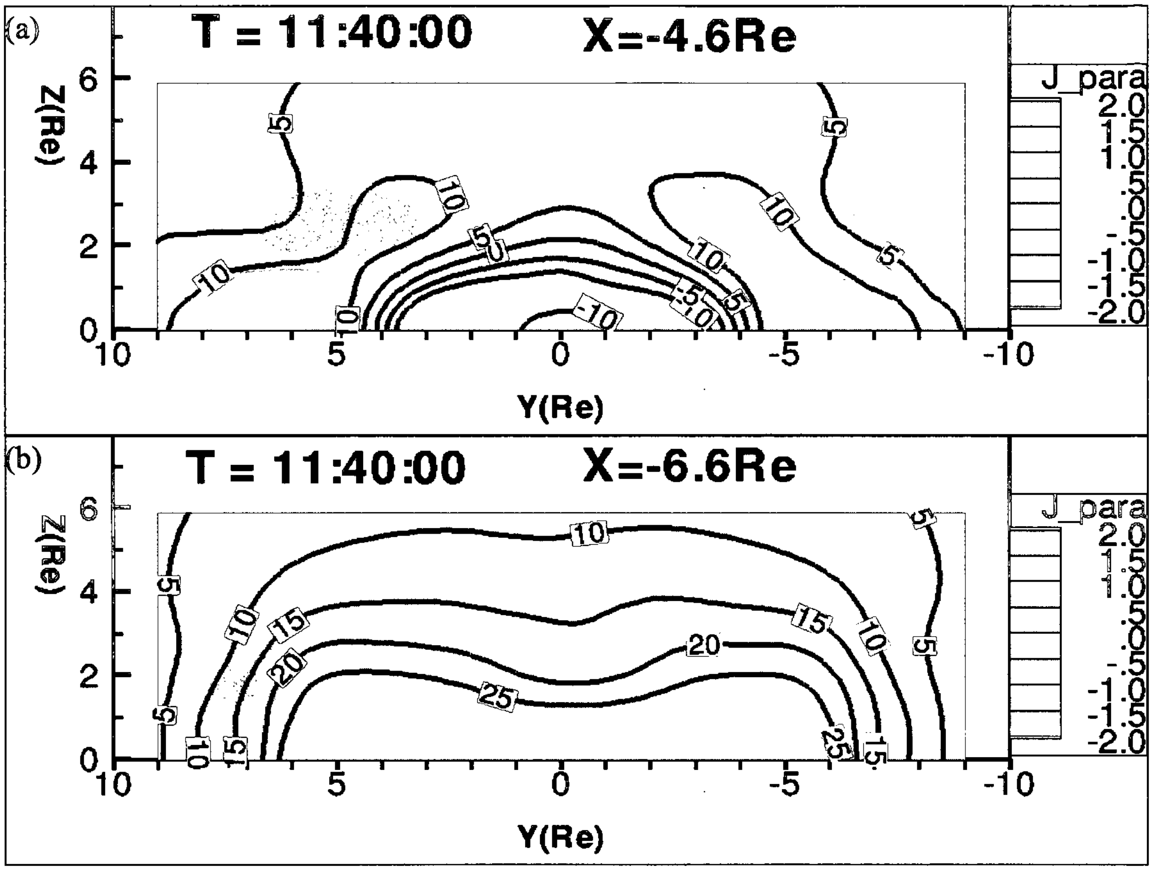

Figure 4.20. Similar to Figure 4.19, but at T=11:40UT.

Starting from the electric current point of view, it would be intuitive to evaluate the magnetic field changes in the inner magnetosphere. Figure 4.19 shows the parallel current density in color contours and the change of B_Z relative to the end of growth phase in line contours at 11:29UT, viewing from tail. The top and bottom panels show YZ planes at X=-4.6R$_E$ well earthward of the enhanced partial ring current and X=-6.6R$_E$ tailward of partial ring current. Comparison of the two panels indicates significant differences in both the current density distribution and magnetic field. On X=-4.6R$_E$ plane, pairs of both R1 and R2 FACs emerge with about 5R$_E$ extension in Y direction and roughly similar order of magnitude for each of them. The contributions of R1 and R2 FACs are opposite to each other, i.e., R2 FACs tend to stretch the magnetic field inside the wedge; while R1 FACs (SCW) tend to dipolarize the magnetic field. Therefore, it is noticeable that the change of B_Z below the SCW (below Z=2R$_E$ in Figure 4.19a) is mostly negative due to the strong R2 FACs; while B_Z above the SCW (above Z=2R$_E$ in Figure 4.19a) is dipolarized slightly. However, at X=-6.6R$_E$ tailward of partial ring current, B_Z dipolarizes as much as 25nT as a response to the SCW and the partial ring current. The total current, integrated of current density over the plane, is (1) approximately equally 1.00×10^6A on the X=-6.6R$_E$ plane for both parallel and anti-parallel FACs, (2) 0.90×10^6A on the post-midnight side and 0.74×10^6A on the pre-midnight side of the X=-4.6R$_E$ plane for R1 FACs, (3) 0.60×10^6A on the post-midnight and 0.57×10^6A on the pre-midnight on the X=-4.6R$_E$ plane for R2 FACs. The magnitude of the total current of SCW consistently falls between the calculation in *Birn and Hesse* [1996] (2×10^6A) and the estimate of *Shiokawa et al.* [1997] (10^5A). Since there is current flowing from/to the magnetopause close to the Earth (Figure 4.19a), the total R1 current on the X=-4.6R_E plane is smaller than that on the tailward plane at X=-6.6R_E. Later at 11:40UT (Figure 4.20), (1) the pairs of both R1 and R2 FACs spread azimuthally; (2) the R2 current density decreases compared to 11:29UT; (3) magnitude of B_z increases more. Note that calculation shows that the total R1 current is actually almost unchanged at both X=-4.6 and X=-6.6 R_E plane, however the total current in R2 FAC decreases by a factor of 2.3. Accompanying with the shrinking of the iso-surface of each branch of SCW (Figure 4.18c to 4.19e), it is fair to illustrate that the current density in SCW is decreasing and the current is spreading azimuthally, but the total current carried by SCW maintained almost unchanged for >10 minutes after plasma injection.

One potential direction of the further research is worth pointing out. Since the SCW is quite dynamic during the expansion phase, there are very few explicit models of its structure. A mathematical representation of SCW was created by *Tsyganenko* [1997], which has been applied as an input model of recent RCM simulations [*Yang et al.*, 2008; *Zhang et al.*, 2009a]. Because the SCW is a short-lived feature and highly variable feature of substorms, the development of parameterized statistical SCW model is a challange. Systematic runs of substorm expansion phases using the same approach in this work but with different model setups (e.g., polar cap potential drop, tail boundary condition, the reduction of $PV^{5/3}$) could be used as a basis for a parameterized SCW model.

4.7 Convergence of the Equilibrium Code

In this section, we will examine the force balance in the equilibrium code. We define the force imbalance parameter F as a measure of the accuracy of the equilibrium code's convergence as averaged over a the volume of the model as

$$F = \int \left| \vec{J} \times \vec{B} - \nabla P \right| d^3x \tag{4.23}$$

Figure 4.21(a) shows F as a function of iterations for the entire computational domain of the magneto-friction code, i.e., $-40.0<X<12.0R_E$, $-15.0<Y<15.0R_E$, $0.0<Z<15.0R_E$. Note that the magneto-friction code only works in the north hemisphere, assuming north-south symmetry about the X-Y plane. Figure 4.21(b) and (c) show the convergence performance only for the inner magnetosphere ($2.0<R<8.0R_E$) and the magnetotail region ($X<-8.0R_E$ and $Z<3.0R_E$), where R is the radial distance from the Earth. The plasma pressure and magnetic field information from RCM is passed to the magneto-friction code at specified times (every 5 minutes in the growth phase from 10:47 to 11:22UT; every minute in the early expansion phase from 11:22 to 11:34UT; every 5 minutes after 11:34UT), indicated by the large discontinuities in the line plots. The magneto-friction code runs for 5000 iterations to dissipate plasma kinetic energy and move towards equilibria. As discussed by *Lemon et al.* [2003], the convergence rate is very fast in the very beginning of the iterations, but slows down significantly later in the run.

In the magnetotail region, the basic trend of the force imbalance is decreasing both in the growth phase and in the expansion phase after the strong plasma injection at 11:27UT. However, the force balance qualities in both the inner magnetosphere region and the entire computational domain show gradual increasing trends, which can be attributed to the open-field line region (not in the RCM's computational region), especially the magnetopause, on which large surface currents are flowing. As shown in Figure 4.22, near the magnetopause, both the plasma pressure and magnetic field become noisier in the late expansion phase.

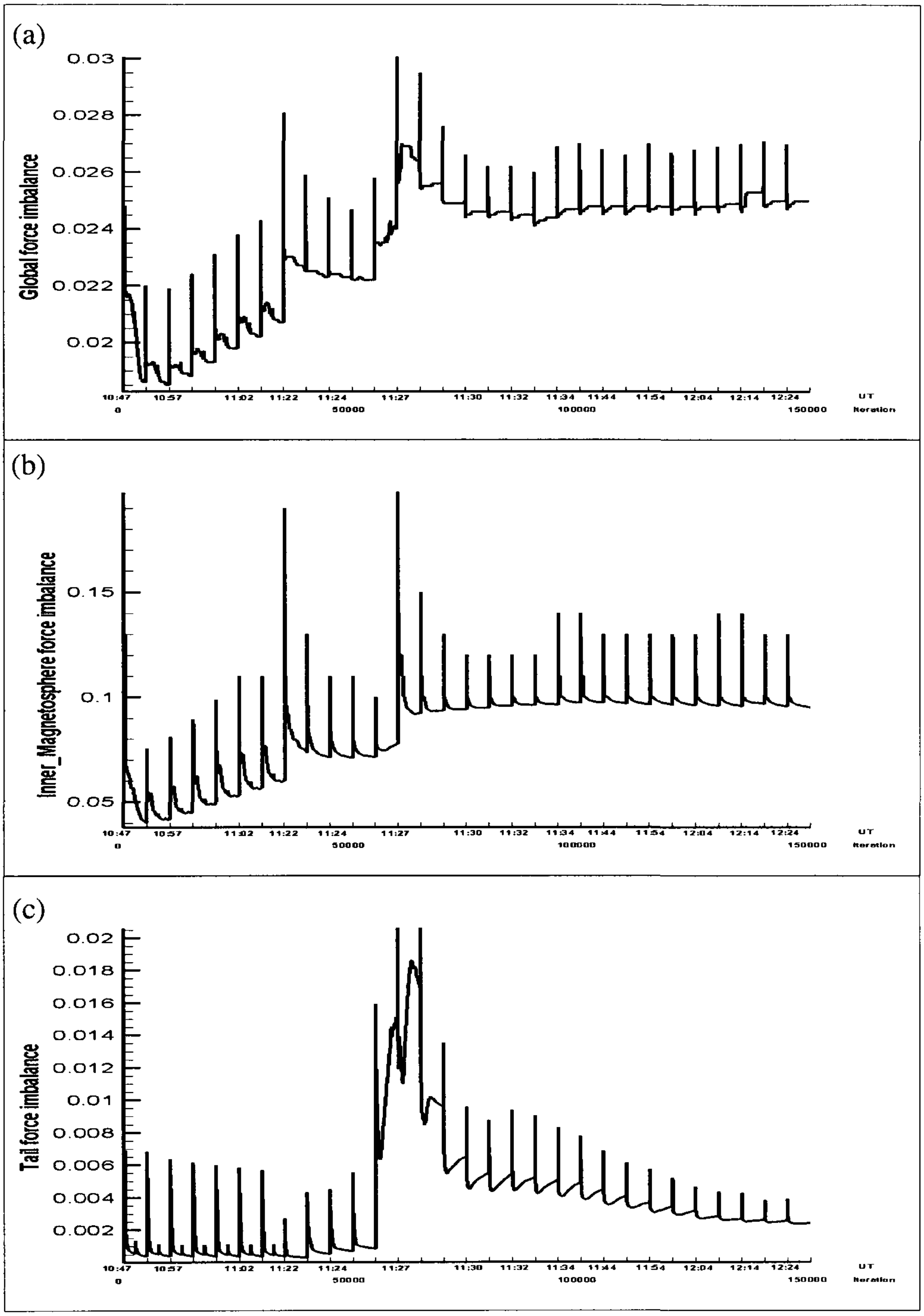

Figure 4.21. From top to bottom are force imbalance parameters for (a) all grid points in the magneto-friction code computation domain; (b) the inner magnetospheric region ($2<R<8.0R_E$); (c) the tail region ($X<-8.0R_E$ and $Z<3.0R_E$). The X-axis is uniform in iteration numbers and non-uniform in universal time.

4.8 Summary

In this chapter, we presented the first attempt to use the RCM-E to simulate a real isolated substorm event. This event occurred on Oct. 29, 2004, during fairly stable solar wind conditions with an average IMF B_Z of about -4nT. An empirical current sheet model is used to transform our simulation result in the zero-tilted model to the observational coordinate system. The modeling of the expansion phase was carried out by imposing a depleted plasma boundary condition at X=-11R_E, and the plasma distribution was tuned to match the Geotail observed plasma moment at ~-9R_E. A series of data-model comparisons, including magnetic field and electric field at Geotail, magnetic field, plasma moments and energetic particle flux at geosynchronous orbit, indicated fairly good agreement as validation of the modeling. Although there are still several aspects of the simulation that can be improved, there are some features of the simulation that are worth noting and are summarized below

1. After careful choice of boundary conditions, the results are compared to multipoint observations with fairly good agreement, including the Geotail (-9 R_E) observed magnetic field; geosynchronous orbit magnetic field, plasma moments and energetic particle fluxes. The magnetic field is more stretched (as noted by the discrepancies in B_Z in Figure 4.6) in the model than in the observations, but this could be further improved by further modifying the plasma boundary conditions.

2. The modeling confirms several classical growth phase pictures, i.e., magnetic field stretching, local B_Z minimum formation, cross tail current density enhancement, earthward motion of the plasma sheet, sharpening of the tail-dipole transition region, and a dropout in the energetic particle fluxes at geosynchronous orbit.

3. The induction electric field significantly alters the plasma convection pattern in the growth phase. The plasma and magnetic field interact in a consistent way such that the earthward convection builds up the plasma pressure in the near-Earth region; the increased plasma pressure balances the magnetic field by stretching; this stretching induces the dusk-to-dawn electric field, which prevents the plasma from further earthward convection.

4. The non-adiabatic reduction of $PV^{5/3}$ in the magnetotail plays a central role in the plasma injection in convective scale. Strong plasma injection and associated partial ring current buildup, magnetic field dipolarization and induction of prompt large dawn-to-dusk electric field occurs when the $PV^{5/3}$ reduces below to a critical value between 0.04 to 0.1 nPa$(R_E/nT)^{5/3}$. This dramatic reduction of $PV^{5/3}$ is suggested as a consequence of magnetic reconnection in the lobes, which is typical several minutes after substorm onset.

5. The modeling provides a global view of electromagnetic dynamics associated with the plasma injection in the inner magnetosphere. The significantly enhanced partial ring current inside geosynchronous orbit, over-shielding electric potential pattern and

dramatic magnetic field dipolarization outside the partial ring current emerge instantaneously with the strong plasma injection. The energetic particle flux elevation is found to be attributed to the acceleration by the induction electric field due to the magnetic field collapse.

6. While the <45keV plasma moments for 1991-080 and LANL-97A showed reasonably good qualitative agreement between the observation and simulation in the growth phase, the results for the expansion phase show only qualitative agreement between the simulated plasma pressure and the observed value. This could also be further improved by careful adjustments of the plasma boundary condition.
7. The model provides an explicit picture of both region-1 (SCW) and region-2 FACs. Each branch of the SCW is spreading and the width of SCW is expanding azimuthally, but the total current carried by SCW remains almost unchanged for at least 10 minutes.

It will be very helpful to carry out a real substorm simulation using the same model but with the plasma boundary condition driven by *in situ* observation in the magnetotail plasma sheet and compare with multipoint observations, which would be a more thorough and persuasive validation. The THEMIS (Time History of Events and Macroscale Interactions during Substorms) mission provides us an opportunity.

Chapter 5

Grid resolution dependence of RCM and RCM-E simulations

Motivated by the results of *Yang et al.* [2008], we present RCM and RCM-E tests primarily to determine the dependence of results on grid resolution. Two forms of field aligned currents (FACs) are found in association with two kinds of auroral displays. One is a quasi-periodically spaced spot-like aurora that is observed near substorm onset and emerges in the simulation near the end of growth phase or in the first few minutes of the expansion phase in both the dusk to pre-midnight sector and the post-midnight to dawn sector. It is still uncertain what physical process is associated with these auroral observations and whether or not the magnetic field fluctuations in the simulation are purely numerical noise. The ballooning instability is a potential explanation of the observed spot-like aurora. The other form of auroral phenomena that we consider are quasi-periodically spaced finger-like aurora that seem to be associated with simulated FACs produced by the RCM during isolated bubble injection events or sawtooth events. The interchange instability is a physical interpretation of this phenomenon.

5.1 Motivation from the RCM simulation of April 18, 2002 sawtooth event

As discussed by *Yang et al.* [2008] and the results presented in chapter 3, synthetic auroral spacing reproduced in the RCM modeling is roughly consistent with the observed spatial periodicity in the sawtooth event, but is also dependent on the longitudinal grid resolution in the model. In preliminary test runs, using a smaller grid size does introduce more downward-upward pairs of Birkeland currents or finer structures, even with identical boundary conditions. Presumably in nature there is some physical limit to the fine structure of the Birkeland currents; whether this limit is captured in our model or whether other physical processes are needed is unclear.

One example of a grid convergence test that concerns the azimuthal width of interchange convection cells on Jupiter, was conducted by *Wu et al.* [2007] using the Rice Convection Model modified for Jupiter's magnetosphere (RCM-J). They showed that, with fixed plasma source in the Io plasma torus distribution, the width of the "fingers" decreased along with the increasing grid resolution roughly when the number of the longitudinal grid points is less than ~300 in a 30-degree sector; while the width of "fingers" stabilized when the model was run with more than ~300 longitudinal grid points.

The high and low grid resolution runs in Figure 5.1, where I and J are latitudinal and longitudinal grid numbers, show the RCM results for a substorm expansion phase with onset at 05:30UT [*Huang et al.*, 2003b] during the 18 April, 2002 sawtooth event. The two runs have identical boundary conditions on the plasma and potential distribution. The results show a clear dependence on the grid resolution. The higher grid resolution run (left of Figure 5.1), with double the number of grid points in longitude, exhibited finer finger structures, more prominent interchange convection cells and implied spatially quasi-periodic aurora patterns. However, to represent aurora in the model more realistically, we need (1) more self-consistent modeling of the electric field, magnetic field and plasma convection, i.e., using RCM-E; (2) an accurate calculation of the parallel potential drops related to the field-aligned currents [*Knight*, 1973]; (3) grid convergent solutions. In the following sections in this chapter, I will present a series of systematic tests on the effect of grid resolution in the RCM and RCM-E simulations, for idealized substorm bubble injection events, rather than sawtooth events.

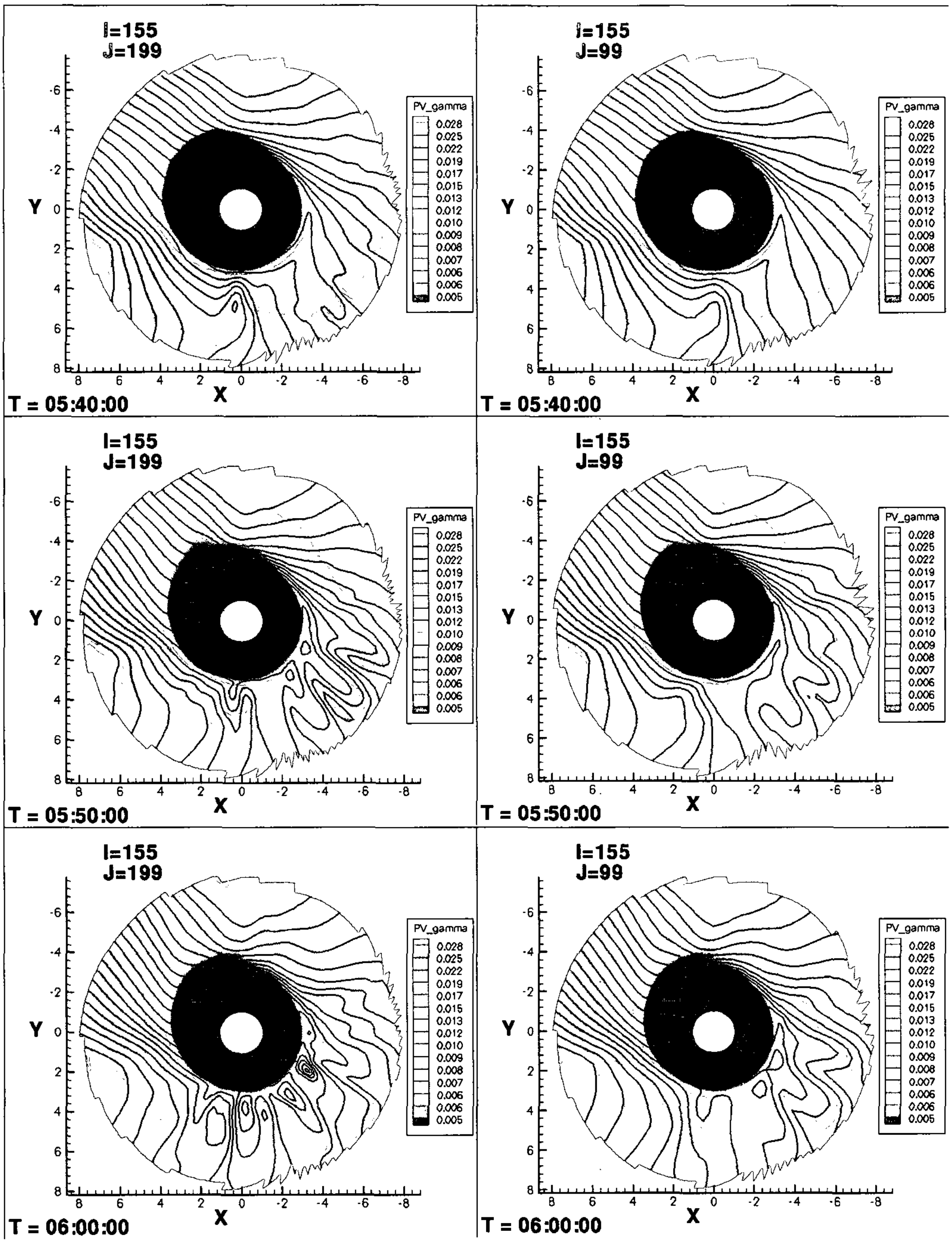

Figure 5.1 Comparison of high (left) and low (right) grid resolution runs for one tooth cycle during April 18, 2002 event. I and J are latitudinal and longitudinal grid numbers of the RCM ionospheric computational domain. The color contours represent $PV^{5/3}$; the black line contours represent equipotentials every 8kV. The sun is to the left.

5.2 Model setup

The initial condition setup for the growth phase run follows the same procedure as the real-event substorm simulation described in Chapter 4 [*Yang et al.*, 2009a, 2009b]. For this idealized event, we assume the solar wind is stable, with IMF B_Z=-5nT, B_X=B_Y=0nT, solar wind velocity V_{SW}=V_X=400km/s and V_Y=V_Z=0km/s, solar wind proton number density N_{SW}=5cm^{-3}, solar wind dynamic pressure P_{SW}=1.34nPa. The event is taken to be an isolated substorm, with Dst=0nT, Kp=3. The polar cap potential drop is set constant of 100.5kV. The initial magnetic field is obtained from T96 model [*Tsyganenko*, 1995; *Tsyganenko and Stern*, 1996], parameterized by the prescribed solar wind and geomagnetic indices. The initial plasma pressure outside 10R_E is set according to the *Tsyganenko and Mukai* [2003] (TM2003) plasma pressure model for the region outside 10R_E; the *Spence and Kivelson* [1993] model is used inside 10 R_E, but scaled by a constant to match the TM2003 model at X=-10R_E at midnight. The initial proton-electron temperature ratio is given by

$$T_i/T_e=4.0+2.0*\tan^{-1}(R-7.0) \tag{5.1}$$

where R is the radial distance. The initial conductance is obtained from IRI-90 model [*Bilitza et al.*, 1990; *Bilitza et al.*, 1993] as a background, with arbitrarily chosen date and indices, i.e., DOY=100, F107(previous day)=100.0, F107(81-day average)=100.0, F107(12-month average)=100.0, Ap=100. The electron precipitation induced conductance is included as an active element during the run. The high latitude boundary is put at X=-15R_E at midnight, with elliptical shape in the equatorial plane. The plasma boundary condition for the 30-minute growth phase run is taken from the TM2003 model for the specified solar wind conditions. The ion and electron temperature ration is taken as

$$T_i/T_e=4.0+2.0*\tan^{-1}(15.0-7.0)=6.89 \tag{5.2}$$

The plasma distribution is a kappa distribution with κ=6. The RCM and equilibrium code exchange information (magnetic field and pressure) every 5 minutes during the growth phase.

The substorm expansion phase is modeled by initiating the reduced $PV^{5/3}$ on the high latitude boundary as described in Chapter 4. Ideally, the equilibrium code resolution should be comparable to the RCM grid resolution (I=200, J=801) in this study, which introduces a technical requirement for running the equilibrium code at this high resolution that is currently not possible. For now, we simulate an idealized bubble injection event only using the RCM with time-independent magnetic field during the whole expansion phase, i.e., using the stretched magnetic field configuration at the end of the growth phase for the expansion phase run. This type of treatment has been utilized by *Zhang et al.* [2008] for an RCM simulation of an idealized bubble injection event, using the empirical solar wind driven T05 magnetic field model [*Tsyganenko and Sitnov*, 2005] model without substorm-expansion-phase related rapid dipolarizations.

The plasma distribution and the electric potential distribution on the boundary during the expansion phase are specified as boundary conditions on the high latitude boundary of the RCM. The basic approach is similar to what has been done in the 2004-Oct-29 substorm event simulation in Chapter 4 [*Yang et al.*, 2009b]. The depleted values of $PV^{5/3}$ at the center of the bubble at midnight in this idealized event are shown in Figure 5.2. At the onset T=0, the $PV^{5/3}$ is 0.19 nPa(R_E/nT)$^{5/3}$; at T=1min, $PV^{5/3}$ is reduced significantly to 0.13 nPa(R_E/nT)$^{5/3}$; at T=2min, $PV^{5/3}$ is continuously reduced to 0.10 nPa(R_E/nT)$^{5/3}$ and remained at this value for 20 minutes.

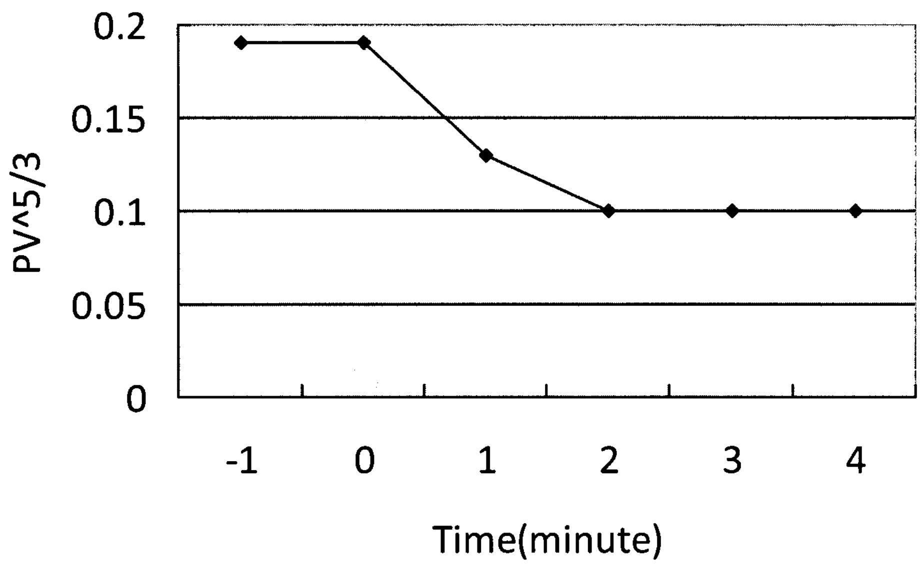

Figure 5.2. The specific entropy $PV^{5/3}$ in units of nPa(R_E/nT)$^{5/3}$ at midnight on the tail boundary as a function of time (minute). T=0min denotes the substorm onset. After T=4min, $PV^{5/3}$ remains to 0.1 nPa(R_E/nT)$^{5/3}$ for 20 minutes.

Since we keep the magnetic field constant during the expansion phase portion of the simulation, the flux tube volume at midnight on the tail boundary V_f is constant and plasma pressure P on the boundary decreases after onset due to the reduction of $PV^{5/3}$. The ion and electron temperatures are assumed to increase due to the non-adiabatic heating/acceleration outside or just on the high-latitude boundary, which is adjusted according to the TM2003 model given by equation 5.4. The ratio of ion temperature to electron temperature is held constant (equation 5.2). The number densities of ions and electrons are given by equation 5.5. A kappa plasma (κ=4) distribution at the center of the bubble is specified by equation 5.6.

$$P = \frac{PV^{5/3}}{V_f^{5/3}} \tag{5.3}$$

$$T_i = \frac{1}{0.65} T_{TM} \tag{5.4}$$

$$N_i = N_e = \frac{P}{k_B(T_i + T_e)} \tag{5.5}$$

$$\eta_{new}(\lambda) = \frac{2}{\sqrt{\pi}}((\kappa - 1.5)k_B T)^{-\frac{3}{2}} \frac{\Gamma(\kappa+1)}{\Gamma(\kappa-0.5)} \frac{N\sqrt{\lambda}\Delta\lambda}{(1+\frac{V^{-2/3}\lambda}{(\kappa-1.5)k_B T})^{\kappa+1}} \tag{5.6}$$

The local time dependence of the plasma distribution can be adjusted according to equation 5.7 and 5.8, where the density invariant of each energy channel is an interpolation of the "old" (at the growth phase) density invariant and the "new" (equation 5.6) density invariant. $\widehat{G}(LT)$, or $\widehat{G}(\phi)$, a function of azimuthal angle ϕ, which is 0 at noon, π at midnight and 0.5π and 1.5π at the dusk and dawn terminators, collapses to unity at midnight, which gives a κ=4 distribution as given by equation 5.6 with $PV^{5/3}$ values shown in Figure 5.2. Beyond the angle $\phi_W = \frac{15}{16}\pi$ and $\phi_E = \frac{17}{16}\pi$, the function $\widehat{G}(\phi)$ declines rapidly to zero, which means the plasma distribution is roughly the same as the old distribution and the $PV^{5/3}$ is not depleted, roughly representing the west and east boundary of the bubble. The parameter K roughly represents the gradient of the depletion of $PV^{5/3}$ as a function of local time, which lacks observational constraint. In this study, we set K=20.

$$\eta(\lambda) = (1-\widehat{G}(LT)) * \eta_{old}(\lambda) + \widehat{G}(LT) * \eta_{new}(\lambda) \tag{5.7}$$

where
$$\widehat{G}(LT) = \widehat{G}(\phi) = \frac{\tanh[K(\phi-\phi_W)] - \tanh[K(\phi-\phi_E)]}{\tanh[K(\pi-\phi_W)] - \tanh[K(\pi-\phi_E)]} \tag{5.8}$$

The potential electric field is believed to be concentrated inside the plasma bubble [e.g., *Nakamura et al.*, 2001]. The potential distribution in the expansion phase is set as a sine function as the background with perturbations due to the bubble.

$$V_b(\phi) = V \frac{F_V(\phi)}{F_{V,MAX} - F_{V,MIN}} \tag{5.9}$$

where
$$F_V(\phi) = -\frac{\sin(\phi)}{2} + \left\{ \frac{1}{4(\phi_e - \phi_w)} \ln[\frac{\cosh(2(\phi-\phi_w))}{\cosh(2(\phi-\phi_e))}] - \frac{\phi}{2\pi} + \frac{1}{2} \right\} \tag{5.10}$$

V=100.5kV, is the polar cap potential drop. $F_{V,MAX}$, and $F_{V,MIN}$ are maximum and minimum values of function $F_V(\phi)$.

5.3 High and low grid resolution runs

Figures 5.3 and 5.4 show the RCM simulation results for the high grid resolution with I=200 in latitude and J=801 in longitude and low grid resolution with I=200 and J=101. All initial and boundary conditions are identical to the runs described in section 5.2, except the grid sizes.

The high resolution run shows finer structure in both the $PV^{5/3}$ configuration and the field-aligned currents (FACs). At T=00:02, 2 minutes after the initiation of the bubble on the boundary, the low $PV^{5/3}$ plasma propagates 1 R_E earthward, with about 50~100km/s speed mainly as E×B drift in the magnetic equatorial plane (Figure 5.3). At this time, the differences emerge. For the high grid resolution run (right), the wave-like deformations of the leading edge of the bubble is clear, and the calculated FACs show downward (red) and upward (blue) pairs of FACs (Figure 5.4); for the low grid resolution run (left), there is no evidence of spatially periodic structures in the equatorial plane, and only a couple of downward and upward FACs flow near the east and west edges of the bubble. Two minutes later, at *T*=00:04, in the high resolution run, the interchange instability violently disturbs the system, with high $PV^{5/3}$ plasma moving tailward and low $PV^{5/3}$ plasma moving earthward, which forms finger-like penetration structures in the near-Earth magnetosphere. The penetration is deep enough and fast enough to get to geosynchronous orbit about 4 minutes after bubble initiation, and is mostly due to E×B drift. At the same time, stripes in the FACs emerge on the equatorial plane near midnight. However, the low $PV^{5/3}$ plasma in the low grid resolution run still produces a coherent bubble moving from near-Earth tail to the inner magnetosphere, with one pair of strong FACs on the edges and another pair of small but also visible FACs. As time goes on, in the high resolution run, much of the high $PV^{5/3}$ plasma in the way of the bubble injection is ejected tailward in the form of interchange convection, and electric potential concentrates more and deeper near the midnight than that in the low resolution run, where the bubble behaves more like a coherent entity and drifts westward more. Comparing the FACs after 10 minutes, the high resolution run produces more fine structures than the low resolution run, not only near the midnight but also extending to the dusk side.

In principle, it is not surprising that with higher grid resolution, computational modeling tends to reproduce more and finer structures until some physical limit is reached. The spatial periodicity of the calculated fingers are much smaller than the results in the sawtooth event simulations, which is mainly due to the much higher grid resolution, although the magnetic field and the boundary condition can also affect results.

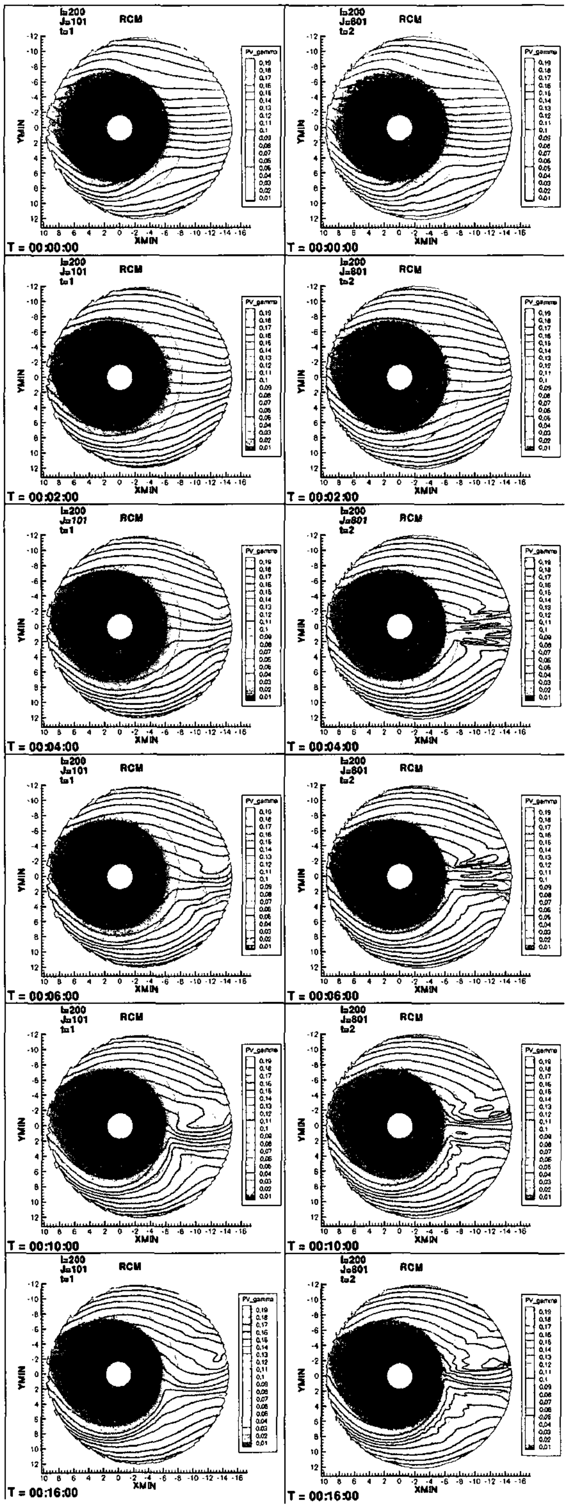

Figure 5.3. RCM simulation of bubble injection for low (left, I=200 and J=101) and high-grid-resolution runs (right, I=200 and J=801). From top to bottom are shown equatorial equatorial $PV^{5/3}$ (nPa(R$_E$/nT)$^{5/3}$) in the expansion phase for T=0, 2, 4, 6, 10 and 16 minutes.

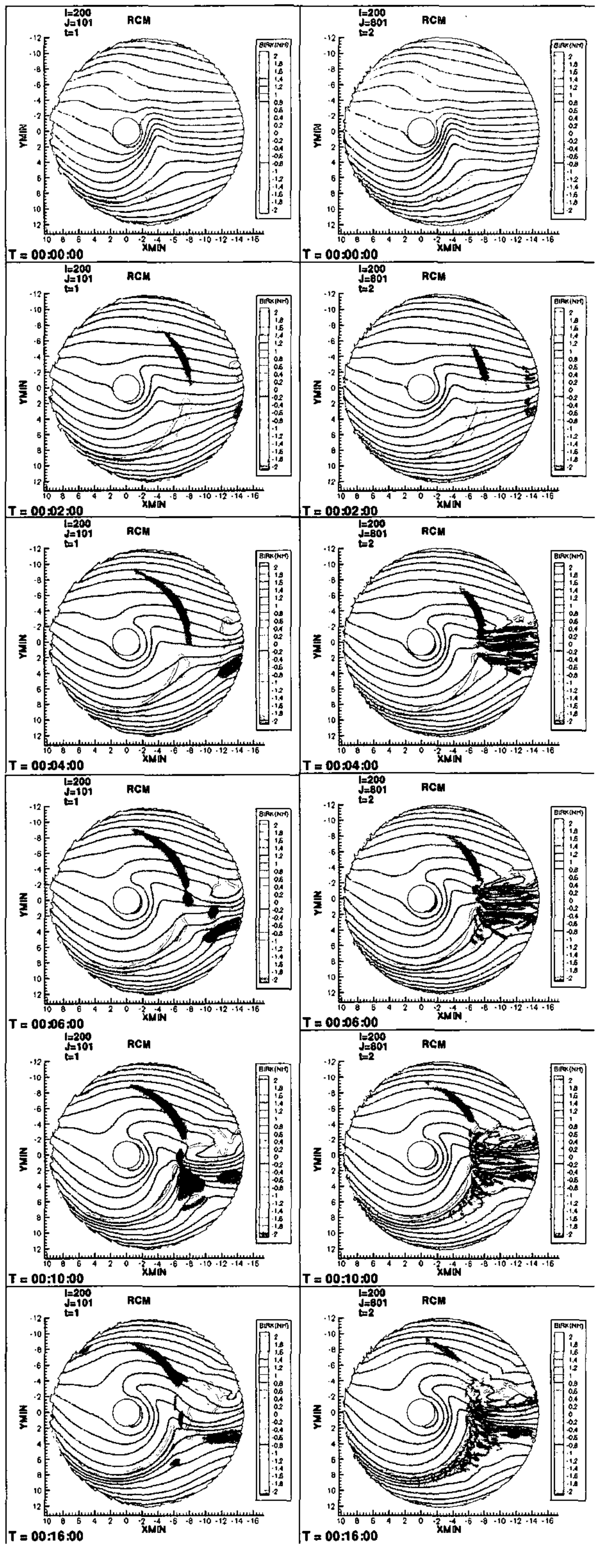

Figure 5.4. RCM simulation of bubble injection for low (left, I=200 and J=101) and high (right, I=200 and J=801) grid resolution runs. From top to bottom are shown equatorial equatorial FAC density ($\mu A/m^2$) for T=0, 2, 4, 6, 10 and 16min.

5.4 High and low conductance runs

The results shown above indicate that, with higher grid resolution, the RCM is able to reproduce finer finger-like structures, in the interchange convection. These fingers mature quickly, within 4 minutes, after the initiation of the depletion of $PV^{5/3}$ along the high latitude boundary, which suggests that the growth rate of the interchange instability is fast. An easy check related the growth rate using the RCM is to vary the conductance on the ionosphere, since the growth rate is inversely-proportional to the Pedersen conductance [*Xing and Wolf*, 2007; *Volkov and Mal'tsev*, 1986].

Figure 5.5 and Figure 5.6 show the results of high resolution (I=200 in latitude and J=801 in longitude) runs with low (left) and high (right) solar radiation induced background conductance. The simulation setup for the low-background-conductance run is identical as described in section 5.2, with initial conductance set by the IRI90 model with an arbitrarily chosen date and indices, i.e., DOY=100, F107 (previous day)=100.0, F107(81-day average)=100.0, F107(12-month average)=100.0, Ap=100. However, the high-background-conductance run is modeled by setting the initial Hall and Pedersen conductance a constant 25S per hemisphere, which is much higher than the low-conductance run. *Vanhamäki et al.* [2009] estimated the highest Hall and Pedersen conductances, ~50S and ~25S, respectively, at the edges of the bright auroral tongue. Besides background conductance, the active conductance induced by electron precipitation is calculated throughout the runs.

Apparently, the RCM simulation results confirm the theoretical analysis that, with higher Pedersen conductance, the interchange instability develops slower than that with lower Pedersen conductance. In the right column, even with the same grid resolution in longitude, no spatial periodicity emerged in the equatorial $PV^{5/3}$ distribution (Figure 5.5) and no finger-like upward-downward FACs (Figure 5.6). It should be noted that the comparison here is an exaggerated test on the role of Pedersen conductance in the interchange instability. The initial Hall and Pedersen conductance given in the high-conductance run are unrealistically high.

It is also notable that, even with low grid resolution (Figure 5.3 at T=00:06min) in the normal ("low") conductance condition, the injected bubble tends to bifurcate near the east and west edges, with two pairs of FACs in the equatorial plane (Figure 5.4). However, with high grid resolution, the bifurcation of the bubble is actually suppressed by the unrealistically high conductance (left row in Figure 5.5), which suggests that an accurate calculation of the ionospheric conductance is also very important for the RCM simulation of the interchange instability/convection. In the present version of the RCM code, a fixed fraction (one-third) of the downward particle flux is considered to be precipitated in the ionosphere, which is an assumption as a result of isotropic pressure along magnetic field. In addition, the magnetic field line is always assumed as an electric equipotential. The additional calculation of field-aligned potential drop may considerably affect the particle drift and consequently the electron precipitation.

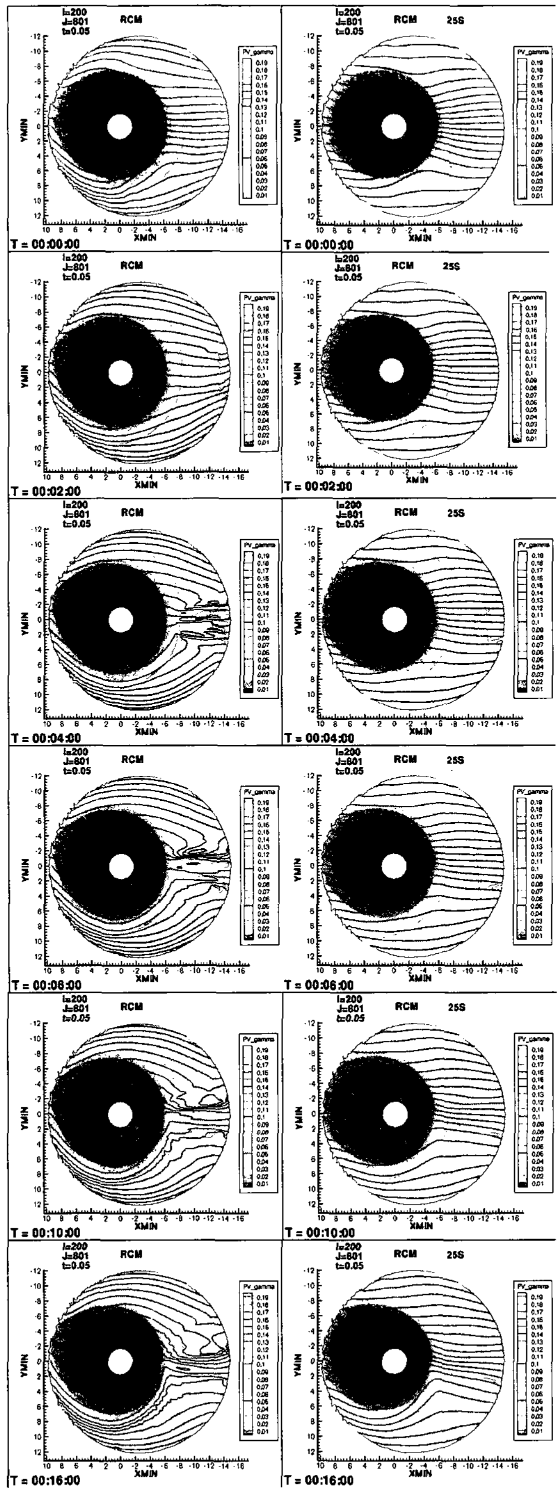

Figure 5.5. RCM simulation of bubble injection for low (left) and high (right) background conductance runs. From top to bottom are shown equatorial $PV^{5/3}$ (nPa(R_E/nT)$^{5/3}$) for T=0, 2, 4, 6, 10 and 16min.

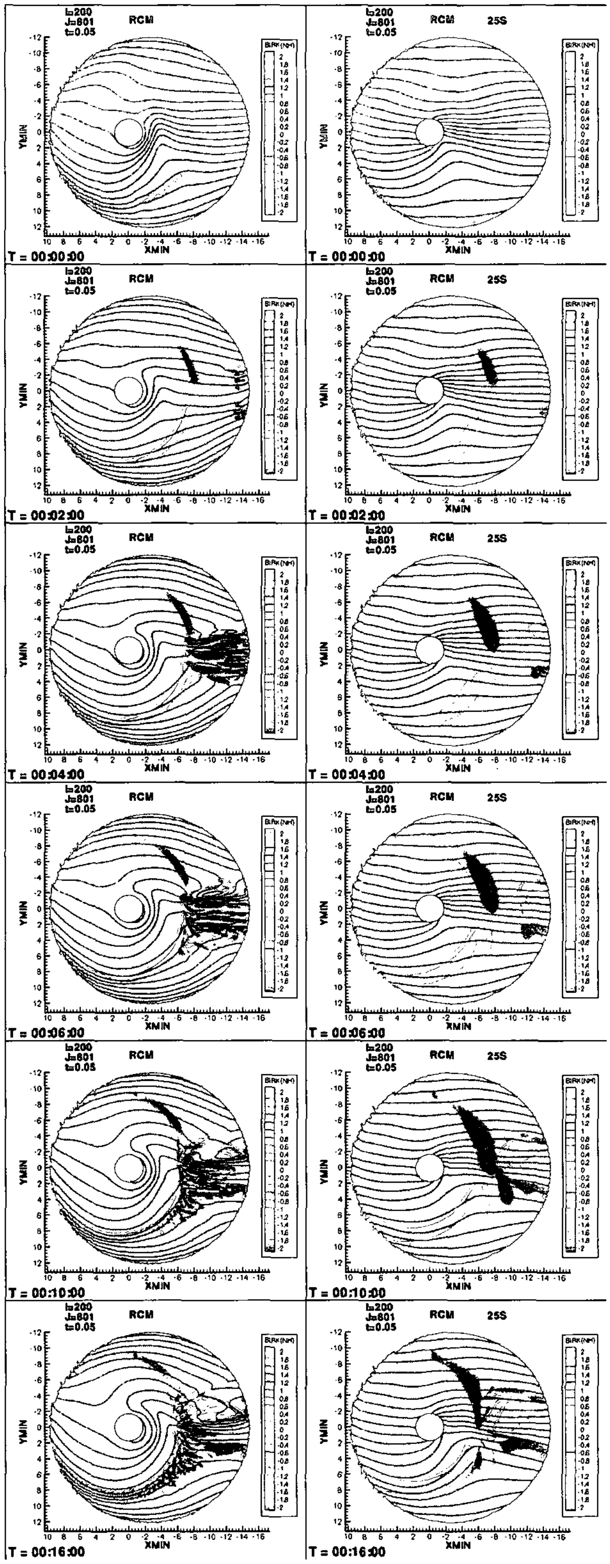

Figure 5.6. RCM simulation of bubble injection for low (left) and high (right) background conductance runs. From top to bottom are shown equatorial equatorial FACs density ($\mu A/m^2$) for T=0, 2, 4, 6, 10 and 16min.

5.5 RCM and RCM-E runs

The grid of the Friction code is carefully designed so that it has finer resolution near the axes and the Earth, and coarser resolution further from the Earth. To investigate the fine structures using the RCM-E, the grid resolution of the coupled codes, the RCM and the equilibrium code, should be (1) comparable with each other and (2) much smaller resolution than the physical spatial periodicity of the fingers.

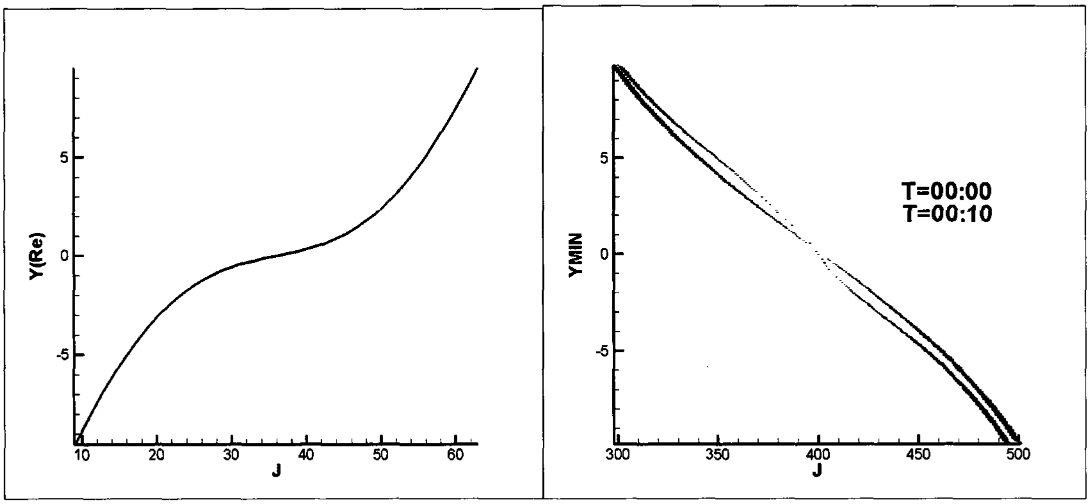

Figure 5.7. Grid distribution along Y-axis in Friction code (left) and in the coupled RCM code (right) at X=-10R_E for T=0min and T=10min.

The setup for the RCM-E simulation presented in this section is identical to that in section 5.2, but with equilibrium code running during the expansion phase. Therefore, the magnetic field in the magnetotail dipolarizes due to the bubble injection. Figure 5.7 compares the grid distribution of the RCM code (right) and the coupled equilibrium code (left) in *Y*-direction at *X*=-10R_E. Due to the dipolarization during the bubble injection, the grid distribution mapped on the equatorial plane changes at time T=00:10 (red line in the right of Figure 5.9). The grid resolution for the equilibrium code is about 0.1R_E per grid space near midnight, which is of similar magnitude to the grid resolution of the RCM on the equatorial plane; while the grid resolution (about 1R_E per grid) of the equilibrium code beyond $|Y|>5R_E$ is much larger than the RCM's grid resolution. This is an indication that the coupled code, RCM-E, may produce physically meaningful results of a bubble injection event in the expansion phase, but just limited in the midnight sector. We should note that the detailed very fine structures, showing spatial periodicity, may be not reliable close to and beyond the edges of the bubble.

The RCM-E result in the bottom plot of Figure 5.8 at 10 minutes after the bubble injection overlaps the grid distribution on the FACs on the equatorial plane near the midnight. There are a lot of fine structures, some of which are rather large that are of 10-grid cells in size, but some of which are such smaller being of only less than 3-grid cells in size. A tentative conclusion is that the presented grid resolution in both the RCM and the friction code is not enough to get convergent results in the bubble injection runs.

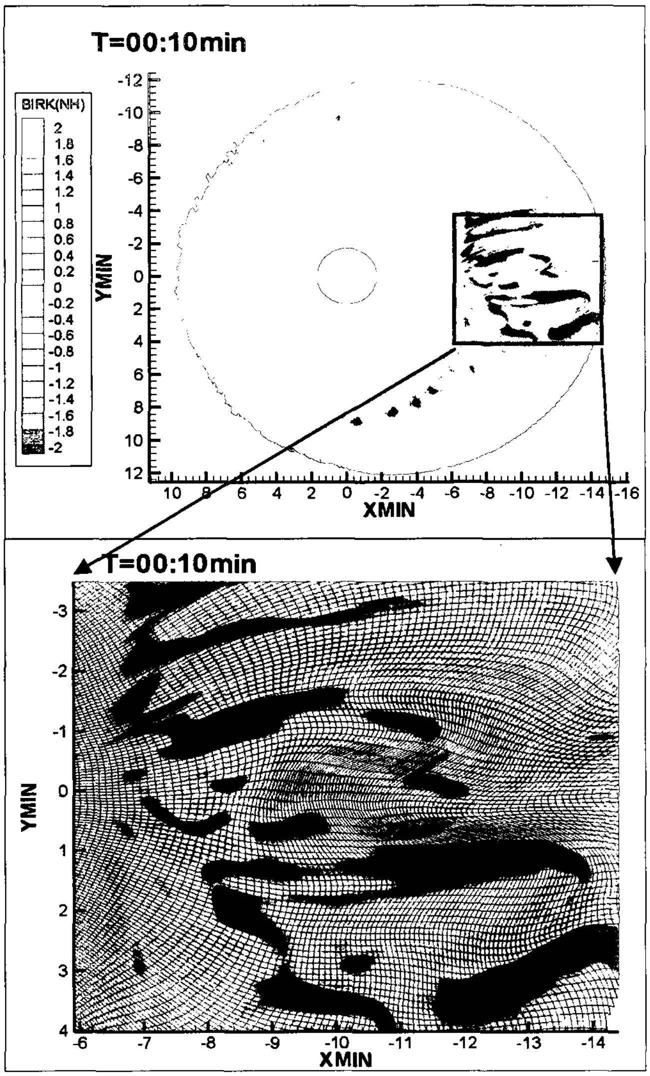

Figure 5.8. (top) Equatorial FACs density ($\mu A/m^2$) at T=00:10 of the RCM-E simulation of the bubble injection. (bottom) Enlarged view of the boxed region overlapped with RCM grid points. The sun is to the left.

Comparing the standalone RCM results with constant magnetic field configuration and the RCM-E results with self-consistently calculated magnetic field (Figure 5.9 and 5.10), similarities are apparent in $PV^{5/3}$ distribution and FACs densities mapped on the equatorial plane. (1) Both simulations show finger-like fine structures during the bubble injection, especially near midnight, which is a natural result of high grid resolution modeling. (2) Both simulations show interchange instability convections. The swirls of the electric potentials and the tailward ejection of high $PV^{5/3}$ plasma are strong indications.

However, we can also distinguish three differences. First, the fingers in the RCM-E simulation are maturing more slowly than those in the RCM. Comparing Figure 5.9 and Figure 5.10 at time 2~4 minutes, the configurations of both $PV^{5/3}$ and the FACs indicate that the penetration speed of the fingers is slower in the RCM-E results, because the $E \times B$ drift velocity in the RCM-E is smaller due to the magnetic field dipolarization. Second, it seems that the RCM-E produces fewer numbers of fine fingers and less intense FACs near the midnight after 10 minutes after the bubble injection (Figure 5.10). Third, a string of pearls of FACs along the pre-midnight sector intensifies, accompanied by both upward and downward FACs as well as swirls in electric potentials. The locations of the pearls are around the dipole-tail transition region, where the spots of pairs of FACs emerge. This configuration is particularly prominent at MLT 18~20 in the RCM-E simulation in the FACs density (Figure 5.10). Although, the self-consistent calculation of magnetic field will dipolarize the field inside the bubble, the field near geosynchronous orbit at MLT 18~20 may probably continue stretching, since the low $PV^{5/3}$ plasma has not reached that region. The smaller the magnetic field is, the bigger chance the instability would build. We will discuss more about this further in section 5.6.

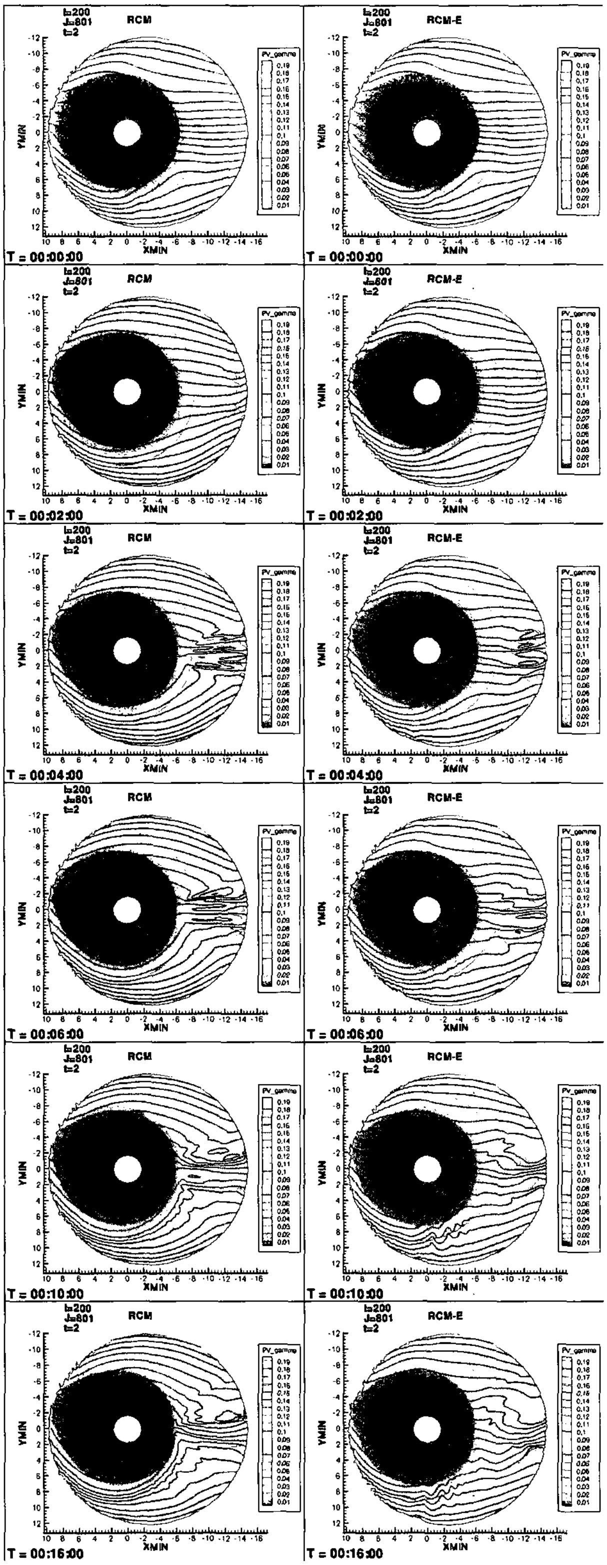

Figure 5.9. RCM with constant magnetic field (left) and RCM-E with force-balanced magnetic field (right) simulations of bubble injection. From top to bottom are equatorial $PV^{5/3}$ (nPa$(R_E/nT)^{5/3}$) for T=0, 2, 4, 6, 10 and 16min.

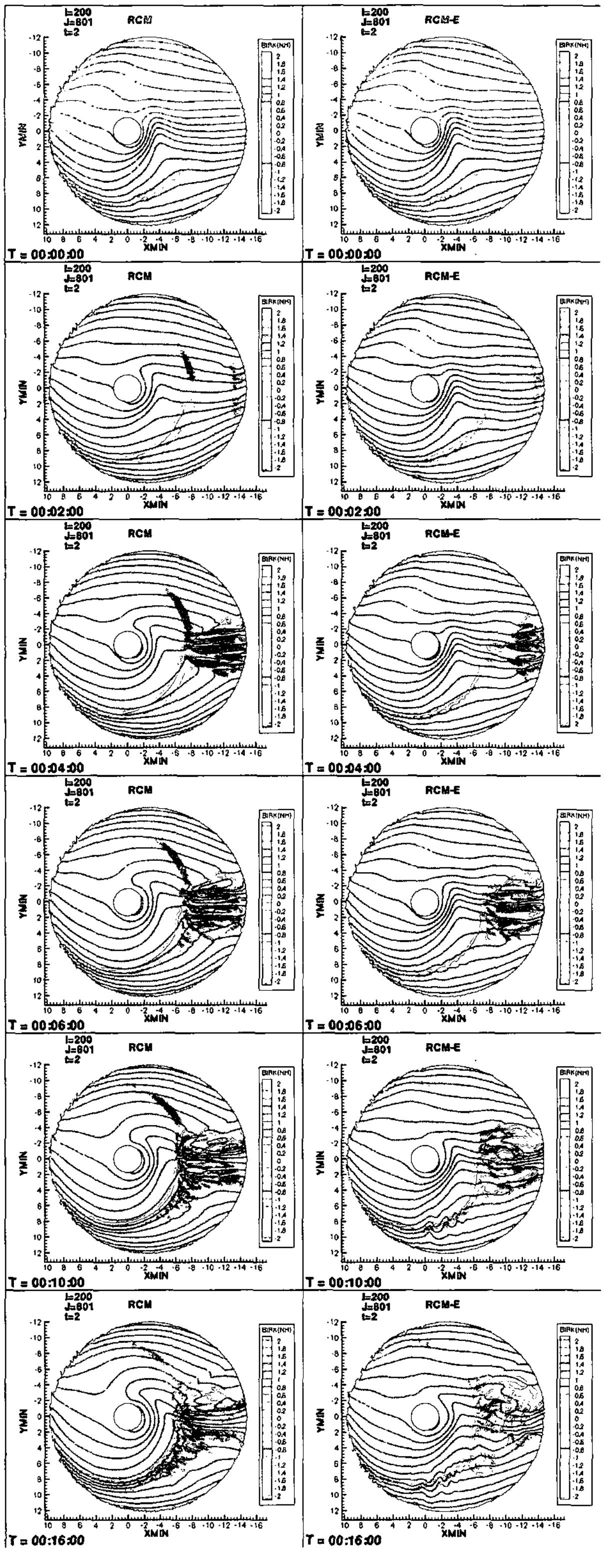

Figure 5.10. RCM with constant magnetic field (left) and RCM-E with force-balanced magnetic field (right) simulations of bubble injection. From top to bottom are equatorial equatorial FAC density ($\mu A/m^2$) for T=0, 2, 4, 6, 10 and 16min.

5.6 Runs with T96 model and with a self-consistently calculated magnetic field

It is worth investigating the formation of the strings of pearls of FACs along the dusk to pre-midnight and post-midnight to dawn regions, not only during the bubble injection, but also at the end of the growth phase.

The FACs are calculated via the Vasyliunas equation [Vasyliunas, 1970]

$$J_{\parallel} = \frac{\hat{b} \cdot \nabla V \times \nabla P V^{5/3}}{V^{5/3}} \tag{5.11}$$

The downward and upward FACs are dependent on the clockwise or anti-clockwise angle between the gradients of flux tube volume V and the entropy parameter $PV^{5/3}$, which could be very sensitive near the transition region, where the gradients are also usually large, and the angle between them is small. This kind of string-aligned pearls of FACs, although also spatially periodic, is more spot-like rather than the finger-like structures that develop near midnight well inside the bubble. While we have some evidence to claim that the finger-like structures are physically interchange instability/convection [*Yang et al.*, 2008]; the cause of pearls of FACs near MLT 18~20 and 4~6 is still uncertain as to whether they are physical real or just numerical noise in code.

To further address this uncertainty, we present two runs. One is that presented in Section 5.2, the RCM simulation of the bubble injection with constant magnetic field, which is a self-consistent configuration of the RCM-E growth phase (left of Figure 5.11

and 5.12); the other is the RCM simulation with unchanged T96 magnetic field model from the beginning of the growth phase to the end of the expansion phase (right sides of Figure 5.11 and 5.12). At time T=00:00 (the end of the growth phase), the FACs exhibit apparently string-like pearls in the MLT=18~20 sector for downward currents and in the MLT=4~6 sector for upward currents, for the run with magnetic field self-consistently calculated in the RCM-E growth phase run (upper left plot of Figure 5.12), but only two bands of FACs near geosynchronous orbit for the constant T96 magnetic field run (upper right plot of Figure 5.12). On the other hand, as demonstrated in Section 5.5, the continuous stretching of the magnetic field in the dusk to pre-midnight and post-midnight to dawn regions in the RCM-E simulation makes the spot-like quasi-periodic FACs more prominent. Usually, the longer we run the RCM-E or the more frequently we call the equilibrium code, the noisier the results become. This suggests that the oscillations in the magnetic field play a central role in the formation of this specific distribution. It is hard to evaluate whether these oscillations are physical disturbances or purely numerical noise or both. However, because the grid resolution of the equilibrium code, especially near the region of the pearls of FACs, is comparable to the size of the FAC spots, the possible cause of these pearls of FACs is numerical noise. At the present stage, the spatial periodicity is likely dependent on the grid resolution. A very careful study of this kind of periodicity is needed in the future.

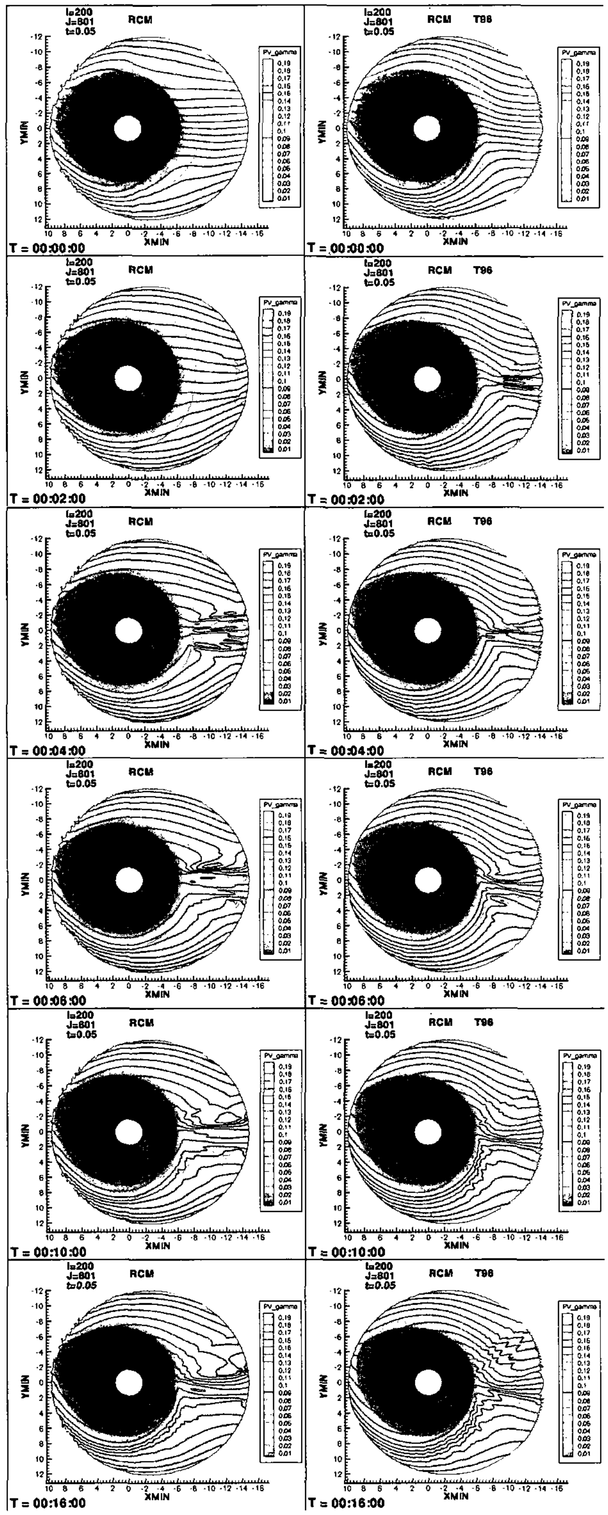

Figure 5.11. (left) RCM simulation with constant magnetic field following an RCM-E growth phase modeling and (right) RCM simulation with unchanged T96 model through growth phase to expansion phase. From top to bottom are shown the equatorial $PV^{5/3}$ (nPa(R_E/nT)$^{5/3}$) for T=0, 2, 4, 6, 10 and 16min.

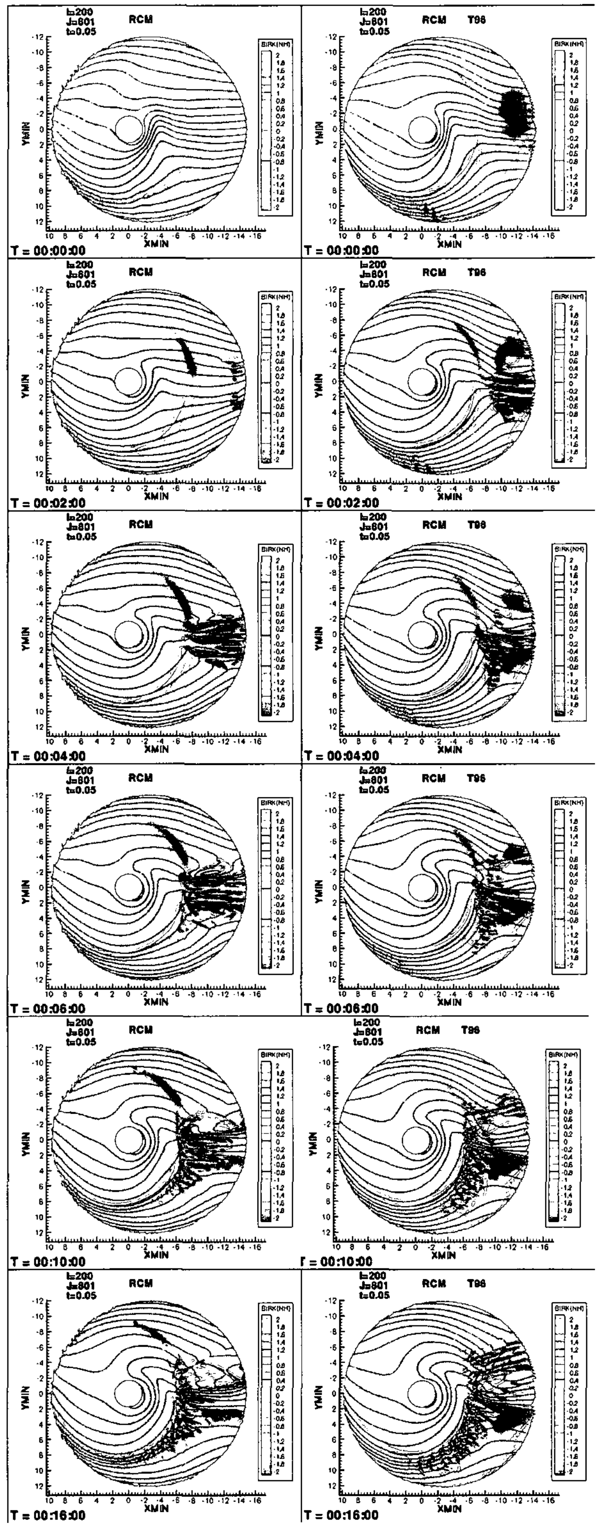

Figure 5.12. (left) RCM simulation with constant magnetic field following an RCM-E growth phase simulation and (right) RCM simulation with unchanged T96 model through growth phase to expansion phase. From top to bottom are shown equatorial equatorial FACs density ($\mu A/m^2$) for T=0, 2, 4, 6, 10 and 16min.

5.7 Observations of spatially quasi-periodic aurora

With sparse coverage of spacecraft in the magnetosphere, the opportunity to observe multiple pairs of downward-upward FACs is unlikely. A more reasonable approach to infer the existence of the spatially interlaced FACs is by remote sensing of the aurora, either from ground-based all-sky imager or from the high latitude spacecraft (e.g., IMAGE-WIC, POLAR-UVI). This approach was used to compare with RCM simulation of a sawtooth event, by using observations from the IMAGE-WIC by *Yang et al.* [2008]. Both the finger-like FACs caused by interchange instability and the spot-like FACs caused by other mechanisms have appeared in auroral photos.

Yang et al. [2008] has suggested that the sawtooth event provided a favorable situation for the interchange instability, in which the $PV^{5/3}$ reduced in unusually wide local times. Although, the spatial periodicity of the RCM simulation of the 2002-04-18 sawtooth event is believed dependent on the grid resolution as shown in Figure 5.1, the association of the interchange convection and the downward-upward pairs of north-south aligned finger-like aurora is probably correct. *Henderson et al.* [2006b] showed this association for 10-11 August 2000 sawtooth event (see the adapted Figure 5.13), where during every tooth cycle (other figures not adapted to the thesis) there were downward-upward north-south aligned finger-like aurora from IMAGE-WIC instrument after each substorm onset, and lasted about half an hour. This has also been observed by Polar-UVI instrument. The examples are shown in Figure 5.14 for 25 September, 1998 sawtooth event and in Figure 5.15 for the 18 February, 1999 sawtooth event. *Sazykin et al.* [2002] showed an RCM simulation, with the outer boundary put at the geosynchronous orbit and the plasma moment set as the LANL-MPA observations, and reproduced the interchange instability in the inner magnetosphere (Figure 5.16). Interestingly, this event was actually during a sawtooth event in which Polar-UVI observed periodically spaced aurora during one tooth cycle (Figure 5.14). However, unfortunately, Polar was not in a suitable location during the period shown in Figure 5.16.

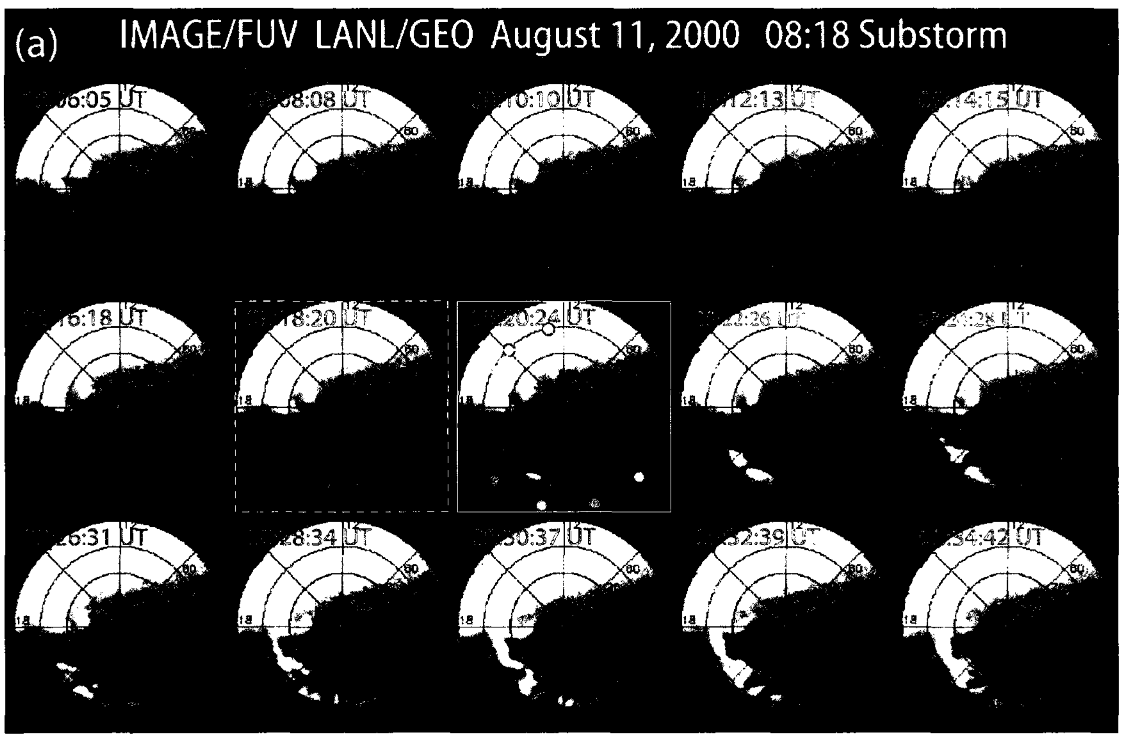

Figure 5.13. IMAGE/FUV WIC images illustrating the behavior of spatially quasi-periodic finger-like auroral distribution (bottom plots) after the 08:18UT onset. Adapted from *Henderson et al.* [2006].

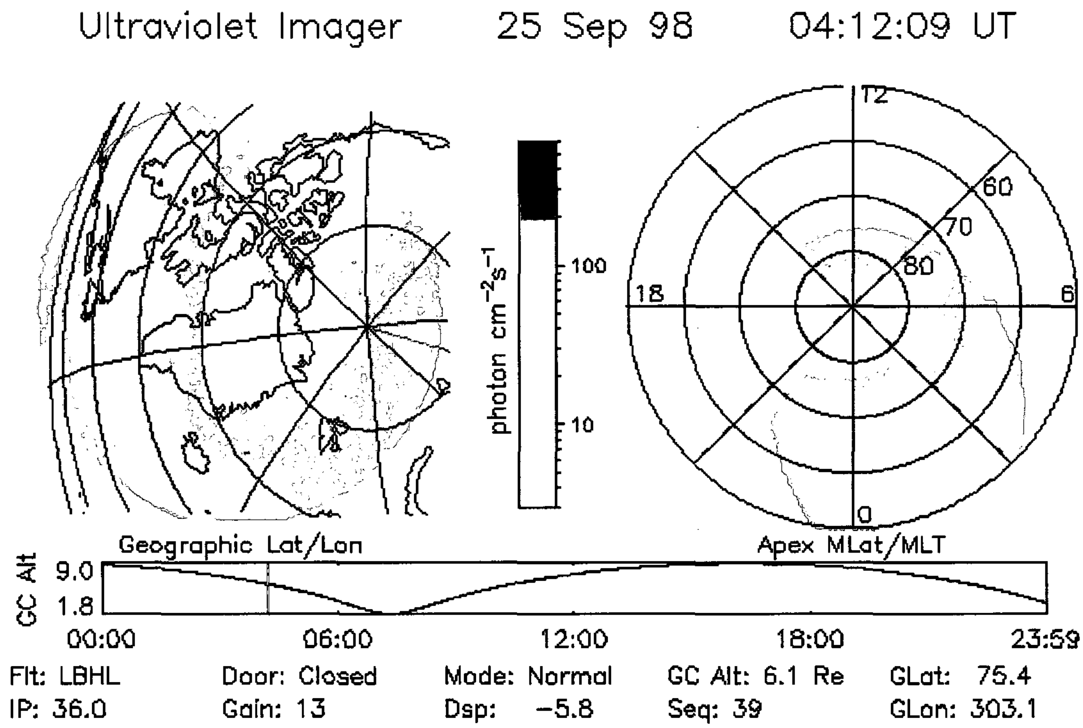

Figure 5.14. Ultraviolet image from Polar-UVI instrument for the 25 September, 1998 sawtooth event. The left image is captured by the instrument; the right image is mapped to MLT-MLAT coordinates, where MLAT is an apex magnetic latitude and MLT is the correspond local time. Image from http://uvi.nsstc.nasa.gov.

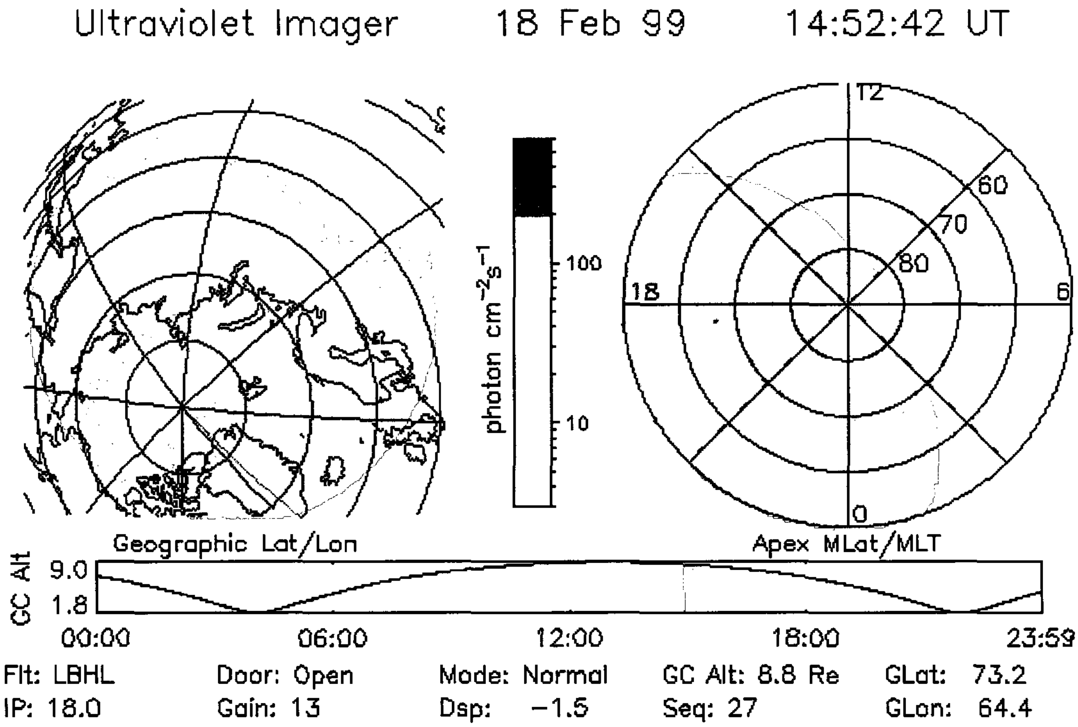

Figure 5.15. Ultraviolet image from Polar-UVI instrument for the 18 February, 1999 sawtooth event. Image from http://uvi.nsstc.nasa.gov.

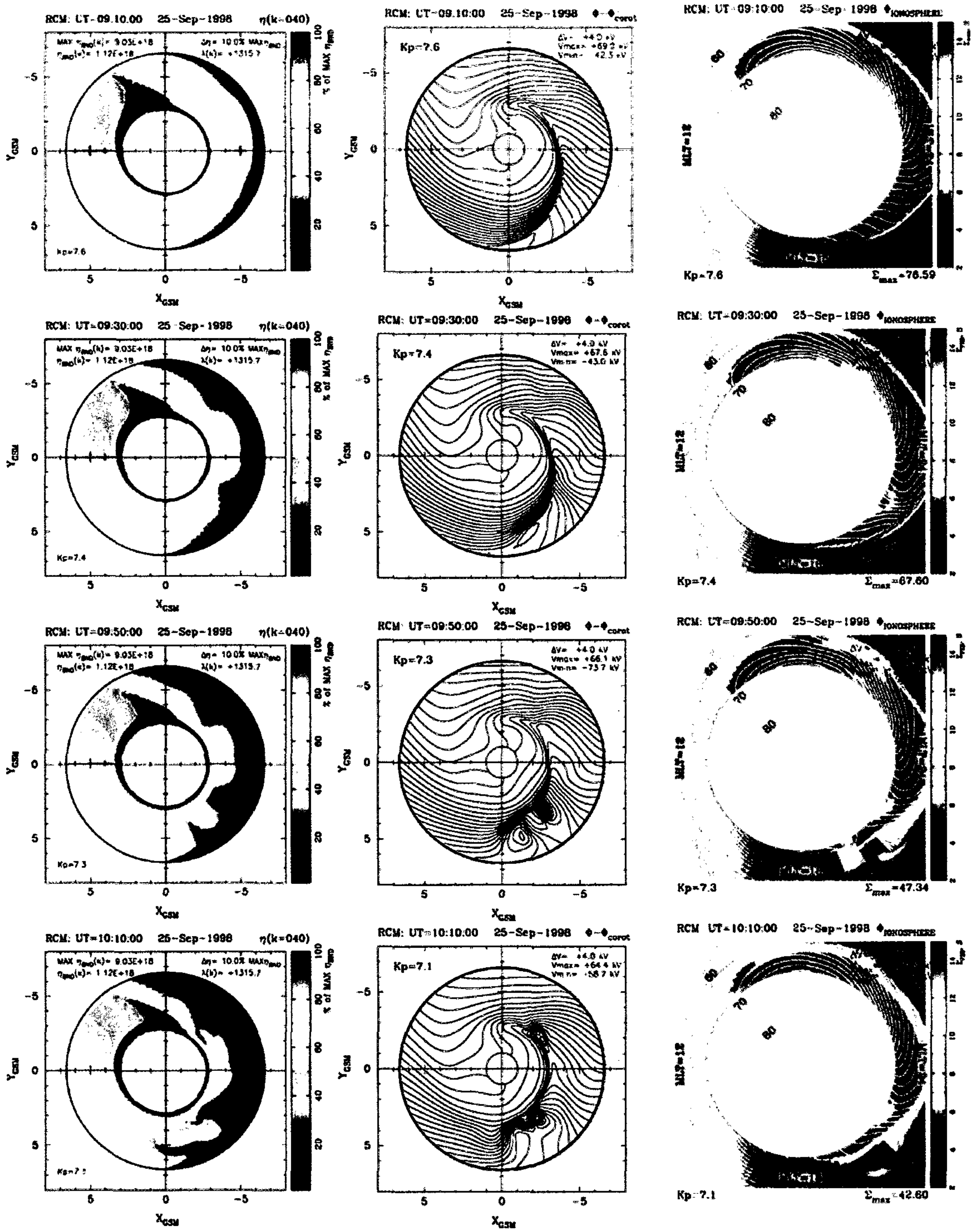

Figure 5.16. Left column, flux-tube content for protons corresponding to 9 keV at L = 6.6 (equatorial view); middle column, electric potential (equatorial view); right column, potential (contours) and Pedersen conductance in the ionosphere. Snapshots are shown four times on September 25. The Sun is to the left. Adapted from *Sazykin et al.* [2002].

The strings of pearls FACs in the RCM/RCM-E simulations at the end of the growth phase or near the onset and several minutes after onset (left column of Figure 5.12) may be associated with spot-like aurora measured by aurora remote sensing instrument [*Henderson*, 2009; *Keiling et al.*, 2008]. (Note, here I assume the RCM/RCM-E modeled strings of pearls of FACs are physically real, not purely numerical noise.) Figure 5.17 is adapted from *Henderson* [2009], which shows that the aurora forms near the substorm aurora onset. The spaced spots of auroral brightening are quite similar to our simulation both in size and in the timing with respect to the onset, although in this case the form is near the midnight, rather than close to dusk and dawn. Figure 5.18 is adapted from *Keiling et al.* [2008], which shows the aurora configuration minutes before a major onset. In this case, the periodicity is closer to the dusk side than in the observations of *Henderson* [2009]. Both of the two papers suggested that those very finely spaced aurora structures are due to the near-Earth instability, likely the ballooning instability [e.g., *Roux et al.*, 1991]. This instability is considered to be associated with substorm onset mechanism, which can produce downward-upward pairs of aurora connected to the wave-like magnetic field oscillations in the inner edge of the plasma sheet. Similar quasi-periodic aurora were also reported as large-scale undulations near the inner edge of diffuse aurora using DMSP data [e.g., *Lui et al.*, 1982], interpreted as a result of Kelvin-Helmholtz instability [e.g., *Kelley*, 1986] since the inner edge of the plasma sheet is unstable to intense shear flows (which is called "shear flow-ballooning instability" by

Viñas and Madden [1986]). A sketch of the connection between the aurora, the instability and the field-aligned currents is shown in Figure 5.19.

One of the perspectives of the RCM/RCM-E simulation for the substorm is that, with the Fast-MHD stability analysis algorithm [*Crabtree et al.*, 2004], we can test whether the configuration of the system is MHD ballooning stable or not [*Toffoletto et al.*, 2007]. An application to the 2004-Oct-29 substorm event [*Yang et al.*, 2009a] has been conducted [*Toffoletto et al.*, 2008], showing that the inner magnetosphere is ballooning unstable at the end of the growth phase, but the growth rate of the instability is slow.

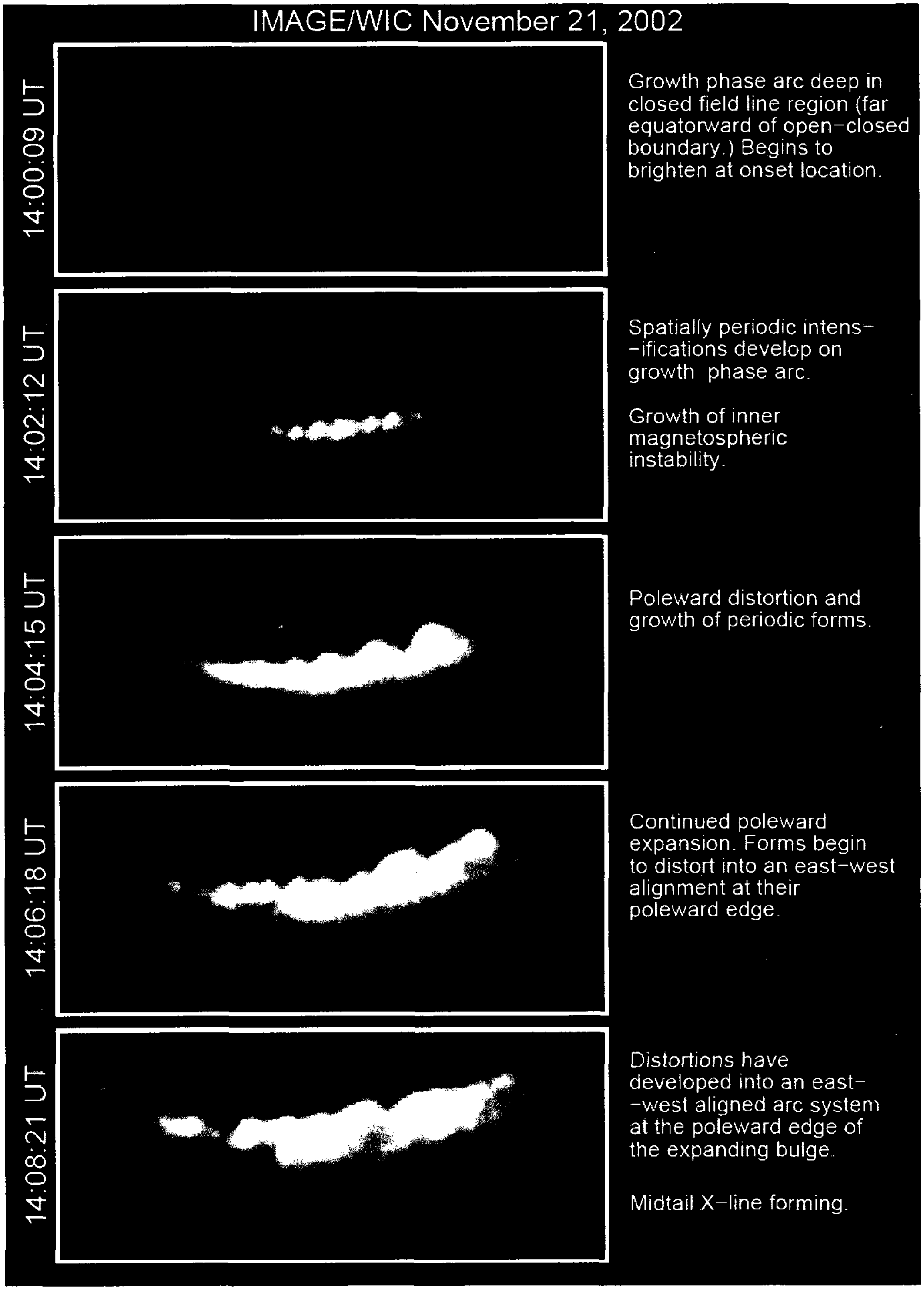

Figure 5.17. Snapshots of spot-like aurora around midnight observed by IMAGE/WIC near the substorm onset. Descriptive comments are given to the right of each image (white text), and an interpretation of the underlying physical cause is given in yellow text. Adapted from *Henderson* [2009].

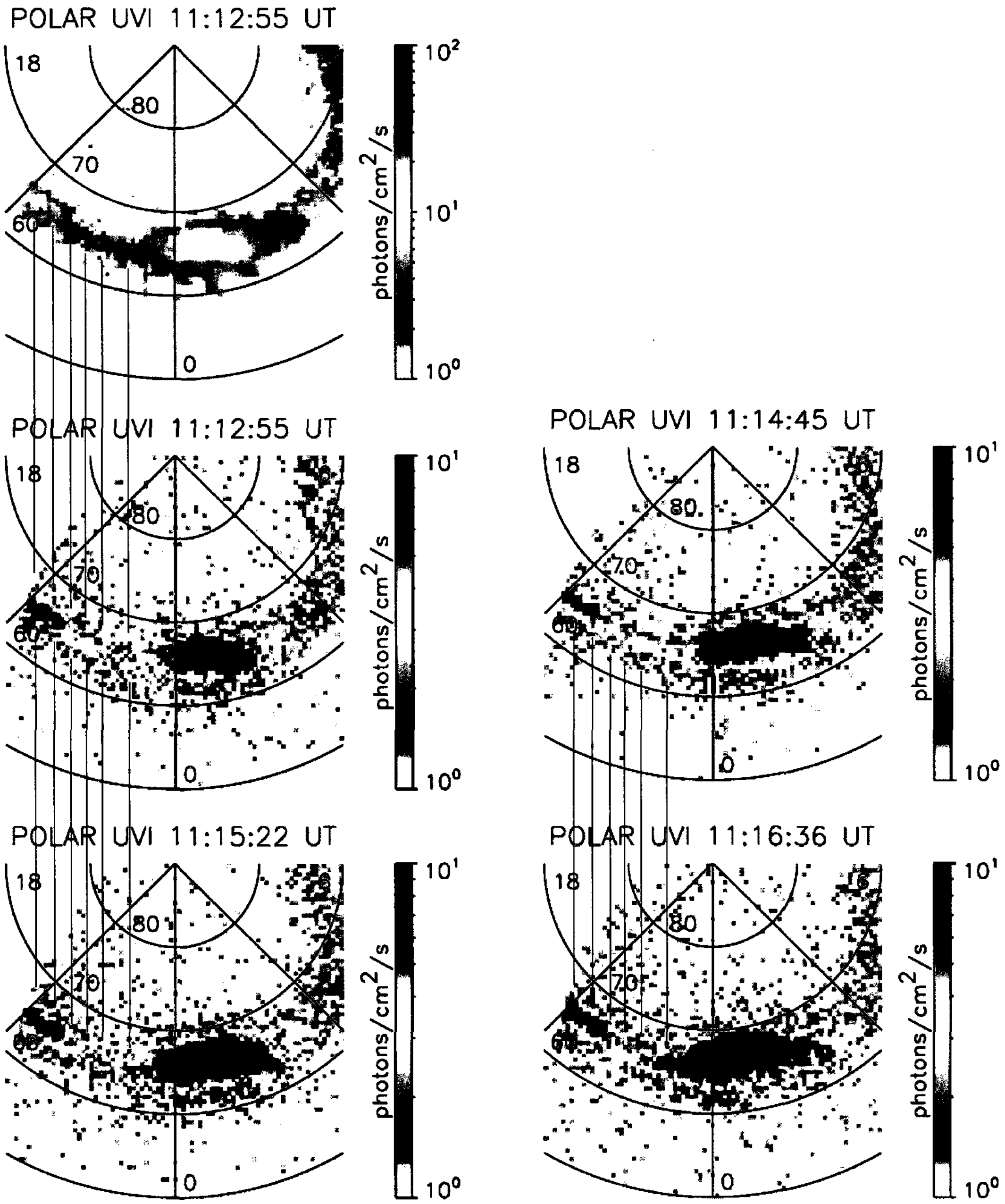

Figure 5.18. Polar-UVI images near a major substorm onset time. Vertical lines are aligned with azimuthally spaced auroral forms. Note that the first and second images are identical but are shown with different color scales for comparison. Adapted from *Keiling et al.* [2008].

5.8 Concluding comments

A series of the RCM/RCM-E simulations are compared in this chapter, focusing on testing the modeling results for the grid resolution dependence. Several interesting findings are listed below.

(1) Unsurprisingly, we find that, with higher grid resolution, finer structures emerge well inside or near the edges of the injection bubble, during the substorm expansion phase. Those fine structures are prominent in the FACs density plots, which can be described as downward-upward pairs of FACs. The periodically spaced north-south aligned finger-like aurora are suggested as a strong support of the existence of these kinds of FACs.

(2) From the RCM/RCM-E simulation point of view, the finger-like aurora are a result of interchange instability, which produces spatial periodicity in FACs, rather than multiple injections or BBFs. We find that in the simulation the interchange instability happens not only in sawtooth events, but also during normal isolated substorms.

(3) The simulations, either with larger background solar-radiation-induced conductance or with magnetic field dipolarizations inside bubble, show slower penetration of interchange convection.

(4) Strings of the pearls of downward-upward pairs of FACs are found in the RCM/RCM-E simulations prior to the onset or in the first few minutes of the expansion phase in from the post-dusk side to the pre-midnight sector and from the post-midnight sector to the pre-dawn side.

(5) Although from the simulation point of view, the size of the pearls of FACs may be dependent on the equilibrium code grid resolution and the numerical noise effect on the formation of these FACs is still under further investigation, they are observationally associated with the quasi-periodic spaced spot-like aurora observed by IMAGE-WIC and Polar-UVI [*Henderson*, 2009; *Keiling et al.*, 2008].

(6) The string-of-pearl-like aurora are suggested to be associated with near-Earth ballooning instability near the transition region [*Keiling et al.*, 2008; *Henderson*, 2009].

These two forms of simulated FACs can be summarized in Figure 5.19 along with their association with feasible mechanisms and auroral observations. Near the substorm onset, the magnetic field line oscillations near the inner edge of the plasma sheet produce pairs of spot-like downward-upward FACs in the inner magnetosphere, which generates the bright spots of aurora in the string-of-pearls form. The ballooning instability is one candidate mechanism. In the expansion phase, when the bubble is injected, it can naturally break up into pieces due to the interchange instability, which can produce multiple injection channels penetrating deep into the inner magnetosphere. This would generate finger-like north-south-aligned aurora associated with pairs of downward-upward FACs.

Several aspects of future studies can improve our understanding of the spatially quasi-periodic FACs modeled by the RCM/RCM-E.

(1) In the RCM/RCM-E modeling perspective, it is still unclear that whether 800 grid points in longitude in the RCM is enough for the finger size and spacing to converge; it is still unknown that whether the magnetic field oscillations calculated by the equilibrium code is purely or partially numerical noise or not. Therefore, higher grid resolution is needed for both the RCM code and the Friction code, which challenges the computational capability. A parallel version of the Friction code is been developed by *Vinod Kumar* and *Frank Toffoletto*, and a parallel version of the RCM-E will be developed by *Bei Hu* and *Frank Toffoletto* in the near future.

(2) The inertial current is currently neglected in the RCM/RCM-E modeling. The inclusion of this current may help us calculate the potentials and plasma drift more accurately, which further affects the pattern of the bubble injection.

(3) An accurate calculation of the parallel potential drops should be implemented in the RCM/RCM-E..

(4) The ballooning instability can be tested with the utilization of the Fast-MHD code [*Toffoletto et al.*, 2008] for more RCM-E simulations.

(5) An ambitious idea to investigate the interchange instability is to use multipoint spacecraft observations, along with self-consistent modeling for the M-I coupling, to establish one-to-one match of the FACs in the plasma sheet and the aurora in the ionosphere. However, to my knowledge, since now there is not direct *in-situ* observation of the interchange instability in the inner magnetosphere. We may expect to find one, if

we are lucky enough, by estimating the $PV^{5/3}$ [*Wolf et al.*, 2006a] with multipoint observations. A promising approach would be to search the sawtooth event list [*Xia Cai*, private communication, 2008], since those events provide a favorable situation for interchange instability [*Yang et al.*, 2008].

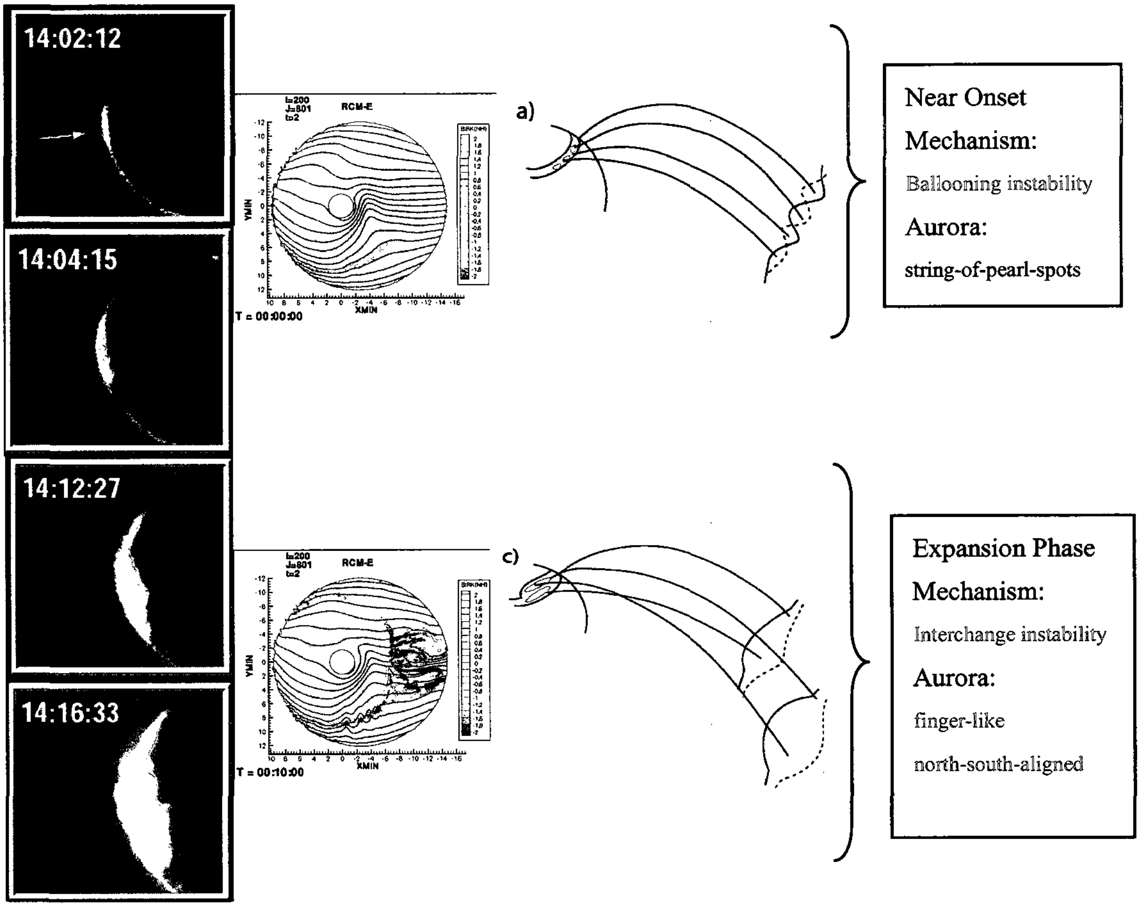

Figure 5.19. Left column plots are adapted from *Henderson* [2009]. Top two show the observed quasi-periodically spaced spot-like aurora around midnight near the substorm onset. Bottom two plots depict the development of quasi-periodically spaced finger-like aurora during the substorm expansion phase. Middle column plots are equatorial views of FACs densities from RCM-E simulation at the substorm onset and 10 minutes after onset. Right column sketches adapted from *Keiling et al.* [2008] indicate the connection between the aurora display and magnetic field mapping.

Chapter 6

Idealized isolated bubble injections modeled by the RCM-E

Based on a number of *in-situ* observations, the reconfiguration of the magnetic field topology and the associated change of the plasma pressure during a substorm expansion phase are highly dynamic. To obtain a qualitative description of this process, we investigate the resulting reconfigurations of equatorial entropy parameter $PV^{5/3}$, plasma pressure P and magnetic field B_Z along the X-axis, during southward IMF B_Z conditions. We do this by modeling an idealized bubble injection with the RCM-E by placing depleted $PV^{5/3}$ along the high latitude boundary near midnight. We find that the time history of the bubble injection into the inner magnetosphere region can be divided into four different regions. The first region is near the tail boundary, where the results show decreases in the plasma pressure associated with magnetic field dipolarizations and the reduction of $PV^{5/3}$ inside the bubble. The second region, which is well inside the peak partial ring current region, shows pressure buildup and a stretching of the magnetic field associated with the increase of $PV^{5/3}$. The last 2 regions are near the inner edge and outer edge of the transition region and show both increasing and decreasing changes of $PV^{5/3}$, P and B_Z along the X-axis. We also present results from two other runs, one that has a much more severe reduction of $PV^{5/3}$ on the tail boundary and one for a northward IMF B_Z condition; these results also show the same four regions, but with the dividing lines between them are at different spatial locations. The locations of these divisions between regions, are possibly related to how deep the bubble can penetrate into the inner magnetosphere and the location of the growth-phase transition region. We also show that the high energy particles (>40keV) can contribute to more than half of total plasma pressure during the expansion phase near the peak of partial ring current. The ion temperature can rise as high as 20~30keV at geosynchronous in the simulations.

6.1 Observational relationship of the near-Earth plasma pressure and magnetic field

The purpose of this section is to briefly review the relationship between pressure and magnetic field in the inner magnetosphere during substorm expansions inferred from *in-situ* observations. During the substorm expansion phase, the ejection of a plasmoid or a flux rope, containing hot plasma, will significantly reduce the plasma pressure in certain spatial regions earthward of the reconnection site, while the magnetic tension drags plasmas that are still attached to the closed field lines to the inner magnetosphere which accelerates particles and builds up the partial ring current with considerably increased plasma pressure. On the other hand, the magnetic field dipolarizes in the tail as a result of large-scale reconfiguration of the magnetic topology, and the field gets stretched earthward of the intensified partial ring current.

Statistical empirical models [e.g., *Tsyganenko and Mukai*, 2003, *Borovsky et al.*, 1998] that use measurements of plasma pressure from, for example, Geotail and LANL spacecraft, are highly averaged, even though some models are binned into different solar wind or geomagnetic conditions. For some models, e.g., TM2003 model, the data points virtually exclude measurements during intervals of high flow velocities [*Tsyganenko and Mukai*, 2003], which is a characteristic feature of a substorm [*Angelopoulos et al.*, 1992]. An alternative approach for obtaining plasma sheet plasma pressures is by mapping low-altitude spacecraft (e.g., DMSP) measurements of plasma pressure to the plasma sheet with the help of a specific magnetic field model, with the assumption that the plasma pressure along the magnetic field line is constant [e.g., *Wing et al.*, 2007]. This approach has a systematic uncertainty introduced by the uncertainty in the magnetic field model. Since there are no statistically-based substorm-time magnetic field models, which include both the thin cross-tail current sheet representation in the growth phase and the substorm current wedge model in the expansion phase, it is reasonable to claim that there are no reliable statistical plasma-sheet plasma pressure models specifically aimed at substorms.

In-situ observations indicate that the plasma pressure and magnetic field reconfigures in a complicated fashion near the transition region at about X~-10R$_E$, where both the magnetic field and the plasma pressure gradients are large. As shown in the following case studies, we may still be able to sort out some basic features of the relationship between plasma pressure and magnetic field reconfiguration.

Kistler et al. [1992] used AMPTE observations to investigate the change of plasma pressure for 0-230keV ions before and after substorm injections in the near-Earth plasma sheet. They found that the ion pressure after substorm injection generally decreased for regions outside $10R_E$ but increased for regions inside $10R_E$ (Figure 6.1). This suggests that, in the situation when the plasma distribution reconfigures significantly, the plasma pressure is not necessarily increasing or decreasing; while there must be a transition region at about $-10R_E$ where the plasma pressure remains roughly unchanged before and after substorm injections.

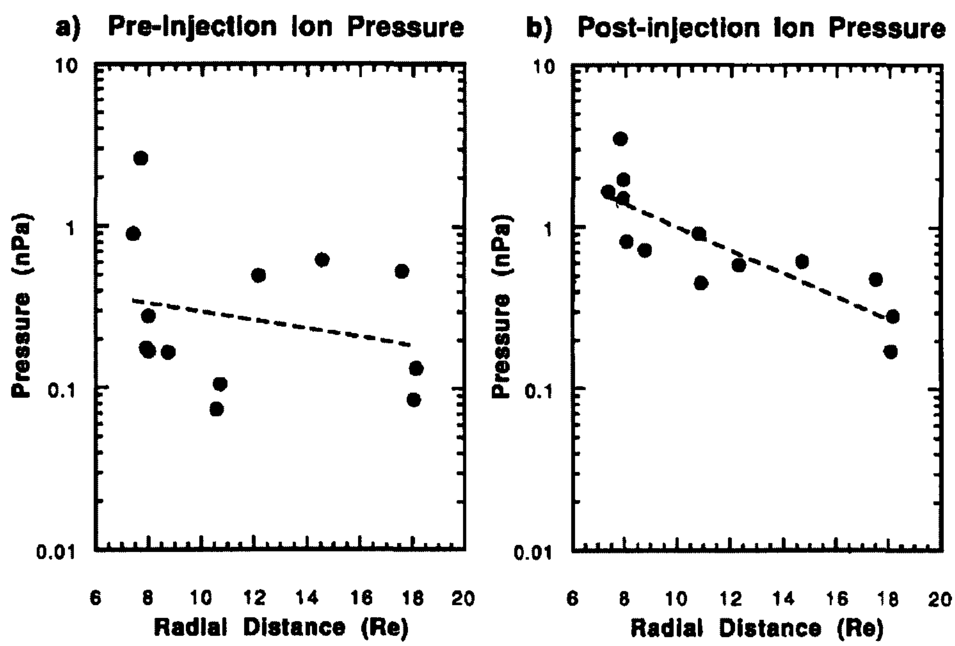

Figure 6.1. The ion pressure as a function of radial distance (a) before and (b) after substorm injections. The dashed lines show the results of least squares fits to the data. (adopted from *Kistler et al.* [1992])

Lyons et al. [2003] estimated the ion pressure by using Geotail LEP (<40keV/charge ions) [*Mukai et al.*, 1994] and/or EPIC (44-265keV/charge ions) [*Williams et al.*, 1994] particle fluxes for selected events. Their results also indicate that the regions where the plasma pressure increases or decreases during substorms are case dependent. Figure 6.2 shows examples of four substorm events with onsets indicated by vertical lines, in which the two events in the top panel, at more tailward (X~-12.5R_E) locations, displayed ion pressure reduction when both low and high energy channels were included; while the events more earthward (X~-10R_E) in the bottom panel displayed modest ion pressure increase or decrease when only low energy channels (LEP instrument) were considered.

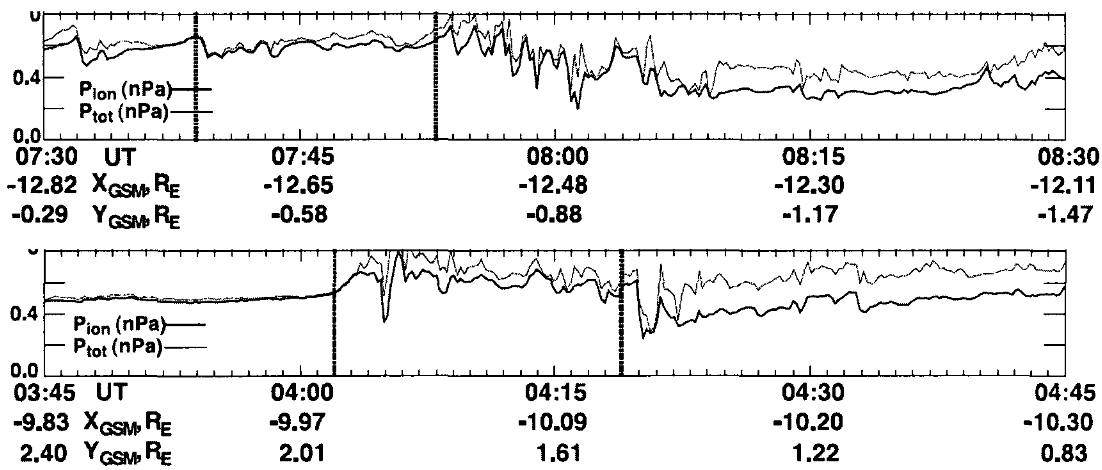

Figure 6.2. (top) Ion pressure, P_{ion} (from LEP and EPIC observations) and the sum of ion pressure and magnetic field pressure, P_{tot}, for two substorm events on 07 June, 2000. (bottom) Ion pressure, P_{ion} (from LEP observations) and the sum of ion pressure and magnetic field pressure, P_{tot}, for two substorm events on 14 August, 1996. Vertical lines indicate ground onsets. Adapted from *Lyons et al.* [2003].

Miyashita et al. [2008] found that in the near-Earth region at about X~-10R_E, the ion pressure for <265keV/charge from both Geotail/LEP and Geotail/EPIC increased at the onset of dipolarization (First and second events in Figure 6.3), in which the high energy particles contributed substantially to the total plasma pressure; while in another event at the more tailward region at about X~-14R_E (bottom plot of Figure 6.3), there was no significant change of ion pressure, except for the first 2~3 minutes, associated with magnetic field dipolarization, and furthermore the contribution of high energy particles was very small. The contribution of the high-energy particles (>40keV) to the total plasma pressure after substorm onset could be smaller further out in the plasma sheet (e.g., X~-14R_E) than that in the transition region (X from -10 to -12R_E).

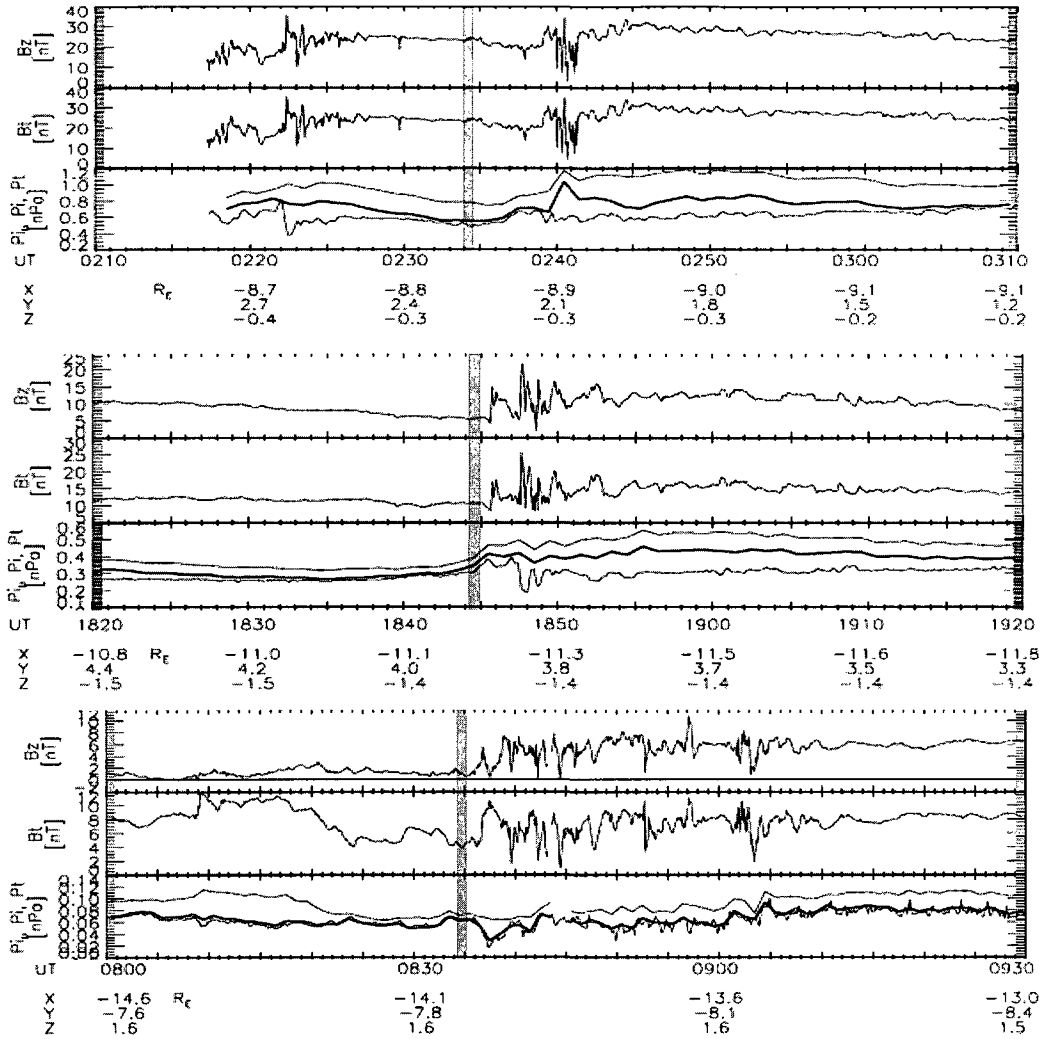

Figure 6.3. Three substorm events (7 September, 1998; 22 December, 2001; 1 May, 2002 from top to bottom) observed by Geotail. Each plot contains B_Z (Z-component of magnetic field in GSM), Bt (magnitude of magnetic field), Pt (sum of ion pressure and magnetic pressure), Pi (ion pressure from LEP and EPIC, thick lines), PiL (ion pressure from LEP). Adapted from Miyashita et al. [2008].

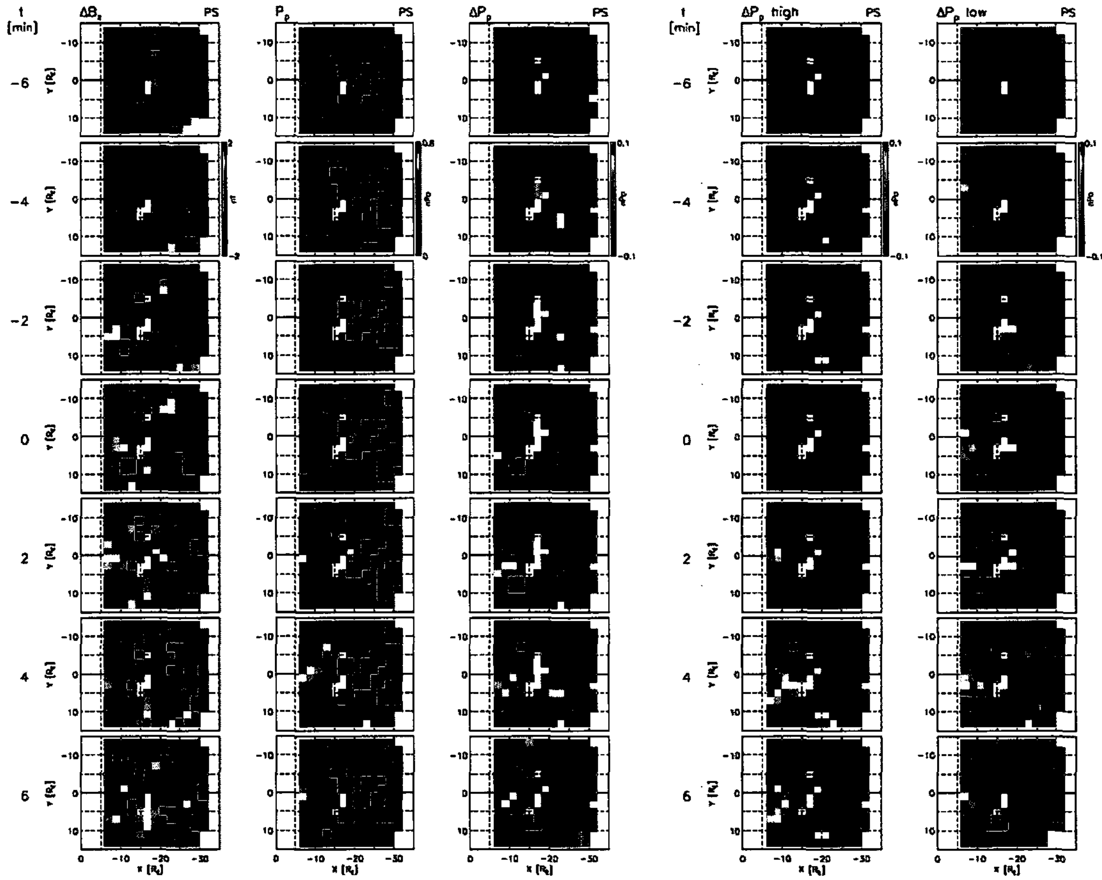

Figure 6.4. Equatorial X-Y plane distribution of ΔB_Z (change of B_Z with respect to the time averaged B_Z), P_p (ion pressure), ΔP_p (change of ion pressure with respect to the time-averaged ion pressure), ΔP_p high (change of high energy ion pressure) and ΔP_p low (change of low energy ion pressure) for time T=-6, -4, -2, 0, 2, 4, 6 minutes with respect to auroral breakup onsets. Adapted from *Miyashita et al.* [2008].

The statistical results for 1287 substorms are shown in Figure 6.4 [*Miyashita et al.*, 2008]. The substorm onsets were identified by using auroral breakups observed by Polar-UVI or IMAGE-FUV. They found that the increase in the Z-component of the magnetic field (column 1) inside $10R_E$ after onset was accompanied with an increase in the ion pressure (column 3). Detailed breakdown of the energy-dependent contributions shows that the high-energy particle pressure (column 4) was increasing and the low-energy particle pressure (column 5) was decreasing in the pre-midnight sector and increasing in the post-midnight sector.

The THEMIS mission, which consists of five identical spacecraft aligned once about every four days in the midnight sector in the tail season (i.e., from December of the previous year to March of the current year), was specifically designed to study substorms [*Angelopoulos*, 2008a]. *Xing et al.* [2008] depicted one of the major conjunction events in detail, shown in Figure 6.5. The plasma pressure consisted of the estimated equatorial plasma pressure, combining both the ion and electron pressures from ESA and SST instruments [*McFadden et al.*, 2008]. The magnetic field at all spacecraft, except the outermost one (TH_B), increased, while the change of plasma pressure was more complicated. In the tail, TH_C (X~-17R_E) and TH_B (X~-23R_E) measured decreasing plasma pressure; in the transition region; even though TH_D (X~-11.3R_E) and TH_E (X~-11.0R_E) were very close to each other, the time history of the plasma pressure was quite different. Near geosynchronous orbit, TH_A (X~-7.5R_E) recorded a sharp pressure increase in the first five minutes, followed by a gradual decrease.

In summary, the relationship between the change of plasma pressure and the magnetic field dipolarization/stretching can be quite complicated in the course of a substorm injection, which seems to be dependent on the location with respect to the transition region, dependent on time with respect to the onset and dependent on the particle energy.

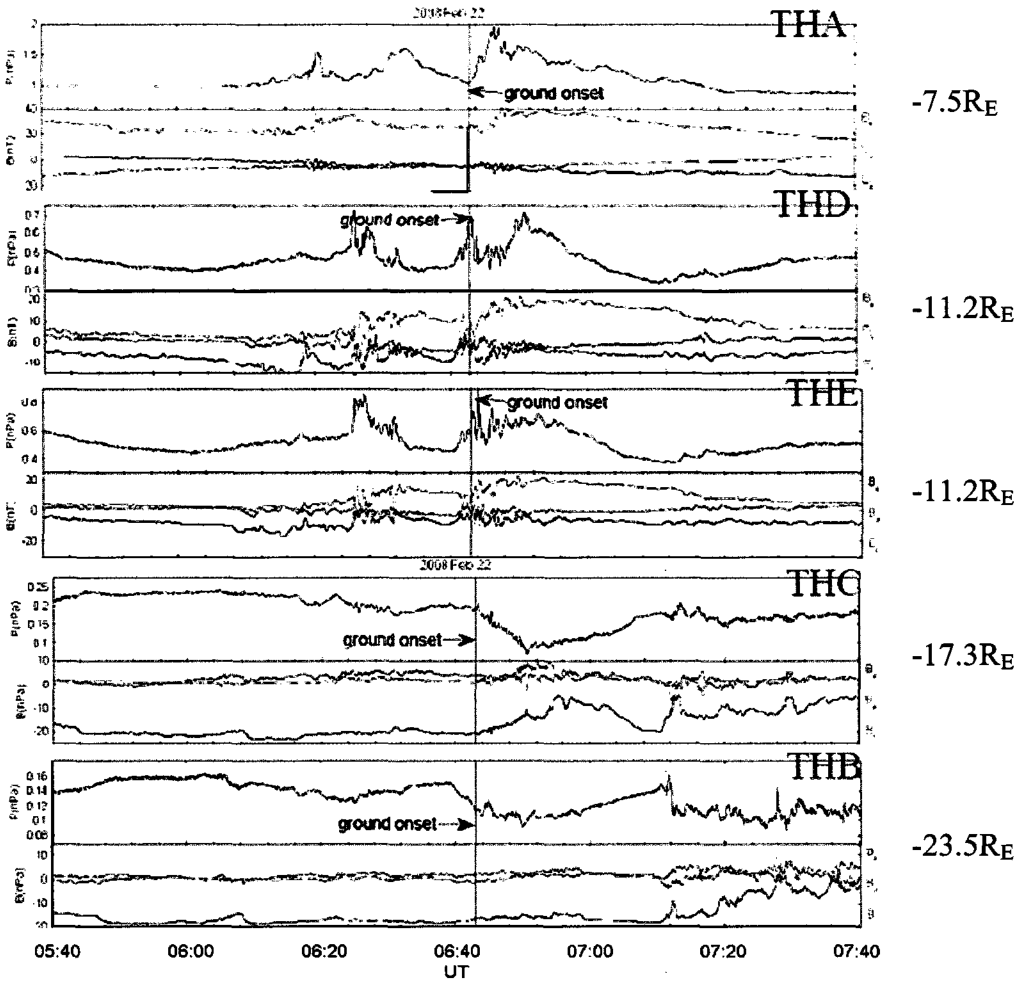

Figure 6.5. Observed magnetic field components (B_X in blue, B_Y in green and B_Z in red) and estimated central plasma sheet plasma pressure for five spacecraft. The X_{GSM} location of each spacecraft is shown to the right. Adapted from *Xing et al.* [2008].

6.2 An example of an RCM-E simulation of an idealized bubble injection

From the theoretical point of view, if one assumes that a plasma bubble, with lower $PV^{5/3}$ than its neighbors, plays a crucial role in the injection of plasma during substorms then modeling the bubble injection could provide an explicit quantitative picture of the plasma pressure and magnetic field changes associated with substorms. With the RCM-E simulations, although very idealized, we will try to integrate the numerous observations into a consistent physical picture and gives a qualitative description of the time series of the magnetic field and plasma pressure reconfigurations and the corresponding interpretations.

The idealized bubble injection presented here is modeled by reducing $PV^{5/3}$ only along a section of the boundary, which is set at X=-15 R_E at midnight on the equatorial plane. This approach is similar to what is described in *Zhang et al.* [2009a, 2009b] and in Chapter 5, but quite different from Chapter 4. As discussed in Chapter 4, the treatment of the spatial extent of the reduction of $PV^{5/3}$ at onset (see section 4.4.4) is quite important. The $PV^{5/3}$ depletion presented here, is only along the boundary in a certain local time range, which suggests that the non-adiabatic process happens outside X=-15R_E and/or the bubble has well formed outside X=-15R_E prior to its injection into the modeling region.

6.2.1 Model setup

The setup of the initial conditions, including the background ionospheric conductances, magnetic field and the plasma distribution, for this RCM-E simulation are the same as the one described in section 5.2 but with lower grid resolution (i.e., 200 grid points in latitude and 101 grid points in longitude). The polar cap potential drop is set as a constant 100.5kV. During the 30-minute growth phase run, the plasma distribution on the boundary is assumed to be a kappa distribution (κ=6) [*Christon et al.*, 1989], with $PV^{5/3}$

set as a constant 0.20 nPa(R_E/nT)$^{5/3}$ (in the range of typical values of $PV^{5/3}$ at this location, see *Xing and Wolf* [2007] for reference).

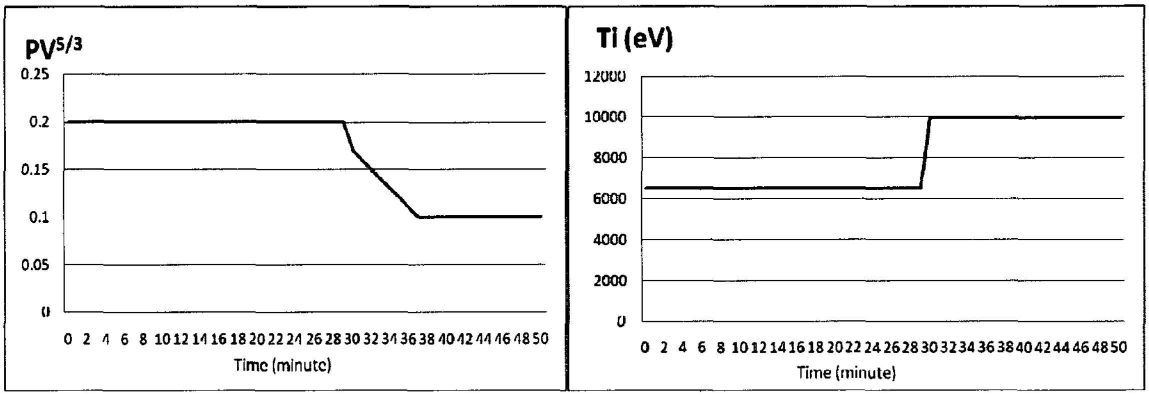

Figure 6.6. The $PV^{5/3}$ in unit of nPa(R_E/nT)$^{5/3}$, and ion temperature versus time, for the high-latitude boundary at the midnight.

The setup for substorm expansion phase run is the same as in section 5.2, except for the time variation of the depleted $PV^{5/3}$ at the boundary. The time scale of the reduction of $PV^{5/3}$ after onset until its final constant value is variable for different events. For example, it takes about 6 minutes for $PV^{5/3}$ to decrease from its peak value to a sustained low value for the event shown in Chapter 4 (Figure 4.5); while it takes only about two minutes for the event shown in Figure 6 of *Wolf et al.* [2006a]. The depleted values of $PV^{5/3}$ and the ion temperature at the center of the bubble at midnight in this idealized event are shown in Figure 6.6. The magneto-friction code convergence is shown in Figure 6.7. Similar to Figure 4.21, the trend of the force imbalance parameter *F* (defined in equation 4.23) is generally decreasing during both the growth phase and the late expansion phase for the "magnetotail" region (X<-8.0R_E and Z<3.0R_E), where the magneto-friction code is working properly in this closed-field line region; while the trends for both the "inner" region ($2.0<R<8.0R_E$) and "global" region ($-40.0<X<-12.0R_E$, $-15.0<Y<15.0R_E$, $0.0<Z<15.0R_E$) are increasing possible due to the numerical noise near the magnetopause and the open field line regions around cusp.

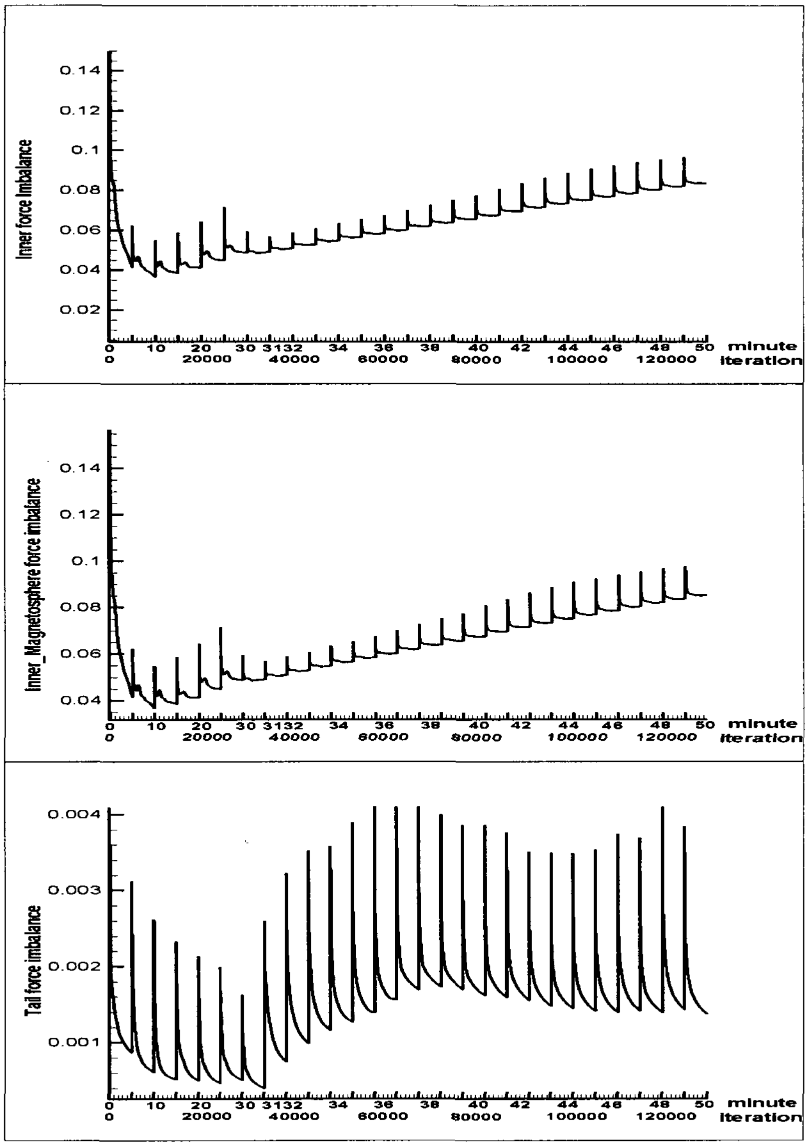

Figure 6.7. From top to bottom are force imbalance parameters for (a) all grid points in the magneto-friction code computational domain; (b) the inner magnetospheric region ($2<R<8.0R_E$); (c) the tail region ($X<-8.0R_E$ and $Z<3.0R_E$). The X-axis is uniform in iteration numbers and non-uniform in universal time.

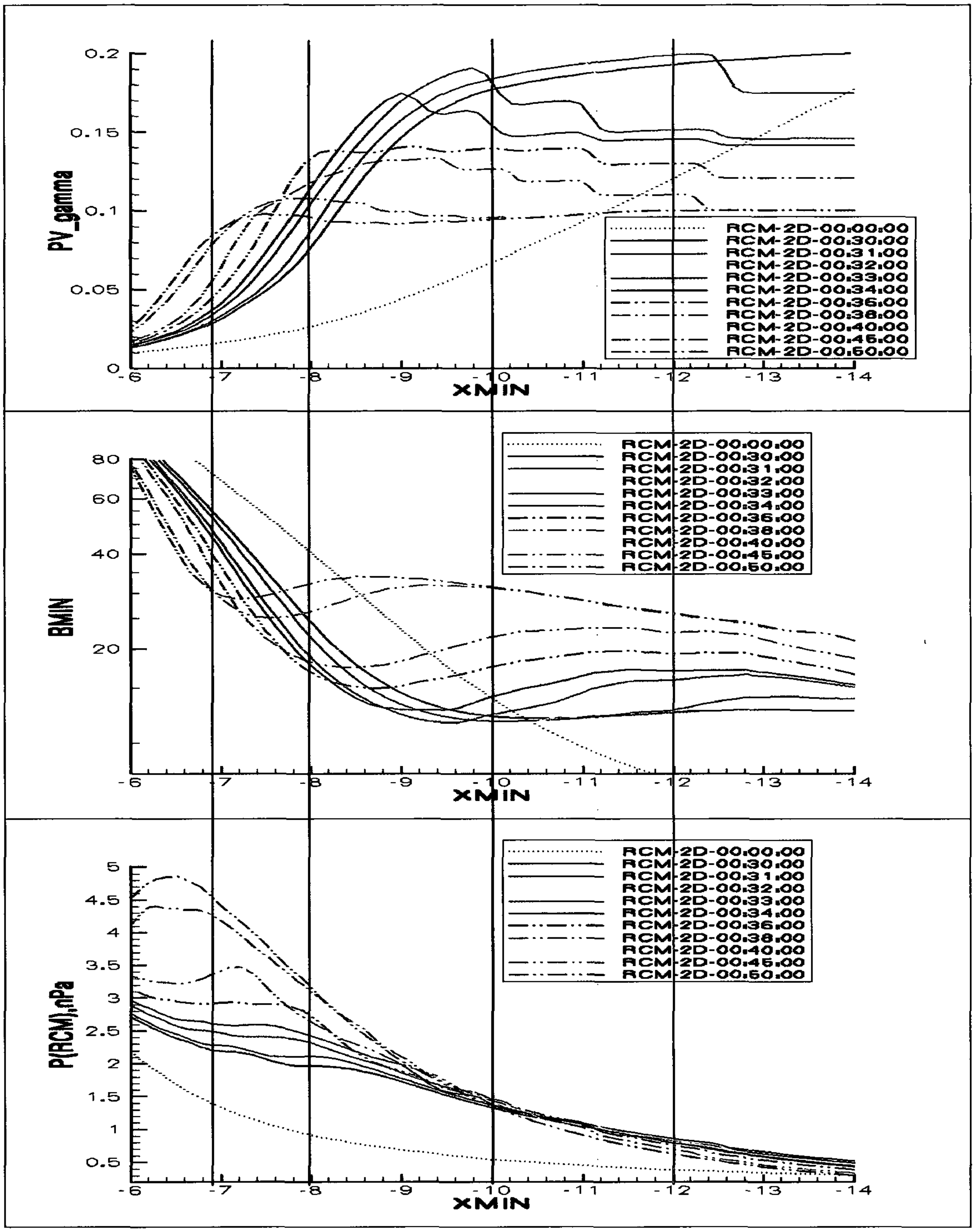

Figure 6.8. $PV^{5/3}$ in unit of $nPa(R_E/nT)^{5/3}$, B_Z (nT) and plasma pressure along X-axis, for times T=0 (black dotted), 30 (black solid), 31 (blue solid), 32 (yellow solid), 33 (green solid), 34 (red solid), 36 (black dash-dotted), 38 (blue dash-dotted), 40 (yellow dash-dotted), 45 (green dash-dotted) and 50 (red dash-dotted) minutes. Four vertical lines are at X=-6.9 (green), -8.0 (blue), -10.0 (black) and -12.0 (red) R_E.

6.2.2 The change of $PV^{5/3}$, P and B_Z along the X-axis

Figure 6.8 shows the $PV^{5/3}$, B_Z and P along X-axis for different times. In the growth phase from T=0min (black dotted) to T=30min (black solid), adiabatic convection moves plasma from plasma sheet to the inner magnetosphere. The $PV^{5/3}$ value increases all the way along the X-axis, increasing substantially near the transition region from -7 to -12R_E. The magnetic field strength decreases significantly inside 10R_E and the plasma pressure builds up, but without buildup of pressure peak in the partial ring current.

After T=30 minutes, $PV^{5/3}$ begins to decrease locally in the azimuthal range from magnetic local time MLT=23.25h to MLT=0.75h. With the help of an enhanced westward electric field, the low $PV^{5/3}$ plasma gets injected into the geosynchronous region. The bubble rushes to push the high $PV^{5/3}$ plasma out of the way, leaving the almost unchanged low values of $PV^{5/3}$ (0.1 nPa(R_E/nT)$^{5/3}$) behind. Because of the injection of lower flux tube content plasma, the plasma pressure gradually decreases in the region outside -10R_E, and the injected plasma increases its pressure considerably in the vicinity of geosynchronous, resulting in a partial ring current with more than doubled plasma pressure at T=50min. The magnetic field gradually dipolarizes outside -8R_E, well inside the bubble, but stretches in the region well earthward of the partial ring current, because the westward partial ring current depresses the magnetic field B_Z component.

Figure 6.9 illustrates the details of the change of the magnetic field B_Z component and the plasma pressure P with respect to end of the growth phase (T=30min), as related to the profile of $PV^{5/3}$ along X-axis. The results suggests that there are four regions: (1) near the tail boundary region (e.g., near the red line), where the magnetic field dipolarizes associated with the plasma pressure decrease and major entropy reduction well inside the bubble; (2) in the partial ring current vicinity and earthward of the pressure peak (e.g., near the green line), where the plasma pressure builds up as a result of the bubble injection, and the magnetic field stretches in response to the westward partial ring current; (3) in the region from X~-9R_E to X~-11R_E, $PV^{5/3}$ increases slightly in the first ~5 minutes followed by a continuously drop to 0.1 nPa$(R_E/nT)^{5/3}$ when that region is embedded well inside the bubble. The magnetic field increases continuously, but the plasma pressure increases only in the first ~10 minutes, after which there is a small decrease; (4) in the region from X~-7.5R_E to X~-9R_E, $PV^{5/3}$ increases in the first ~10 minutes, but gradually decreases to 0.1 nPa$(R_E/nT)^{5/3}$, as the bubble's interior covers the region The change of plasma pressure is nearly always positive in this region, but B_Z decreases first and later increases.

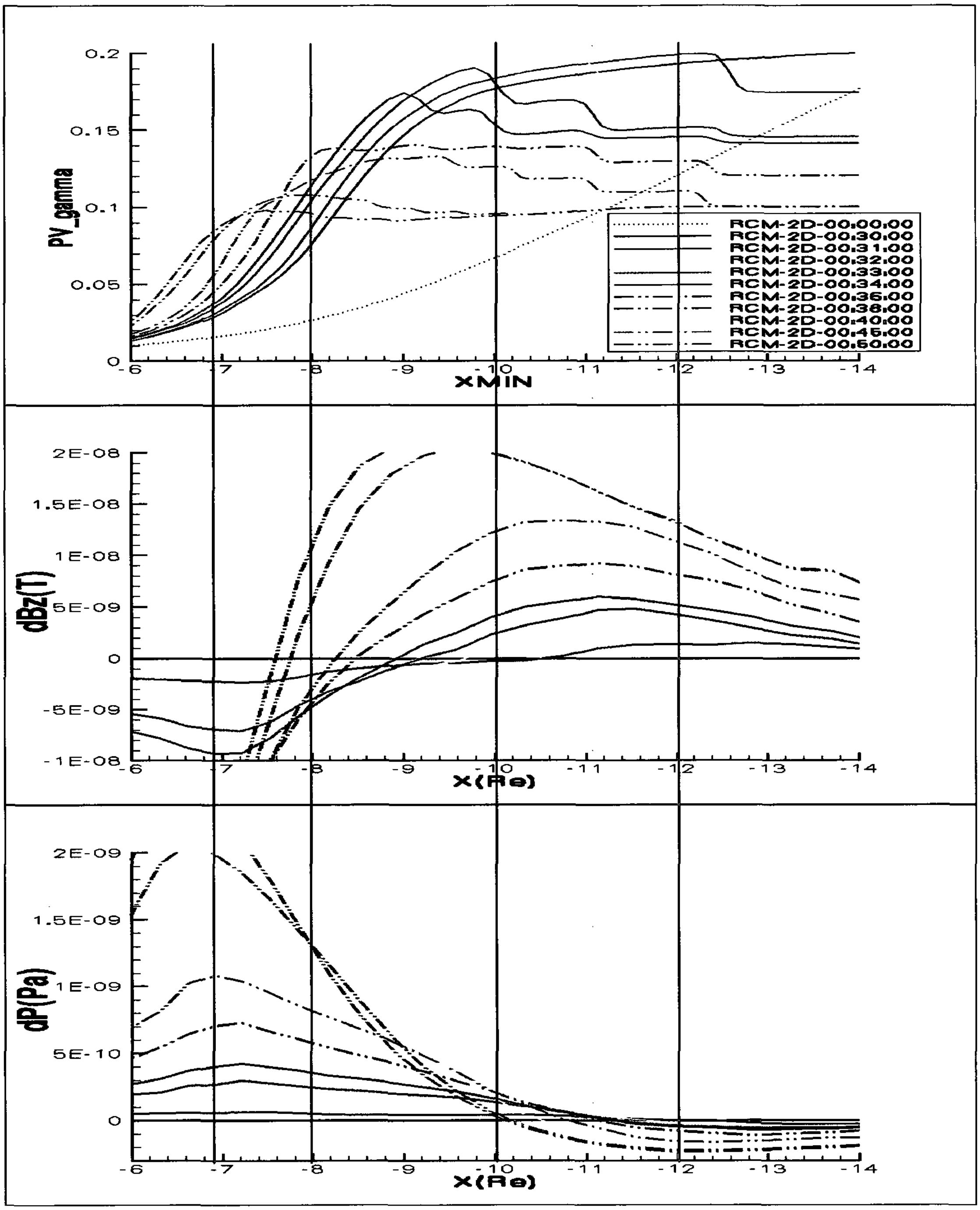

Figure 6.9. $PV^{5/3}$ in unit of $nPa(R_E/nT)^{5/3}$, change of B_Z and change of plasma pressure P with respect to end of the growth phase (T=30min) along X-axis, for times T=30 (black solid), 31 (blue solid), 32 (yellow solid), 33 (green solid), 34 (red solid), 36 (black dash-dotted), 38 (blue dash-dotted), 40 (yellow dash-dotted), 45 (green dash-dotted) and 50 (red dash-dotted) minutes. Four vertical lines are at X=-6.9 (green), -8.0 (blue), -10.0 (black) and -12.0 (red) R_E.

At T=34min (Figure 6.10), the bubble just gets injected to X~-13R$_E$ (region 1), where $PV^{5/3}$ has decreased significantly. As a result, plasma pressure decreases and the magnetic field dipolarizes. The plasma has higher $PV^{5/3}$ in the region around X~-10R$_E$ (region 2), which is pushed ahead of the bubble. The plasma is compressed, so that the plasma pressure increases and magnetic field increases very slowly and by a small amount. Further earthward, the region around X~-8R$_E$ (region 3) experiences higher $PV^{5/3}$ plasma, but the plasma pressure peak is still tailward of this region. Therefore, $PV^{5/3}$ increases slightly and plasma pressure begins to increase, but magnetic field becomes more stretched due to its location earthward of the enhanced partial-ring-current-like pressure peak. Near the innermost region at X~-6R$_E$ (region 4) the high $PV^{5/3}$ plasma is pushed inward, still well earthward of the bubble. Therefore, $PV^{5/3}$ and plasma pressure increase and the magnetic field stretches. Later, at T=38min (Figure 6.11), the bubble gets moves closer to the Earth and the high $PV^{5/3}$ plasma ahead of the bubble is pushed inward. At the outer most and the innermost regions, (regions 1 and 4) the changes of $PV^{5/3}$, P and B_Z follow the same trend as before. The pressure peak ahead of the bubble is pushed to the region around X~-10R$_E$ (region 2), thus both the $PV^{5/3}$ and P almost reach a maximum value, and the magnetic field continues to dipolarize. Earthward of the region, at X~-8R$_E$ (region 3), both $PV^{5/3}$ and P increase, but the magnetic field begins to dipolarize. As the bubble moves, reaching X~-8R$_E$ at T=43min (Figure 6.12), the partial ring current increases and the peak pressure is well inside 8R$_E$, thus P and B_Z increase and $PV^{5/3}$

increases to its maximum at X~-8R_E (region 3). The region at X~-10R_E (region 2), both $PV^{5/3}$ and P have dropped since the region is now well inside the bubble with depleted $PV^{5/3}$, where B_Z dipolarizes more and more. At time T=47min (Figure 6.13), the bubble well reaches geosynchronous orbit and the partial ring current is well formed with the peak just inside geosynchronous orbit. At this time, the sharp gradient of $PV^{5/3}$ is now pushed near and earthward of 6.6R_E and the enhanced $PV^{5/3}$ and P and the stretched B_Z start to level off in region 4. Close to the outer boundary (region 1), $PV^{5/3}$ and P reduce significantly and B_Z enhances to the dipole-like values. Tailward of the westward partial ring current, both X~-8R_E (region 3) and X~-10R_E (region 2) regions experience an increased B_Z, and the $PV^{5/3}$ at roughly the same level as the value at the tail boundary at 0.1 nPa$(R_E/nT)^{5/3}$, but the plasma pressure at X~-8R_E is larger.

In summary, the complexity of the time series of the change of key parameters, $PV^{5/3}$, P and B_Z, are critically related to the course of the bubble injection. These four regions experience considerably different sequences of reconfiguration. The details, both in spatial and temporal scale, are dependent on the location of these regions with respect to the region of partial ring current peak, the region well inside the bubble and the region just ahead of the bubble.

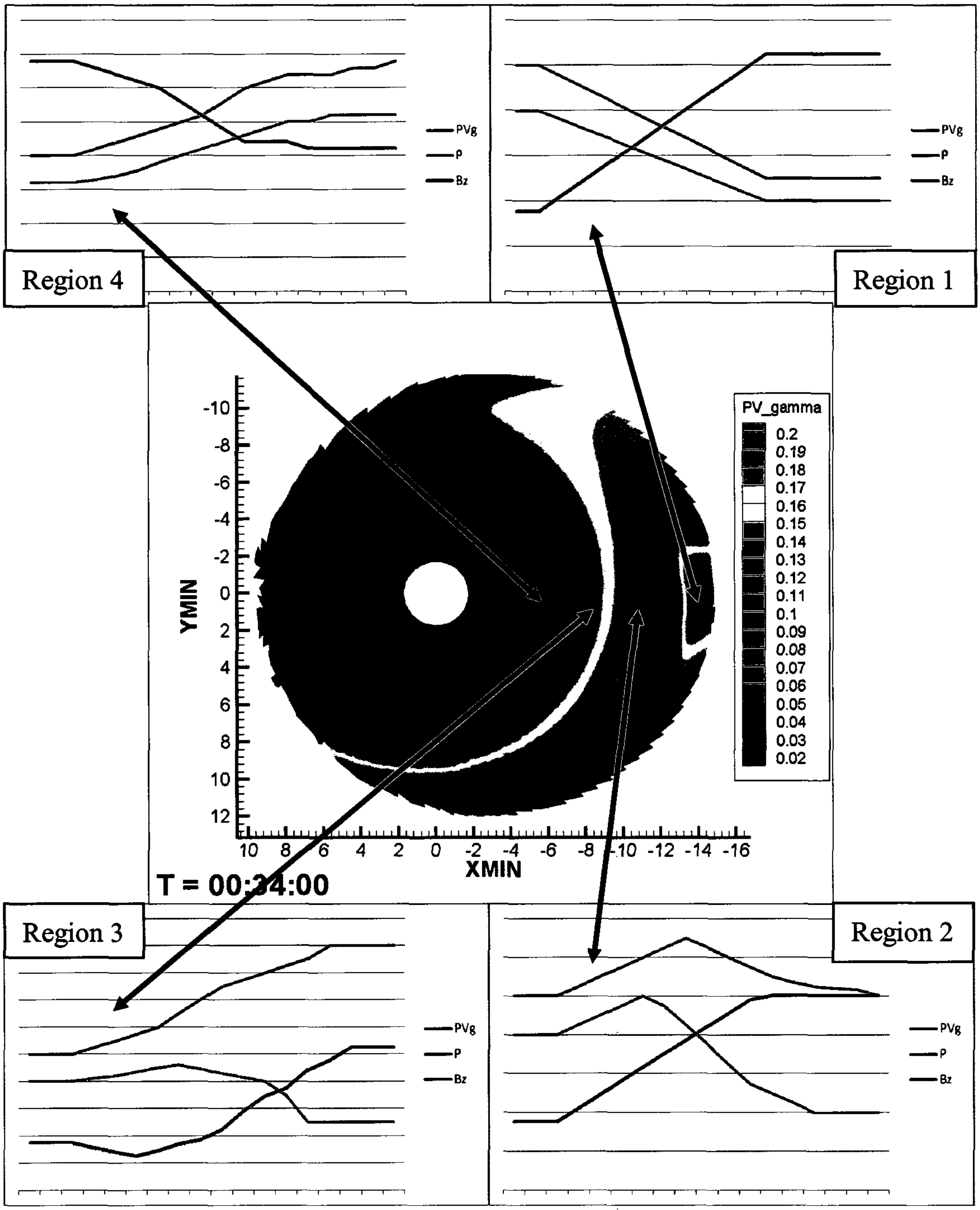

Figure 6.10. (center) $PV^{5/3}$ on the equatorial plane. (corners) Sketch of time dependence of $PV^{5/3}$ (blue), P (red) and B_Z (black) for four representative regions. Black double arrows point to the representative regions in the center plot and the values of key parameters in corner plots at time T=34min.

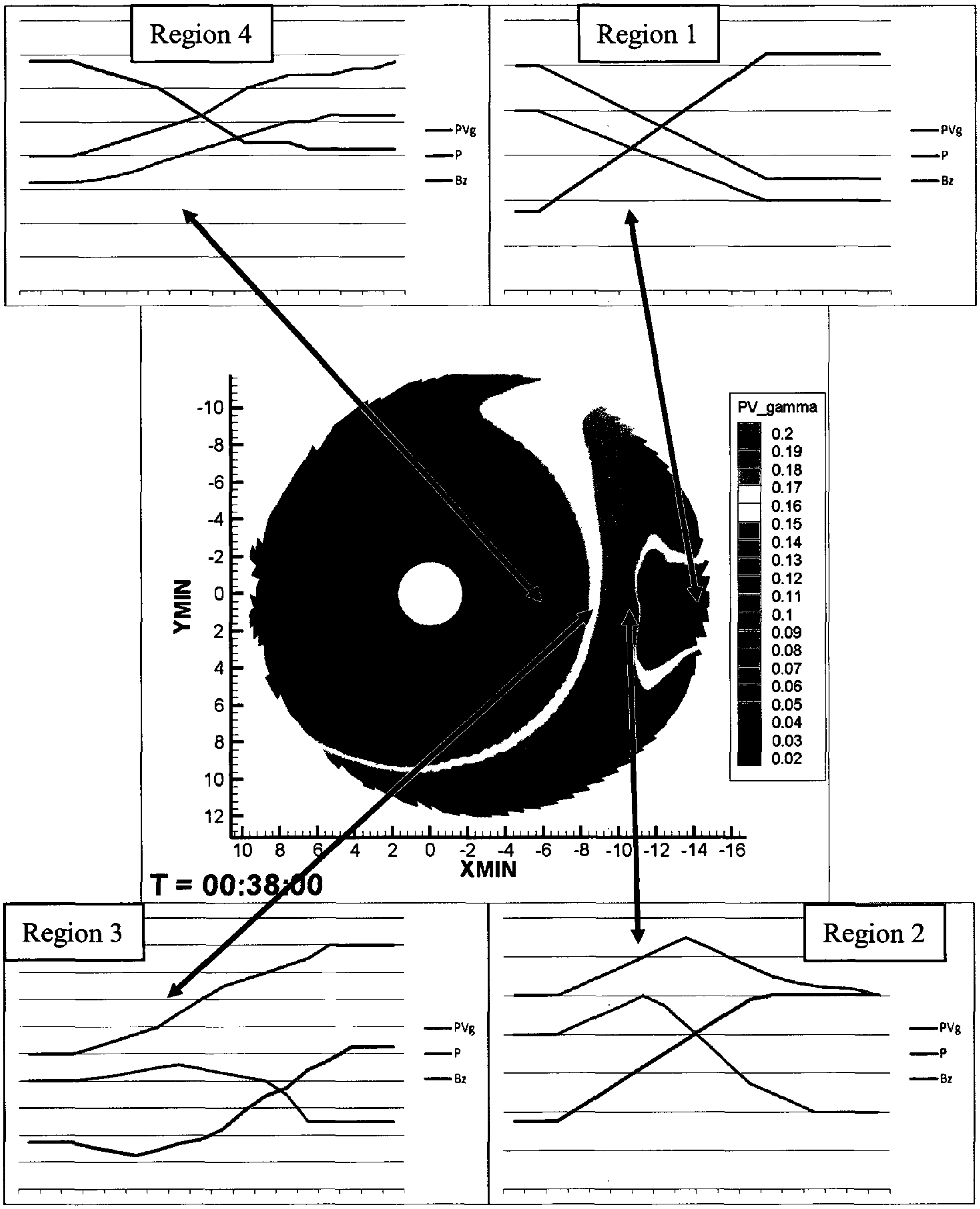

Figure 6.11. Similar to Figure 6.10, but for T=38min.

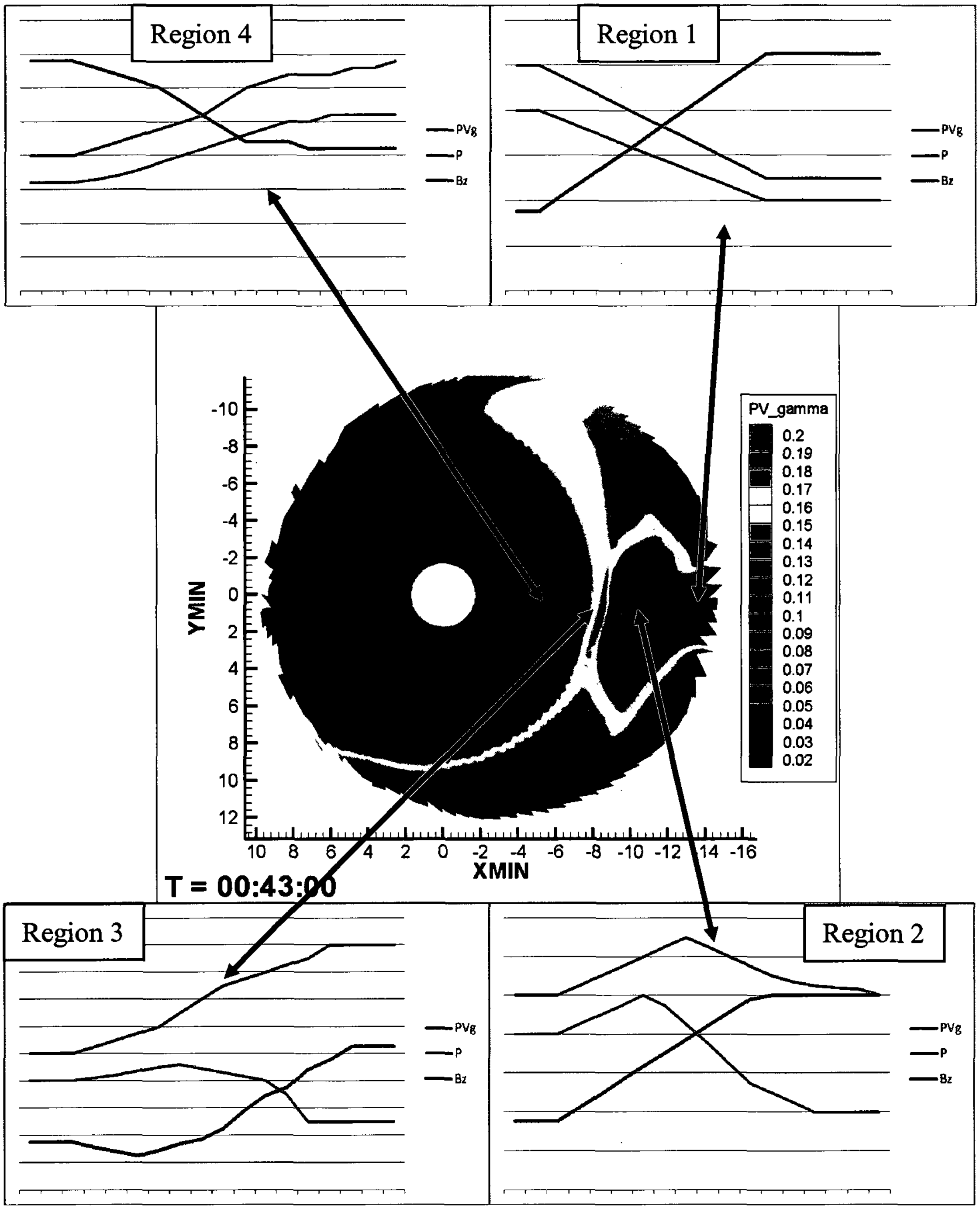

Figure 6.12. Similar to Figure 6.10, but for T=43min.

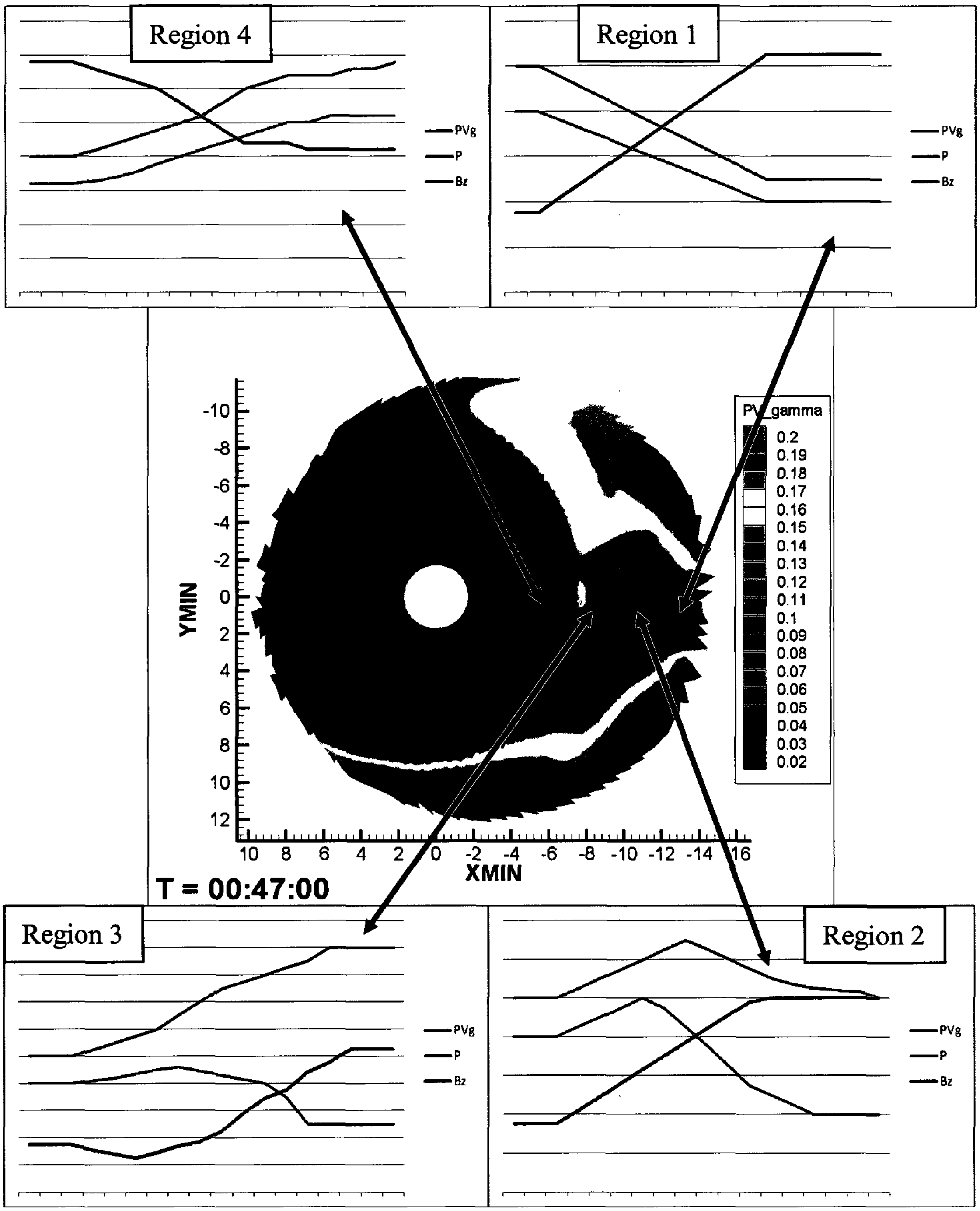

Figure 6.13. Similar to Figure 6.10, but for T=47min.

6.2.3 Contribution of higher energy particles

Figure 6.14 shows the ion pressure contributed by particles of energy less than 40keV (Pi_40keV, upper left) and by particles of energy greater than 40keV (Pi_40up, upper right) for different times. Due to the buildup of the partial ring current, both the pressures increase near the pressure peak from -6 to -8R_E, but the pressure from higher energy particles are increasing along the *X*-axis from inside the bubble to well inside geosynchronous orbit; while the pressure contribution from the lower energy particles actually decreases outside ~-8R_E. It has been suggested that the lower energy particle contribution to the pressure inside the bubble is lower than it is during growth phase, consistent with *Lyons et al.* [2003]. In the vicinity of the partial ring current region, the high energy particle pressure increases by a factor of 5, in contrast to only a 50% to 100% increase from the lower energy particle pressure. This result is more obvious 5~10 minutes later when the bubble reaches that region. The fraction of the high energy ion pressure (lower left plot), indicates that the >40keV ions can contribute as much as 60% to the total ion pressure in the inner magnetosphere at the peak of the ring current, which is a factor of 3 higher than that in the growth phase. Even in the near-Earth plasma sheet from -10 to -14R_E, the fraction can be up to 2 times larger than that in the growth phase. Because of the abundance of high energy ions, the ion temperature (lower right plot) nearly doubles in the transition region and enhances 50% in the plasma sheet. It has been found that higher energy particles can contribute more to the total plasma pressure during the substorm expansion phase than that during the growth phase or during quiet times [*Miyashita et al.*, 2008]. This was also seen in recent RCM simulations [*Zhang et al.*, 2009a, 2009b; *Yang et al.*, 2008]. The particle energization can be attributed to three factors: (1) the non-adiabatic heating outside the simulation region, represented by the lower-Kappa and higher-temperature plasma distribution placed on the high latitude boundary; (2) the enhanced electric field across the bubble channel; (3) the induced electric field due to the adiabatic collapse of the flux tubes. A useful further study would be to investigate the effect of each of these factors individually and quantitatively.

The ion differential fluxes shown in Figure 6.15 closely resemble kappa distributions. The peak of the distribution is in the range of 10keV to 50keV during the expansion phase (left plot). In addition, the main contribution to the expansion-phase partial ring current pressure at $6.6R_E$ comes from keV to tens of keV ions (right plot). This suggests that if we only consider the particle fluxes from the low energy particle instruments, which usually have 30-45keV energy limit (e.g., MPA on the LANL spacecraft, LEP on Geotail spacecraft, and ESA on the THEMIS spacecrafts) we may miss a plasma population that carries a significant fraction of the pressure [e.g., *Zhang et al.*, 2009a, 2009b; *Lui et al.*, 2009]. Therefore, including the higher energy LANL-SOPA, Geotail-EPIC and THEMIS-SST measurements is necessary in a substorm expansion phase study.

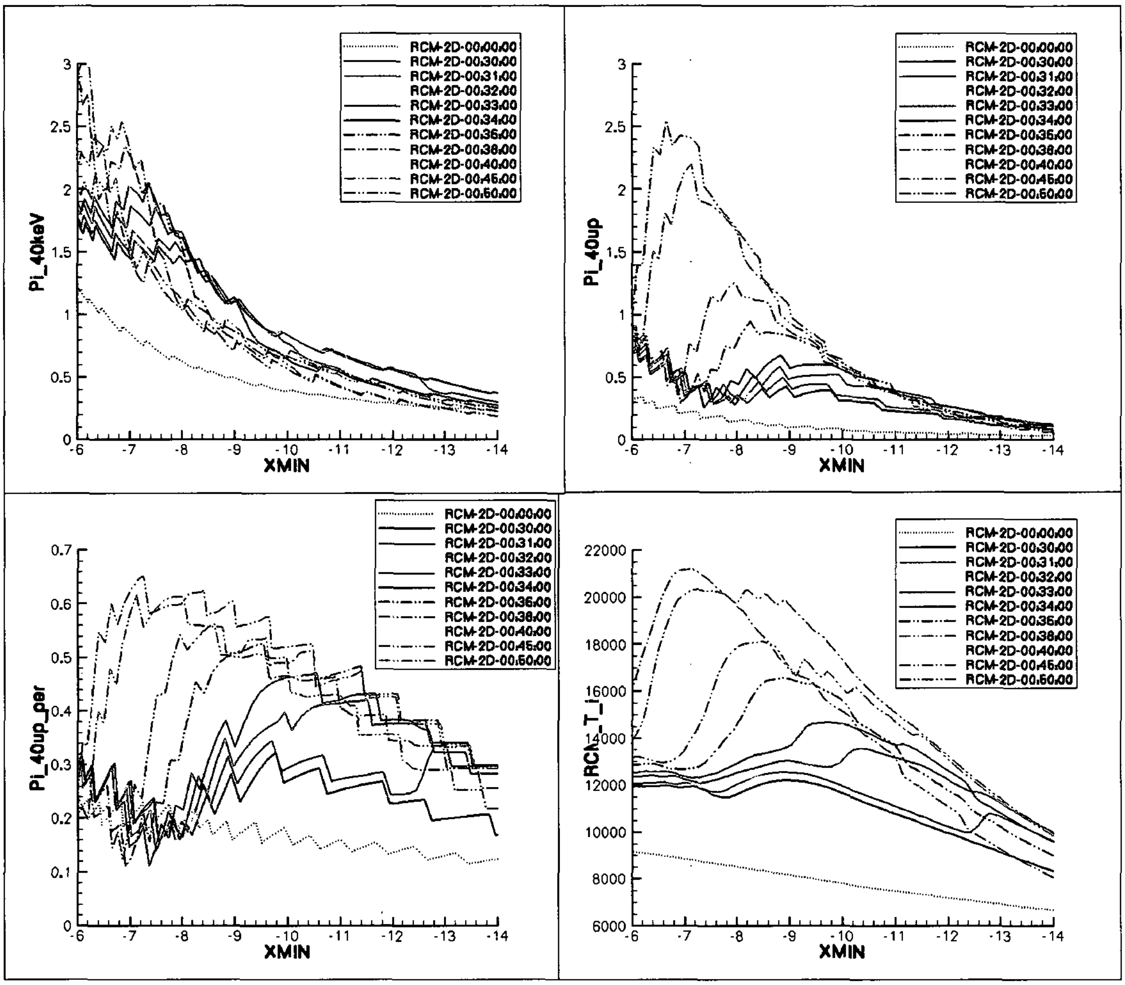

Figure 6.14. (upper left) Pi_40keV (partial pressure for <40keV ions) in unit of nPa, (upper right) Pi_40up (partial pressure for >40keV ions) in unit of nPa, (lower left) Pi_40up_per (fraction of partial pressure for <40keV ions to total ion pressure), (lower right) RCM_T_i (ion temperature) in unit of eV, along X-axis, for time T=0 (black dotted), 30 (black solid), 31 (blue solid), 32 (yellow solid), 33 (green solid), 34 (red solid), 36 (black dash-dotted), 38 (blue dash-dotted), 40 (yellow dash-dotted), 45 (green dash-dotted) and 50 (red dash-dotted) minutes.

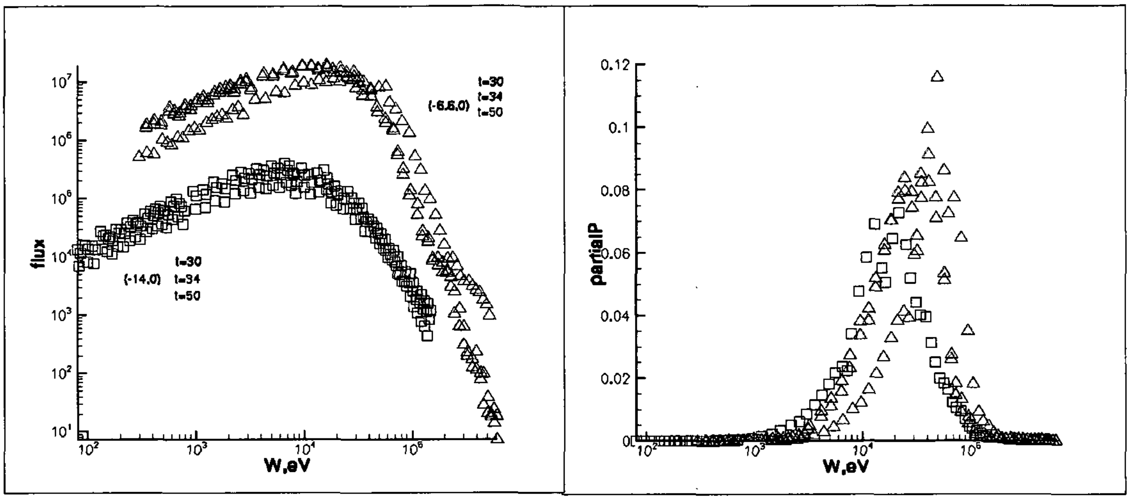

Figure 6.15. (Left) ion differential fluxes in unit of $cm^{-2}s^{-1}sr^{-1}keV^{-1}$ for each energy channel at (X, Y)=(-14, 0)R_E (lower left) and (X, Y)=(-6.6, 0)R_E (upper right) for T=30 (black), 34 (red) and 50 (blue) minute; (right) fraction of partial pressure to total ion pressure for each energy channel for different times at (X, Y)=(-6.6, 0.0)R_E.

6.3 RCM-E runs with different conditions

The basic features obtained in section 6.2 suggested co-existence of four regions with different time series of changes of entropy parameter $PV^{5/3}$, plasma pressure P and magnetic field B_Z along X-axis during the bubble injection event and demonstrated that the relatively high energy particles (>40keV) can contribute more than 50% to the total ion pressure in the RCM-E simulation during the expansion phase. One natural question is to ask how these basic features are dependent on the physical characteristics of bubbles. To answer this question, we have run the model with the following changes: (1) a different degree of the reduction of $PV^{5/3}$ on the high latitude boundary (section 6.3.1) and (2) with different IMF B_Z (section 6.3.2).

6.3.1 The degree of reduction of $PV^{5/3}$

The setup of this simulation is the same as the one described in section 6.2, except that the $PV^{5/3}$ is reduced to a smaller value, 0.04 nPa(R_E/nT)$^{5/3}$ at midnight, within the same 7 minutes (upper right plot of Figure 6.16). The changes along X-axis are similar to the previous run (see plots in the left column in Figure 6.16), but in this case the bubble penetrates closer to the Earth, as it continues to move until it is no longer interchange unstable. In this run, since there was a larger depletion of $PV^{5/3}$, the plasma pressure decreases more in the region well inside the bubble, which also results in a stronger magnetic field dipolarization. In the partial ring current region, the deeper penetration of the bubble results in a stronger dipolarization and larger energization of the particles, and both the pressure peak and the ion temperature are about 50% larger than those in the previous run.

The basic conclusion here is that the smaller sustained value of $PV^{5/3}$ in the bubble, the deeper it can penetrate into the inner magnetosphere until the bubble reaches the location that has roughly the same value of $PV^{5/3}$ as its own (suppose the bubble does not mix with the background), resulting in a stronger enhanced partial ring current and more dipolarized magnetic field. On the other hand, the four-region configuration discussed in section 6.3 still exists in this new run, but the boundaries between those regions are pushed inward.

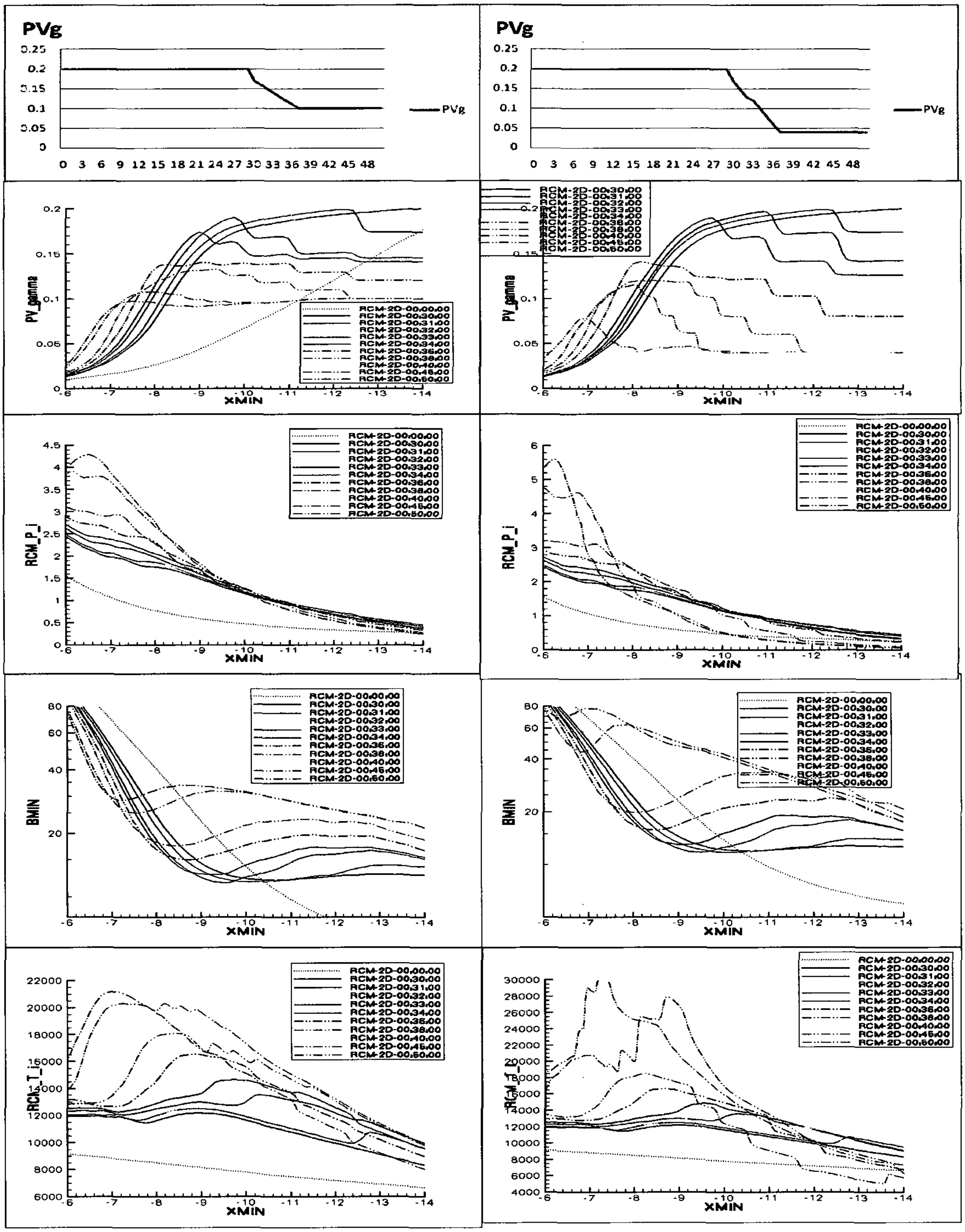

Figure 6.16. Two runs for different reduction of $PV^{5/3}$ (left for $(PV^{5/3})_{bubble}$=0.1, right for $(PV^{5/3})_{bubble}$=0.04) on the tail boundary at midnight and the resulting profiles of $PV^{5/3}$ in unit of nPa$(R_E/nT)^{5/3}$, ion pressure (RCM_P_i) in unit of nPa, B_Z (BMIN) in unit of nT and ion temperature (RCM_T_i) in unit of eV, along X-axis for different times.

6.3.2 Northward IMF B_Z

Substorms can occur during varying solar wind conditions. *Kamide et al.* [1977] showed that, statistically, the substorm occurrence probability increases as the IMF B_Z decreases (more southward), but substorms do occur even when IMF B_Z has a large northward component. In this section, we change the setup of the RCM-E model to mimic a northward IMF B_Z condition. The TM2003 and T96 models for setting up the initial condition are taken for IMF B_Z=+5nT, and other parameters are set as the same as those in section 6.2. Based on the *Boyle et al.* [1997] empirical formula, the polar cap potential drop for northward B_Z is set to only 17.6kV, much smaller than in southward IMF B_Z. The plasma boundary conditions for both growth and expansion phases are set by the same procedure, but applying a colder and denser plasma sheet as specified by the TM2003 model.

Figure 6.17 compares the runs with southward IMF B_Z=-5nT (left) and with northward IMF B_Z=+5nT (right). The configurations of the plasma and magnetic field are different at the end of the growth phase. Since convection for northward IMF B_Z is much weaker and the plasma is colder and denser, the model produces a more moderate transition region at a more tailward location with lower plasma pressure and ion temperature. With the same amount of $PV^{5/3}$ reduction but with a less concentrated electric field (the PCP drops are different), the bubble injection only reaches X=-9~-10R$_E$ associated with ~1 nPa peak value of partial ring current about 2R$_E$ outside the geosynchronous orbit. The four-regions discussed earlier exist in this run, but the changes in each of the key parameters are relatively small.

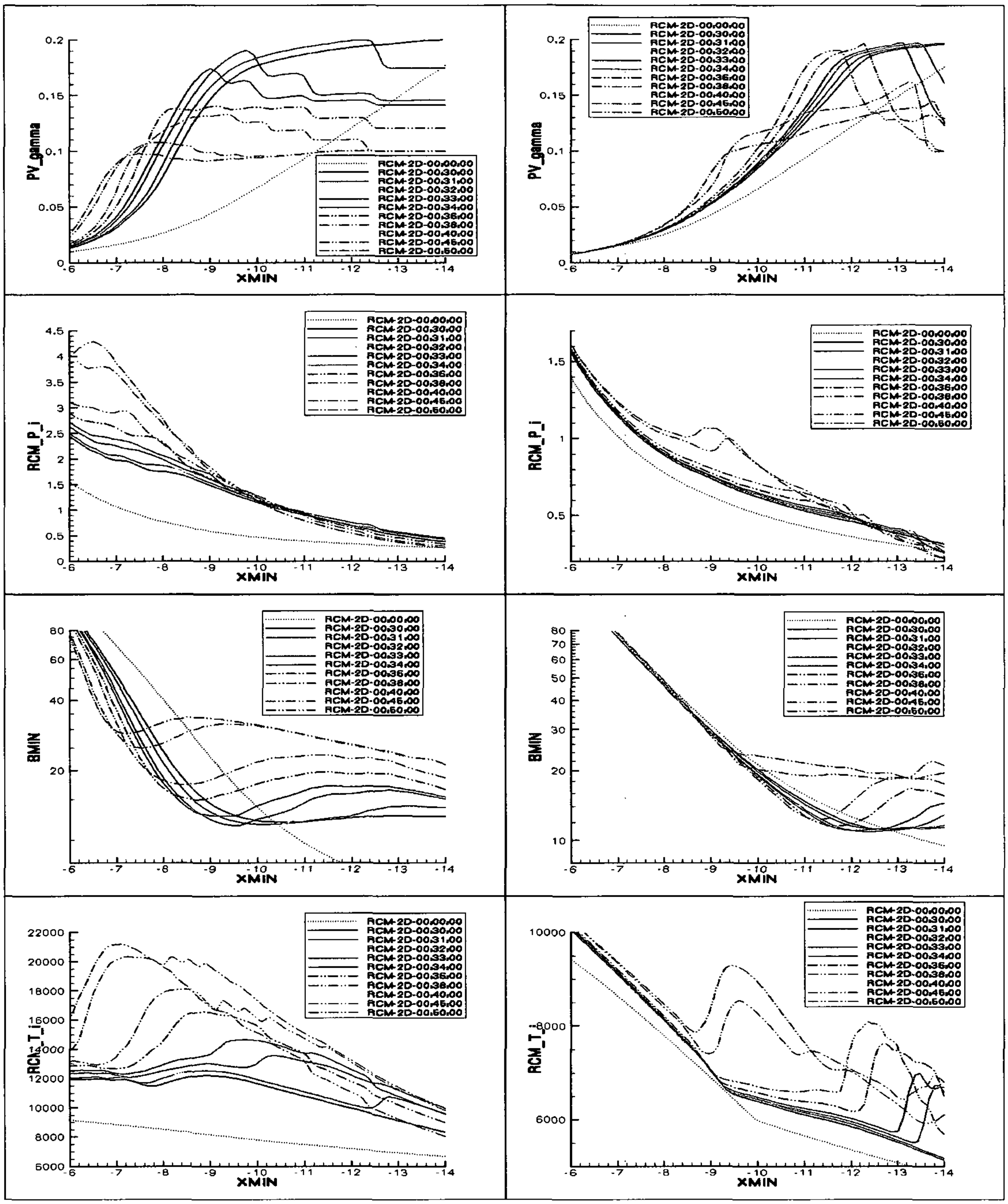

Figure 6.17. Two runs for IMF B_Z=-5nT (left) and IMF B_Z=+5nT (right) conditions and the resulting profiles of $PV^{5/3}$ in unit of nPa$(R_E/nT)^{5/3}$, ion pressure (RCM_P_i) in unit of nPa, B_Z (BMIN) in unit of nT and ion temperature (RCM_T_i) in unit of eV, along X-axis for different times.

6.4 Conclusions

The RCM-E simulations of idealized bubble injections were modeled by placing a depleted $PV^{5/3}$ along high-latitude boundary localized near the midnight. We found several basic features, listed below:

(1) We have carefully studied the time variation in the key parameters P, $PV^{5/3}$, and B_Z that should theoretically be observed by a near-equatorial spacecraft as it encounters a bubble, and we found the behavior to be complicated.

(2) Part of the complexity is due to the fact that the spacecraft may encounter plasma that is pushed earthward ahead of the bubble as well as the bubble itself.

(3) More severe reduction of the entropy in the center of the bubble tends to move features more earthward and increase the peak pressure more remarkably.

(4) Conditions of northward IMF, rather than southward, move the spatial features outward and distort them.

(5) The simulation suggests that high energy particles (e.g., >40keV) can contribute more than half of total plasma pressure during the expansion phase near the peak of partial ring current. The ion temperature can rise to as high as 20~30keV at geosynchronous in the simulations.

The reviews of observations suggest both the magnetic field dipolarization accompanied with plasma pressure depletion in the tail and magnetic field depression close to the Earth accompanied with a pressure buildup near geosynchronous orbit.

However, near the transition region, the relationship of B_Z and P can be quite complicated and sometimes the change of B_Z and P can be in the similar trend in short time scale. The ideal test of the simulation against data is to find an event with the four regions co-existing that is observed by aligned spacecraft near the center of the current sheet. Data from the THEMIS mission is a candidate for this.

The interesting features are obtained from careful analysis of initial results of idealized bubble injections based on RCM-E simulations. However, it is limited in the following aspects:

(1) The particle drift calculation neglects the inertial drift, and correspondingly the current calculation neglects the inertial current. Therefore, some features of observations, which usually exhibits large-amplitude and low-frequent wave-like structures, are excluded in our model.

(2) In this study, we have only investigated the reconfigurations of key parameters, e.g., P, $PV^{5/3}$ and B_Z component, and only along the X-axis. The changes in Y- and Z-directions remain for future study.

(3) It should also be noted that the substorm bubble injection is modeled by depleting the $PV^{5/3}$ only on the high latitude boundary at X=-15R$_E$, which is likely adapted from the NENL scenario. The non-adiabatic reduction of $PV^{5/3}$ in the CD scenario probably happens in the transition region at X=-7~-12R$_E$ [e.g., *Lui et al.*, 1992; *Wolf et al.*,

2009]. The simulation of the CD related mechanism in our model is one that will be left for future study.

Chapter 7

Superposed epoch study of $PV^{5/3}$ during substorms, pseudo-breakups and convection bays and associated RCM-E simulations

We have used a superposed epoch study to examine the changes in the entropy parameter $PV^{5/3}$ for 57 isolated substorms, 17 pseudo-breakups and 10 convection bays observed by Geotail in the near plasma sheet region. It is found that the entropy changes for all these processes are distinct: (1) for substorms, $PV^{5/3}$ increases continuously during the growth phase, decreases after dipolarization, and maintains a low value of about 0.08 nPa$(R_E/nT)^{5/3}$; (2) for pseudo-breakups, $PV^{5/3}$ changes in a way similar to substorms, but decreases more moderately and then gradually increases; (3) for convection bays, $PV^{5/3}$ maintains a nearly constant value of about 0.06 nPa$(R_E/nT)^{5/3}$ for an extended period. Three self-consistent simulations using the RCM-E were conducted to model an idealized substorm expansion, a pseudo-breakup and a convection bay event. Substorm expansion is modeled by placing a sustained low $PV^{5/3}$ plasma boundary condition along the near-Earth boundary, resulting in a poleward expansion of the polar boundary, a large-scale and continuous dipolarization of the magnetic field and a significant buildup of the partial ring current. The pseudo-breakup is modeled by enforcing a transient depleted $PV^{5/3}$ boundary condition, which only generates very limited and localized effects on both the magnetic field and plasma pressure inside the bubble. The convection bay event is modeled by specifying the low $PV^{5/3}$ condition further out in the plasma sheet for about ~2 hours, which introduces an enhanced partial ring current but results in a dipole-like magnetic field in the near-Earth region. The simulations are roughly consistent with the superposed epoch results in the near-Earth plasma sheet along with some other observations. These results suggest that the characteristics of the process that violates $PV^{5/3}$ conservation, such as magnetic reconnection in the magnetotail, play a central role in the temporal and spatial reduction of $PV^{5/3}$ and thus determine the mode of earthward plasma transport during active times.

7.1 Introduction to pseudo breakup and convection bay events

A pseudo-breakup occurs during the substorm growth phase, between several minutes and tens of minutes prior to the substorm onset, and is usually believed to be more localized [*Baker et al.*, 1996] and less intense [*Koskinen et al.*, 1993] than onset. It is distinct from the substorm expansion phase primarily because the activities in pseudo-breakup do not immediately lead to a full expansion of aurora, yet it is also similar to a substorm expansion phase in several features, including localized magnetic field dipolarization, an increase of energetic particle fluxes and the formation of a wedge-like current system in the ionosphere [*Koskinen et al.*, 1993]. A pseudo-breakup is interpreted in the Near-Earth-Neutral-Line (NENL) model as an insufficient and interrupted energy release tapped by very localized magnetic reconnection triggered by certain instabilities in the plasma sheet, such that it never reaches some critical threshold for lobe field reconnection [*Baker et al.*, 1996]. In the current disruption model, a pseudo-breakup happens when local turbulence triggers current reduction in the near-Earth tail, but the spatial scale of this initial disruption does not meet the global constraint [*Ohtani et al.*, 1993; *Lui*, 1996]. Therefore, a growth phase is not necessarily accompanied with pseudo-breakup. Following a pseudo-breakup, the magnetosphere continues in a growth phase until the system reaches substorm onset.

A convection bay event occurs during an enhanced earthward convection interval, usually lasting for 1~2 substorm timescales (3~4 hours), and is directly driven by continuous southward IMF B_Z, but lacks definite substorm-expansion-related activities [e.g., *Pytte et al.*, 1978, *Sergeev et al.*, 2001]. Shorter isolated bay intervals (<1 hour) have also been reported by *Pellinen et al.* [1982] and *Sergeev et al.* [1998]. Longer enhanced convection intervals are referred as Steady Magnetospheric Convection (SMC) by *Sergeev and Lennartsson* [1988] (up to 10 hours) and *Sergeev et al.* [1996a] (>4-6 hours), although similar intervals less than 2 hours are also named as SMC events by *O'Brien et al.* [2002]. Intervals of enhanced convection are associated by enhanced westward and eastward electrojet activity in the auroral zone [*Sergeev and Lennartsson*, 1988], so that these intervals are selected by intense AU (a proxy of maximum strength of the eastward auroral electrojet) and AL (a proxy of maximum strength of the westward auroral electrojet) indices [e.g., *Pytte et al.*, 1978; *Sergeev and Lennartsson*, 1988; *Sergeev et al.*, 1998] or the threshold values of AE index (AE=AU-AL) [e.g., *Sergeev et al.*, 1996a; *O'Brien et al.*, 2002]. On the other hand, although the terms "steady convection" or "quasi-steady convection" are used as a characteristic description for either convection bays or SMCs, the magnetosphere in these intervals is never in a situation of absolute steady state, but is better characterized as one where there is a balance between dayside reconnection and nightside reconnection. Therefore, *DeJong et al.* [2008] suggested renaming these events as Balanced Reconnection Intervals (BRIs). Phenomena accompanying these events include narrow and soft particle injections and BBFs [*Sergeev et al.*, 2001], as well as localized ground disturbances [e.g., *Pytte et al.*, 1978, *Segeev et al.*, 2001], but have no indication of substorm expansion.

In this chapter, rather than investigating individual pseudo-breakup and convection bay events, we first present a superposed epoch study of estimated $PV^{5/3}$ for isolated substorms, pseudo-breakups and convection bays in section 7.2. Then in section 7.3, we present three corresponding idealized event simulations using the RCM-E with different time variations of $PV^{5/3}$ on the RCM's high latitude boundary, to see if our results are consistent with observations.

7.2 Superposed epoch study of $PV^{5/3}$

7.2.1 Approach and event selection

We utilize the formula developed by *Wolf et al.* [2006a] to estimate local plasma sheet $PV^{5/3}$, using Geotail data (see descriptions of the data and the method in section 2.4). All data were scaled to 12s time resolution.

We selected 57 substorms, 17 pseudo-breakups and 10 convection bays in this study from the Geotail observation during the years 1995-2005 (compiled by Dr. Gary Erickson, private communication, 2009). The selection criteria are based on: (1) a clear magnetic disturbance signature (e.g., sharp decrease of H component) on ground magnetometer(s), which is labeled as an onset, T=0; (2) a clear *in-situ* magnetic dipolarization within the region $-20<X_{GSM}<-6R_E$ observed by Geotail, associated with the ground magnetic signature; (3) proximity of Geotail to the center of the plasma sheet ($0<B_r/B_Z<4$) for most of the time (>90% of the data points) during -30min<T<30min, so that the method of estimating $PV^{5/3}$ is likely valid; (4) a relatively isolated event, i.e., no other event met the above criteria within the time period -30min<T<30min. The determination of the category of each event was based on the analysis of auroral development, the values of AE index and the time derivative of AL index [*O'Brien et al.*, 2002].

In this study, we are more interested in the change of the $PV^{5/3}$ than the absolute value of itself. Figure 7.1 shows the Geotail position in XY plane in GSM for each event. The size of each mark represents the absolute value of $\Delta PV^{5/3}$, which is the change of averaged $PV^{5/3}$ over time $0<T<20$min with respect to the averaged $PV^{5/3}$ over time $-20<T<0$min, i.e.,

$$\Delta PV^{5/3} = \overline{PV^{5/3}}(0\,\mathrm{min} < T < 20\,\mathrm{min}) - \overline{PV^{5/3}}(-20\,\mathrm{min} < T < 0\,\mathrm{min}) \tag{7.1}$$

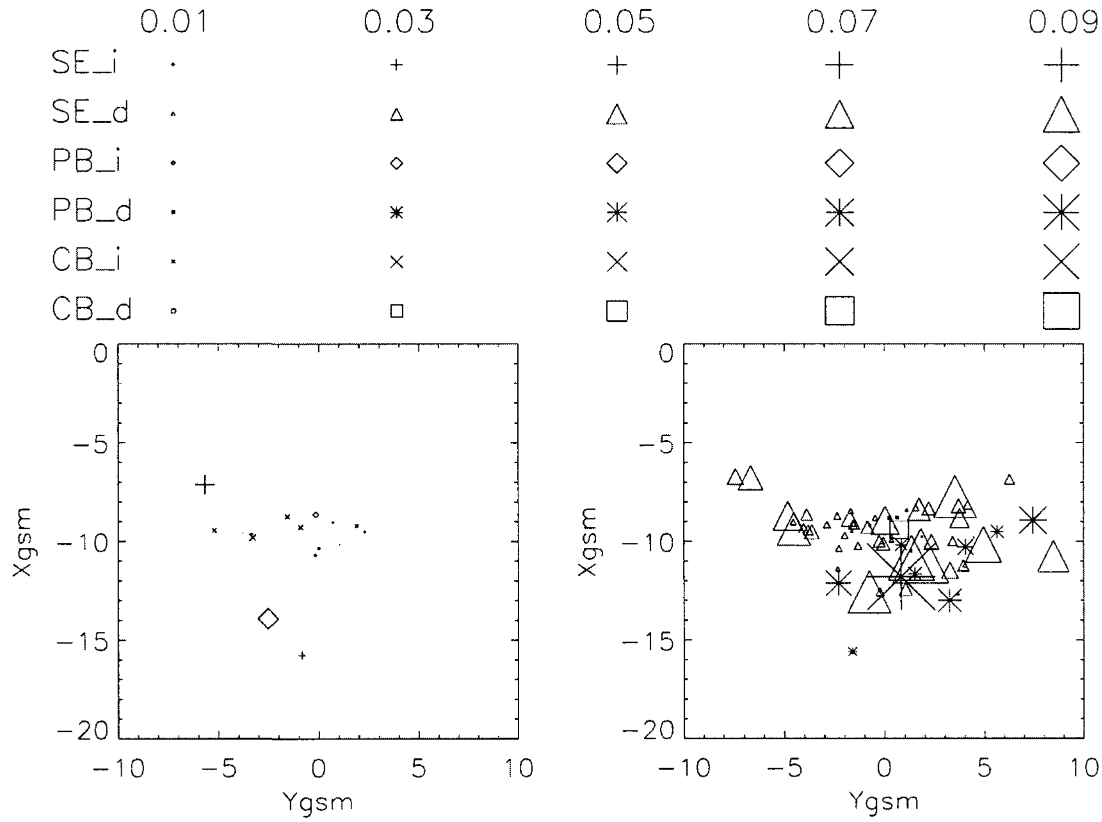

Figure 7.1. Geotail positions in the XY plane in GSM for each event at T=0. The size of each mark represents the absolute value of $\Delta PV^{5/3}$ (in units of $\mathrm{nPa}(R_E/\mathrm{nT})^{5/3}$) (see text for definition). The left and right plots show positive and negative $\Delta PV^{5/3}$ events respectively. Substorm expansions with $\Delta PV^{5/3}>0$ (SE_i) and $\Delta PV^{5/3}<0$ (SE_d), the pseudobreakups with $\Delta PV^{5/3}>0$ (PB_i) and $\Delta PV^{5/3}<0$ (PB_d), and convection bays with $\Delta PV^{5/3}>0$ (CB_i) and $\Delta PV^{5/3}<0$ (CB_d) are marked as pluses, triangles, diamonds, asterisks, crosses and squares, respectively.

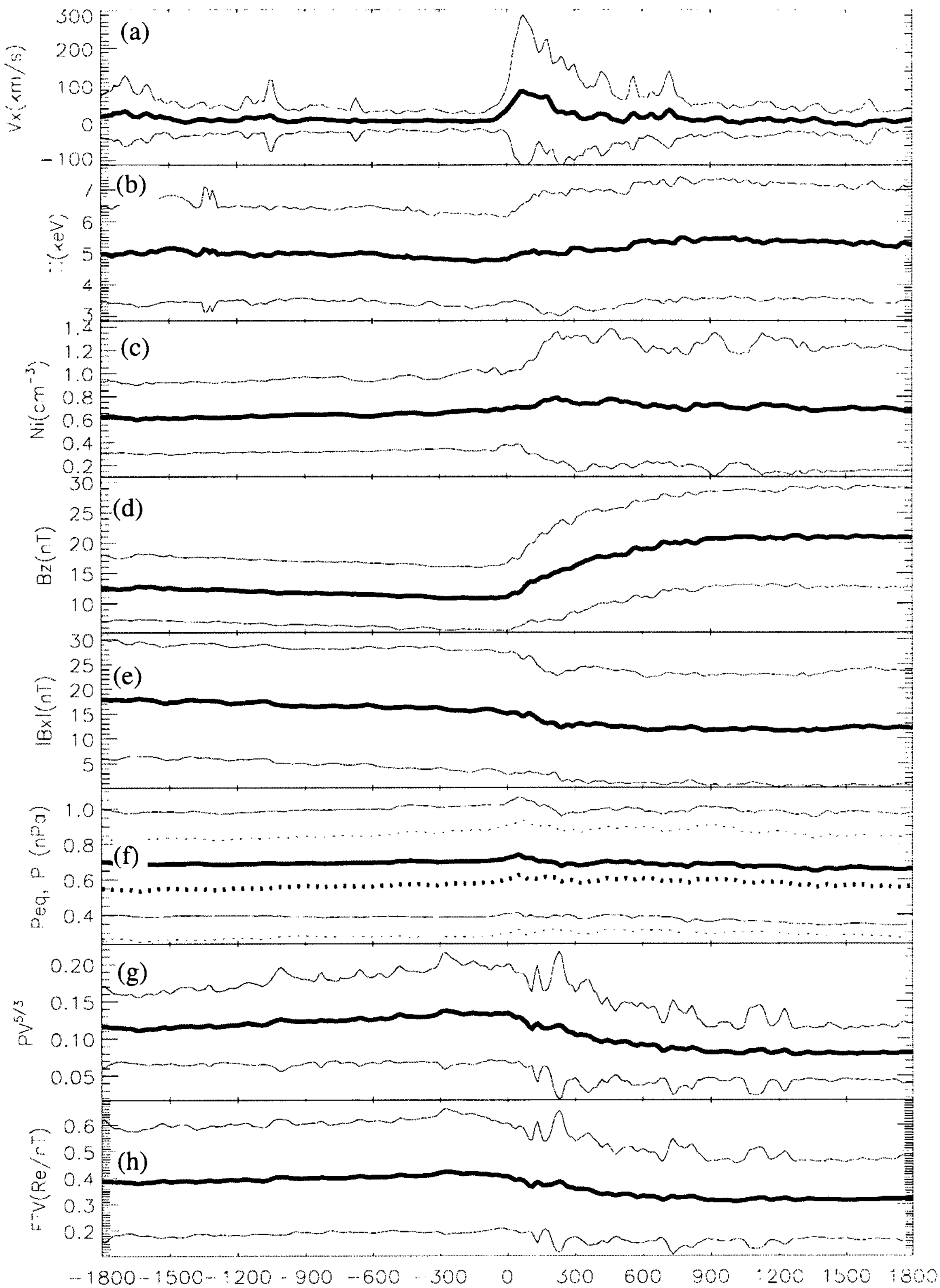

Figure 7.2. The superposed epoch (in GSM) parameters for 57 substorms. From top to bottom are (a) X-component of velocity, V_X; (b) ion temperature, T_i; (c) ion number

density, N_i; (d) Z-component of magnetic field, B_Z; (e) absolute value of X-component of magnetic field, $|B_X|$; (f) *in-situ* plasma pressure P (dotted line) and equatorial plasma pressure P_{eq} (solid line); (g) entropy parameter $PV^{5/3}$ in units of nPa$(R_E/nT)^{5/3}$; and (h) flux tube volume, FTV. The thick lines show the mean values, and the upper and lower envelopes in thin lines indicate the standard deviations. The bottom line represents the superposed time in seconds.

7.2.2 Substorm Expansion

Within the 57 substorm events, 6 of them show $\Delta PV^{5/3}>0$ (plus signs in the left plot of Figure 7.1); 51 of them show $\Delta PV^{5/3}<0$ (triangles in the right plot of Figure 7.1), which indicates that in most cases, $PV^{5/3}$ decreases during substorm expansion phase in the $-20<X<-6R_E$ region. Furthermore, it is evident that the increasing magnitude of $PV^{5/3}$ is rather small for these 6 $\Delta PV^{5/3}>0$ events, i.e., only one as large as 0.05, others being smaller than 0.02; many of the 51 $\Delta PV^{5/3}<0$ events exhibit considerably larger reductions, and 11 have $\Delta PV^{5/3}<-0.05$.

Figure 7.2 shows averaged parameters (thick lines) of the superposed epoch substorm in the GSM coordinate system along with the standard deviation (thin lines). Several features that are closely related to the change of $PV^{5/3}$ are as follows. (1) The earthward flow (Figure 7.2a), magnetic field dipolarization (Figure 7.2d and 7.2e), reduction of $PV^{5/3}$ (Figure 7.2g) and V (Figure 7.2h) are approximately coincident. (2) During the growth phase, $PV^{5/3}$ and V increase slightly as a result of magnetic field stretching, indicated as the decrease in B_Z in Figure 7.2d. (3) The reduction of $PV^{5/3}$ at onset is mainly attributed as the reduction of V in contrast to the almost unchanged P

(Figure 7.2f). (4) The reduction of $PV^{5/3}$ to 0.08 nPa(R_E/nT)$^{5/3}$ is gradual in the first 15 minutes after onset, followed by a leveling off. The variation of $PV^{5/3}$ during the superposed-epoch substorm is similar to the two isolated substorms presented by *Wolf et al.* [2006a], except that the individual substorms showed sharper decreases after onset than in the superposed epoch analysis.

7.2.3 Pseudo-breakups

Among 17 pseudo-breakups summarized in Figure 7.1, 2 of them show $\Delta PV^{5/3}>0$ with values of 0.05 and 0.02; the other 15 events show $\Delta PV^{5/3}<0$ with 8 being smaller than -0.03. Therefore, it is not surprising that $PV^{5/3}$ decreases after T=0 in the superposed results. Although the pseudo-breakup is similar to the substorm event in that the evident earthward flow and the significant magnetic field dipolarization take place simultaneously, there are also major differences. First, the magnitude of the increase in B_Z (from 12 to 16nT, Figure 7.3d) is much weaker than that in substorm (12 to 22nT, Figure 7.2d). Consequently, the reduction of $PV^{5/3}$ to 0.10 nPa(R_E/nT)$^{5/3}$ (Figure 7.3g) and V to 0.35 R_E/nT (Figure 7.3h) are weaker than the substorm values (down to 0.08 nPa(R_E/nT)$^{5/3}$ (Figure 7.2g) and 0.30 R_E/nT (Figure 7.2h)). Second, the noticeable decrease in B_Z and the increase in $|B_x|$ (Figure 7.3e) and roughly unchanged equatorial plasma pressure lead a slightly increasing trend of $PV^{5/3}$ after its minimum at about T=10min.

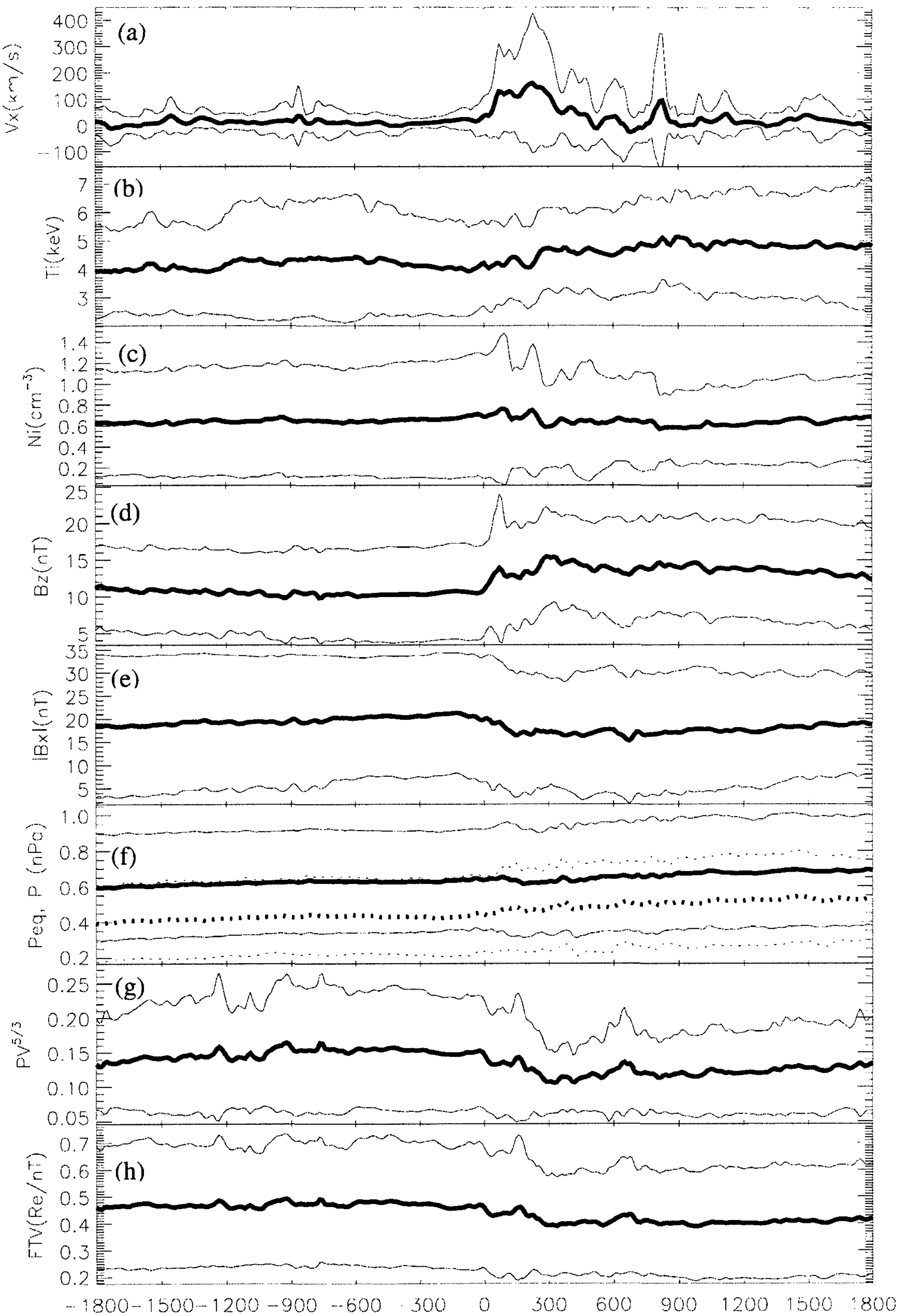

Figure 7.3. Same as Figure 7.2, but for pseudobreakups.

7.2.4 Convection bays

As shown in Figure 7.1, there are 9 convection bay events with $\Delta PV^{5/3}$~0.01 or less and one event with $\Delta PV^{5/3}$~-0.04. The superposed epoch result indicate a clear difference from both the substorms and pseudo-breakups, namely that the earthward flow (Figure 7.4a) associated with soft magnetic field dipolarization as shown as a increase in B_Z (Figure 7.4d) and a decrease in $|B_X|$ (Figure 7.4e) after T=0 is accompanied with approximately unchanged $PV^{5/3}$ (Figure 7.4g) and V (Figure 7.4h). Before and after the earthward flow and dipolarization, $PV^{5/3}$ maintains about the same low value near 0.06 nPa$(R_E/nT)^{5/3}$. The magnitude of both $|B_X|$ and B_Z are significantly larger than those in the superposed substorm and pseudo-breakup. Additionally, the magnitude of estimated equatorial plasma pressure (solid line in Figure 7.4f) is roughly similar to those in substorm and pseudo-breakups while the *in-situ* observed pressure (dotted line in Figure 7.4f) is only about half. This result is quite consistent with observations in a single event made by *Sergeev et al.* [2001], in which they concluded that the plasma sheet is thick during the convection bay intervals; therefore, the magnetic field is large associated with small local plasma pressure, and the low value $PV^{5/3}$ is a natural consequence.

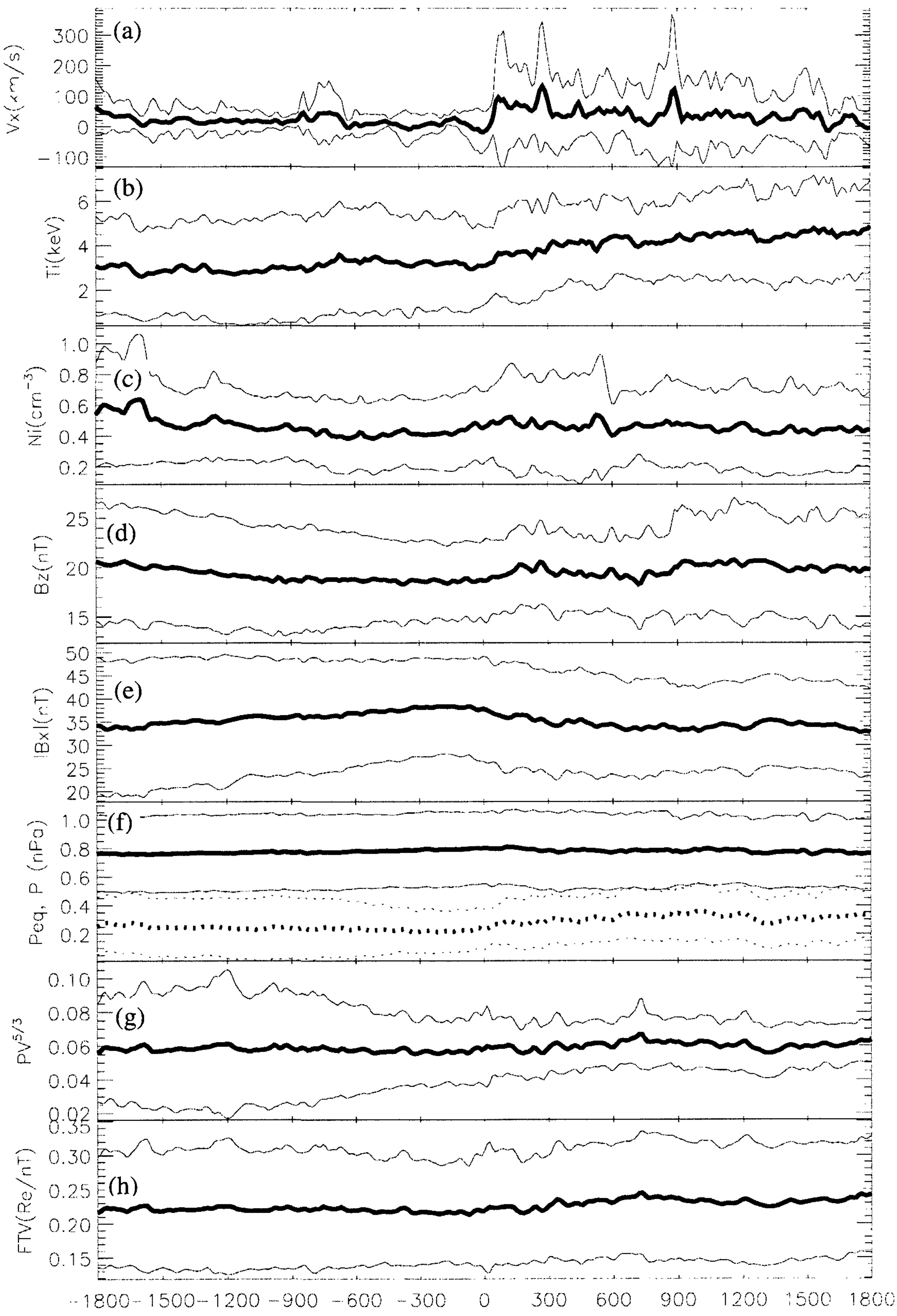

Figure 7.4. Same as Figure 7.2, but for convection bays.

7.3 The RCM-E simulations of idealized substorm expansion, pseudo-breakup and convection bay

The modeling approach is the same as what was described in section 6.2, but the depletion of the $PV^{5/3}$ on the high latitude boundary is designed to represent distinct depleted $PV^{5/3}$ plasma for the different types of events, i.e., a sustained bubble in the near-Earth plasma sheet for the substorm expansion phase (X=-15R$_E$), a transient bubble in the near-Earth plasma sheet (X=-15R$_E$) for pseudo-breakup, and sustained low $PV^{5/3}$ in the more tailward plasma sheet (X=-19R$_E$) for convection bay event.

7.3.1 The RCM-E simulation of idealized substorm expansion event

Figure 7.5 shows the entropy parameter $PV^{5/3}$ as a function of time at local midnight on the RCM high-latitude boundary. The reduction is significant from 0.2 to 0.04 within 4 minutes, and lasts at this small value for another 16 minutes. This time sequence of $PV^{5/3}$ resembles a continuous injection of a low entropy plasma bubble from magnetotail.

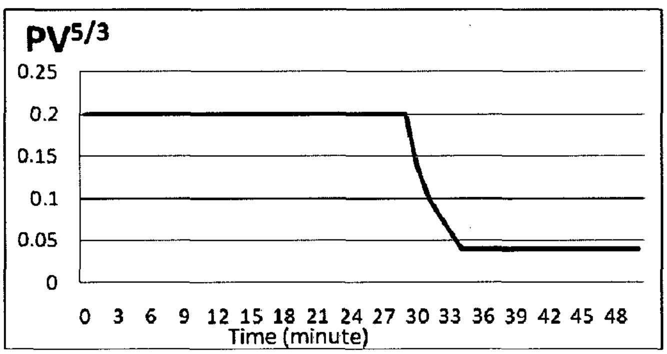

Figure 7.5. The entropy parameter $PV^{5/3}$ in units of nPa(R$_E$/nT)$^{5/3}$ on the midnight of high latitude boundary as a function of time (minutes) for the idealized substorm expansion phase run.

Figures 7.6 to 7.8 show the entropy parameter $PV^{5/3}$ ($nPa(R_E/nT)^{5/3}$), magnetic field B_Z component (nT) and plasma pressure P (nPa) on the equatorial plane respectively, and Figure 7.9 shows the Birkeland current densities ($\mu A/m^2$) in the ionosphere. T=00:00:00 in the figures denotes the end of the growth phase. In the first few minutes (T=00:00:00 to T=00:04:00) in the expansion phase, $PV^{5/3}$ on the boundary deceases sharply and the plasma bubble begins to move earthward but does not reach geosynchronous orbit. During this time period, the magnetic field dipolarizes near the tail boundary, and the plasma pressure does not increase noticeably, although FACs are seen near the poleward boundary in the ionosphere. When the bubble reaches the inner edge of the transition region near geosynchronous orbit around T=00:08:00, the plasma pressure shows a considerable enhancement, and begins to form a prominent partial ring current and the B_Z increases to 40 nT near X=-10R_E. The self-consistently calculated potential electric field concentrates well inside the bubble, while near the edges of the bubble, vortices of potential lines emerge which are associated with the downward and upward FACs flowing along the current wedges. In the ionosphere, the poleward motion of the high latitude boundary is about 3 degrees with intensified FACs. At T=00:12:00, the bubble has penetrated well inside geosynchronous orbit, the magnetic field dipolarizes and the partial ring current increases further. Around this time it seems that the poleward expansion has reached the maximum and stabilized. From T=00:12:00 until T=00:20:00, both the magnetic field dipolarization and the partial ring current peak and are stable; while the FACs begin to fade.

Although the simulation results presented here are a first try and preliminary, since it is difficult to determine the typical spatial and temporal characteristics of the depletion of $PV^{5/3}$ at X=-15R$_E$, it is still useful to compare the modeled results in the near-Earth region to the superposed epoch results at X~-10R$_E$ presented in section 7.2. The change of $PV^{5/3}$ in the superposed epoch study (Figure 7.2g) varies from 0.15 at the end of growth phase to 0.08, about 10~15 minutes after onset. A closer look at the Figure 7.6 shows that the $PV^{5/3}$ at X=~-10R$_E$ does change in a similar fashion as the superposed epoch study both in magnitude and the time scale. Analogously, the magnetic field B_Z component and the plasma pressure peak at X=~-10R$_E$ in the simulation rise to their almost stable maxima in about 5~10 minutes. Figure 7.7 shows that B_Z increases to ~40nT there, roughly consistent with the total magnetic field (including both B_X and B_Z) in Figure 7.2. An interesting feature in Figure 7.2 (f) is that the plasma pressure remains almost unchanged, which can also be seen in the simulation (Figure 7.8) since the partial ring current peak forms well inside geosynchronous orbit, and consistently the plasma pressure at X=~-10R$_E$ remains approximately unchanged before and after the bubble injection. The ionospheric view (Figure 7.9) shows that the FACs intensify in the auroral zone and the high-latitude boundary moves poleward for about 3~5 degrees, resembling the "expansion" feature of aurora.

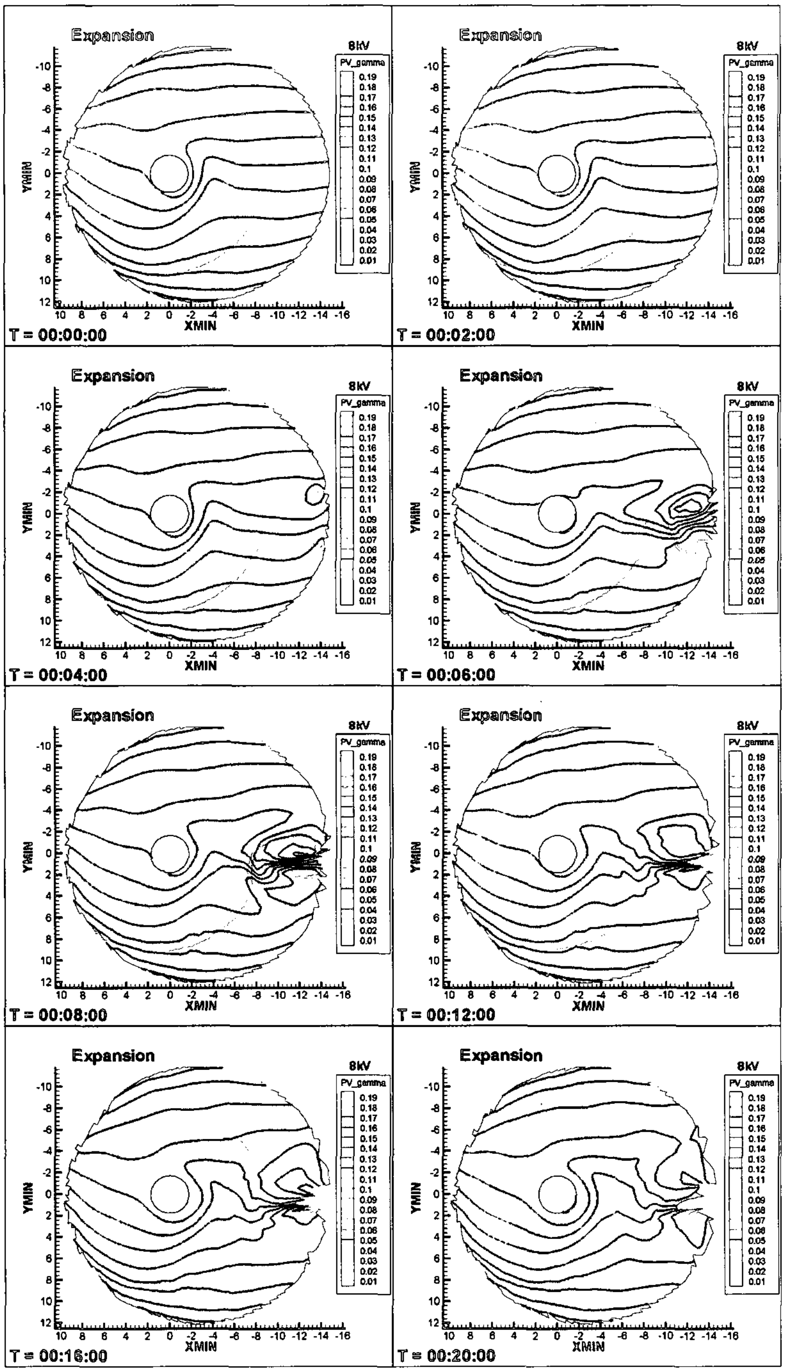

Figure 7.6. $PV^{5/3}$ in units of $nPa(R_E/nT)^{5/3}$ (color contours) on the equatorial plane and the electric equipotentials (black solid lines) every 8kV for 0 to 20 minutes in the idealized substorm expansion-phase run. The sun is to the left.

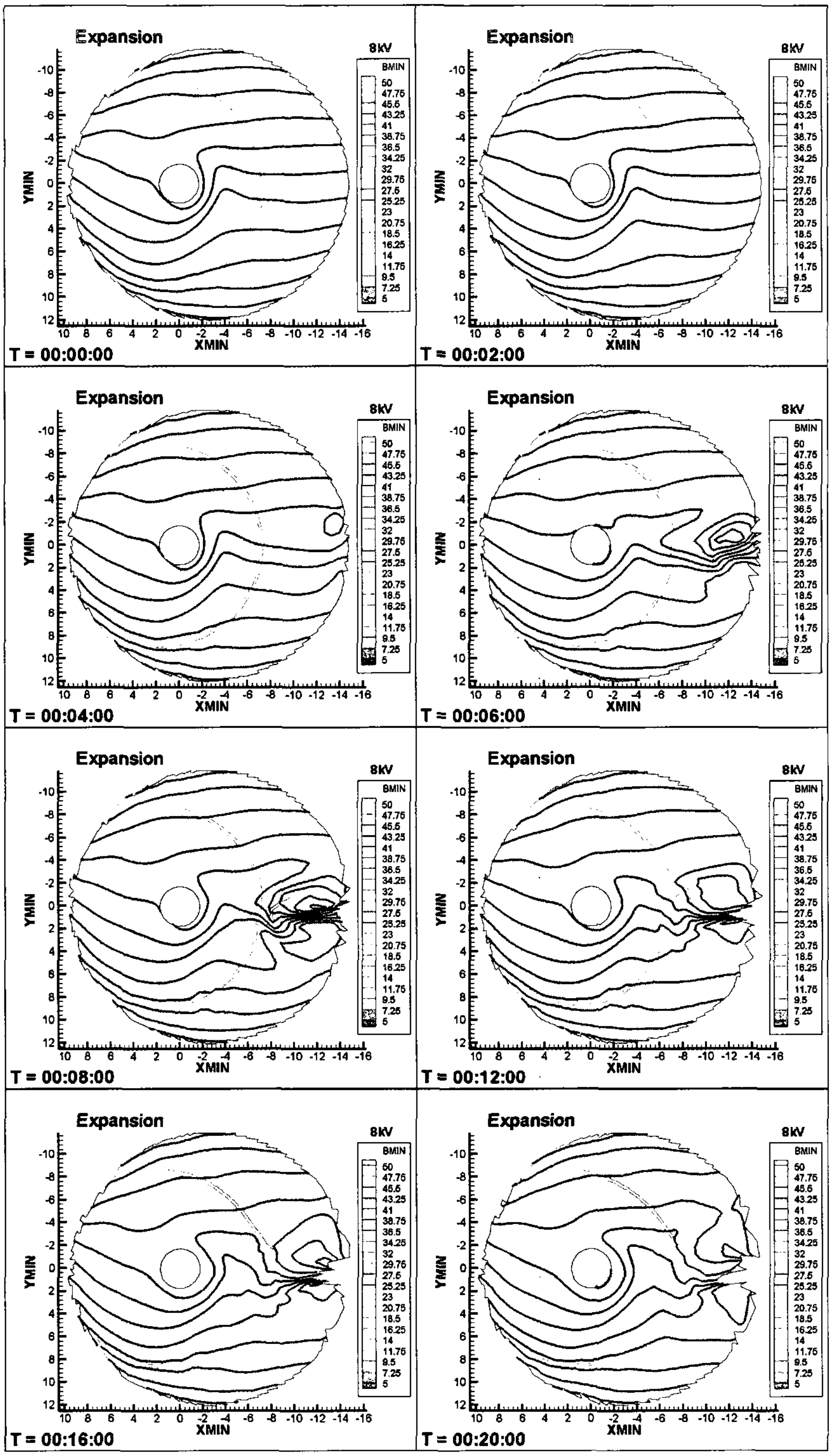

Figure 7.7. Similar to Figure 7.6, but for B_Z (nT).

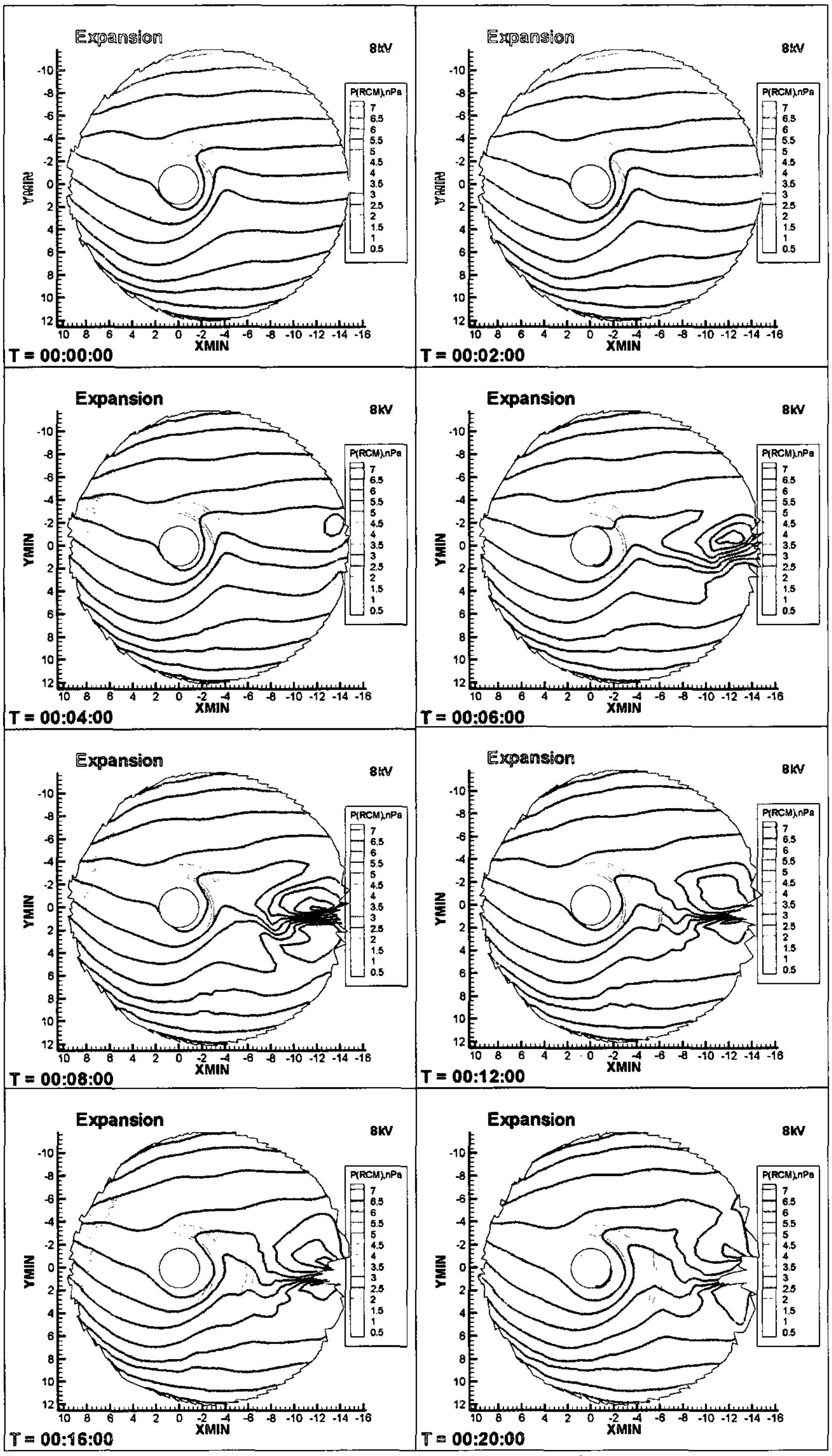

Figure 7.8. Similar to Figure 7.6, but for plasma pressure P (nPa).

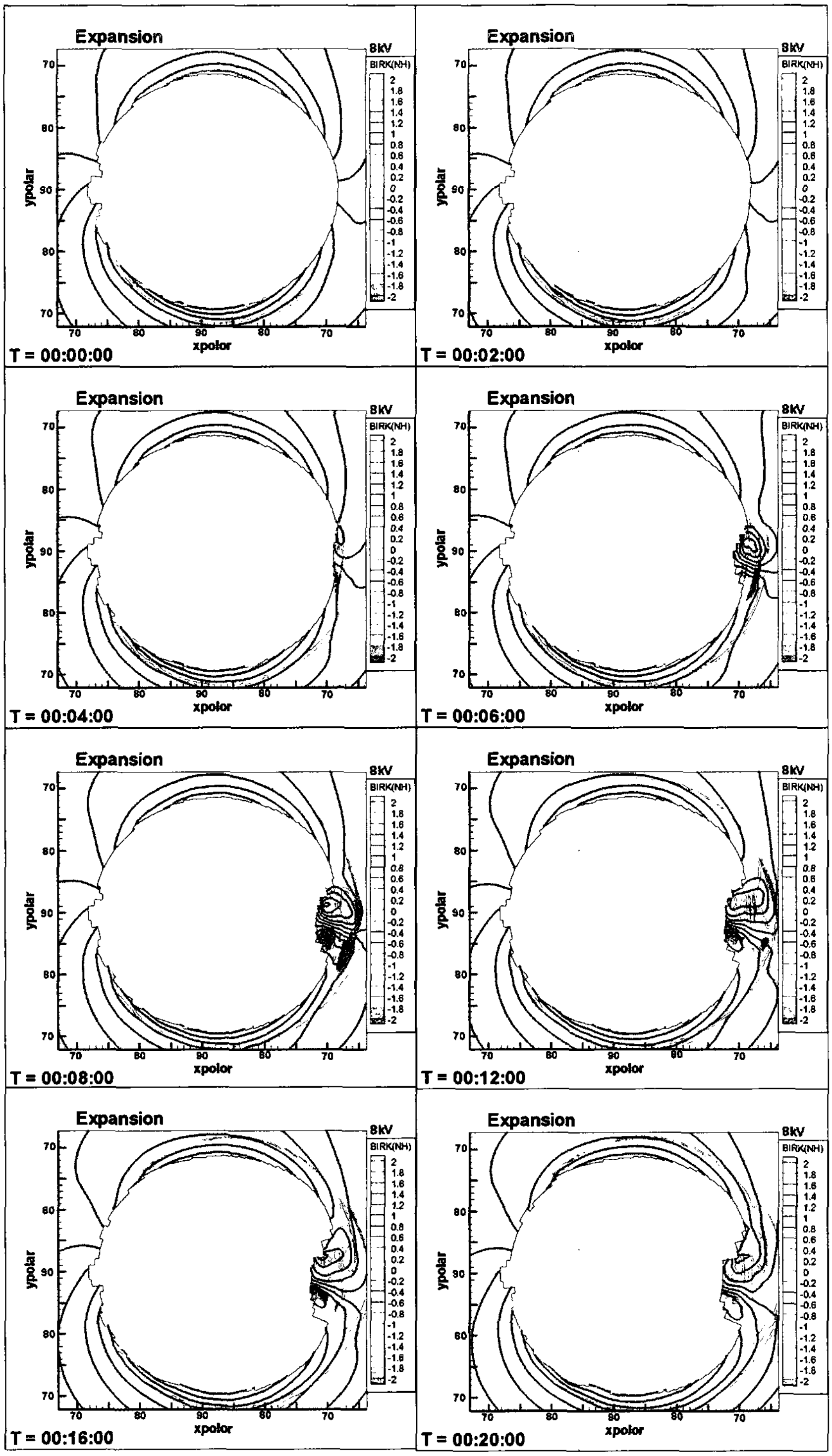

Figure 7.9. Birkeland current density in units of $\mu A/m^2$ (color contours) on the ionosphere and the electric equipotentials (black solid lines) every 8kV for different times in the idealized substorm expansion phase run. The sun is to the left.

7.3.2 The RCM-E simulation of idealized pseudo-breakup event

The setup for this simulation is the same as for the idealized substorm expansion run, except the depletion of $PV^{5/3}$, as shown in Figure 7.10, represents a transient bubble lasting for about 6 minutes on the high latitude boundary at X=-15R$_E$ near midnight.

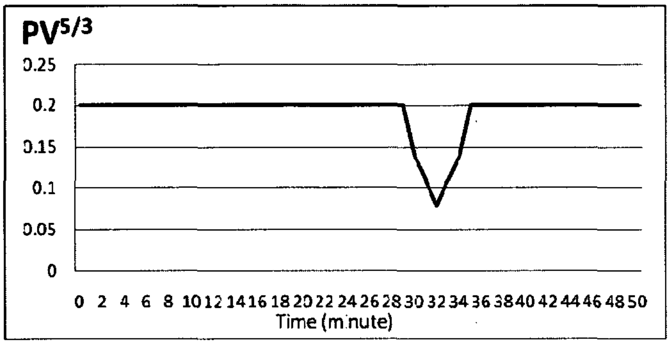

Figure 7.10. The entropy parameter $PV^{5/3}$ in units of nPa(R$_E$/nT)$^{5/3}$ on the midnight of high latitude boundary as a function of time (minutes) for the idealized pseudo-breakup event run.

Figure 7.11 clearly shows the track of the bubble emerging on the tail boundary and then being injected into the inner magnetosphere. The electric equipotential lines are squeezed just inside the bubble but by a very limited amount. The bubble causes a dipolarization of the magnetic field well inside the bubble, but almost no B_Z increase outside (Figure 7.12). The plasma pressure does enhance slightly near geosynchronous orbit (Figure 7.13). In the ionosphere, the poleward motion of the boundary is very limited, moving only about 1 degree in latitude, while the FACs intensify but also fade away quickly (Figure 7.14). These features are consistent with the observations shown by *Koskinen et al.* [1993] that plasma injection near geosynchronous orbit was soft or weak in pseudo-breakup events and the aurora did not fully expand.

Comparing the substorm expansion event run, this simulation demonstrates that a transient bubble injected into the inner magnetosphere will only have very localized and limited effects on the configuration of the inner magnetosphere. There is no sustained energy to power the inner magnetospheric reconfiguration, and to support the "expansion". An observer sitting at X=~-10R_E, who sees an earthward moving bubble, experiences distinct features of dipolarization. When the bubble is only transient, as modeled in the pseudo-breakup event run, the magnetic field tries to stretch again and $PV^{5/3}$ gradually increases to its pre-bubble value after the bubble has passed. It is interesting to note that, during a pseudo-breakup, there are clearly intensified region-1 sense FACs, which are connected to the edges of the bubble. These FACs, of course, will have an effect on ground magnetometers, but will be localized and will fade away quickly. In addition, as shown in Figure 7.14, a distinct feature of a pseudo-breakup is that there is no explosive expansion of aurora, as inferred by the FACs. The simulation results consistently reproduce the observations in a typical pseudo-breakup [*Koskinen et al.*, 1993]. In that event, the ground magnetometer did record a sharp decrease of horizontal component of magnetic field, but not a full-scale substorm-like expansion. The current system also had a weak wedge-like system near midnight sector. The *in-situ* observations also show local magnetic field dipolarization and energetic particle flux increases, which is consistent with our simulation.

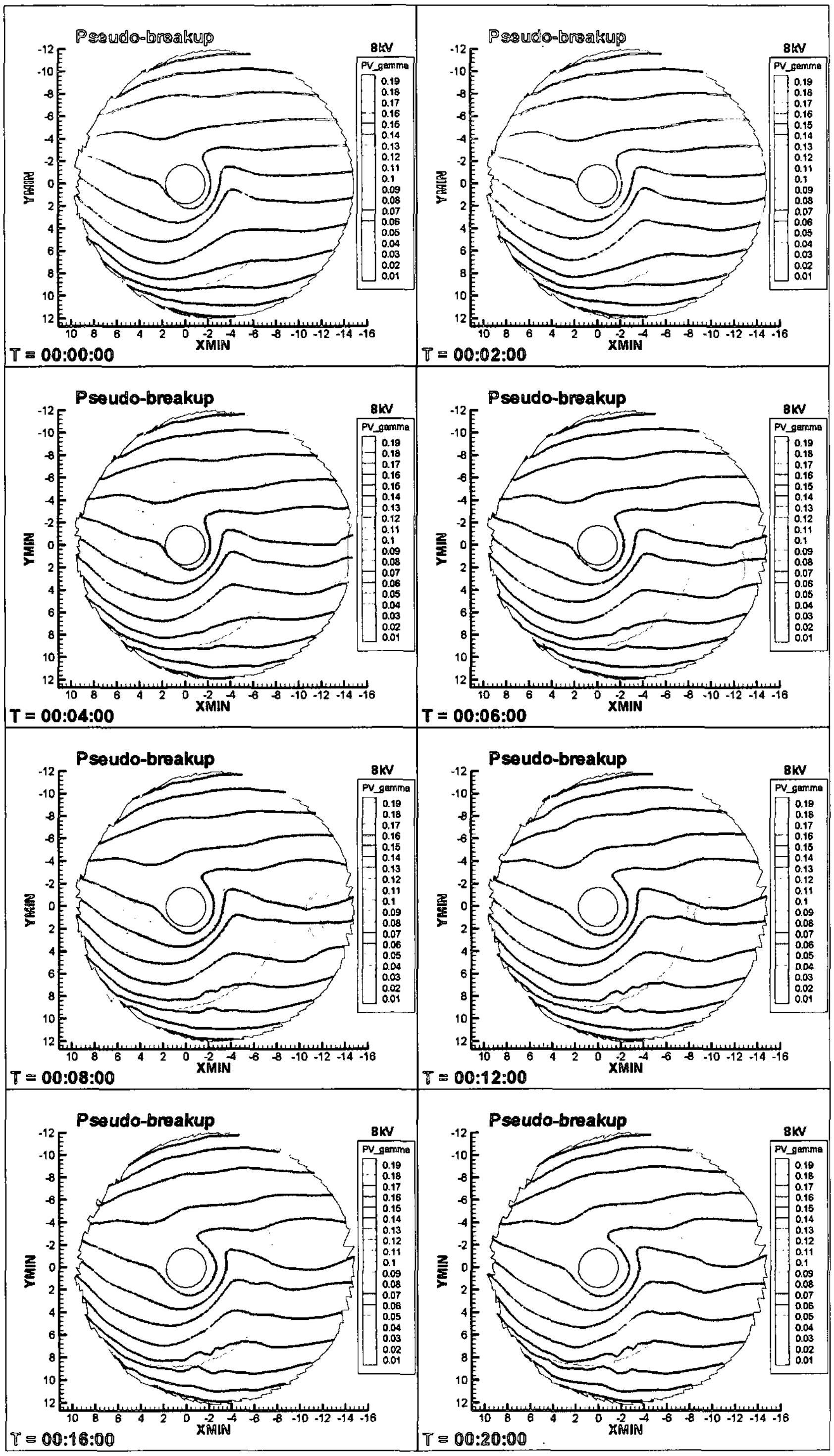

Figure 7.11. $PV^{5/3}$ in units of nPa $(R_E/nT)^{5/3}$ (color contours) on the equatorial plane and the electric equipotentials (black solid lines) every 8kV for 0 to 20 minutes in the idealized pseudo-breakup event run. The sun is to the left.

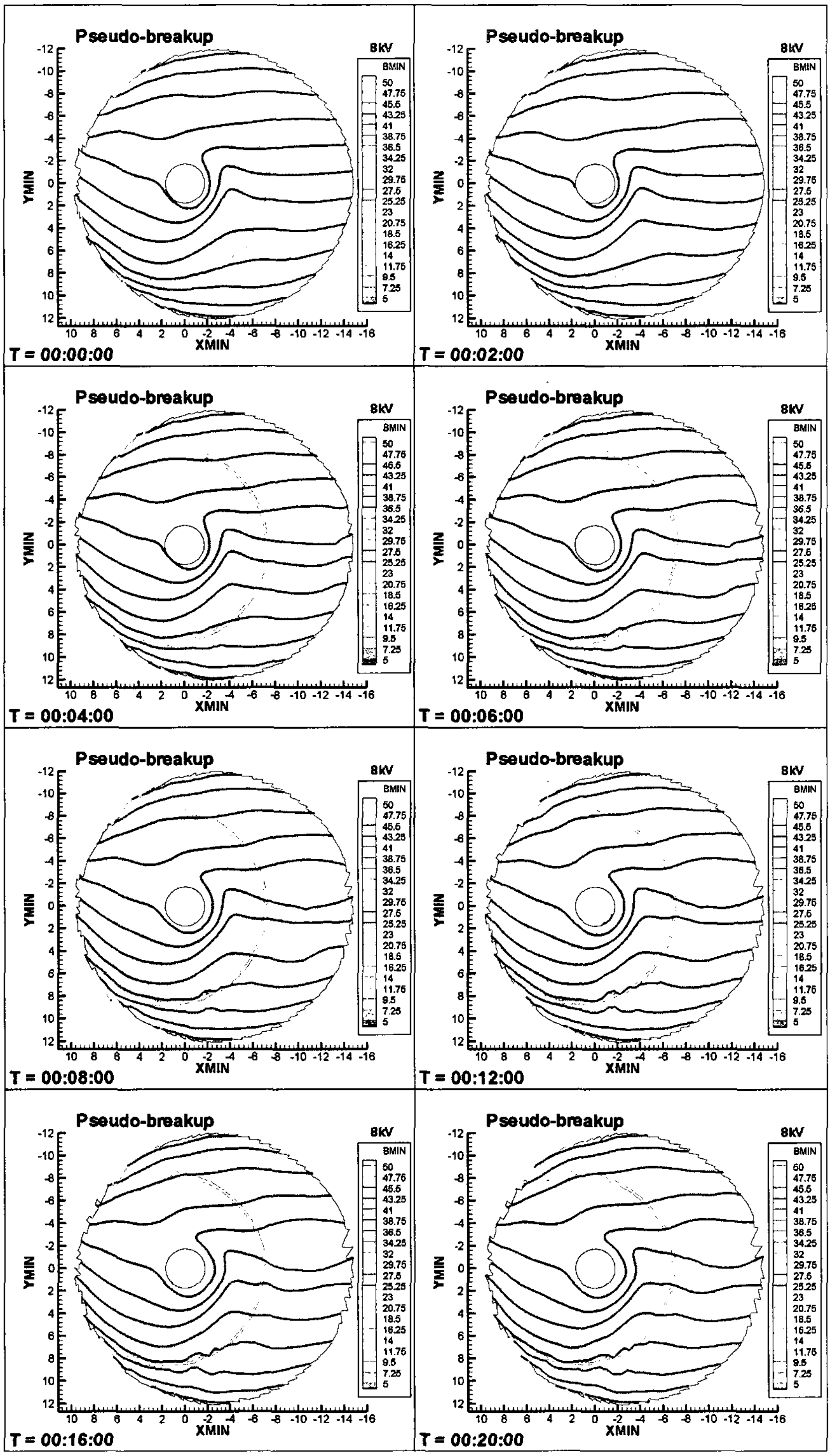

Figure 7.12. Similar to Figure 7.11, but for B_Z (nT).

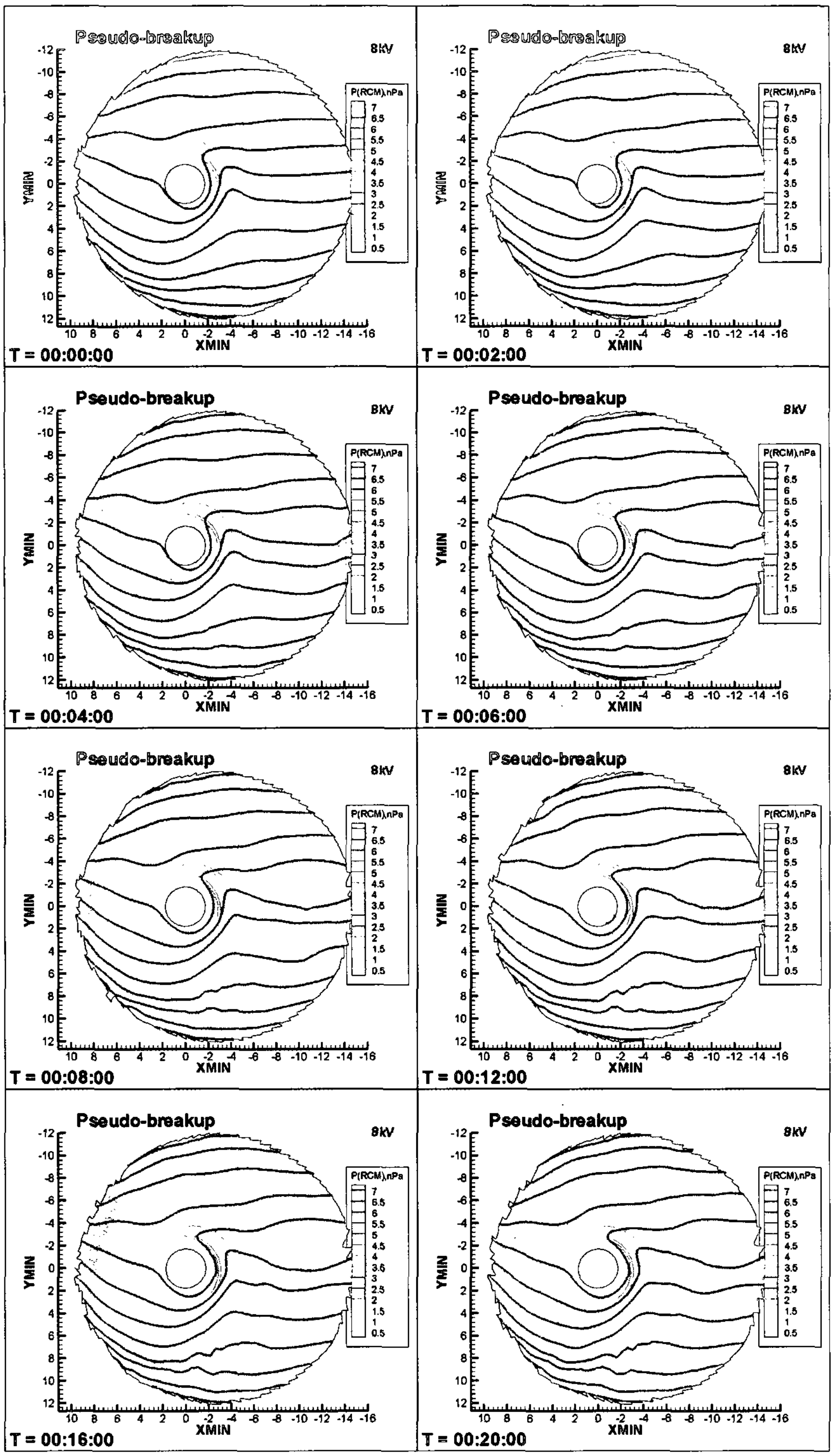

Figure 7.13. Similar to Figure 7.11, but for plasma pressure P (nPa).

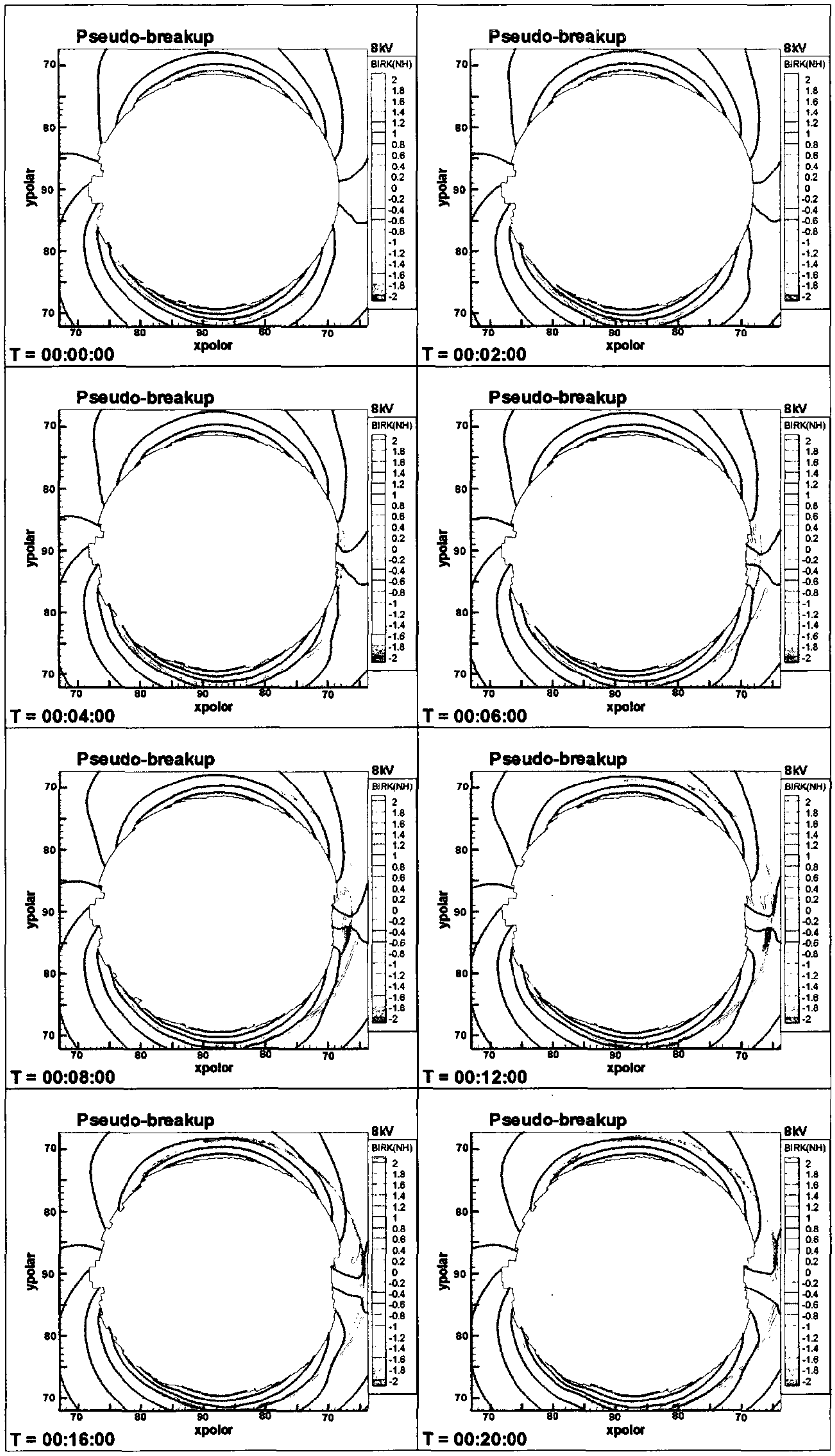

Figure 7.14. Birkeland current density in units of $\mu A/m^2$ (color contours) on the ionosphere and the electric equipotentials (black solid lines) every 8kV for different times in the idealized pseudo-breakup event run. The sun is to the left.

7.3.3 The RCM-E simulation of an idealized convection bay event

As suggested by *Sergeev et al.* [1996a, 2001], there is roughly steady balance between dayside and nightside reconnection where the tail X-line is in the mid-tail, which produces lower $PV^{5/3}$ plasma than that in the growth phase, which has distant magnetotail reconnection. Therefore, we specify plasma distribution with a much smaller $PV^{5/3}$ on the midnight boundary, about 0.14 nPa$(R_E/nT)^{5/3}$ at X=-19R_E (Figure 7.15), which is about 50% lower than the usual $PV^{5/3}$ (see statistical results in Chapter 2). The plasma distribution is a kappa function and is given as,

$$\eta(\lambda) = 0.5\left(\frac{2}{\sqrt{\pi}}((\kappa-1.5)k_B T)^{-\frac{3}{2}}\frac{\Gamma(\kappa+1)}{\Gamma(\kappa-0.5)}\frac{N\sqrt{\lambda}\Delta\lambda}{\left(1+\frac{V^{-2/3}\lambda}{(\kappa-1.5)k_B T}\right)^{\kappa+1}}\right) \tag{7.2}$$

with a coefficient 0.5 to reduce the flux tube content in every channel, compared with equation 5.6. The plasma number density N and the temperature T in equation 7.2 are taken from the TM2003 model for the specified solar wind conditions similar to section 6.2. The ion and electron temperature ration is taken as

$$T_i/T_e = 4.0 + 2.0 * \tan^{-1}(19.0 - 7.0) = 6.97 \tag{7.3}$$

The plasma distribution is kappa=6 distribution. The RCM and equilibrium code exchange information (magnetic field and pressure) every 5 minutes.

Figure 7.15 shows the $PV^{5/3}$ on the equatorial plane after two hours, which is roughly of the time period for persistent southward IMF B_Z for the convection bay events 1~2 hours [*Sergeev et al.*, 2001]. The $PV^{5/3}$ at X=~-10R_E is only about half magnitude in the substorm growth phase (Figure 7.6), but of the same level as the superposed epoch result (Figure 7.4g), i.e., less than 0.1 $nPa(R_E/nT)^{5/3}$. The magnetic field B_Z component outside -10R_E (Figure 7.16) is much larger than the ~<10nT magnetic field in growth phase (Figure 7.7), making the flux tube volume very small in the convection bay event (Figure 7.4). As modeled by *Sergeev et al.* [1994, 2001], using a modified Tsyganenko model, the magnetic field in convection bay events have both local B_Z minimum as in the growth phase in the near-Earth region and a large B_Z in the mid-tail plasma sheet. Our simulation produces a large B_Z component in the region the near-Earth to mid-tail plasma sheet outside -10R_E, similar to the thick plasma sheet inferred by the even-oriented modeling [*Sergeev et al.*, 2001], but there is no deep B_Z minimum in the near-Earth plasma sheet. The modeled partial ring current in Figure 7.17 is more symmetric and stronger than partial ring current in the substorm growth phase (Figure 7.8), which suggests that during convection bay intervals we expect to get an enhanced ring current, consistent with the fact that the Dst index is usually depressed up to ~-50nT [e.g., *Sergeev et al.*, 1996a; *Sergeev et al.*, 2001].

The proposed physical picture of steady magnetospheric convection or convection bay events is that the magnetic reconnection site located in the mid-tail region at about -40 to -60R_E, produces lower $PV^{5/3}$ plasma than in the growth phase, with reconnection at a greater distance (~-100R_E) but higher $PV^{5/3}$ than in an expansion phase, with reconnection at ~-20R_E [*Sergeev and Lennartsson*, 1988]. The lower-than-growth-phase

$PV^{5/3}$ overcomes the so-called "pressure crisis" as discussed in chapter 2 [*Erickson and Wolf*, 1980], so that the magnetic field earthward of the reconnection site does not need to stretch to equilibrate that lower plasma content. This results in a thick plasma sheet (large magnetic field and small plasma pressure), associated with enhanced earthward convection, as reproduced in the idealized simulation.

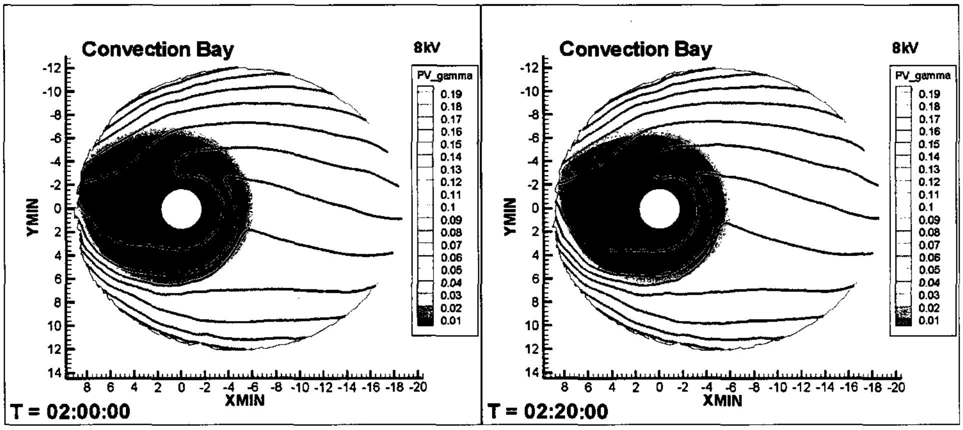

Figure 7.15. $PV^{5/3}$ in units of nPa(R_E/nT)$^{5/3}$ (color contours) on the equatorial plane and the electric equipotentials (black solid lines) every 8kV for T=02:00:00 and T=02:20:00 in the idealized convection bay event run. The sun is to the left.

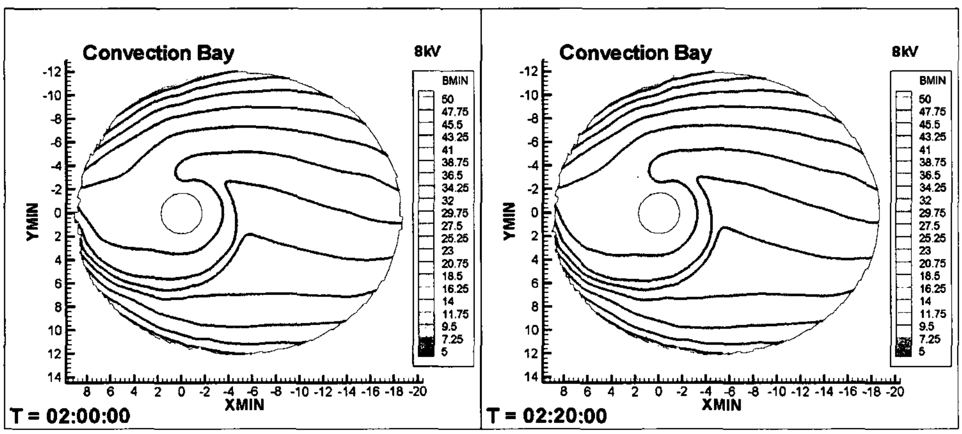

Figure 7.16. Similar to Figure 7.15, but for B_Z (nT).

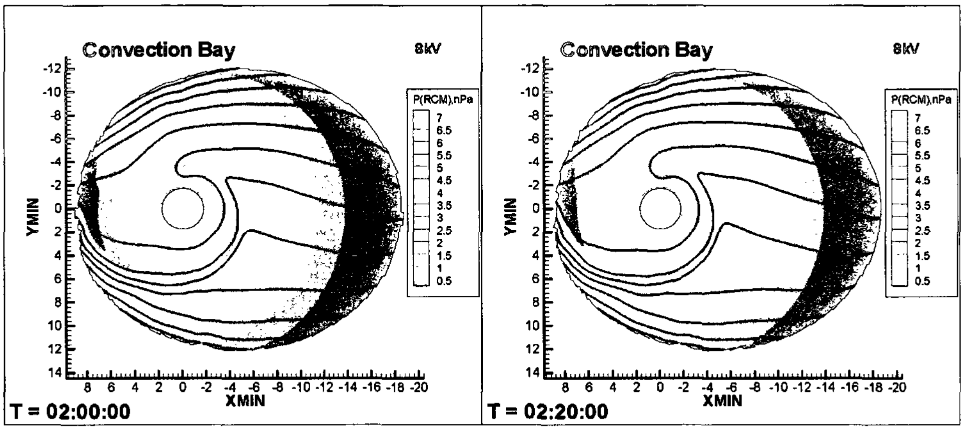

Figure 7.17. Similar to Figure 7.15, but for plasma pressure *P* (nPa).

7.4 Summary

By analyzing the superposed epoch study of the entropy parameter $PV^{5/3}$ for the corresponding RCM-E simulations during substorms, pseudo-breakups and convection bays, we find quite distinct features of time variations of $PV^{5/3}$ at the near-Earth plasma sheet (~-10R_E), which confirms $PV^{5/3}$ as a key parameter that controls the modes of earthward plasma convection. We suggest that the characteristics of non-adiabatic processes, such as reconnection in the magnetotail and other instabilities play an important role in the generation of bubble with different characteristics. Substorm expansions are associated with sustained bubble injections involving lobe reconnection; pseudo-breakups are associated with transient bubble injections involving plasma sheet reconnection or constrained instabilities; while convection bays are associated with mid-tail reconnection.

Chapter 8

Summary and comments

The role of $PV^{5/3}$ in the plasma transport from the plasma sheet to the inner magnetosphere has been studied and presented in this thesis with both statistical observations and RCM and RCM-E based simulations.

The statistical distribution of $PV^{5/3}$ as estimated from Geotail data (section 2.5) show that: (1) consistent with other empirical models [e.g. *Xing and Wolf*, 2007], on average, $PV^{5/3}$ decreases towards the Earth; (2) $PV^{5/3}$ is smaller when there are higher earthward flow velocities, which suggests that plasma bubbles in the plasma sheet are an important element in easing the "pressure crisis" [e.g., *Erickson and Wolf*, 1980] or more precisely the "entropy inconsistency" [*Wolf et al.*, 2009].

The "entropy inconsistency" is prevalent when there is no fast earthward flow, i.e., during a substorm growth phase (black lines in Figure 8.1). A preliminary RCM-E simulation of the 29 Oct., 2004 substorm event (Chapter 4) shows that the inner magnetosphere can accept the steady earthward-convected high values of $PV^{5/3}$ plasma from the distant reconnection site, by stretching the magnetic field in the near-Earth region.

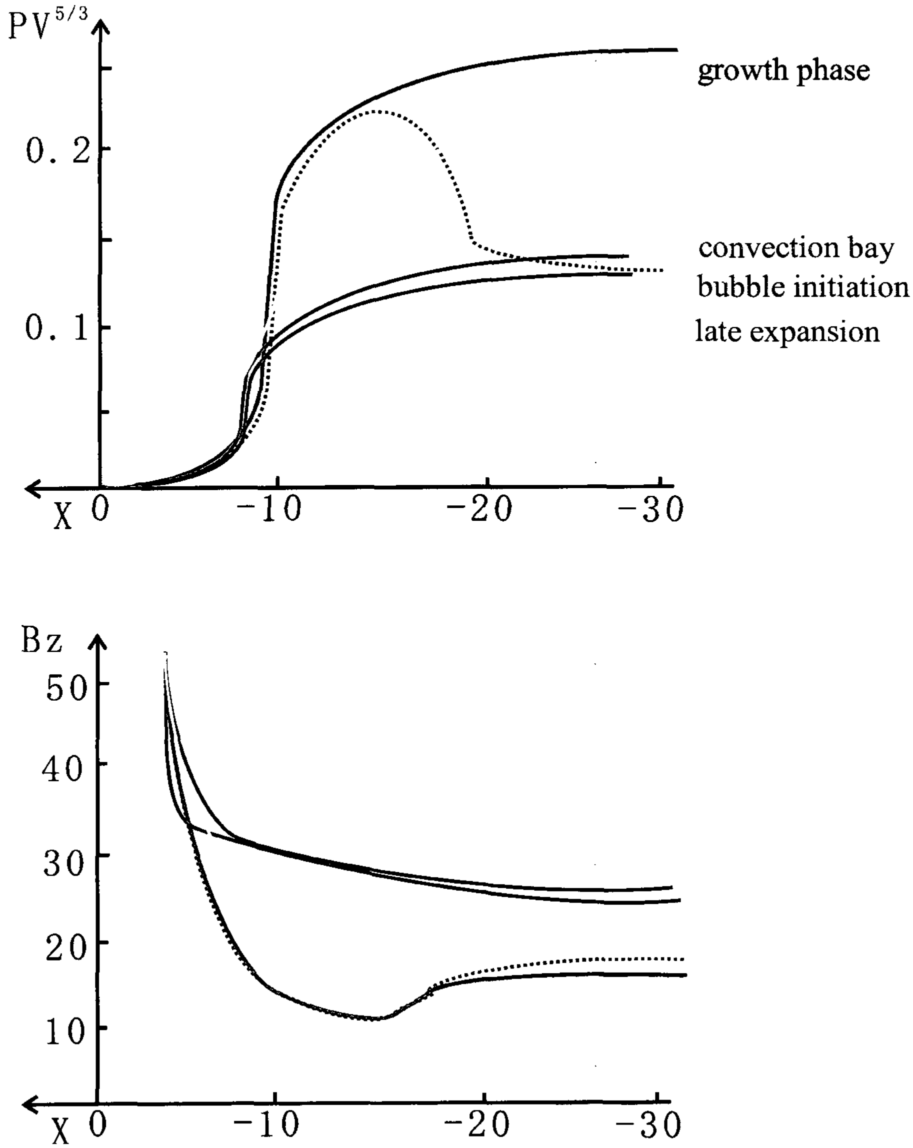

Figure 8.1. Sketch of configurations of $PV^{5/3}$ (nPa(R$_E$/nT)$^{5/3}$) and B_Z (nT) along X-axis for (1) prevalent entropy inconsistency during growth phase (black lines) with large $PV^{5/3}$ in the plasma sheet and B_Z minimum in the near-Earth region; (2) reduced entropy inconsistency during convection bay events (red lines) with reduced $PV^{5/3}$ and dipole-like B_Z in the plasma sheet; (3) abruptly reduced entropy inconsistency during a sustained bubble injection event (dotted blue lines for the initiation of the bubble and solid blue lines for the late expansion phase); (4) averaged configuration (yellow lines).

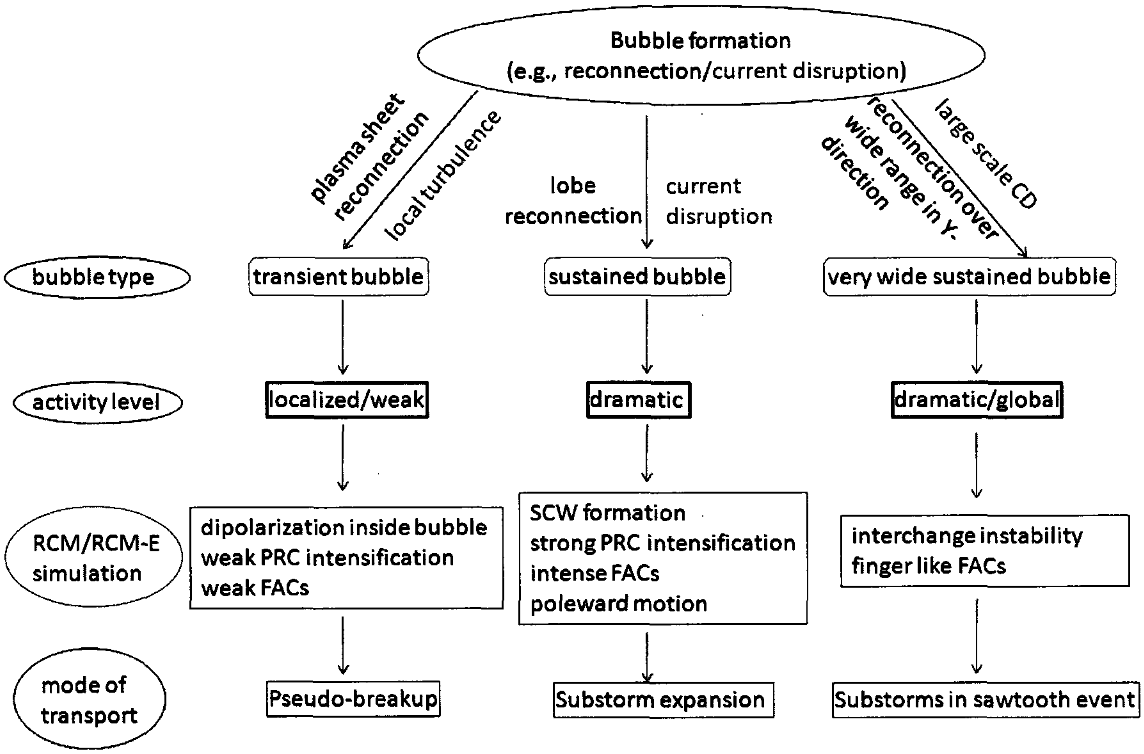

Figure 8.2. A flow chart illustrating the relationship between different types of bubbles and the modes of transport. The mechanism of bubble formation related to NENL model is in black and the mechanism related to CD model is in red. PRC represents partial ring current; FACs represent field-aligned currents; SCW represents substorm current wedge.

The "entropy inconsistency" can be reduced (red lines in Figure 8.1), if the reconnection site moves from distant tail to mid-tail [*Sergeev and Lennartsson*, 1988; *Sergeev et al.*, 1996a], when the magnetosphere goes into a convection bay [e.g., *Pytte et al.*, 1978; *Sergeev et al.*, 2001], or an SMC [e.g., *Sergeev et al.*, 1996a and references therein] interval. During this transport mode, earthward-convected flux tubes contain lower $PV^{5/3}$ plasma, and the magnetic field in the near-Earth plasma sheet does not stretch very much, resulting in a dipole-like magnetic field configuration (see superposed epoch study of $PV^{5/3}$ in convection bay events and associated RCM-E simulation in Chapter 7).

The "entropy inconsistency" can also be reduced abruptly (blue lines in Figure 8.1), due to the earthward flow of depleted $PV^{5/3}$ plasma generated by near-Earth reconnection [e.g., *Kan et al.*, 2007; *Sitnov et al.*, 2005] or by current disruption [e.g., *Lui*, 1996; *Wolf et al.*, 2009]. However, our studies show that different spatial and temporal extent of depleted $PV^{5/3}$ plasma (or bubbles) leads to different types of events (Figure 8.2). If the bubble injection is sustained (e.g., >20~30 minutes) and has an azimuthal width of several hours in local time, then the inner magnetosphere reconfiguration will be dramatic, including the intensification of the partial ring current, dipolarization of the magnetic field, poleward motion of polar boundary, and formation of the SCW. This represents the isolated substorm expansion phase (see Chapters 4, 6 and 7). If the bubble injection is on a shorter time scale (e.g., ≤10 minutes), the inner magnetic field reconfiguration will be transient and localized, which represents a pseudo-breakup event (see Chapter 7). The transient bubble may form when tail reconnection only involves the plasma sheet magnetic field and never expands into the lobe [e.g., *Baker et al.*, 1996] or some global constraint is not met [e.g., *Lui*, 1996]. If plasma depletion in the tail is sustained and unusually wide in local time (e.g.., ~10 hours), then the inner magnetosphere goes into a state that could be favorable to the interchange instability, which usually results in the spatially quasi-periodic north-south-aligned finger-like aurora, although the width of the fingers is found grid-size dependent in RCM or RCM-E simulations (see Chapter 3 and 5). This situation seems to happen during substorms that occur during sawtooth events [e.g. *Sazykin et al.*, 2002; *Yang et al.*, 2008; *Henderson et al.*, 2006b].

It would be constructive to point out a potential new direction of the RCM-E at the end of this thesis. From my personal experience, the model works well in the sense that it reproduces the basic features of substorms in the close field line regions. However, as with any model it is not perfect, especially in the sense that it is unable to respond to the change of solar wind conditions, particularly changes that involve compression or rarefaction of the magnetosphere. Therefore, developing a new version of RCM-E that can assimilate solar wind condition either from parameterized empirical model or from *in-situ* observations will make for a more powerful computational model.

Bibliography

Akasofu, S.-I. (1964), The development of the auroral substorm, *Planet. Space Sci.,* 12(4), 273.

Akasofu, S.-I. (1968), *Polar and Magnetospheric Substorms*, Dordrecht, Reidel.

Akasofu, S.-I. (1981), Energy Coupling Between the Solar Wind and the Magnetosphere, *Space Sci. Rev.,* 28, 121.

Angelopoulos, V., W. Baumjohann, C. F. Kennel, F. V. Coroniti, M. G. Kivelson, R. Pellat, R. J. Walker, H. Lühr, and G. Paschmann (1992), Bursty Bulk Flows in the Inner Central Plasma Sheet, *J. Geophys. Res.*, 97(A4), 4027–4039.

Angelopoulos, V., C. Kennel, F. Coroniti, R. Pellat, M. Kivelson, R. Walker, C. Russell, W. Baumjohann, W. Feldman, and J. Gosling (1994), Statistical Characteristics of Bursty Bulk Flow Events, *J. Geophys. Res.*, 99(A11), 21257-21280.

Angelopoulos, V., (2008a), The THEMIS Mission, *Space Sci. Rev.*, doi: 10.1007/s11214-008-9336-1.

Angelopoulos, V., J.P. McFadden, D. Larson, C.W. Carlson, S.B. Mende, H. Frey, T. Phan, D.G. Sibeck, K.-H. Glassmeier, U. Auster, E. Donovan, I.R. Mann, I.J. Rae, C.T. Russell, A. Runov, X. Zhou, and L. Kepko (2008b), Tail reconnection triggering substorm onset, *Science*, doi:10.1126/science.1160495.

Baker, D. N., and R. L. McPherron (1990), Extreme Energetic Particle Decreases Near Geostationary Orbit: A Manifestation of Current Diversion within the Inner Plasma Sheet, *J. Geophys. Res.*, 95(A5), 6591–6599.

Baker, D. N. (1992), Driven and Unloading Aspects of Magnetospheric Substorms, in Substorms 1, *Eur. Space Agency Spec. Publ.* 335, 185.

Baker, D., T. Pulkkinen, V. Angelopoulos, W. Baumjohann, and R. McPherron (1996), Neutral line model of substorms: Past results and present view, *J. Geophys. Res.*, 101(A6), 12975-13010.

Baumjohann, W., G. Paschmann, and C. A. Cattell (1989), Average plasma properties in the central plasma sheet, *J. Geophys. Res., 94*, 6597.

Baumjohann, W., G. Paschmann, and H. Lühr (1990), Characteristics of high-speed ion flows in the plasma sheet, *J. Geophys. Res.*, 95, 3801.

Belian, R. D., T. E. Cayton, and G. D. Reeves (1995). Quasi-periodic global substorm-generated variations observed at geosynchronous orbit, in Space Plasmas: Coupling Between Small and Medium Scale Processes, *Geophys. Monogr. Ser.*, vol. 86, p. 143, AGU, Washington, D. C.

Bilitza, D. (ed.) (1990), International Reference Ionosphere 1990, NSSDC 90-22, Greenbelt, Maryland.

Bilitza, D., K. Rawer, L. Bossy, and T. Gulyaeva (1993), International Reference Ionosphere - Past, Present, Future, *Adv. Space Res.,* 13, #3, 3-23, 1993.

Birmingham, T. (1992), Birkeland Currents in an Anisotropic, Magnetostatic Plasma, *J. Geophys. Res.*, 97(A4), 3907-3917.

Birn, J., and M. Hesse (1996), Details of current disruption and diversion in simulations of magnetotail dynamics, *J. Geophys. Res.*, 101, 15,345.

Birn, J., M. Hesse, G. Haerendel, W. Baumjohann, and K. Shiokawa (1999), Flow braking and the substorm current wedge, *J. Geophys. Res.*, 104(A9), 19895-19903.

Birn, J., et al. (2004), On the propagation of bubbles in the geomagnetic tail, *Annales Geophysicae*, *22*(5), 1773-1786.

Birn, J., M. Hesse, and K. Schindler (2006), Entropy conservation in simulations of magnetic reconnection, *Phys. Plasmas,* 13, 092117, DOI:10.1063/1.2349440.

Borovsky, J. E., R. J. Nemzek, and R. D. Belian (1993), The occurrence rate of magnetospheric-substorm onsets: Random and periodic substorms, *J. Geophys. Res., 98*, 3803.

Borovsky, J. E., M. F. Thomsen, R. C. Elphic, T. E. Cayton, and D. J. McComas (1998), The transport of plasma sheet material from the distant tail to geosynchronous orbit, *J. Geophys. Res., 103*, 20,297.

Botherm, V., and I. A. Daglis (2006), *Space Weather-Physics and Effects*, Springer-Verlag, Berlin.

Boyle, C. B., P. H. Reiff, and M. R. Hairston (1997), Empirical polar cap potentials, *J. Geophys. Res., 102*, 111.

Chapman, S. and J. Bartels (1940), *Geomagnetism*, Vol. 1, Chap. IX, Clarendon, Oxford.

Chen, C. X., and R. Wolf (1993), Interpretation of High-Speed Flows in the Plasma Sheet, *J. Geophys. Res.*, 98(A12), 21409-21419.

Chen, C. X., and R. Wolf (1999), Theory of thin-filament motion in Earth's magnetotail and its application to bursty bulk flows, *J. Geophys. Res.*, 104(A7), 14613-14626.

Cheng C. Z., and S. Zaharia (2004), MHD ballooning instability in the plasma sheet, *Geophys. Res. Lett.*, 31, L06809, doi:10.1029/2003GL018823.

Christon, S., D. Williams, D. Mitchell, L. Frank, and C. Huang (1989), Spectral Characteristics of Plasma Sheet Ion and Electron Populations During Undisturbed Geomagnetic Conditions, *J. Geophys. Res.*, 94(A10), 13409-13424.

Chung J.-K., Q. Wu, Y.H. Kim, Y.-I. Won, S. Solomon, J.U. Park, and B.G. Choi (2007), Enhancement of OI 630.0 nm emission at mid-latitudes during an intense magnetic storm, *J. Atmos. Sol. Terr. Phys*, Volume 69, Issue 6, Pages 697-706

Clauer, C. R., X. Cai, D. Welling, A. DeJong, and M. G. Henderson (2006), Characterizing the 18 April 2002 storm-time sawtooth events using ground magnetic data, J. Geophys. Res., 111, A04S90, doi:10.1029/2005JA011099.

Coleman, P.J., L. Davis, and C. P. Sonett (1960), Steady component of the Interplanetary Magnetic Field: Pioneer V, *Physical Review Letters,* 5, 43-46.

Crabtree, C., and L. Chen (2004), Finite gyroradius theory of drift compressional modes, *Geophys. Res. Lett.*, 31, L17804, doi:10.1029/2004GL020660.

Daglis, I. A., S. Livi, E. T. Sarris, B. Wilken (1994), Energy density of ionospheric and solar wind origin ions in the near-Earth magnetotail during substorms, *J. Geophys. Res.*, *99*(A4), 5691-5704, 10.1029/93JA02772.

Daley, R. (1991), *Atmospheric Data Analysis*, Cambridge University Press, Cambridge.

DeJong, A. D., A. J. Ridley, and C. R. Clauer (2008), Balanced reconnection intervals: four case studies, *Ann. Geophys.*, 26, 3897-3912.

Delcourt, D. C. (2002), Particle acceleration by inductive electric fields in the inner magnetosphere, *J. Atmos. Sol. Terr. Phys.*, 64, 551– 559.

Dungey, J. W. (1961), Interplanetary magnetic field and the auroral zones, *Phys. Rev. Lett.*, 6, 47.

Erickson, G. M., and R. A. Wolf (1980), Is steady convection possible in the Earth's magnetotail?, *Geophys. Res. Lett.*, 7(11), 897–900.

Erickson, G. M. (1984), On the cause of x-line formation in the near-Earth plasma sheet: results of adiabatic convection of plasma sheet plasma, in Magnetic Reconnection in Space and Laboratory Plasmas, *Geophys. Monogr.*, 30, E. W. Hones, ed., 296.

Erickson, G. M. (1992), A quasi-static magnetospheric convection model in two dimensions, *J. Geophys. Res.*, 97(A5), 6505– 6522, doi:10.1029/91JA03141.

Fejer, J. A. (1953), Semidiurnal currents and electron drifts in the ionosphere, *J. Atm. Terrest. Phys.*, 4, 184-203.

Fejer, B. G., R. W. Spiro, R. A. Wolf, and J. C. Foster (1990), Latitudinal variation of perturbation electric fields during magnetically disturbed periods: 1986 SUNDIAL observations and model results, *Ann. Geophys.*, *8*, 441-454.

Fok, M.-C., J. U. Kozyra, A. F. Nagy, and T. E. Craven (1991), Lifetime of ring current particles due to Coulomb collisions in the plasmasphere, *J. Geophys. Res.*, 96, 7861.

Fok, M.-C., R. Wolf, R. Spiro, and T. Moore (2001), Comprehensive computational model of Earth's ring current, *J. Geophys. Res.*, 106(A5), 8417-8424.

Fujimoto, M., T. Terasawa, T. Mukai, Y. Saito, T. Yamamoto, and S. Kokubun (1998), Plasma entry from the flanks of the near-Earth magnetotail: Geotail observations, *J. Geophys. Res., 103*(A3), 4391.

Garner, T. W., R. A. Wolf, R. W. Spiro, and M. F. Thomsen (1999), First attempt at assimilating data to constrain a magnetospheric model, *J. Geophys. Res.*, 104(A11), 25,145–25,152.

Garner, T. W., R. A. Wolf, R. W. Spiro, W. J. Burke, B. G. Fejer, S. Sazykin, J. L. Roeder, and M. R. Hairston (2004), Magnetospheric electric fields and plasma sheet injection to low L-shells during the 4–5 June 1991 magnetic storm: Comparison between the Rice Convection Model and observations, *J. Geophys. Res.*, 109, A02214, doi:10.1029/2003JA010208.

Gonzalez, W. D. and B. T. Tsurutani (1987), Criteria of interplanetary parameters causing intense magnetic storms (Dst<-100nT), *Planet. Space Sci.*, 35, 1101.

Gonzalez, W.D., A.L.C. Gonzalez, and B.T. Tsurutani (1990), Dual-peak solar cycle distribution of intense geomagnetic storms, *Planet. Space Sci.*, 38, 181.

Gonzalez, W. D., J. A. Joselyn, Y. Kamide, H. W. Kroehl, G. Rostoker, B. T. Tsurutani, and V. M. Vasyliunas (1994), What is a Geomagnetic Storm?, *J. Geophys. Res.*, 99(A4), 5771–5792.

Goodrich, C. C., T. I. Pulkkinen, J. G. Lyon, and V. G. Merkin (2007), Magnetospheric convection during intermediate driving: Sawtooth events and steady convection intervals as seen in Lyon-Fedder-Mobarry global MHD simulations, *J. Geophys. Res., 112*, A08201, doi:10.1029/2006JA012155.

Hau, L.-N., and R. Wolf (1987), Effect of a Localized Minimum in Equatorial Field Strength on Resistive Tearing Instability in the Geomagnetotail, *J. Geophys. Res.*, 92(A5), 4745-4750.

Hau, L.-N. (1991), Effect of steady-state adiabatic convection on the configuration of the near-Earth plasma sheet, 2, *J. Geophys. Res.*, 96, 5591–5596, doi:10.1029/90JA02619.

Heinemann, M., and D. Pontius Jr. (1990), Representations of Currents and Magnetic Fields in Isotropic Magnetohydrostatic Plasma, *J. Geophys. Res.*, 95(A1), 251-257.

Henderson, M. G. (2004), The May 2–3, 1986 CDAW-9C interval: A sawtooth event, *Geophys. Res. Lett., 31*, L11804, doi:10.1029/2004GL019941.

Henderson, M. G., G. D. Reeves, R. Skoug, M. T. Thomsen, M. H. Denton, S. B. Mende, T. J. Immel, P. C. Brandt, and H. J. Singer (2006a), Magnetospheric and auroral activity during the 18 April 2002 sawtooth event, *J. Geophys. Res., 111*, A01S90, doi:10.1029/2005JA011111.

Henderson, M. G., et al. (2006b), Substorms during the 10–11 August 2000 sawtooth event, *J. Geophys. Res.*, 111, A06206, doi:10.1029/2005JA011366.

Henderson, M. G. (2009), Observational evidence for an inside-out substorm onset scenario, *Ann. Geophys.*, *27*, 2129-2140.

Hesse, M., and J. Birn (1993), Three-Dimensional Magnetotail Equilibria by Numerical Relaxation Techniques, *J. Geophys. Res.*, 98(A3), 3973-3982.

Hill, T. W., A. J. Dessler, and R. A. Wolf (1976), Mercury and Mars: The role of ionospheric conductivity in the acceleration of magnetospheric particles, *Geophys. Res. Lett.*, 3, 429, doi:10.1029/GL003i008p00429.

Hill, T. W. (1983), Solar-wind magnetosphere coupling. In: Carovillano, R. L., Forbes, J. M. (Eds.), *Solar-Terrestrial Physics*. D. Reidel Publishing Company, 261–302.

Hones, E. W., Jr. (1977), Comments on ''On hot, tenuous plasmas, fireballs, and boundary layers in the Earth's magnetotail,'' by L. A. Frank, K. L. Ackerson, and R. P. Lepping, *J. Geophys. Res.*, 82, 5633.

Huang, C.-S., G. D. Reeves, J. E. Borovsky, R. M. Skoug, Z. Y. Pu, and G. Le (2003a), Periodic magnetospheric substorms and their relationship with solar wind variations, *J. Geophys. Res., 108*(A6), 1255, doi:10.1029/2002JA009704.

Huang, C.-S., J. C. Foster, G. D. Reeves, G. Le, H. U. Frey, C. J. Pollock, and J.-M. Jahn (2003b), Periodic magnetospheric substorms: Multiple space-based and ground-based instrumental observations, *J. Geophys. Res., 108*(A11), 1411, doi:10.1029/2003JA009992.

Jordanova, V. K., J. U. Kozyra, A. F. Nagy, and G. V. Khazanov (1997), Kinetic model of the ring current-atmosphere interactions, *J. Geophys. Res.*, 102(A7), 14,279–14,291.

Kamide, Y., P. Perreault, S.-I. Akasofu, and J. Winningham (1977), Dependence of Substorm Occurrence Probability on the Interplanetary Magnetic Field and on the Size of the Auroral Oval, *J. Geophys. Res.*, 82(35), 5521-5528.

Kan, J. R., X. Xing, and R. A. Wolf (2007), Intensity of geomagnetic storms depends on the X-line location in the plasma sheet, *J. Geophys. Res.*, 112, A04216, doi:10.1029/2006JA011945.

Kaufmann, R. L., and W. R. Paterson (2006), Magnetic flux and particle transport in the plasma sheet, *J. Geophys. Res., 111*, A10214, doi:10.1029/2006JA011734.

Kauristie, K., V. A. Sergeev, M. Kubyshkina, T. I. Pulkkinen, V. Angelopoulos, T. Phan, R. P. Lin, and J. A. Slavin (2000), Ionospheric current signatures of transient plasma sheet flows, *J. Geophys. Res.*, 105(A5), 10,677–10,690.

Keiling, A., et al. (2008), Multiple intensifications inside the auroral bulge and their association with plasma sheet activities, *J. Geophys. Res.*, 113, A12216, doi:10.1029/2008JA013383.

Kennel, C. F. (1969), Consequences of a magnetospheric plasma, *Rev. Geophys.*, 7, 379.

Kistler, L., E. Möbius, W. Baumjohann, G. Paschmann, and D. Hamilton (1992), Pressure Changes in the Plasma Sheet During Substorm Injections, *J. Geophys. Res.*, 97(A3), 2973-2983.

Kivelson, M. G., and H. E. Spence (1988), On the possibility of quasi-static convection in the quiet magnetotail, *Geophys. Res. Lett., 15*, 1541-1544.

Knight, S. (1973), Parallel electric fields, *Planet. Space Sci.,* 21, 741-750.

Kokubun, S., T. Yamamoto, M. H. Acuna, K. Hayashi, K. Shiokawa, and H. Kawano (1994), The Geotail Magnetic Field Experiment, *J. Geomag. Geoelectr.*, 46, 7-21.

Koskinen, H. E. J., R. E. Lopez, R. J. Pellinen, T. I. Pulkkinen, D. N. Baker, and T. Bosinger (1993), Pseudobreakup and substorm growth phase in the ionosphere and magnetosphere, *J. Geophys. Res.*, 98, 5801-5813.

Kuznetsova, M. M., M. Hesse, L. Rastatter, A. Taktakishvili, G. Toth, D. L. De Zeeuw, A. Ridley, and T. I. Gombosi (2007), Multiscale modeling of magnetospheric reconnection, *J. Geophys. Res., 112*, A10210, doi:10.1029/2007JA012316.

Kubyshkina, M., V. Sergeev, and T. Pulkkinen (1999), Hybrid Input Algorithm: An event-oriented magnetospheric model, *J. Geophys. Res.*, 104(A11), 24977-24993.

Kubyshkina M. V., V. A. Sergeev, S. V. Dubyagin, S. Wing, P. T. Newell, W. Baumjohann, and A. T. Y. Liu (2002), Constructing the magnetospheric model including pressure measurements, *J. Geophys. Res.*, 107 (A6), 1070, doi:10.1029/2001JA900167.

Lee, D.-Y., L. R. Lyons, and K. Yumoto (2004), Sawtooth oscillations directly driven by solar wind dynamic pressure enhancements, *J. Geophys. Res., 109*, A04202, doi:10.1029/2003JA010246.

Lemon C., F. Toffoletto, M. Hesse, J. Birn (2003), Computing magnetospheric force equilibria, *J. Geophys. Res.*, 108 (A6), 1237, doi:10.1029/2002JA009702.

Lemon, C., R. A. Wolf, T. W. Hill, S. Sazykin, R. W. Spiro, F. R. Toffoletto, J. Birn, and M. Hesse (2004), Magnetic storm ring current injection modeled with the Rice Convection Model and a self-consistent magnetic field, *Geophys. Res. Lett., 31*, L21801, doi:10.1029/2004GL020914.

Lopez, R. E., A. T. Y. Lui, D. G. Sibeck, K. Takahashi, R. W. McEntire, L. J. Zanetti, and S. M. Krimigis (1989), On the Relationship Between the Energetic Particle Flux Morphology and the Change in the Magnetic Field Magnitude During Substorms, *J. Geophys. Res.*, 94(A12), 17,105–17,119.

Lui, A. (1991), A Synthesis of Magnetospheric Substorm Models, *J. Geophys. Res.*, 96(A2), 1849-1856.

Lui, A. T. Y., R. E. Lopez, B. J. Anderson, K. Takahashi, L. J. Zanetti, R. W. McEntire, T. A. Potemra, D. M. Klumpar, E. M. Greene, and R. Strangeway (1992), Current disruptions in the near-earth neutral sheet region, *J. Geophys. Res., 97*, 1461-1480.

Lui, A. T. Y. (1996), Current disruption in the Earth's magnetosphere: Observations and models, *J. Geophys. Res.*, 101(A6), 13067-13088.

Lui, A., K. Liou, M. Nosé, S. Ohtani, D. Williams, T. Mukai, K. Tsuruda, and S. Kokubun (1999), Near-Earth Dipolarization: Evidence for a Non-MHD Process, *Geophys. Res. Lett.*, 26(19), 2905-2908.

Lui, A. T. Y. (2009), Pressure gradient effect on a particle velocity distribution, *Geophys.*

Res. Lett., 36, L01107, doi:10.1029/2008GL036458.

Lyons, L. R., C.-P. Wang, T. Nagai, T. Mukai, Y. Saito, and J. C. Samson (2003), Substorm inner plasma sheet particle reduction, *J. Geophys. Res.*, 108(A12), 1426, doi:10.1029/2003JA010177.

Mauk, B. H., and C. I. Meng (1983), Characterization of geostationary particle signatures based on the ''injection boundary'' model, *J. Geophys. Res., 86*, 3055– 3071.

McFadden, J.P., Carlson, C.W., Larson, D., Angelopoulos, V., Ludlam, M., Abiad, R., Elliott, B., Turin, P., Marckwordt, M. (2008), The THEMIS ESA plasma instrument and in-flight calibration, *Space Sci. Rev.*, doi: 10.1007/s11214-008-9440-2.

McIlwain, C. E. (1974). Substorm injection boundaries. In *Magnetospheric Physics*, edited by B. M. McCormac. Dordrecht-Holland, D. Reidel: 143-154.

McPherron, R. L., C. T. Russell, and M P. Aubry (1973), Satellite studies of magnetospheric substorms on August 15, 1968, 9.Phenomenological model for substorms, *J. Geophys.* Res., 78, 3131-3149.

Miyashita, Y., et al. (2008), Pressure Change Associated with Dipolarization in the Near-Earth Plasma Sheet, *AGU*, Fall Meeting 2008, SM43A-1702.

Moldwin, M. (2008), *An Introduction to Space Weather*, Cambridge University Press, New York.

Mukai, T., S. Machida, Y. Saito, M. Hirahara, T. Terasawa, N. Kaya, T. Obara, M. Ejiri, and A. Nishida (1994), The low energy particle (LEP) experiment onboard the Geotail satellite, *J. Geomag. Geoelectr.*, 46, 669-692.

Nagai, T., M. Fujimoto, Y. Saito, S. Machida, T. Terasawa, R. Nakamura, T. Yamamoto, T. Mukai, A. Nishida, and S. Kokubun (1998), Structure and dynamics of magnetic reconnection for substorm onsets with Geotail observations, *J. Geophys. Res.*, 103(A3), 4419-4440.

Nakamura, R.,W. Baumjohann, R. Schödel,M. J. Brittnacher, V. A. Sergeev, M. Kubyshkina, T. Mukai, and K. Liou (2001), Earthward flow bursts, auroral streamers, and small expansions, *J. Geophys. Res.*, 106, 10,791.

Ness, N. F. (1968), Observed properties of the interplanetary plasma, *Annual Review of Astronomy and Astrophysics*, Vol. 6, 79-114, doi:10.1146/annurev.aa.06.090168.000455.

Northrop, T. G. (1961), The guiding center approximation to charged particle motion, *Annals of Physics*, 15, Issue 1, p.79-101.

Northrop, T. G. (1963), *The Adiabatic Motion of Charged Particles*, Wiley and Sons, New York.

O'Brien, T. P., S. M. Thompson, and R. L. McPherron (2002), Steady magnetospheric convection: Statistical signatures in the solar wind and AE, *Geophys. Res. Lett.*, 29(7), 1130, doi:10.1029/2001GL014641.

Ohtani, S., et al. (1993), A Multisatellite Study of a Pseudo-Substorm Onset in the Near-Earth Magnetotail, *J. Geophys. Res.*, 98(A11), 19,355–19,367.

Ohtani, S., et al. (2007), Cluster observations in the inner magnetosphere during the 18 April 2002 sawtooth event: Dipolarization and injection at $r = 4.6\ R_E$, *J. Geophys. Res., 112*, A08213, doi:10.1029/2007JA012357.

Ontiveros, P. A. (2009), Synthetic Magnetogram Calculations from Magnetosphere-Ionosphere Coupling Models, PhD Dissertation, Rice University.

Parker, E. N. (1958), Dynamics of the Interplanetary Gas and Magnetic Fields, *The Astrophysical Journal,* Vol. 128, 664.

Pellinen, R., W. Baumjohann, W. Heikkila, V. A. Sergeev, A. G. Yahnin, G. Marklund, and A. O. Mel'nikov (1982), Event study on presubstorm phases and their relation to the energy coupling between solar wind and magnetosphere, *Planet. Space Sci.*, 30, 371.

Pontius, D. H., Jr., and R. A. Wolf (1990), Transient flux tubes in the terrestrial magnetosphere, *Geophys. Res. Lett.*, 17, 49.

Pulkkinen, T., A Study of Magnetic Field and Current Configurations in the Magnetotail at the time of a Substorm Onset (1991a), *Planet. Space Sci.*, 39, 833-845.

Pulkkinen, T. I., H. E. J. Koskinen, and R. J. Pellinen (1991b), Mapping of auroral arcs during substorm growth phase, *J. Geophys. Res.*, *96*(A12), 21087–21094.

Pulkkinen, T., D. Baker, D. Fairfield, R. Pellinen, J. Murphree, R. Elphinstone, R. McPherron, J. Fennell, R. Lopez, and T. Nagai (1991c), Modeling the Growth Phase of a Substorm using the Tsyganenko Model and Multi-Spacecraft Observations: CDAW-9, *Geophys. Res. Lett.*, 18(11), 1963-1966.

Pulkkinen, T. I., et al. (1992), Particle scattering and current sheet stability in the geomagnetic tail during the substorm growth phase, *J. Geophys. Res.*, 97(A12), 19283–19297.

Pulkkinen, T., D. Baker, D. Mitchell, R. McPherron, C. Huang, and L. Frank (1994), Thin Current Sheets in the Magnetotail During Substorms: CDAW 6 Revisited, *J. Geophys. Res.*, 99(A4), 5793-5803.

Pulkkinen, T. I., N. Y. Ganushkina, E. I. Tanskanen, M. Kubyshkina, G. D. Reeves, M. F. Thomsen, C. T. Russell, H. J. Singer, J. A. Slavin, and J. Gjerloev (2006), Magnetospheric current systems during stormtime sawtooth events, *J. Geophys. Res., 111*, A11S17, doi:10.1029/2006JA011627.

Pytte, T., R. L. McPherron, E. W. Hones Jr., and H. I. West Jr. (1978), Multiple-Satellite Studies of Magnetospheric Substorms: Distinction Between Polar Magnetic Substorms and Convection-Driven Negative Bays, *J. Geophys. Res.*, 83(A2), 663–679.

Raeder, J., D. Larson, W. Li, L. Kepko, and T. Fuller-Rowell (2008), OpenGGCM Simulations for the THEMIS Mission, *Space Sci. Rev.*, 141, 535–555, doi:10.1007/s11214-008-9421-5.

Rassoul, H. K., R. P. Rohrbaugh, B. A. Tinsley, and D. W. Slater (1993), Spectrometric and Photometric Observations of Low-Latitude Aurorae, *J. Geophys. Res.*, 98(A5), 7695–7709.

Reeves, G. D., and M. G. Henderson (2001), The storm-substorm relationship: Ion injections in geosynchronous measurements and composite energetic neutral atom images, *J. Geophys. Res.*, 106(A4), 5833–5844.

Reeves G. D., M. F. Thomsen, J. E. Borovsky, M. G. Henderson, and R. M. Skoug (2004), Sawtooth injection and the extension of substorm effects to the day side, *International Conference on Substorms* (ICS-7), Lapland, Finland.

Reiff, P., R. Spiro, and T. Hill (1981), Dependence of Polar Cap Potential Drop on Interplanetary Parameters, *J. Geophys. Res.*, 86(A9), 7639-7648.

Roederer, J.G. (1970), *Dynamics of Geomagnetically Trapped Radiation*, Springer-Verlag, Berlin.

Roux, A., S. Perraut, P. Robert, A. Morane, A. Pedersen, A. Korth, G. Kremser, B. Aparicio, D. Rodgers, and R. Pellinen (1991), Plasma Sheet Instability Related to the Westward Traveling Surge, *J. Geophys. Res.*, 96(A10), 17697-17714.

Russell, C. T. (1971), Geophysical coordinate transformations, *Cosmic Electrodynamics*, Vol. 2, 184-196.

Russell, C. T. (2000), How northward turnings of the IMF can lead to substorm expansion onsets, *Geophys. Res. Lett.*, 27(20), 3257–3259.

Sauvaud, J. A., T. Beutier, and D. Delcourt (1996), On the origin of flux dropouts near geosynchronous orbit during the growth phase of substorms 1. Betatron effects, *J. Geophys. Res.*, 101(A9), 19,911–19,919.

Sazykin, S. (2000), Theoretical Studies of Penetration of Magnetospheric Electric Fields to the Ionosphere, PhD Dissertation, University of Utah.

Sazykin S., R. A. Wolf, R. W. Spiro, T. I. Gombosi, D. L. De Zeeuw, and M. F. Thomsen (2002), Interchange instability in the inner magnetosphere associated with geosynchronous particle flux decreases, *Geophys. Res. Lett.*, 29 (10), 1448, doi:10.1029/2001GL014416.

Schmidt, G., *Physics of High Temperature Plasmas*, Academic Press, New York, 1979.

Schulz, M. and L. J. Lanzerotti (1974), Particle Diffusion in the Radiation Belts, *Physics and Chemistry in Space*, Volume 7, 215 pp., DM 78., edited by J.G. Roederer, Springer, Berlin, Heidelberg, New York.

Sergeev, V. A. and W. Lennartsson (1988), Plasma Sheet at X ~ -20 R_E During Steady Magnetospheric Convection, *Planetary Space Sci.* 36, 353.

Sergeev, V., T. Pulkkinen, R. Pellinen, and N. Tsyganenko (1994), Hybrid State of the Tail Magnetic Configuration during Steady Convection Events, J. Geophys. Res., 99(A12), 23571-23582.

Sergeev, V. A., R. J. Pellinen, and T. I. Pulkkinen (1996a), Steady magnetospheric convection: A review of recent results, *Space Sci. Rev.*, 75, 551.

Sergeev, V. A., V. Angelopoulos, J. T. Gosling, C. A. Cattell, and C. T. Russell (1996b), Detection of localized, plasma-depleted flux tubes or bubbles in the midtail plasma sheet, *J. Geophys. Res.*, 101, 10,817.

Sergeev, V. A., L. I. Vagina, R. D. Elphinstone, J. S. Murphree, D. J. Hearn, L. L. Cogger, and M. L. Johnson (1996c), Comparison of UV optical signatures with the substorm current wedge as predicted by an inversion algorithm, *J. Geophys. Res.*, 101(A2), 2615–2627.

Sergeev, V. A., and M.V. Kubyshkina (1996d), Low altitude image of particle acceleration and magnetospheric reconfiguration at a substorm onset, *J. Geomagn. Geoelectr.*, 48, 877-885.

Sergeev, V., et al. (1998), Short-duration convection bays and localized interplanetary magnetic field structures on November 28, 1995, *J. Geophys. Res.*, 103(A10), 23593-23609.

Sergeev, V., M. Kubyshkina, K. Liou, P. Newell, G. Parks, R. Nakamura, and T. Mukai (2001), Substorm and convection bay compared: Auroral and magnetotail dynamics during convection bay, *J. Geophys. Res.*, 106(A9), 18843-18855.

Shiokawa, K., W. Baumjohanna, and G. Haerendel (1997), Braking of high-speed flows in the near-Earth tail, *Geophys. Res. Lett.*, 24, 1179.

Shue, J.-H., P. Song, C. T. Russell, J. T. Steinberg, J. K. Chao, G. Zastenker, O. L. Vaisberg, S. Kokubun, H. J. Singer, T. R. Detman, H. Kawano (1998), Magnetopause location under extreme solar wind conditions, *J. Geophys. Res., 103* (A8), 17691-17700, doi:10.1029/98JA01103.

Siscoe, G. L., G. M. Erickson, B. U. Ö. Sonnerup, N. C. Maynard, J. A. Schoendorf, K. D. Siebert, D. R. Weimer, W. W. White, and G. R. Wilson (2002), Hill model of transpolar potential saturation: Comparisons with MHD simulations, *J. Geophys.*

Res., 107(A6), 1075, doi:10.1029/2001JA000109.

Sitnov, M. I., P. N. Guzdar, and M. Swisdak (2005), On the formation of a plasma bubble, *Geophys. Res. Lett.*, 32, L16103, doi:10.1029/2005GL023585.

Spence, H. E., and M. G. Kivelson (1990), The Variation of the Plasma Sheet Polytropic Index Along the Midnight Meridian in a Finite Width Magnetotail, *Geophys. Res. Lett.*, *17*, 591-594.

Spence, H. E., and M. G. Kivelson (1993), Contributions of the low-latitude boundary layer to the finite width magnetotail convection model, *J. Geophys. Res.*, *98*(A9), 15487.

Stiles, G., E. Hones Jr., S. Bame, and J. Asbridge (1978), Plasma Sheet Pressure Anisotropies, *J. Geophys. Res.*, 83(A7), 3166-3172.

Sugiura, M., and S. Chapman (1960), The average morphology of geomagnetic storms with sudden commencement, *A bandl. Akad. Wiss., Gottingen Math. Phys.*, K1 (4).

Sugiura, M. (1980), What do we expect in magnetic activity in the current solar cycle?, *Eos, Trans. AGU*, 61, 673.

Taktakishvili, A., M. M. Kuznetsova, M. Hesse, M.-C. Fok, L. Rastatter, M. Maddox, A. Chulaki, T. I. Gombosi, and D. L. De Zeeuw (2007), Buildup of the ring current during periodic loading-unloading cycles in the magnetotail driven by steady southward interplanetary magnetic field, *J. Geophys. Res., 112*, A09203, doi:10.1029/2007JA012317.

Toffoletto, F. R., J. Birn, M. Hesse, R.W. Spiro, and R.A. Wolf (2001), Modeling inner magnetospheric electrodynamics, in *Proceedings of the Chapman Conference on Space Weather*, edited by P. Song, G.L. Siscoe, and H.J. Singer, Am. Geophys. Un., Washington, D. C., pp. 265-272.

Toffoletto, F. R., S. Sazykin, R. W. Sprio, and R. A. Wolf (2003), Inner magnetospheric modeling with the Rice Convection Model, *Space Sci. Rev., 107*, 175.

Toffoletto, F. R., R. A. Wolf, S. Sazykin, C. Crabtree, W. Horton (2007), Tests and consequences of ballooning in the RCM-E, *Eos Trans. AGU, 88*(52), Fall Meet. Suppl., Abstract SM13A-1113.

Toffoletto, F. R., J. Yang, R. A. Wolf, S. Sazykin, C. Crabtree (2008), Simulation of a substorm Growth and Expansion phases using the RCM-E, *Eos Trans. AGU, 89*(23), West. Pac. Geophys. Meet. Suppl., Abstract SP51A-01.

Tsyganenko, N. A. (1989), Magnetospheric magnetic field model with a warped tail current sheet, *Planet. Space Sci.*, 37, 5– 20.

Tsyganenko, N.A. (1995), Modeling the Earth's magnetospheric magnetic field confined within a realistic magnetopause, *J.Geophys.Res.*, v.100, 5599-5612.

Tsyganenko, N.A. and D.P. Stern (1996), Modeling the global magnetic field of the large-scale Birkeland current systems, *J.Geophys.Res.*, v.101, 27187-27198.

Tsyganenko, N. A. (1997), An empirical model of the substorm current wedge, *J. Geophys. Res.*, 102, 19,935-19,941.

Tsyganenko, N. A. A model of the near magnetosphere with a dawn-dusk asymmetry 1. Mathematical structure (2002a), *J. Geophys. Res. 107*, 2001JA000219, 2002.

Tsyganenko, N. A. A model of the near magnetosphere with a dawn-dusk asymmetry 2. Parameterization and fitting to observations (2002b), *J. Geophys. Res.* 107, 2001JA000220, 2002.

Tsyganenko, N. A., and T. Mukai (2003), Tail plasma sheet models derived from Geotail particle data, *J. Geophys. Res., 108*(A3), 1136, doi:10.1029/2002JA009707.

Tsyganenko, N. A., and D. H. Fairfield (2004), Global shape of the magnetotail current sheet as derived from Geotail and Polar data, *J. Geophys. Res.*, 109, A03218, doi:10.1029/2003JA010062.

Tsyganenko N. A., M. I. Sitnov (2005), Modeling the dynamics of the inner magnetosphere during strong geomagnetic storms, *J. Geophys. Res.*, 110, A03208, doi:10.1029/2004JA010798.

Tung, Y.-K., C. W. Carlson, J. P. McFadden, D. M. Klumpar, G. K. Parks, W. J. Peria, and K. Liou (2001), Auroral polar cap boundary ion conic outflow observed on FAST, *J. Geophys. Res., 106*, 3603.

Vanhamäki, H., K. Kauristie, O. Amm, A. Senior, D. Lummerzheim and S. Milan (2009), Electrodynamics of an omega-band as deduced from optical and magnetometer data, *Ann. Geophys.*, 27, 3367-3385.

Vasyliunas, V. M. (1970), Mathematical models of magnetospheric convection and its coupling to the ionosphere, in *Particles and Fields in the Magnetosphere*, edited by B. M. McCormac, pp. 60– 71, Springer, New York.

Voigt, G.-H., and R. A. Wolf (1988), Quasi-static magnetospheric MHD processes and the ''ground state'' of the magnetosphere, *Rev. Geophys.*, 26, 823.

Volkov, M. A., and Y. P. Mal'tsev (1986), A slot instability of the inner boundary of the plasma layer, *Geomagn. Aeron.*, 26, 671.

Walsh, A. P., Fazakerley, A. N., Lahiff, A. D., Volwerk, M., Grocott, A., Dunlop, M. W., Lui, A. T. Y., Kistler, L. M., Lester, M., Mouikis, C., Pu, Z., Shen, C., Shi, J., Taylor, M. G. G. T., Lucek, E., Zhang, T. L., and Dandouras, I. (2009), Cluster and Double Star multipoint observations of a plasma bubble, *Ann. Geophys.*, 27, 725-743.

Wang, C.-P., L. R. Lyons, M. W. Chen, and R. A. Wolf (2001), Modeling the quiet time inner plasma sheet protons, *J. Geophys. Res.*, 106(A4), 6161–6178.

Wang, C.-P., L. R. Lyons, M. W. Chen, and F. R. Toffoletto (2004), Modeling the transition of the inner plasma sheet from weak to enhanced convection, *J. Geophys. Res.*, 109, A12202, doi:10.1029/2004JA010591.

Wang, C.-P., L. R. Lyons, R. A. Wolf, T. Nagai, J. M. Weygand, and A. T. Y. Lui (2009), Plasma sheet $PV^{5/3}$ and nV and associated plasma and energy transport for different convection strengths and AE levels, *J. Geophys. Res.*, 114, A00D02, doi:10.1029/2008JA013849.

Williams, D. J., R. W. McEntire, C. Schlemm II, A. T. Y. Lui, G. Gloeckler, S. P. Christon, and F. Gliem (1994), The Geotail Energetic Particles and Ion Composition (EPIC) instrument, *J. Geomag. Geoelectr.*, 46, 39-57.

Wilson, G. R., D. M. Ober, G. A. Germany, and E. J. Lund (2004), Nightside auroral zone and polar cap ion outflow as a function of substorm size and phase, *J. Geophys. Res., 109*, A02206, doi:10.1029/2003JA009835.

Wing, S., J. W. Gjerloev, J. R. Johnson, and R. A. Hoffman (2007), Substorm plasma sheet ion pressure profiles, *Geophys. Res. Lett., 34*, L16110, doi:10.1029/2007GL030453.

Wolf, R. A. (1983), The quasi-static (slow-flow) region of the magnetosphere, in *Solar Terrestrial Physics*, edited by R. L. Carovillano and J. M. Forbes, pp. 303–368, Series, D. Reidel, Hingham, Mass.

Wolf, R. A., R. W. Spiro and F. J. Rich (1991), Extension of the Rice Convection Model into the high-latitude ionosphere, *J. Atm. Terrest. Phys.*, 53, 817.

Wolf, R. A. (1995), *Physics of the Magnetosphere*, "Magnetospheric Physics" course notes.

Wolf, R. A., F. R. Toffoletto, R. W. Spiro, M. Hesse, and J. Birn (2002), Magnetospheric substorms: An inner-magnetospheric modeling perspective, in *Space Weather Study Using Multi-Point Techniques,* ed. L. H. Lyu, pp. 221-229, Elsevier Science Ltd. Oxford, England.

Wolf, R. A., V. Kumar, F. R. Toffoletto, G. M. Erickson, A. M. Savoie, C. X. Chen, and C. L. Lemon (2006a), Estimating local plasma sheet $PV^{5/3}$ from single-spacecraft measurements, *J. Geophys. Res., 111*, A12218, doi:10.1029/2006JA012010.

Wolf, R. A., R. W. Spiro, S. Sazykin, F. R. Toffoletto, P. L. Sager, and T. S. Huang (2006b), Use of Euler potentials for describing magnetosphere-ionosphere coupling, *J. Geophys. Res.*, *111*, A07315, doi: 10.1029/2005JA011558.

Wolf, R. A., Y. Wan, X. Xing, J.-C. Zhang, and S. Sazykin (2009), Entropy and plasma sheet transport, *J. Geophys. Res.*, 114, A00D05, doi:10.1029/2009JA014044.

Wu, H., T. W. Hill, R. A. Wolf, and R. W. Spiro (2007), Numerical simulation of fine structure in the Io plasma torus produced by the centrifugal interchange instability, *J. Geophys. Res.*, 112, A02206, doi:10.1029/2006JA012032.

Xing, X., and R. A. Wolf (2007), Criterion for interchange instability in a plasma connected to a conducting ionosphere, *J. Geophys. Res.*, 112, A12209, doi:10.1029/2007JA012535.

Xing, X., et al. (2008), Plasma Sheet Pressure Evolution Associated With Substorm Onset, *AGU*, Fall Meeting 2008, SM43A-1703.

Yang, J., F. R. Toffoletto, R. A. Wolf, S. Sazykin, R. W. Spiro, P. C. Brandt, M. G. Henderson, and H. U. Frey (2008), Rice Convection Model simulation of the 18 April 2002 sawtooth event and evidence for interchange instability, *J. Geophys. Res.*, 113, A11214, doi:10.1029/2008JA013635.

Yang, J., F. R. Toffoletto, R. A. Wolf, G. M. Erickson, and S. Sazykin (2009a), Modeling of a substorm event using the Rice Convection Model with an equilibrium magnetic field: 1. Growth Phase, *J. Geophys. Res.,* to be submitted.

Yang, J., F. R. Toffoletto, R. A. Wolf, G. M. Erickson, and S. Sazykin (2009b), Modeling of a substorm event using the Rice Convection Model with an equilibrium magnetic field: 2. Expansion Phase, *J. Geophys. Res.,* to be submitted.

Yang, J., F. R. Toffoletto, G. M. Erickson, and R. A. Wolf (2009c), Superposed epoch study of $PV^{5/3}$ during substorms, pseudo-breakups and convection bays, *Geophys. Res. Lett.,* to be submitted.

Yau, A. W., P. H. Beckwith, W. K. Peterson, and E. G. Shelley (1985), Long-term (solar cycle) and seasonal variations of upflowing ionospheric ion events at DE1 altitudes, *J. Geophys. Res., 90*, 6395.

Zaharia S., C. Z. Cheng (2003), Near-Earth thin current sheets and Birkeland currents during substorm growth phase, *Geophys. Res. Lett.*, 30 (17), 1883, doi:10.1029/2003GL017456.

Zaharia, S., V. K. Jordanova, M. F. Thomsen, and G. D. Reeves (2006), Self-consistent modeling of magnetic fields and plasmas in the inner magnetosphere: Application to a geomagnetic storm, *J. Geophys. Res.*, 111, A11S14, doi:10.1029/2006JA011619.

Zhang, J.-C., R. A. Wolf, S. Sazykin, and F. R. Toffoletto (2008), Injection of a bubble into the inner magnetosphere, *Geophys. Res. Lett.*, 35, L02110, doi:10.1029/2007GL032048.

Zhang, J.-C., R. A. Wolf, G. M. Erickson, R. W. Spiro, F. R. Toffoletto, and J. Yang (2009a), Rice Convection Model simulation of the substorm associated injection of an observed bubble into the inner magnetosphere: Magnetic-field and other inputs, J.

Geophys. Res., doi:10.1029/2009JA014130, in press.

Zhang, J.-C., R. A. Wolf, R. W. Spiro, G. M. Erickson, S. Sazykin, F. R. Toffoletto, and J. Yang (2009b), Rice Convection Model simulation of the substorm associated injection of an observed bubble into the inner magnetosphere: Simulation results, *J. Geophys. Res.*, doi:10.1029/2009JA014131, in press.

Zhu, P., J. Raeder, K. Germaschewski, and C. C. Hegna (2009), Initiation of ballooning instability in the near-Earth plasma sheet prior to the 23 March 2007 THEMIS substorm expansion onset, *Ann. Geophys.*, 27, 1129-1138.